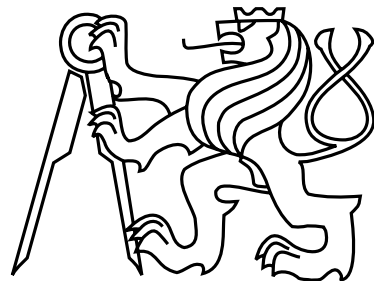


**Czech Technical University in Prague
Faculty of Nuclear Sciences and Physical Engineering**



DOCTORAL THESIS
Metamaterials for the terahertz spectral range

Prague 2016

Ing. Filip Dominec

Bibliografický záznam

| | |
|-----------------------|---|
| Autor: | Ing. Filip Dominec České vysoké učení technické v Praze Fakulta jaderná a fyzikálně inženýrská Katedra fyzikální elektroniky |
| Název práce: | Metamateriály pro terahertzovou spektrální oblast |
| Studijní program: | Aplikace přírodních věd |
| Studijní obor: | Fyzikální inženýrství |
| Školitel: | Mgr. Filip Kadlec, Dr. Fyzikální ústav Akademie věd České republiky |
| Školitel specialista: | Doc. Ing. Ivan Richter, Dr. České vysoké učení technické v Praze Fakulta jaderná a fyzikálně inženýrská Katedra fyzikální elektroniky |
| Akademický rok: | 2015/16 |
| Počet stran: | 205 |
| Klíčová slova | metamateriály, fotonické krystaly, terahertzová technologie, elektrodynamické simulace, homogenisace efektivních prostředí |

Bibliographic entry

| | |
|------------------------|--|
| Author: | Ing. Filip Dominec Czech Technical University in Prague Faculty of Nuclear Sciences and Physical Engineering Department of Physical Electronics |
| Title of Dissertation: | Metamaterials for the terahertz spectral range |
| Degree Programme: | Applications of natural sciences |
| Field of Study: | Physical engineering |
| Supervisor: | Mgr. Filip Kadlec, Dr. Institute of Physics Academy of Sciences of the Czech Republic |
| Supervisor specialist: | doc. Ing. Ivan Richter, Dr. Czech Technical University in Prague Faculty of Nuclear Sciences and Physical Engineering Department of Physical Electronics |
| Academic Year: | 2015/2016 |
| Number of Pages: | 205 |
| Keywords | metamaterials, photonic crystals, terahertz technology, computational electrodynamics, homogenisation of effective media |

Abstrakt

Při interakci elektromagnetických vln s periodickými strukturami lze pozorovat neobvyklé jevy, jako jsou záporný index lomu, fotonický zakázaný pás nebo silná prostorová disperze. Tyto struktury lze navrhnout tak, aby se chovaly žádoucím způsobem, a označují se jako metamateriály nebo jako fotonické krystaly. Část z jejich navrhovaných využití je v technice terahertzových vln, kde můžou překlenout poměrně slabé možnosti klasických součástek.

Teoretický základ práce vychází z elektrodynamiky prostředí s frekvenční disperzí, která je dále zobecněna na prostředí s prostorovou disperzí a na Blochovu-Floquetovu teorii vln v periodických strukturách. Závěr teoretické části se pokouší vyjasnit pojmy používané v literatuře a ukázat, že myšlenky metamateriálů i fotonických krystalů jsou ve skutečnosti starší, než se často uvádí.

Obecná teorie je doplněna příklady terahertzového chování různorodých periodických struktur, které bylo vypočteno metodou konečných diferencí v časové doméně (FDTD). V některých případech byly její výsledky podloženy jinými simulačními algoritmy nebo měřeními pomocí terahertzové spektroskopie v časové doméně.

Srovnání různých struktur si klade za cíl srozumitelnou formou prezentovat a vysvětlit nejpodstatnější principy. Podobné srovnání zřejmě v dosavadní literatuře chybělo. Klíčové výsledky spočívají v popisu přechodu mezi režimy metamateriálu a fotonického krystalu v periodickém poli dielektrických tyčinek a v důkazech toho, že k popisu chování řady uvedených struktur je zcela nezbytné uvažovat prostorovou dispersi. V neposlední řadě práce dokládá možnosti simulačních skriptů, které autor vyvinul a uveřejnil na internetu s úmyslem podpořit další výzkum v této oblasti.

Abstract

Unusual phenomena such as negative index of refraction, photonic band gaps, or strong spatial dispersion are observed when electromagnetic waves interact with periodic structures. These can be designed to manipulate the wave in an advantageous way, and are known either as metamaterials or photonic crystals. Part of their proposed applications are for the terahertz technology, where they may address relatively poor performance of classical components.

The theoretical background is derived from the electrodynamics of media with classical dispersion, which is later generalized to spatially dispersive media and to the Bloch-Floquet theory of waves in periodic structures. The end of the theoretical part attempts to clarify the terminology used in the literature, and to show that the concepts of metamaterials and photonic crystals are in fact older than is sometimes assumed.

The general theory is complemented with examples of the behaviour of diverse periodic structures in the terahertz range, which was numerically simulated by the finite-difference time-domain method. In some cases, the results of this simulation method were supported by other simulation algorithms or by the experimental measurement by the terahertz time-domain spectroscopy.

The comparison of different structures encompassed in this thesis attempts to present and explain most relevant principles in a didactic way. Arguably, such a comparison was missing in the previous literature. The key results are in the description of the transition between metamaterial and photonic crystal regimes in a periodic array of dielectric rods, and in the demonstration of the fact that considering spatial dispersion is essential for the description of the behaviour of many periodic structures. Last but not least, the thesis demonstrates the capabilities of the simulation environment which the author developed and completely published online to stimulate further research in this field.

Acknowledgements

Preparation of this thesis was not without difficulties. However, it appears that overcoming such difficulties is essential to gain some sort of valuable knowledge that cannot be conveyed through textbooks, and of experience that cannot be gained through straightforward and focused work only. At the first place I wish to express thanks to my advisor, Dr. Filip Kadlec, and all other people who helped this project to be finished, namely Dr. Christelle Kadlec and doc. Petr Kužel from the Institute of Physics, and doc. Ivan Richter from the Faculty of Nuclear Engineering and Physical Sciences, Czech Technical University.

Discussions with doc. Lukáš Jelínek and prof. Jan Macháč convinced me about the value in proper handling of the theoretical background, which later proved essential for explaining the results of the thesis. During my stay in France in 2013, the collaboration with Dr. Mathias Vanwolleghem not only greatly contributed to my experience with the numerical simulations, but presented also a great motivation for me.

Almost surprisingly, all my scientific aspirations found a permanent and selfless support from all my family members, who always had patience with my focusing on abstract problems instead of the more practical aims and with my stubborn attitude towards some of their good advices.

The numerical results presented in the thesis could be hardly obtained without the work of hundreds of volunteers contributing to the open-source scientific software: Most of the plots were made using the Matplotlib library [1] and computations were based on MEEP [2] and MPB programs [3].

This work was financially supported by the Czech Science Foundation under Grant No. 14-25639S.

Contents

| | | |
|----------|--|-----------|
| 1 | Introduction | 9 |
| 1.1 | Electromagnetic waves in periodic structures | 9 |
| 1.2 | Motivation for terahertz photonics | 10 |
| 1.3 | Goals of the thesis | 10 |
| 1.4 | Thesis outline | 11 |
| 1.5 | Conventions used | 13 |
| 2 | Theory | 15 |
| 2.1 | Electrodynamics of local homogeneous media | 15 |
| 2.1.1 | Electromagnetic wave in vacuum | 15 |
| 2.1.2 | Local response of media to the electromagnetic field | 18 |
| 2.1.3 | Dispersion relations in local Lorentz media | 23 |
| 2.2 | Electrodynamics of nonlocal homogeneous media | 31 |
| 2.2.1 | Nonlocal response | 31 |
| 2.2.2 | Dispersion relations in nonlocal homogeneous media | 36 |
| 2.2.3 | Reflectance and transmittance at an interface of two local media | 40 |
| 2.2.4 | Phase, group, energy and signal velocities | 42 |
| 2.3 | Electromagnetic waves in periodic structures | 44 |
| 2.3.1 | Periodic structures and the Bloch's theorem | 44 |
| 2.3.2 | Dispersion in periodic structures | 50 |
| 2.3.3 | Band gaps | 53 |
| 2.4 | Historical notes on metamaterials and photonic crystals | 56 |
| 2.4.1 | One history of three paradigms | 56 |
| 2.4.2 | Photonic band-gap structures | 56 |
| 2.4.3 | Homogeneous media with uncommon parameters | 58 |
| 2.4.4 | Artificial dielectrics and metamaterials | 61 |
| 2.4.5 | First unification: metamaterials with uncommon parameters . | 62 |
| 2.4.6 | Second unification: metamaterials with photonic crystals . . | 65 |
| 2.5 | The boundary between photonic crystals and metamaterials | 66 |
| 3 | Numerical methods | 70 |
| 3.1 | Numerical simulation algorithms | 70 |
| 3.1.1 | Finite-difference time-domain method | 70 |
| 3.1.2 | Finite-difference frequency-domain method | 79 |
| 3.1.3 | Plane-wave expansion method | 81 |
| 3.2 | Simulation set-ups for metamaterial homogenisation | 81 |

| | | |
|----------|---|------------|
| 3.2.1 | Retrieval of the scattering parameters | 82 |
| 3.2.2 | Current-driven homogenisation | 95 |
| 3.2.3 | Other effective parameter retrieval methods | 99 |
| 4 | Experimental methods | 102 |
| 4.1 | Short review of the terahertz technology | 102 |
| 4.1.1 | Terahertz sources | 103 |
| 4.1.2 | Terahertz detectors | 107 |
| 4.2 | Terahertz time-domain spectroscopy | 108 |
| 4.2.1 | Simultaneous reflectance and transmittance measurement . . | 110 |
| 4.3 | Preparation of the titanium dioxide microspheres | 112 |
| 4.4 | Optical determination of microparticle statistics | 117 |
| 4.5 | Laser cutting | 118 |
| 5 | Results | 121 |
| 5.1 | Dielectric slab | 121 |
| 5.2 | Wire medium | 126 |
| 5.3 | Cut wires | 130 |
| 5.4 | Split-ring resonator | 135 |
| 5.5 | Combined electric and magnetic resonator | 143 |
| 5.6 | Dielectric spheres | 149 |
| 5.7 | Dielectric rods parallel to the magnetic field | 158 |
| 5.8 | Dielectric rods parallel to the electric field | 160 |
| 5.9 | Metallic sheet with slits | 170 |
| 5.10 | Fishnet | 175 |
| 6 | Conclusion | 181 |

Chapter 1

Introduction

1.1 Electromagnetic waves in periodic structures

The peculiar behaviour of light in periodic structures has attracted human attention for ages, long before anybody perceived that light is an *electromagnetic wave* or that it is the *periodicity* which is responsible for the brilliant and irreproducible colours of opal gemstones and many living creatures, such as various beetles, butterflies or peacocks.

The scientific community started to rigorously study the underlying phenomena in the late 19th century. Simultaneous theoretical and technological progress through the 20th century allowed to design custom structures that interact with electromagnetic waves in a desired way. In analogy with the rapidly growing field of *electronics*, the term of *photonics* was coined for the design of optical fibres and other waveguides, sources, filters, detectors etc. The rapid development in this field was enabled by the modern technology of microfabrication, along with the unprecedented power of computers used for numerical simulations. Nowadays, photonics-based devices play a vital role in the high-bandwidth telecommunication, science and industry.

Out of all structures studied in photonics, particularly detailed theoretical studies were devoted to structures that are periodic. Three paradigms related to the physics of periodic structures developed independently. While *photonic crystals* were inspired by the electron waves, *metamaterials* were inspired by the electromagnetic waves in crystals. Early treatises on electrodynamics of *media with negative or unusual parameters* did not assume any structuring or other way of how these parameters should be achieved. As a result of a natural development, the paradigms unified into one, and this thesis tries to describe them in an unified manner.

The essential concept is that the electromagnetic properties of a periodic structure can be, at least partially, understood as those of a homogeneous medium, but in fact they are determined predominantly by the spatial arrangement of the structure's unit cell. The actual constituent materials can be relatively freely chosen. While it is unlikely that a radically new homogeneous material will be invented for construction of optical elements, periodic structuring of ordinary materials provides unprecedented freedom in tuning the electromagnetic properties and even enables to obtain phenomena unusual in homogeneous materials.

1.2 Motivation for terahertz photonics

This work focuses on the electromagnetic behaviour of periodic structures operating in the terahertz (THz) spectral range, which spans roughly from 100 GHz to 10 THz. While the electrodynamic theory presented in this work is scale-invariant and can be used in the whole electromagnetic spectrum, the selected frequency range defines the properties of available constituent materials and technological processes. Compared to the well established optical technology (400—700 THz), the range of materials suitable for THz frequencies gives additional possibilities, such as the use of superconductors, extremely high-permittivity dielectrics and tunable ferroelectrics. Additionally, the much longer wavelength of terahertz waves, e.g. 300 μm for 1 THz in free space, also enables much easier fabrication of relevant structures. On the other hand, materials such as glass and most plastics, commonly used in other spectral ranges, must be avoided, since they exhibit excessively high losses in the terahertz range.

The terahertz range is located in the electromagnetic spectrum at the boundary between the microwave region where most often the approaches of high-frequency electronics are used, and the infrared and optical region where the classical optics is used [4]. At THz frequencies, both approaches are often seamlessly used together: waves emitted from lumped semiconductor components can be collimated by lenses, picosecond pulses generated in nonlinear crystals can be detected by photoconductive sampling, etc.

Yet none of these two approaches is optimal for the THz applications; from the electronic point of view, there is still demand for fast-enough semiconductor devices and also the microstrip circuits become too lossy at high frequencies. The optical approach is often burdened by the strong wave-optics phenomena such as diffraction, and moreover some light-matter interactions are weaker than at the optical frequencies, limiting the possibilities for e.g. amplitude modulation by the Pockels effect.

These deficiencies provide additional reasons to search for the new possibilities opened by photonic devices and periodic structures operating in the terahertz range.

1.3 Goals of the thesis

1. During the preparation of the thesis, its author realized that it is difficult to find a focused, accessible, yet rigorous enough tutorial covering the necessary theory. The main aim of the theoretical section therefore lies in bridging the fundamental electrodynamics with the concepts used for a description of metamaterials and photonic crystals.
2. The importance of the more general *spatially-dispersive* electrodynamics is emphasized, although it is unfortunately often neglected in the literature in favour of the simpler *local* electrodynamics. Both approaches are compared throughout the thesis.

3. The third aim of this thesis is to promote the unification of paradigms, i.e. *photonic crystals*, *metamaterials*, by showing that they can – and should – be described by the same theoretical approaches. This is supported by elaborating the concept of spatial dispersion in the theoretical section and by providing historical review of the surprisingly long parallel development of such structures.
4. A overview of the electromagnetic behaviour of diverse periodic structures is provided in the Results section, taking into account also the properties of materials available for THz photonics, with the realistic level of absorption in particular. This section is more than just results – proceeding from simpler structures to the more complex ones, it aims to explain all observed phenomena in a didactic manner. Some of the simulations are verified against the experimental results from the terahertz measurements.
5. Last but not least, the numerical results present a small demonstration of the use of the extensive simulation scripts, which were developed during the doctoral project and were published online for the scientific community. The basic concepts of the numerical simulations are described to help others in adapting the simulations for their further research.

1.4 Thesis outline

Theory The theoretical chapter starts with a review of linear *electrodynamics of continuous media*; the concepts of harmonic oscillators, dispersion curves, isofrequency contours and the generalized index of refraction are introduced, and it is demonstrated how the wave refraction depends on the shape of isofrequency contours.

The electrodynamic theory is generalized to account for the *nonlocal* response, or equivalently *spatial dispersion*, in the medium – a phenomenon which can be usually neglected in natural media, but is of key importance in any conscientious treatise on electrodynamics of periodic structures. The more general Landau-Lifshitz formulation of nonlocal medium parameters is also introduced and shown to be compatible with the customary model.

The third part of the theoretical section is dedicated to periodic structures, starting with the Bloch theorem that enables one to transfer some of the concepts from continuous optics even to waves propagating in periodic structures. Its impact on the form of dispersion curves and on the ambiguity of the wave vector is shown.

The distinction of two widely recognized types of periodic structures, namely *metamaterials* and *photonic crystals*, is discussed from historical aspects, with an emphasis on the author’s view that the theoretical approaches used for each field can be unified and used for the other field as well.

Experimental methods As a part of the research several experiments in the terahertz laboratory were performed. This section is opened by a systematic review of the terahertz sources and detectors, followed by the description of the terahertz

time-domain spectroscopy setup used in our laboratory for characterisation of the samples.

The fabrication and characterisation of the titanium dioxide microspheres samples is described in detail, with particular emphasis on the newly developed technique of acoustic-wave assisted sorting on anisotropic sieves. The section is concluded by the description of laser micromachining of the sieves and of the metallic meshes, which were used as electromagnetic filters.

Numerical methods This section describes the tools and methods used to calculate the electromagnetic behaviour of periodic structures and, even more importantly, to understand the physical nature of the predicted phenomena. Its structure reflects the separation between the algorithms that solve the Maxwell equations as a purely numerical problem, and between their particular application.

Its first part provides a comparison of the finite-difference time-domain simulation (FDTD), its frequency-domain modification (FDFD) and the plane-wave expansion methods (PWEM). We point out the capabilities of each of them and we also briefly review multiple other methods that were not used here. Defining numerically stable FDTD simulations with realistic materials, one encounters several pitfalls. They were painstakingly resolved during the preparation of the thesis, and are also presented here.

The second part describes the setups of the "numerical experiments" that are built atop the algorithms. The time-domain simulation is first used in conjunction with the scattering-parameter retrieval setup, which is based on transmitting a broadband pulse towards a metamaterial unit cell and recovering its effective parameters from the reflected and transmitted fields. While this setup is shown to give mostly realistic results, however, it has its limitations which are also presented. Although the scattering-parameter retrieval seems by far the most commonly used, different setups were described in the literature which are briefly noted. One of such simulation setups of the current-driven homogenisation is presented in details, and it is shown that its weaker prior assumptions on the structure behaviour lead to higher reliability.

Results, conclusion and appendices The Results section puts the common metamaterial types into a perspective, pointing out what they have in common and how they differ. While the space of all imaginable structures can never be covered, most metamaterials fall into one of several classes, of which each can be demonstrated by few examples. Another aim of this section is to demonstrate the capabilities of the simulation scripts used.

The scale of the simulated structures is chosen for the structures to operate in the terahertz range. Thanks to the scale invariance of Maxwell equations, many of the designs and observations can be transposed also into other spectral regions, be it microwave or infrared. However, one has to bear in mind that the properties of the constituent materials may be different in other spectral regions. Naturally, also the techniques of fabrication and characterisation may be different.

Some of the structures discussed were also fabricated and experimentally characterized during this PhD project. The results from the simulations were verified against experimental data and analytic models.

At the end of the thesis, somewhat critical conclusions from the above results are drawn, along with directions in which the research could be pursued in future.

1.5 Conventions used

Throughout the thesis, a single or double apostrophe (x', x'') refers to the real and imaginary part of a complex number (x). Italic symbols represent the magnitudes of vectors, which are denoted by respective bold symbols (e.g. $k = |\mathbf{k}|$). Components of vectors are denoted by small indices, such as k_x, k_y, k_z . The index and lists of symbols and abbreviations are included at the end of the thesis.

An important note shall be made on the sign convention for the complex wave, as introduced in Eq. (2.9). The ‘engineering’ convention of time dependence of the complex exponential $e^{+i\omega t}$ is used, but this is only due to the author’s feeling that it is more natural when the wave phase grows in time. Such a convention is shared with roughly a half of the literature, e.g. [5, p. 9], [6, pp. 21 and 99], [7, Chapters 1-4, 6, 9 and 10]. In the remaining part, e.g. [7, chapters 5, 7, 8], [8], [9], [10], [11], [12, p. 5], the opposite, ‘optical’, convention is used with time dependence of $e^{-i\omega t}$. The choice of $e^{+i\omega t}$ or $e^{-i\omega t}$ determines the sign of the imaginary part in virtually all complex quantities discussed in this thesis, but with correct interpretation it makes no difference in the physical conclusions. In the real world, observable fields do not have any imaginary component so the real part of the result has to be taken.

In the $e^{+i\omega t}$ convention, many parameters of a passive (lossy) system are restricted to have a *negative imaginary part*. An additional complication arises from that a part of the authors using $e^{+i\omega t}$ convention still wish to represent the imaginary part as *positive*, and they define complex quantities as, e.g., $\varepsilon = \varepsilon' - i\varepsilon''$, thus in their case $\varepsilon'' \equiv -\text{Im}(\varepsilon)$. This is not the case of this thesis, and the real and imaginary parts are represented naturally as $\varepsilon := \varepsilon' + i\varepsilon''$.

The unit system differs across the literature, too. Some of the references, e.g. [13, 14, 15] use the older centimetre-gram-second (CGS) system, which for instance leaves out the dimension constants of ε_0, μ_0 . The whole thesis uses consistently the metre-kilogram-second (SI) system.

Having listed conventions we use, we should mention one convention we will avoid using. The term *transverse-magnetic* (TM, or equivalently, *p-polarized*) wave has its established meaning for oblique incidence on a homogeneous interface: it means that the magnetic field is perpendicular to the plane of incidence, and thus always parallel to the interface. The term *transverse-electric* (TE, or, *s-polarized*) denotes the opposite situation.

Unfortunately, the same notation is used by many papers also for a perpendicular incidence on a grating or other structure with 1-D periodicity. In majority of cases “TM” denotes that *the magnetic field is transverse to the translation axis of the structure, the electric field parallel to it* [16, 17]. Alas, in numerous other cases the same term “TM” denotes an opposite interpretation, i.e., that *the magnetic field is*

perpendicular to the 2-D plane that represents the whole electromagnetic problem, and the electric field component lies in this plane [18]. Even greater complication arises under oblique illumination of a grating. These two different meanings of apparently identical terms can either come into a confusing discrepancy (TE+TM), an even more confusing agreement (TE+TE or TM+TM), or may also become inapplicable under general geometry of the wave or its polarisation.

Chapter 2

Theory

“There is nothing more practical than a good theory.” — probably K. Lewin

2.1 Electrodynamics of local homogeneous media

2.1.1 Electromagnetic wave in vacuum

Maxwell equations In the realm of classical physics, the electromagnetic phenomena are governed by the *Maxwell equations* in the following form. We assume here that no free charges and no sources of currents are present:

$$\nabla \cdot \mathbf{D} = 0, \quad (2.1)$$

$$\nabla \cdot \mathbf{B} = 0, \quad (2.2)$$

$$\nabla \times \mathbf{E} = -\frac{\partial \mathbf{B}}{\partial t}, \quad (2.3)$$

$$\nabla \times \mathbf{H} = \frac{\partial \mathbf{D}}{\partial t}, \quad (2.4)$$

where \mathbf{E} and \mathbf{H} are the electric and magnetic vector fields, and \mathbf{D} and \mathbf{B} are the electric and magnetic displacements, respectively. These two pairs of field and displacement are related in a similar way as a force is related to the deformation. The *constitutive relations* depend on the properties of the medium the wave propagates in, and in vacuum they take the simplest possible form:

$$\mathbf{D} = \epsilon_0 \mathbf{E}, \quad \mathbf{B} = \mu_0 \mathbf{H}, \quad (2.5)$$

$\epsilon_0 \approx 8.85 \cdot 10^{-12}$ F/m being the *vacuum permittivity* and $\mu_0 = 4\pi \cdot 10^{-7} \approx 1.25 \cdot 10^{-6}$ H/m the *vacuum permeability*. Pages 16–187 of this thesis will be concerned with computation, interpretation, and experimental verification of the solutions of Eq. (2.1–2.4) for specific choices of constitutive relations.

Wave equation in vacuum The pair of first-order differential equations (2.3, 2.4) can be converted to a single second-order differential equation. To this end, we apply an extra curl operator $\nabla \times$ from the left, and substituting one equation into the other, we obtain two curl operators on the left hand side and two derivatives on the right hand side:

$$\nabla \times (\nabla \times \mathbf{E}) = \nabla \times \left(-\frac{\partial \mathbf{B}}{\partial t} \right) = -\mu_0 \frac{\partial}{\partial t} (\nabla \times \mathbf{H}) = -\mu_0 \frac{\partial^2 \mathbf{D}}{\partial t^2} = -\mu_0 \epsilon_0 \frac{\partial^2 \mathbf{E}}{\partial t^2}. \quad (2.6)$$

Using the vector calculus identity

$$\nabla \times (\nabla \times \mathbf{E}) \equiv \nabla(\nabla \cdot \mathbf{E}) - \nabla^2 \mathbf{E}, \quad (2.7)$$

we obtain the *wave equation* for the electric field in vacuum:

$$\nabla(\nabla \cdot \mathbf{E}) - \nabla^2 \mathbf{E} = -\mu_0 \epsilon_0 \frac{\partial^2 \mathbf{E}}{\partial t^2}. \quad (2.8)$$

Starting with Eq. (2.4) instead of (2.3), an analogous result can also be easily obtained for the magnetic field \mathbf{H} .

Plane wave The solutions of the linear wave equation (2.8) can be decomposed into a sum of *harmonic plane waves*, where *harmonic* means that the amplitude depends on the time t as a harmonic function (e.g. $\sin(\omega t)$ or $e^{i\omega t}$). As a *plane wave* we denote a spatial shape of the fields that is a function of a single scalar parameter $\mathbf{k} \cdot \mathbf{r}$, where \mathbf{k} is an arbitrary vector and \mathbf{r} is the position vector. Assuming the wave propagates with a nonzero constant velocity, it follows that also the spatial dependence of the fields is harmonic. Any other complicated shape of the fields can be decomposed into a linear superposition of more such waves and treated separately [9].

The electromagnetic field can be described as a complex exponential, i.e. as a superposition of two waves differing by a quarter-period phase shift, one defining the real part, one the imaginary part of the field. In comparison with the straightforward description of a plane wave in terms of a cosine (or sine) function, the complex notation formally simplifies some mathematical operations, namely, it allows one to identify easily the *phase of a wave* (divided by the imaginary unit) with the exponent.

We define the electric field as a function of time t and position in space \mathbf{r} , corresponding to a plane wave in the complex notation:

$$\mathbf{E}(t, \mathbf{r}) := \mathbf{E}_0 e^{i\omega t - i\mathbf{k} \cdot \mathbf{r}} \quad (2.9)$$

The plane wave is fully characterised by its *amplitude vector* \mathbf{E}_0 , *frequency* f or *angular frequency* $\omega = 2\pi f$ and *wave vector* \mathbf{k} . Note that no restrictions were put to the amplitude vector \mathbf{E}_0 so far, thus Eq. (2.9) can describe both *transverse wave* of any polarization, with $\mathbf{E}_0 \perp \mathbf{k}$, and *longitudinal wave* with $\mathbf{E}_0 \parallel \mathbf{k}$. As discussed in the introduction, the time dependence of complex fields with positive evolution in time ($e^{+i\omega t}$) was chosen without any impact on the physical conclusions.

Dispersion relations in vacuum Only some combinations of (E_0, ω, k) provide a physical solution of the wave equation (2.8). In vacuum, the allowed solutions can be obtained by first substituting the differential operators by their equivalents for a particular plane wave:

$$\nabla \rightarrow -ik, \quad \frac{\partial}{\partial t} \rightarrow i\omega, \quad (2.10)$$

so the wave equation (2.8) can be modified in the following way:

$$\begin{aligned} \nabla(\nabla \cdot \mathbf{E}) - \nabla^2 \mathbf{E} &= -\mu_0 \varepsilon_0 \frac{\partial^2 \mathbf{E}}{\partial t^2}, \\ -ik(-ik \cdot \mathbf{E}) - (-ik \cdot -ik)\mathbf{E} &= -\mu_0 \varepsilon_0 (i\omega)^2 \mathbf{E}, \\ -k(\mathbf{k} \cdot \mathbf{E}) + k^2 \mathbf{E} &= +\mu_0 \varepsilon_0 \omega^2 \mathbf{E}, \\ \perp_{\mathbf{k}} \mathbf{E} &= \frac{\mu_0 \varepsilon_0 \omega^2}{k^2} \mathbf{E}. \end{aligned} \quad (2.11)$$

The linear operation $\perp_{\mathbf{k}}$ of the left hand side can be geometrically interpreted as taking the transverse component of the field \mathbf{E} , that is, perpendicular to the wavevector \mathbf{k} .

$$\perp_{\mathbf{k}} \mathbf{E} := -\frac{\mathbf{k}(\mathbf{k} \cdot \mathbf{E})}{k^2} + \mathbf{E} \equiv -\frac{\mathbf{k} \times (\mathbf{k} \times \mathbf{E})}{k^2} \quad (2.12)$$

Rewriting it explicitly, in this thesis we define the *wavefront projection tensor* that will be useful in the following chapters, too:

$$\perp_{\mathbf{k}} = \frac{1}{k^2} \begin{pmatrix} k_y^2 + k_z^2 & -k_x k_y & -k_x k_z \\ -k_y k_x & k_x^2 + k_z^2 & -k_y k_z \\ -k_z k_x & -k_z k_y & k_x^2 + k_y^2 \end{pmatrix} \text{ or equivalently, } (\perp_{\mathbf{k}})_{ij} = -\frac{k_i k_j}{k^2} + \delta_{ij}. \quad (2.13)$$

The solutions of Eq. (2.11) for a harmonic plane wave in vacuum can be divided into two groups:

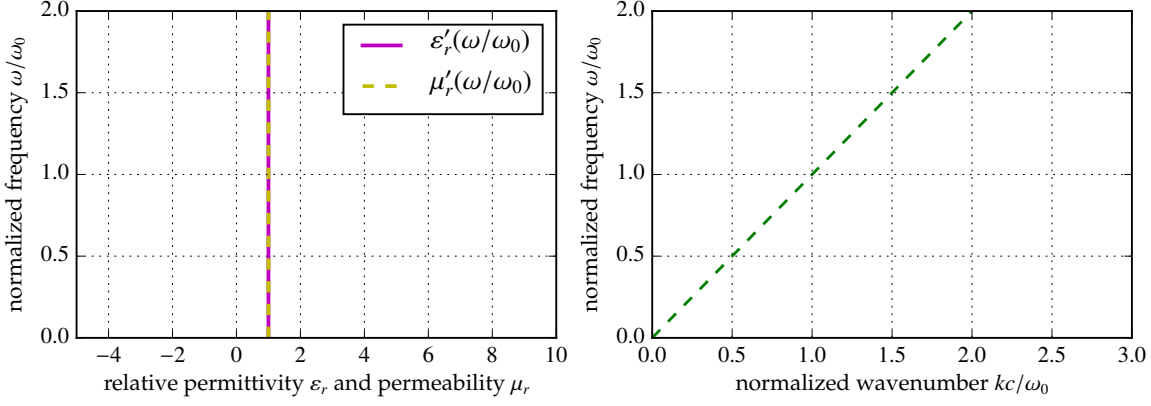
1. *Transverse electromagnetic waves*, with the electric field and wave vector being perpendicular, i.e. $(\mathbf{k} \cdot \mathbf{E}) = 0$ and thus $\perp_{\mathbf{k}} \mathbf{E} = \mathbf{E}$. Therefore, the *dispersion relation* for a transverse plane wave in vacuum is linear:

$$k = \sqrt{\mu_0 \varepsilon_0} \omega = \frac{\omega}{c}, \quad (2.14)$$

where we defined the *light velocity* $c := \frac{1}{\sqrt{\mu_0 \varepsilon_0}}$. The corresponding solution is plotted in Fig. 2.1, independent of the orientation of the wavevector \mathbf{k} . As an unanimously accepted convention, the pseudovector \mathbf{H} is chosen to be oriented so that the perpendicular *right-handed triplet* $\mathbf{E}, \mathbf{H}, \mathbf{k}$ can be easily indicated with the thumb, index and middle finger of the right hand (cf. Fig. 3.7). Vacuum is thus an example of the broad group of *right-handed* media.

2. *Longitudinal electromagnetic waves*, with $\mathbf{k} \parallel \pm \mathbf{E}$ and $\perp_{\mathbf{k}} \mathbf{E} = 0$, require the right side of Eq. (2.11) to be zero. In vacuum, there is no such a solution, except for a homogeneous static electric field ($k = 0, \omega = 0$), but they will be shown to exist in dispersive media.

Figure 2.1: Left panel shows the permittivity ϵ'_r and permeability μ'_r of vacuum being equal to 1; as a result, the dispersion curve for a transverse wave in vacuum forms a straight line in the right panel. As in the case of similar plots later, both axes of the right panel are normalized to an arbitrary frequency of ω_0 , because the characteristic curve shapes are independent of the scale.



2.1.2 Local response of media to the electromagnetic field

Local response definition In the whole chapter, we expect the medium properties to be time-invariant, linear, and homogeneous (i.e. independent of time, field amplitude and position in space, respectively). In this section, we focus on the special case when the response of the medium in point r is not influenced by the electric field in any other point $\rho \neq r$. The medium is then said to be *local*. For most media found in nature, this approximation is very close to reality, except for optics on the nanometric scale [19]. Hence, most electrodynamics textbooks omit the discussion of nonlocal effects. However, using the local theory to a Bloch's wave propagating through periodic structures has a priori no justification and may lead to completely wrong results. The local theory presented here will serve as a basis for the nonlocal theory developed in following chapters.

When an electric field \mathbf{E} is applied, the medium responds by a change of the electric displacement \mathbf{D} in a characteristic way. The immediate linear relation between \mathbf{E} and \mathbf{D} observed in vacuum, appearing at the right side of the constitutive equations (2.5), remains unchanged, but the response of the matter complements it with a new term called *electric polarisation*. The polarisation is not instantaneous, so it is generally expressed as a convolution of the *response function* χ_e with the values of electric field in the previous time τ :

$$\mathbf{D}(t, \mathbf{r}) = \epsilon_0 \mathbf{E}(t, \mathbf{r}) + \epsilon_0 \int_{-\infty}^t \chi_e(t - \tau) \mathbf{E}(\tau, \mathbf{r}) d\tau. \quad (2.15)$$

Let us assume that a harmonic plane wave propagates through the medium, so $\mathbf{E}(t, \mathbf{r}) := \mathbf{E}_0 e^{i\omega t - i\mathbf{k} \cdot \mathbf{r}}$, as given by Eq. (2.9). This can be inserted in the above equation:

$$\mathbf{D}(t, \mathbf{r}) = \epsilon_0 \mathbf{E}_0 e^{i\omega t - i\mathbf{k} \cdot \mathbf{r}} + \epsilon_0 \int_{-\infty}^t \chi_e(t - \tau) \mathbf{E}_0 e^{i\omega\tau - i\mathbf{k} \cdot \mathbf{r}} d\tau. \quad (2.16)$$

Substituting $T := t - \tau$, the exponent can be separated into two parts: one of which factors out from the integral, and one which turns the convolution into a temporal Fourier transform of the medium response:

$$\begin{aligned}\mathbf{D}(t, \mathbf{r}) &= \varepsilon_0 \mathbf{E}_0 e^{i\omega t - i\mathbf{k} \cdot \mathbf{r}} + \varepsilon_0 \int_{-\infty}^0 \chi_e(T) \mathbf{E}_0 e^{i\omega(t-T) - i\mathbf{k} \cdot \mathbf{r}} dT, \\ \mathbf{D}(t, \mathbf{r}) &= \varepsilon_0 \mathbf{E}_0 e^{i\omega t - i\mathbf{k} \cdot \mathbf{r}} + \varepsilon_0 \left(\int_{-\infty}^0 \chi_e(T) e^{-i\omega T} dT \right) \mathbf{E}_0 e^{i\omega t - i\mathbf{k} \cdot \mathbf{r}}.\end{aligned}$$

This can be viewed as an application of the convolution theorem: convolution in the time domain is equivalent to multiplication in the frequency domain. Consequently, we may introduce the local *relative permittivity*, or also *dielectric function*, $\varepsilon_r(\omega)$ as a function of frequency. It is a property of the medium that determines how strongly it develops the electric displacement \mathbf{D} in response to the electric field \mathbf{E} of a harmonic wave. From Eq. (2.5) it is clear that in vacuum, $\varepsilon_r = 1$. In the medium, the permittivity may be obtained as

$$\varepsilon_r(\omega) = \frac{\mathbf{D}(t, \mathbf{r})}{\varepsilon_0 \mathbf{E}(t, \mathbf{r})} \Big|_{\mathbf{E}(t, \mathbf{r}) := \mathbf{E}_0 e^{i\omega t - i\mathbf{k} \cdot \mathbf{r}}} = 1 + \int_{-\infty}^0 e^{-i\omega T} \chi_e(T) dT. \quad (2.17)$$

In general, the function $\varepsilon_r(\omega)$ is complex to account for possible phase delay between the harmonic driving field and the medium response. Phase delay different than 0 (or integer multiple of π) corresponds to energy being dissipated in the medium. Let us note that the definition of the Fourier transform is never subject to the sign change, even when the convention of $e^{i\omega t}$ is exchanged for $e^{-i\omega t}$.

Response of a harmonic oscillator The response function $\chi_e(T, \mathbf{R})$ of usual media is composed of different phenomena. Each of them may react on a different time scale, thus the response of the medium usually has a relatively complicated shape in the time domain. However, to a reasonable degree of approximation, each of the contributions can be treated separately, as it is demonstrated in the following.

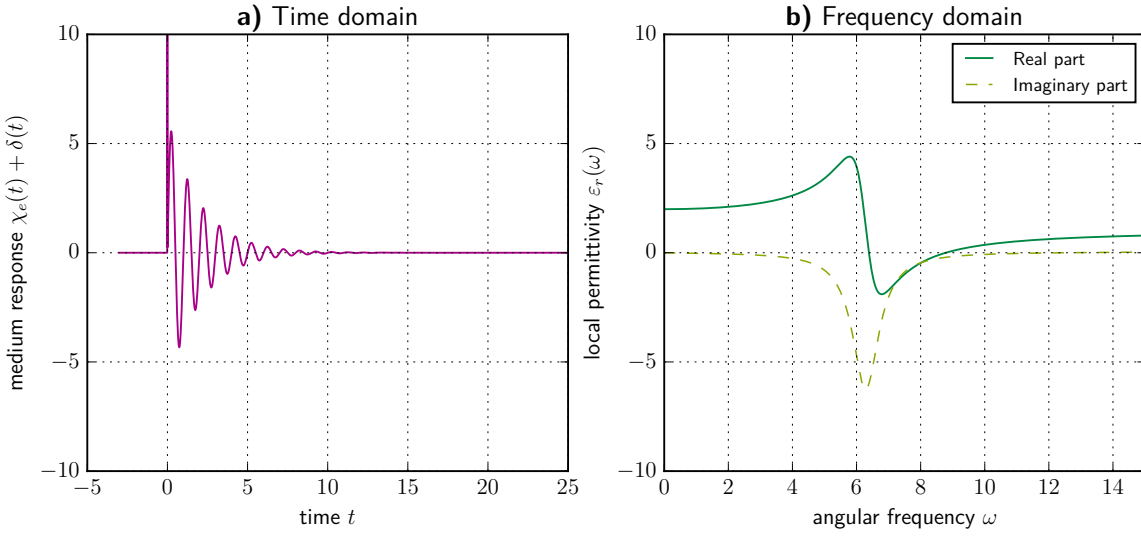
Linear physical systems with an inertial load, friction force and a restoring force are known as *damped harmonic oscillators*. Under weak fields, this theory applies well to the electrons elastically bound to an atomic nucleus, as well as to the atoms elastically bound to their equilibrium positions in the lattice. The molecular rotations can also be modelled as (possibly overdamped) harmonic oscillators. Even free electrons in conductive media can fit into the model of a harmonic oscillator provided the restoring force is set to nearly zero. The response of a harmonic oscillator is easy to describe both in time and frequency domains, even without the explicit use of the Fourier transform from Eq. (2.17). The harmonic oscillator model thus becomes a convenient starting point to approximate the response of materials.

A damped harmonic oscillator is described by a second-order differential equation:

$$\alpha \frac{\partial^2 x(t)}{\partial t^2} + \beta \frac{\partial x(t)}{\partial t} + \zeta x(t) = f(t). \quad (2.18)$$

Provided the driving term on the right hand side is harmonic, $f(t) = e^{+i\omega t}$, the system response is also a harmonic function, $x(t) = \chi(\omega) e^{+i\omega t}$. The differential equation

Figure 2.2: (a) Illustration of how a simplified medium responds to an electric field impulse in the shape of Dirac delta function $E(t) = \delta(t)$. The response is composed from an instantaneous part from vacuum, $\delta(t)$, and from a delayed ringdown of one damped harmonic oscillator, described by $\chi_e(t) := 2\pi \sin(2\pi t) e^{-x/2}$; (b) The corresponding local permittivity $\varepsilon_r(\omega)$, computed by the Fourier transform of the response. Note that the imaginary part of permittivity is negative due to the fact that the material is lossy (it dissipates energy) and that the $e^{i\omega t}$ convention is used.



(2.18) can be easily solved to show that the complex amplitude of the driven oscillations, $\chi(\omega)$, depends on the angular frequency and on the positive real parameters α , β and ζ in the following way:

$$\chi(\omega) \equiv \frac{x(t)}{f(t)} = \frac{1}{\zeta - \alpha\omega^2 + i\omega\beta} = \frac{\alpha^{-1}}{\frac{\zeta}{\alpha} - \omega^2 + i\omega\frac{\beta}{\alpha}}. \quad (2.19)$$

The physical meaning of α , β and ζ is of little importance in this text, but without loss of generality the result of Eq. (2.19) can be rewritten into

$$\chi(\omega) = \frac{F}{\omega_0^2 - \omega^2 + i\omega\gamma}, \quad (2.20)$$

where the physical interpretation of the three (real and positive) parameters is as follows:

- $\omega_0 = \sqrt{\zeta/\alpha}$ is the angular *resonant frequency*, at which the response is purely imaginary and usually its modulus $|\chi(\omega = \omega_0)|$ is near its maximum.
- $\gamma = \beta/\alpha$ is the *damping rate*. In time domain, it determines the time constant of exponential amplitude decay.
- $F = \alpha^{-1}$ is the *oscillator strength*, determining the amplitude of the response function.

Permittivity of Lorentz media Within the approximation of relatively weak fields, the oscillators act independently of each other. The response of usual media in frequency domain can thus be decomposed with acceptable precision into a sum of Q independent harmonic oscillators, each q -th oscillator having the angular resonant frequency ω_{0q} , damping rate γ_q and strength F_q . The permittivity function of the material is a solution of the differential equation of a damped harmonic oscillator, driven by a harmonic source:

$$\varepsilon_r(\omega) = 1 + \sum_{q=1}^Q \frac{F_q}{\omega_{0q}^2 - \omega^2 + i\omega\gamma_q}. \quad (2.21)$$

Advancing from the general formulation in Eq. (2.17) to the Lorentz oscillator model in Eq. (2.21) is of great importance for theoretical interpretation of the material response, and it has also become a framework for description of periodic structures even in the presence of spatial dispersion. A sample time- and frequency-domain response of a medium with one harmonic oscillator is shown in Fig. 2.2.

One can see that each oscillator increases the real part of the low-frequency permittivity, but in the high-frequency limit the contribution of the oscillator vanishes. This can be understood intuitively as that at low frequencies $\omega \ll \omega_0$, the system reacts fast enough to simultaneously follow the driving force, whereas at very high frequencies $\omega \gg \omega_0$, the system cannot respond to the driving force.

The contribution of one oscillator to the low-frequency permittivity $\Delta\varepsilon_r(0)$, is inversely proportional to the oscillator restoring force, which links it to the inverse square of the resonant frequency:

$$\Delta\varepsilon'_r(\omega \rightarrow 0) = \frac{F}{\omega_0^2}. \quad (2.22)$$

A more detailed treatment of the permittivity spectra $\varepsilon_r(\omega)$ may be found in many textbooks, e.g. [8, p. 454], [20].

We will return to the Lorentz oscillator model also in the Chapter 3.1.1, where it appears to be essential for realistic definition of materials for accurate numerical simulations. The chapter also describes how a *Debye relaxator* (e.g. from over-damped molecular rotation) and the *Drude term* (from unbound motion of free charges) can be represented using correct parameters of an oscillator.

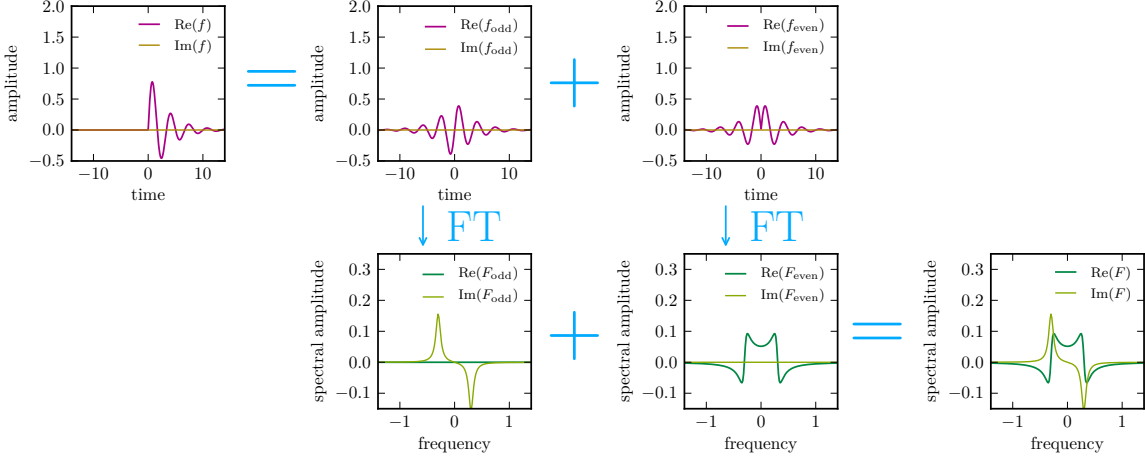
Permeability In a manner very similar to the above derivation of the local permittivity, the *local permeability* can be introduced by means of a response of the medium to the magnetic field:

$$\mu_r(\omega) = 1 + \chi_m(\omega) = \left. \frac{\mathbf{B}(t, \mathbf{r})}{\mu_0 \mathbf{H}(t, \mathbf{r})} \right|_{\mathbf{H}(t, \mathbf{r}) := \mathbf{H}_0 e^{i\omega t - ik \cdot r}} = 1 + \int_{-\infty}^0 e^{-i\omega T} \chi_m(T) dT, \quad (2.23)$$

where $\chi_m(T)$ is the *magnetic response function* of the medium and \mathbf{H}_0 is the amplitude of the magnetic field. This obviously results in an analogous expression for the local permeability in the frequency domain:

$$\mu_r(\omega) = 1 + \sum_{q=1}^Q \frac{F_q}{\omega_{0q}^2 - \omega^2 + i\omega\gamma_q}, \quad (2.24)$$

Figure 2.3: Illustration of how a real causal function $f(t)$ can be decomposed into the odd and even parts, which then yield pure imaginary and pure real functions in the spectrum, respectively. Mathematically this is expressed in Eqs. (2.25–2.30).



where formally the same notation was used as in Eq. (2.21): ω_{0q} , γ_q and F_q are here the magnetic oscillator's angular frequency, damping frequency and strength. Unlike the electric response, most ordinary media have either almost no response to the magnetic field or their response is limited to low frequencies.

Kramers-Kronig relations in local media Causality prevents any medium from reacting to the future electric (or magnetic) field, so the integration in Eq. (2.15) goes up to the current time only, $\tau \in (-\infty, t)$. The response of the medium to a real-valued field must moreover be also real, no matter that the computations are often done with complex field amplitude [Eq. (2.9)] for sake of convenience.

Thus, the basic physical laws impose relatively strict constraints on the time-domain response function $f(t)$, which translate into other constraints for the possible shape of the response in frequency domain $F(\omega)$. The intuitive physical derivation is based on the fact that any time-domain response function can be trivially separated into its odd and even parts, as shown in Fig. 2.3.

$$f(t) = f_{odd}(t) + f_{even}(t) = -f_{odd}(-t) + f_{even}(-t) \quad (2.25)$$

The Fourier transform of a real odd function is an imaginary function:

$$\begin{aligned} F_{odd}(\omega) &= \int_{-\infty}^{+\infty} e^{-i\omega t} f_{odd}(t) dt = \int_{-\infty}^{+\infty} \frac{e^{-i\omega t}}{2} f_{odd}(t) dt + \int_{-\infty}^{+\infty} \frac{e^{-i\omega(-t)}}{2} [-f_{odd}(-t)] dt \\ &= \int_{-\infty}^{+\infty} \frac{e^{-i\omega t} - e^{+i\omega t}}{2} f_{odd}(t) dt = -i \underbrace{\int_{-\infty}^{+\infty} \sin(\omega t) f_{odd}(t) dt}_{\in \mathbb{R}} \end{aligned} \quad (2.26)$$

whereas the Fourier transform of a real even function yields a real function:

$$F_{even}(\omega) = \dots = \int_{-\infty}^{+\infty} \frac{e^{-i\omega t} + e^{+i\omega t}}{2} f_{even}(t) dt = \underbrace{\int_{-\infty}^{+\infty} \cos(\omega t) f_{even}(t) dt}_{\in \mathbb{R}}. \quad (2.27)$$

The odd and even components of the time-domain response function correspond to the imaginary and real part of the response spectrum, respectively:

$$F_{odd}(\omega) + F_{even}(\omega) = F(\omega), \text{ where } F_{odd}(\omega) = F''(\omega) \text{ and } F_{even}(\omega) = F'(\omega). \quad (2.28)$$

At the same time, $f_{even}(t)$ and $f_{odd}(t)$ are related to each other by having the opposite sign for $t < 0$ and the same sign for $t > 0$, that is

$$f_{even}(t) = \text{sign}(t) f_{odd}(t). \quad (2.29)$$

The multiplication in the time domain translates into a convolution in the frequency domain

$$F'(\omega) = \int_{-\infty}^{+\infty} \frac{-2i}{\omega - \Omega} F''(\omega) d\Omega \equiv \left[\frac{-2i}{\omega} \right] * F''(\omega), \quad (2.30)$$

where we used the knowledge that the $-2i/\omega$ function is the Fourier transform of $\text{sign}(t)$. Convolution with this function is also known as the *Hilbert transform*.

Obviously, Eq. (2.29) can also be converted to $f_{odd}(t) = \text{sign}(t) f_{even}(t)$, thus the relation between the real and imaginary parts of the response spectrum also holds when $F_{odd}(\omega)$ and $F_{even}(\omega)$ are exchanged in Eq. (2.30).

A related mathematical proof of the Kramers-Kronig relations can be derived from the analyticity of the response function in the complex plane of frequency. [8, p. 125]

2.1.3 Dispersion relations in local Lorentz media

Lower and upper polariton branches of transverse waves Returning to the derivation of dispersion relations, we start with modifying the constitutive relations (2.5) to a plane wave propagating in a medium:

$$\mathbf{D} := \varepsilon_0 \varepsilon_r(\omega) \mathbf{E}, \quad \mathbf{B} := \mu_0 \mu_r(\omega) \mathbf{H}, \quad (2.31)$$

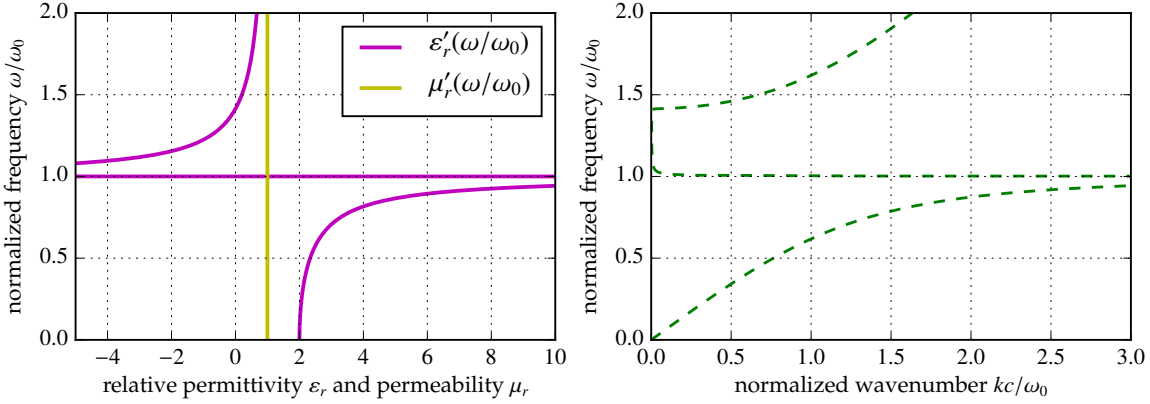
with the relative permittivity $\varepsilon_r(\omega)$ and permeability $\mu_r(\omega)$ being two dimensionless functions of frequency, defined in Eq. (2.21, 2.24). The wave equation (2.11) then changes to

$$\perp_k \mathbf{E} = \varepsilon_0 \mu_0 \varepsilon_r(\omega) \mu_r(\omega) \frac{\omega^2}{k^2} \mathbf{E}. \quad (2.32)$$

For transverse waves in isotropic media, the electric field is perpendicular to the wave vector ($\perp_k \mathbf{E} = \mathbf{E}$), and Eq. (2.32) can be simplified to

$$k(\omega) = \sqrt{\varepsilon_0 \mu_0} \sqrt{\varepsilon_r(\omega) \mu_r(\omega)} \omega = \sqrt{\varepsilon_r(\omega) \mu_r(\omega)} \frac{\omega}{c}, \quad (2.33)$$

Figure 2.4: Influence of a single resonance in the real part of relative permittivity $\varepsilon'_r(\omega)$ (magenta line in the left panel) to the shape of dispersion curves in the right panel (dashed green line, computed using Eq. (2.33). The lower and upper polariton branches are separated by a spectral region $\omega \in (0.3, 0.65)$, where the wave does not propagate on an appreciable distance.



with the added frequency-dispersive term responsible for the deviation of the curve in Fig. 2.4 from the original straight light line in Fig. 2.1.

In the simplest example of a single electric resonance with negligible losses, as shown in Fig. 2.4, the curve is divided into two separate branches. The *lower polariton branch* is below the angular resonant frequency ω_0 and it is characterized by the Lorentz oscillator being in phase with the electric field. Above ω_0 , the dipoles of the Lorentz oscillator can no more follow the electric field and point in the opposite direction. With further increase of the frequency, the permittivity crosses zero at the frequency ω_L where the *upper polariton branch* starts. In case of a single (or well-isolated) Lorentz oscillator, the difference $\omega_L - \omega_0$ can be computed from the magnitude of the oscillator (using the Lydanne-Sachs-Teller relation) [8].

The same behaviour is observed for a single resonance in the permeability $\mu_r(\omega)$, and will be typical also of the spectra of resonances of macroscopic structures described later.

Note that the formation of upper and lower polariton branches can be also interpreted [13] using the theory of coupled oscillators as the result of *anticrossing*, or also *avoided crossing*, between the oscillator at the frequency ω_0 (forming a horizontal line) and the photon branch (forming a straight growing light-line).

When losses are present, the lower and upper polariton branches (in Fig. 2.4) are connected by a smooth line of *anomalous* dispersion and very high losses.

Longitudinal waves in dispersive media The wave equation in local dispersive media (2.32) also allows the existence of longitudinal waves with electric field parallel to the wave vector $\mathbf{E} \parallel \mathbf{k}$. It was shown earlier that there is no solution for longitudinal waves in vacuum except for a static homogeneous field.

If a local medium is assumed, and the wavenumber k is nonzero, such waves can have a solution with nonzero \mathbf{E} when $\varepsilon_r(\omega)' = 0$, or with nonzero \mathbf{H} when $\mu_r(\omega)' = 0$. Therefore, the corresponding dispersion curve for a longitudinal wave

is a horizontal line at $\omega = \omega_L$, independent of k . This would be equivalent to a standing oscillation that maintains the spatial amplitude envelope that was originally excited.

Different physical phenomena can lead to $\varepsilon_r(\omega)' = 0$, some of which introduce relatively low losses at the corresponding ω_L ; namely lattice vibrations in nonconductive crystals or electrons in inductive media (like metals and dilute plasma).

At the interface of two media with differing signs of permittivity, another type of waves can be excited with an intermediate frequency $\omega < \omega_L$ that cannot propagate in either of the bulk medium. The dispersion curve of such waves is not flat, allowing them to propagate along the interface. Depending on the mechanism, they are known as *surface plasmons* or *surface phonon-polaritons* [8, p. 87], respectively. Accordingly, *surface magnons* should be observed at interfaces where μ changes its sign.

Anisotropy of permittivity It shall be noted here that the permittivity ε_r was introduced as a scalar, assuming that the vector of electric field \mathbf{E} and electric induction \mathbf{D} are always parallel:

$$\mathbf{D} = \varepsilon_0 \varepsilon_r(\omega) \mathbf{E} \equiv \varepsilon_0 \begin{pmatrix} \varepsilon_r(\omega) & 0 & 0 \\ 0 & \varepsilon_r(\omega) & 0 \\ 0 & 0 & \varepsilon_r(\omega) \end{pmatrix} \cdot \mathbf{E} \quad (2.34)$$

In some media with a lower rotational symmetry (such as many crystals, or liquids under static electric field), the medium response depends on the electric or magnetic field direction, and the medium is denoted as *anisotropic*. At the beginning of the chapter we assumed the fields to be relatively weak, which enables one to describe the medium as *linear*. Whatever the linear relation of $\mathbf{D} := \mathcal{L}(\mathbf{E})$, it must obey the rule

$$\mathbf{D}_1 + \mathbf{D}_2 = \mathcal{L}(\mathbf{E}_1) + \mathcal{L}(\mathbf{E}_2) = \mathcal{L}(\mathbf{E}_1 + \mathbf{E}_2)$$

for any vectors $\mathbf{E}_1, \mathbf{E}_2$. Such a relation can be fully described by a *tensor of permittivity*

$$\mathbf{D} = \varepsilon_0 \varepsilon_r(\omega) \mathbf{E} \equiv \varepsilon_0 \begin{pmatrix} \varepsilon_{rxx}(\omega) & \varepsilon_{rxy}(\omega) & \varepsilon_{rxz}(\omega) \\ \varepsilon_{ryx}(\omega) & \varepsilon_{ryy}(\omega) & \varepsilon_{ryz}(\omega) \\ \varepsilon_{rzx}(\omega) & \varepsilon_{rzy}(\omega) & \varepsilon_{rzz}(\omega) \end{pmatrix} \cdot \mathbf{E}. \quad (2.35)$$

An elaborate discussion on all possible forms of this tensor and their physical interpretations can be found e.g. in [11, pp. 678–686]. An analogous treatment can be applied to the magnetic permeability, though it is less often needed.

Dispersion relations in anisotropic local media If the medium response depends on the direction of the field, the dispersion relations cannot be directly obtained by substitution into the wave equation as in Eq. (2.33). The dispersion relation can however still be solved [11, pp. 667] as a set of three linear algebraic equations based on Eq. (2.32). For simplicity, we assume here that the relative permeability $\mu_r = 1$; the extension to other cases is possible, too. A solution of Eq. (2.11) can exist

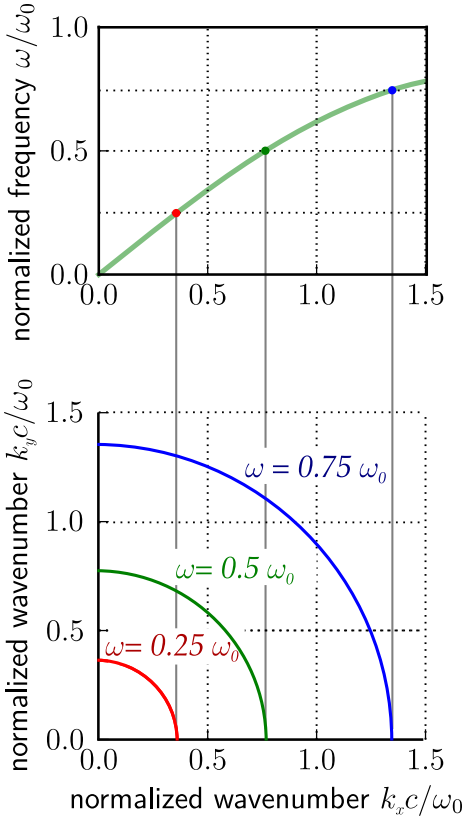


Figure 2.5: Relation between a dispersion curve for one photonic branch and the corresponding isofrequency contours. At a selected frequency, all points in the k_x - k_y plane are drawn for which a nonzero solution of Maxwell equations exists. For transverse waves in local media, this is equivalent to finding a solution to the dispersion equation (2.33).

Multiple frequencies can be plotted to describe the frequency dependence. For illustration, an isotropic medium was used, thus all IFCs take the form of a circle. To save space, only one quarter of the circle was plotted here.

with nonzero \mathbf{E} if and only if the determinant of the set of three linear equations is zero:

$$\det \left[\perp_{\mathbf{k}} - \frac{\mu_0 \epsilon_0 \omega^2}{k^2} \begin{pmatrix} \epsilon_{r11}(\omega) & \epsilon_{r21}(\omega) & \epsilon_{r31}(\omega) \\ \epsilon_{r12}(\omega) & \epsilon_{r22}(\omega) & \epsilon_{r32}(\omega) \\ \epsilon_{r13}(\omega) & \epsilon_{r23}(\omega) & \epsilon_{r33}(\omega) \end{pmatrix} \right] = 0, \quad (2.36)$$

The search for dispersion curves in an anisotropic medium is thus transformed into finding zeroes of this function of four scalar variables, k_x , k_y , k_z and ω . In the most general case, it can be solved by means of numerical algebra software.

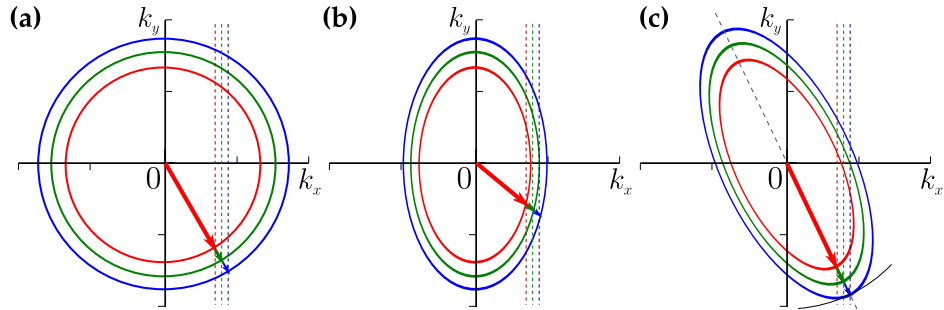
Isofrequency contours It is often important to describe the dispersion curves also for different wave angles, which is the best accomplished by plotting the frequency ω as the function of *wave vector* \mathbf{k} . In three dimensions, this would require mapping a function of three independent variables, $\omega(\mathbf{k}) = \omega(k_x, k_y, k_z)$. However, in most cases the projection of two selected components of \mathbf{k} is sufficient to understand all relevant phenomena, and naturally it is much easier to visualize.

Such plots are known as *isofrequency contours* (IFC), or also *equifrequency contours* (EFC), and they allow intuitive geometrical analysis [21] of various phenomena such as light refraction, beam walk-off, total internal reflection etc. The relation between a dispersion curve for one photonic branch and the corresponding isofrequency contours in an isotropic medium is illustrated in Fig. 2.5.

The limitation is, however, that IFC plots do not show the imaginary part and thus are applicable to plot the dispersion in media with no or negligible losses only.

Each photonic branch also has to be plotted in a separate plot to prevent the contours from overlapping (see the right panel of Fig. 2.4). Moreover, in every single photonic band, Eq. (2.36) yields two solutions for two possible polarisations of transverse waves [8, p. 46]. The IFCs for these solutions are in general different in anisotropic media, but we always restrict the discussion only to one polarisation in the following figures for simplicity.

Figure 2.6: Isofrequency contours for three different frequencies: (a) IFCs in the isotropic medium are circular and centered in the $k = 0$ point. (b) An anisotropic medium with the optical axis perpendicular to the interface, where IFCs take the form of ellipses. (c) A similar case of another anisotropic medium, with the orientation of the optical axis (drawn as the dashed black line) that warrants introducing the index of refraction for the shown direction of the wave vector \mathbf{k} . Note that for clarity, the plots (b) and (c) show the IFCs only for one wave polarisation.



IFCs are valuable for graphical prediction of wave refraction on interface of two media [22, p. 118], [23]. Starting, e.g., by an isotropic medium in Fig. 2.6a, the wavevectors are known for given frequencies (as three coloured arrows). The component of wave vector parallel to the interface (chosen as k_x here and indicated by the vertical dashed lines) must be conserved upon refraction. This rule can be intuitively deduced from the continuity of the wave phase at the interface, as well as from the Noether theorem applied to the infinite translational symmetry of the interface. Transferring the vertical dashed lines to an IFC plot of another medium and finding the intersections with an IFC of the corresponding frequency, one can find the new wavevector. In Fig. 2.6, we provide examples of IFCs for one isotropic and two anisotropic media.

Index of refraction and its applicability With the background of the theory developed above, the notion of the *index of refraction* N can be properly introduced and discussed. In the strictest sense, the index of refraction is defined only for *isotropic* media. Then it is equivalent to the ratio of the wavenumber $k(\omega) \equiv |\mathbf{k}|$ to the wavenumber in vacuum at the same frequency:

$$N(\omega) := k(\omega) \frac{c}{\omega} \equiv \sqrt{\epsilon_r(\omega)\mu_r(\omega)}, \quad (2.37)$$

as directly follows from Eq. (2.33).

Starting with a harmonic plane wave with the frequency ω and the wave vector $\mathbf{k}^{(1)}$ refracting at an interface of two isotropic media, the projection of $\mathbf{k}^{(1)}$ to the

interface is given as

$$k_x = k^{(1)} \sin \alpha^{(1)},$$

where $\alpha^{(1)}$ is the angle between the wavevector in the first medium $\mathbf{k}^{(1)}$ and the normal to the interface. In the second medium, a similar relation must apply. Therefore, the wavenumber $k^{(2)}$ may be different and as a result, the angle in the second medium is

$$\alpha^{(2)} = \arcsin \left(\frac{k^{(1)}}{k^{(2)}} \sin \alpha^{(1)} \right) = \arcsin \left(\frac{N_1}{N_2} \sin \alpha^{(1)} \right), \quad (2.38)$$

which is known as the *Snell* (or also *Snell-Descartes*) law.

The majority of (effective) media discussed in this thesis are, however, more or less anisotropic, and somewhat surprisingly, the notion of *effective index of refraction* N_{eff} seems to be widely used for them in the literature anyway. The author thus feels there is a need for a conscientious extension of N_{eff} for anisotropic cases, too. An extremely loose definition of N_{eff} could be based on computing the ratio $N_{\text{eff}}(\omega, \mathbf{k}) := kc/\omega$ for any medium. This could be formally done, but then the wavenumber k would also depend on the direction α , and the Snell law in Eq. (2.38) would become an implicit equation, losing its original purpose of making the computation explicit and notably simple.

The author proposes instead to restrict the term *index of refraction* to all cases where IFCs are perpendicular to \mathbf{k} . This covers not only all isotropic media, but also those cases when the waves propagate close the optical axis of any anisotropic media. Fig. 2.6c shows an example of such an anisotropic medium with its optical axis oriented parallel to the light wave vector, thus enabling one to approximate the IFC by an osculating circle and to use the Snell law to retrieve the correct angle of refraction. This approximation, however, can be used for a narrow range of angles only.

$$\frac{\partial k}{\partial \alpha} \ll k, \quad (2.39)$$

We will show in the following that the prediction of the *beam* propagation is more complex, because it is sensitive to the *curvature of IFCs*.

Group velocity So far, only the propagation and refraction of a plane harmonic wave was discussed, and it was shown that it is determined by the shape of IFC at the given frequency. Temporal modulation of the wave is equivalent to the wave being formed by superposition of multiple frequency components in the frequency domain, with their respective amplitudes given by the Fourier transform of the field envelope. The temporal position of the envelope is determined by their *mutual phase difference*, not by the absolute wave phase.

A similar argument can be made with regard to the spatial modulation of the wave. Any wave shape other than the infinite plane wave can be expanded into a superposition of waves with different wavevectors, and the direction of propagation of its spatial envelope is given by mutual phase difference of the constituent waves.

The velocity vector of the envelope propagation, denoted as the *group velocity* \mathbf{v}_g , can be found [24] as the gradient of frequency by the wavevector:

$$\mathbf{v}_g := \frac{\partial \omega}{\partial \mathbf{k}} \equiv \begin{pmatrix} \partial \omega / \partial k_x \\ \partial \omega / \partial k_y \\ \partial \omega / \partial k_z \end{pmatrix} \quad (2.40)$$

In the IFC plot, the group velocity can be found visually as directing always perpendicular to the IFC, with a magnitude being proportional to the density of the IFCs.

If the group velocity is different from the phase velocity, the envelope $\mathbf{E}_0(t)$ is maintained in time, but it continuously shifts against the underlying wave. Thus the actual temporal shape of $\mathbf{E}(t)$ changes upon passing through a dispersive medium. On the contrary, in vacuum or media with negligible dispersion, each frequency component of the wave acquires an additional phase strictly proportional to its frequency. Then the group velocity coincides with the phase velocity:

$$\mathbf{v}_g = \mathbf{k}\omega/k^2 \quad (\text{in nondispersive isotropic media}).$$

Usually, in spectral regions near a resonance, also the quadratic or even higher terms in the Taylor expansion of the $\omega(\mathbf{k})$ dependence shall be taken into account. This effect is known as the *group velocity dispersion* as it is equivalent to the group velocity $\mathbf{v}_g(\mathbf{k})$ being dependent on the wavevector (or, if reformulated, on frequency). It results in a temporal distortion of the wave envelope $\mathbf{E}_0(t)$.

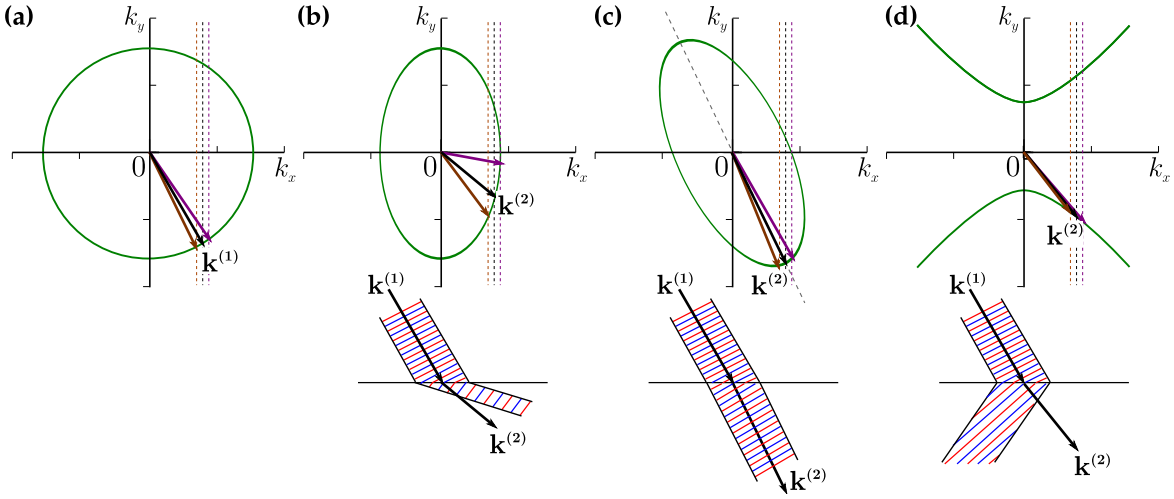
Beam propagation in anisotropic media The refraction of a beam is illustrated in Fig. 2.7 by means of three slightly different wavevectors it is composed of. For simplicity, a monochromatic wave was used, so brown, black and violet were chosen for the three example wavevectors to prevent confusion with the rainbow-like frequency colour map used in Fig. 2.6.

In the first plot, 2.7a, the case of an isotropic medium is illustrated. Upon refraction into a general anisotropic medium in Fig. 2.7b, each component must maintain its wavevector projection to the interface, thus the wavevectors spread their directions. The resulting beam propagates along the group velocity that is different from the central wavevector; this is also known as the spatial *walk-off*.

Fig. 2.7c shows again the special case of the anisotropic medium, where the wave propagates near an optical axis, and thus where the Snell law can still be used to determine the refraction of a plane wave, based the generalized notion of the index of refraction. However, there is a pitfall if one tries to apply the Snell law for prediction of how the beam will refract. The problem originates from the differential nature of the group velocity definition in Eq. (2.40). While the phase velocity of a monochromatic wave at the frequency ω_0 does not appreciably change upon a small deviation of the angle α from the optical axis [cf. Eq. (2.39)], the group velocity direction does, because it has a nonzero linear component in its dependence on the wavevector:

$$\frac{\partial \mathbf{v}_g(\mathbf{k})}{\partial \alpha} \neq 0.$$

Figure 2.7: Examples of IFCs similar to Fig. 2.6, but now at a single frequency and different wavevectors, corresponding to a monochromatic beam refracting on the interface. (a) The wavevectors in the isotropic medium lie on a circle. (b) Generally, anisotropic media exhibit different orientations of the wave vector \mathbf{k} and the beam propagation. (c) For the special cases of propagation along the optical axis, the beam refracts similarly as in isotropic media. (d) In anisotropic media with hyperbolic shape of the IFC, the beam refracts to the opposite direction than the wave vector [21].



As a result, the group velocity in anisotropic media is always much more sensitive to the angle than the phase velocity, and Snell law does not predict it correctly. It can be regarded as a spatially-dependent manifestation of the group velocity dispersion.

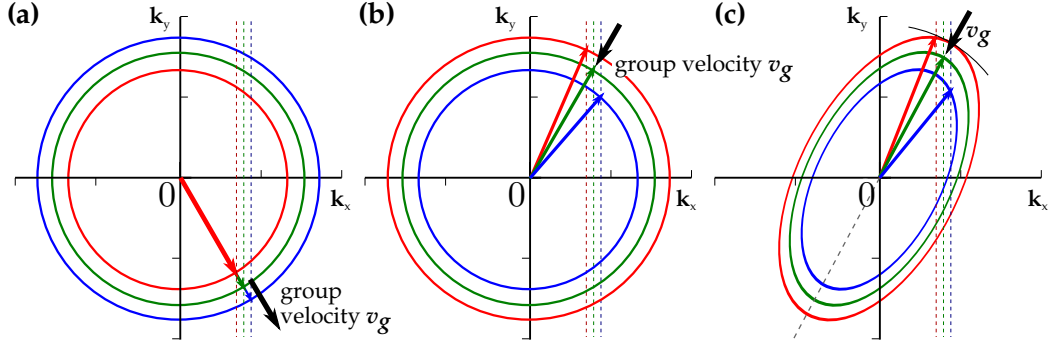
In Fig. 2.7d, an extreme case of spatial walk-off is shown on the example of a *hyperbolic* medium with different signs of the permittivity along different axes. The normal to its IFC is nearly perpendicular to the wavevector, and accordingly, the beam refracts in opposite angle with regard to the incident wave. The k_x component of the wave vector is however still maintained. Further geometrical treatise of the beam refraction is in Ref. [8, p. 46].

The sign of the phase and group velocities In the discussion of refraction both in Fig. 2.6 and 2.7, the solution of the vertical wave vector component k_y pointing downwards was always selected without justification. In fact, both upwards and downwards pointing wave vectors provide a valid solution. The choice was made so that in the first medium represented by the leftmost plots (Fig. 2.6a and 2.7a), the incident wave propagates downwards to the interface, and it was assumed that also the refracted wave will propagate downwards, from the interface.

A more complicated case occurs when the wave vector \mathbf{k} and group velocity \mathbf{v}_g point in opposite directions (or, more generally, when they have opposite projections on the normal to the interface). This manifests itself by the IFC radius *decreasing* with frequency growing, as shown in Fig. 2.8b,c. Such a case can indeed occur in natural or artificial media, as described in more detail below.

Whenever the wave vector \mathbf{k} is nearly perpendicular to the isofrequency contour

Figure 2.8: Frequency-dependent IFCs of (a) an ordinary medium, (b) an isotropic medium with a negative index of refraction and (c) an anisotropic medium with a negative index of refraction.



the Snell law is still applicable and we then speak of a *negative index of refraction*. This is typically, but not exclusively, observed in isotropic media or in media where the wave vector points in a direction close to the optical axis. The refraction between ordinary media and two examples involving negative-index media are plotted in Fig. 2.8. It should be noted that the negative-index media always exhibits temporal dispersion. Therefore, the refraction of temporally short pulses disperses different frequencies into different angles, as can be seen from the wavevector orientation dependent on frequency in Fig. 2.8b,c.

2.2 Electrodynamics of nonlocal homogeneous media

2.2.1 Nonlocal response

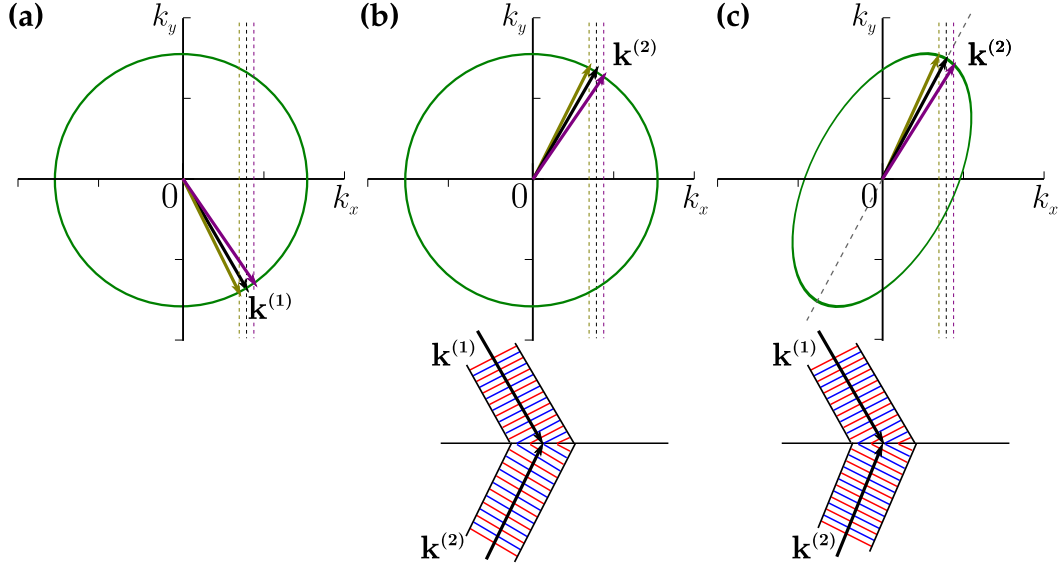
Definition of nonlocal media The previous two chapters that concerned local media can be generalized into the theory of *nonlocal* (or, *spatially dispersive*) media. The downside of the spatial-dispersive model of media is that it is more complicated, leading e.g. to an implicit dispersion equation. Its great advantage is however that it provides a necessary level of generality for the description of periodic structures discussed below.

Some phenomena observed in the frequency spectrum are in fact consequences of the spatial dispersion [13, p. 359], which is the case, for example, of the Doppler broadening of resonance lines in gases [25]. These phenomena are primarily dependent on the wave vector \mathbf{k} , and the apparent broadening on the frequency axis is only due to the dispersion curve defining a simple relation between the frequency broadening and wavevector broadening.

In this section, a general class of media is discussed, where the medium response depends explicitly on the history of $\mathbf{E}(\tau, \rho)$ in previous time $\tau < t$ and in all surrounding points ρ , and therefore it is described by a spatio-temporal convolution:

$$\mathbf{D}(t, \mathbf{r}) = \varepsilon_0 \mathbf{E}(t, \mathbf{r}) + \varepsilon_0 \int_V \int_{-\infty}^t \chi_e(t - \tau, \mathbf{r} - \boldsymbol{\rho}) \mathbf{E}(\tau, \boldsymbol{\rho}) d\tau d^3\rho. \quad (2.41)$$

Figure 2.9: Wavevector-dependent IFCs for one frequency, for the same examples of media as in Fig. 2.8. At an interface of ordinary medium (a) with an isotropic medium of opposite group and phase velocity (b), both wavevector and beam direction refract under negative angle. The principle of refractive index can be applied to compute the wave vector of a wave propagating along the optical axis of anisotropic media (c), but the beam refraction follows a different rule as discussed in the text.



In a very similar manner as in the local theory above, we assume that a plane wave $\mathbf{E}(t, \mathbf{r}) := \mathbf{E}_0 e^{i\omega t - i\mathbf{k} \cdot \mathbf{r}}$ propagates through the medium. This is without loss of generality, since it is possible to express any wave as a superposition of monochromatic plane waves.

$$\mathbf{D}(t, \mathbf{r}) = \varepsilon_0 \mathbf{E}_0 e^{i\omega t - i\mathbf{k} \cdot \mathbf{r}} + \varepsilon_0 \int_V \int_{-\infty}^t \chi_e(t - \tau, \mathbf{r} - \boldsymbol{\rho}) \mathbf{E}_0 e^{i\omega\tau - i\mathbf{k} \cdot \boldsymbol{\rho}} d\tau d^3\rho. \quad (2.42)$$

After two substitutions, $T := t - \tau$, $\mathbf{R} := \mathbf{r} - \boldsymbol{\rho}$, the exponent can again be separated into the original plane wave (which factors out), and a spatio-temporal Fourier transform of the medium response:

$$\begin{aligned} \mathbf{D}(t, \mathbf{r}) &= \varepsilon_0 \mathbf{E}_0 e^{i\omega t - i\mathbf{k} \cdot \mathbf{r}} + \varepsilon_0 \int_V \int_{-\infty}^0 \chi_e(T, \mathbf{R}) \mathbf{E}_0 e^{i\omega(t-T) - i\mathbf{k} \cdot (\mathbf{r}-\mathbf{R})} dT d^3\rho, \\ \mathbf{D}(t, \mathbf{r}) &= \varepsilon_0 \mathbf{E}_0 e^{i\omega t - i\mathbf{k} \cdot \mathbf{r}} + \varepsilon_0 \left(\int_V \int_{-\infty}^0 \chi_e(T, \mathbf{R}) e^{-i\omega T + i\mathbf{k} \cdot \mathbf{R}} dT d^3\mathbf{R} \right) \mathbf{E}_0 e^{i\omega t - i\mathbf{k} \cdot \mathbf{r}}. \end{aligned}$$

The response of the medium to the electric field of any harmonic plane wave can now be expressed as a function of frequency ω and wave vector \mathbf{k} . It is defined as the ratio between the electric displacement and the electric field:

$$\varepsilon_r(\omega, \mathbf{k}) = \frac{\mathbf{D}(t, \mathbf{r})}{\varepsilon_0 \mathbf{E}(t, \mathbf{r})} \Big|_{\mathbf{E}(t, \mathbf{r}) := \mathbf{E}_0 e^{i\omega t - i\mathbf{k} \cdot \mathbf{r}}} = 1 + \int_V \int_{-\infty}^0 \chi_e(T, \mathbf{R}) e^{-i\omega T + i\mathbf{k} \cdot \mathbf{R}} dT d^3\mathbf{R} \quad (2.43)$$

Converting the problem from the spatio-temporal domain into the wavenumber-frequency domain allows to express the relation between \mathbf{D} and \mathbf{E} by the *permittivity* function $\varepsilon_r(\omega, \mathbf{k})$ and completely avoid the convolution from Eq. (2.42). Note that both the response function χ_e and the permittivity ε_r may be either scalar functions, or rank-2 tensor functions; the latter case accounts for possible anisotropy of the medium.

The terms of *nonlocality* and of *spatial dispersion* are used interchangeably in the literature. The difference seems to be related to the way one thinks about the medium – while *nonlocality* is obviously related to the description in the real space [cf. Eq. (2.41)], *spatial dispersion*, in contrast, derives from that the response is not a constant function in the reciprocal \mathbf{k} -space. The term *spatial dispersion* is therefore of a slightly narrower meaning, as it implies that an infinite plane wave of a defined wavevector is being considered.

Power expansion of the medium parameters Assuming the permittivity $\varepsilon_r(\omega, \mathbf{k})$ or permeability $\mu_r(\omega, \mathbf{k})$ are smooth functions varying slowly with \mathbf{k} , we can express them in general as power series [13, p. 367]:

$$\left. \begin{aligned} \varepsilon_r(\omega, \mathbf{k}) &= 1 + \chi_e(\omega) + i\gamma_e(\omega)\mathbf{k} + [\alpha_e(\omega)\mathbf{k}]\mathbf{k} + \dots, \\ \mu_r(\omega, \mathbf{k}) &= 1 + \chi_m(\omega) + i\gamma_m(\omega)\mathbf{k} + [\alpha_m(\omega)\mathbf{k}]\mathbf{k} + \dots, \end{aligned} \right\} \quad (\text{in any media}) \quad (2.44)$$

where $\chi_{e,m}(\omega)$ are second rank tensors, $\gamma_{e,m}(\omega)$ third rank tensors, $\alpha_{e,m}(\omega)$ fourth rank, and similarly for possible higher orders of expansion. After the corresponding number of matrix multiplication with \mathbf{k} , they all yield rank-2 tensors that add up to form the tensor of permittivity or permeability.

Note the response function for a local medium can be formally derived from its nonlocal formulation by replacing the spatial dependence in Eq. (2.41) by a Dirac delta function as follows:

$$\chi_e(t - \tau, \mathbf{r} - \boldsymbol{\rho}) \rightarrow \delta^3(\mathbf{r} - \boldsymbol{\rho}) \chi_e(t - \tau), \quad (2.45)$$

which allows to simplify Eq. (2.41) so that in local media only the temporal convolution has to be computed. Then the higher order terms including $\gamma_{e,m}$ and $\alpha_{e,m}$ in Eqs. (2.44) vanish and

$$\left. \begin{aligned} \varepsilon_r(\omega, \mathbf{k}) &= 1 + \chi_e(\omega) = \varepsilon_r(\omega), \\ \mu_r(\omega, \mathbf{k}) &= 1 + \chi_m(\omega) = \mu_r(\omega). \end{aligned} \right\} \quad (\text{in local media}) \quad (2.46)$$

Magnetic effects can be described by nonlocal permittivity Here, we will follow the approach of Landau and Lifshitz [13] to show that the magnetic response of any medium can be fully expressed by a certain form of permittivity dependence on \mathbf{k} . (For more details, see Refs. [14], [6, pp. 95-130] and [26, p. 19].) This leads to introducing new *Landau-Lifshitz* permittivity ε_r^{LL} and permeability μ_r^{LL} , which are, in general, different from those used in the more customary symmetric model:

$$\varepsilon_r^{LL}(\omega, \mathbf{k}) \not\equiv \varepsilon_r(\omega, \mathbf{k}), \quad 1 = \mu_r^{LL}(\omega, \mathbf{k}) \not\equiv \mu_r(\omega, \mathbf{k}).$$

The Maxwell equations (2.1-2.4) however still hold when these new parameters are substituted for the original ones. Requiring the relative permeability to be unity implies a trivial dependence of the magnetic field on the magnetic induction in this model:

$$\mu_0 \mathbf{H}^{\text{LL}} = \mathbf{B}.$$

The advantage is that the relative magnetic permeability is defined as a mere constant of the magnetic response of vacuum $\mu_r^{\text{LL}}(\omega, \mathbf{k}) := 1$, thus reducing the complexity of the computation compared to the symmetric spatial-dispersive model. Therefore, the *Landau-Lifshitz* model developed below is also denoted as the EDB-model, since it allows the substitution into the Maxwell equations to avoid explicit use of the magnetic field \mathbf{H} .

Local medium in the Landau-Lifshitz model An important step towards using the Landau-Lifshitz model is to derive how a classical, local medium with the magnetic response is represented. From the principle of correspondence, all local media can be expressed with this model without any change in the dispersion curves predicted.

In the Landau-Lifshitz model, the new spatial-dispersive permittivity $\epsilon_r^{\text{LL}}(\omega, \mathbf{k})$ consists of

1. the component caused by the local electric response of matter,
2. a new component fully accounting for the local *magnetic* response of matter, thanks to a particular shape of its spatial dispersion.

Later, higher-order expansion terms can be easily added to describe all sorts of the nonlocal response.

Recalling the Maxwell equation (2.4) that links the magnetic field \mathbf{H} with the electric induction \mathbf{D} ,

$$\nabla \times \mathbf{H} = \frac{\partial \mathbf{D}}{\partial t}, \quad (2.4 \text{ again})$$

it is clear that if one defines a new pair of vector fields

$$\mathbf{H}^{\text{LL}} = \mathbf{H} + \frac{\partial \mathbf{X}}{\partial t}, \quad (2.47)$$

$$\mathbf{D}^{\text{LL}} = \mathbf{D} + \nabla \times \mathbf{X}, \quad (2.48)$$

then Eq. (2.4) maintains exactly the same form with the new fields, for any differentiable vector field \mathbf{X} :

$$\nabla \times \mathbf{H}^{\text{LL}} = \nabla \times \mathbf{H} + \left(\nabla \times \frac{\partial \mathbf{X}}{\partial t} \right) = \frac{\partial \mathbf{D}}{\partial t} + \frac{\partial (\nabla \times \mathbf{X})}{\partial t} = \frac{\partial \mathbf{D}^{\text{LL}}}{\partial t}, \quad (2.49)$$

because for reasonably shaped functions the temporal and spatial derivatives commute.

With the *gauge freedom* of choice of \mathbf{X} , we impose the above mentioned requirement that whole magnetic response of the matter is expressed by the constitutive

equation for permittivity. Therefore in the spatially dispersive theory, the constitutive equation for magnetic induction is defined as the same as in vacuum, cf. Eq. (2.5):

$$\mu_0 \mathbf{H}^{\text{LL}} := \mu_0 \mu_r(\omega) \mathbf{H} = \mathbf{B}. \quad (2.50)$$

When this equation is rearranged into the form similar to 2.47, we obtain a prescription for the sought \mathbf{X} :

$$\mathbf{H}^{\text{LL}} = \mathbf{H} + (\mu_r(\omega) - 1) \mathbf{H} = \mathbf{H} + \underbrace{\left(\frac{\mu_r(\omega) - 1}{\mu_0 \mu_r(\omega)} \right) \mathbf{B}}_{=: \partial \mathbf{X} / \partial t}$$

Without loss of generality, we again restrict the discussion to a plane wave (2.9), thus the time derivative equals to multiplication by $i\omega$.

$$\mathbf{X} = \frac{1}{i\omega} \left(\frac{\mu_r(\omega) - 1}{\mu_0 \mu_r(\omega)} \right) \mathbf{B} = \frac{1}{i\omega \mu_0} \left(1 - \frac{1}{\mu_r(\omega)} \right) \mathbf{B}. \quad (2.51)$$

The new electric displacement \mathbf{D}^{LL} in the Landau-Lifshitz model, that also accounts for magnetic phenomena, is obtained by substitution of Eq. (2.51) into Eq. (2.48):

$$\mathbf{D}^{\text{LL}} := \mathbf{D} - ik \times \mathbf{X} = \mathbf{D} - i \frac{1}{i\omega \mu_0} \left(1 - \frac{1}{\mu_r(\omega)} \right) \mathbf{k} \times \mathbf{B} \quad (2.52)$$

By means of the other Maxwell equation (2.3), the magnetic induction \mathbf{B} can be substituted by $\mathbf{k} \times \mathbf{E}/\omega$ to obtain an expression that contains the electric quantities only.

$$\mathbf{D}^{\text{LL}} = \mathbf{D} - \frac{1}{\omega^2 \mu_0} \left(1 - \frac{1}{\mu_r(\omega)} \right) \mathbf{k} \times (\mathbf{k} \times \mathbf{E}). \quad (2.53)$$

Double vector multiplication on the right hand side can be identified with the wave-front projection tensor $\perp_{\mathbf{k}}$, cf. Eqs. (2.7, 2.12):

$$\mathbf{D}^{\text{LL}} = \mathbf{D} + \frac{k^2}{\omega^2 \mu_0} \left(1 - \frac{1}{\mu_r(\omega)} \right) \perp_{\mathbf{k}} \mathbf{E}, \quad (2.54)$$

Tensor form of the Landau-Lifshitz permittivity of local isotropic media From Eq. (2.53) we can derive the tensor form of spatial-dispersive permittivity $\varepsilon_r^{\text{LL}}(\omega, \mathbf{k})$:

$$\left. \begin{aligned} \varepsilon_r^{\text{LL}}(\omega, \mathbf{k}) &= 1 + \chi_e(\omega) + \frac{k^2}{\omega^2 \mu_0} \left(1 - \frac{1}{\mu_r(\omega)} \right) \perp_{\mathbf{k}}, \\ \mu_r^{\text{LL}}(\omega, \mathbf{k}) &= 1, \end{aligned} \right\} \quad \text{(in local media)} \quad (2.55)$$

where we make use of the wavefront projection tensor defined as

$$\perp_{\mathbf{k}} = \frac{1}{k^2} \begin{pmatrix} k_y^2 + k_z^2 & -k_x k_y & -k_x k_z \\ -k_y k_x & k_x^2 + k_z^2 & -k_y k_z \\ -k_z k_x & -k_z k_y & k_x^2 + k_y^2 \end{pmatrix} \quad \text{or equivalently, } (\perp_{\mathbf{k}})_{ij} = -\frac{k_i k_j}{k^2} + \delta_{ij}. \quad (2.13 \text{ again})$$

Other formulations Let us note that the classical approach using symmetric parameters $\varepsilon_r(\omega, \mathbf{k})$, $\mu_r(\omega, \mathbf{k})$, and the Landau-Lifshitz approach of gathering all medium properties in the permittivity $\varepsilon_r^{\text{LL}}(\omega, \mathbf{k})$ are only two examples of all possible gauge transformations of medium parameters under which the Maxwell equations are invariant. Formally, one can distribute the medium electric and magnetic responses between these parameters arbitrarily – the distribution weight may be even frequency dependent, leading to a physically realistic pair of parameters with custom spectral shape [27].

2.2.2 Dispersion relations in nonlocal homogeneous media

Dispersion relation as an implicit equation In the dispersion relation for local media, Eq. (2.36), the wave vector could be found by solving a set of linear equations. In the particular case of *isotropic* local media, the computation has an even simpler form of an explicit computation of one square root, see Eq. (2.33).

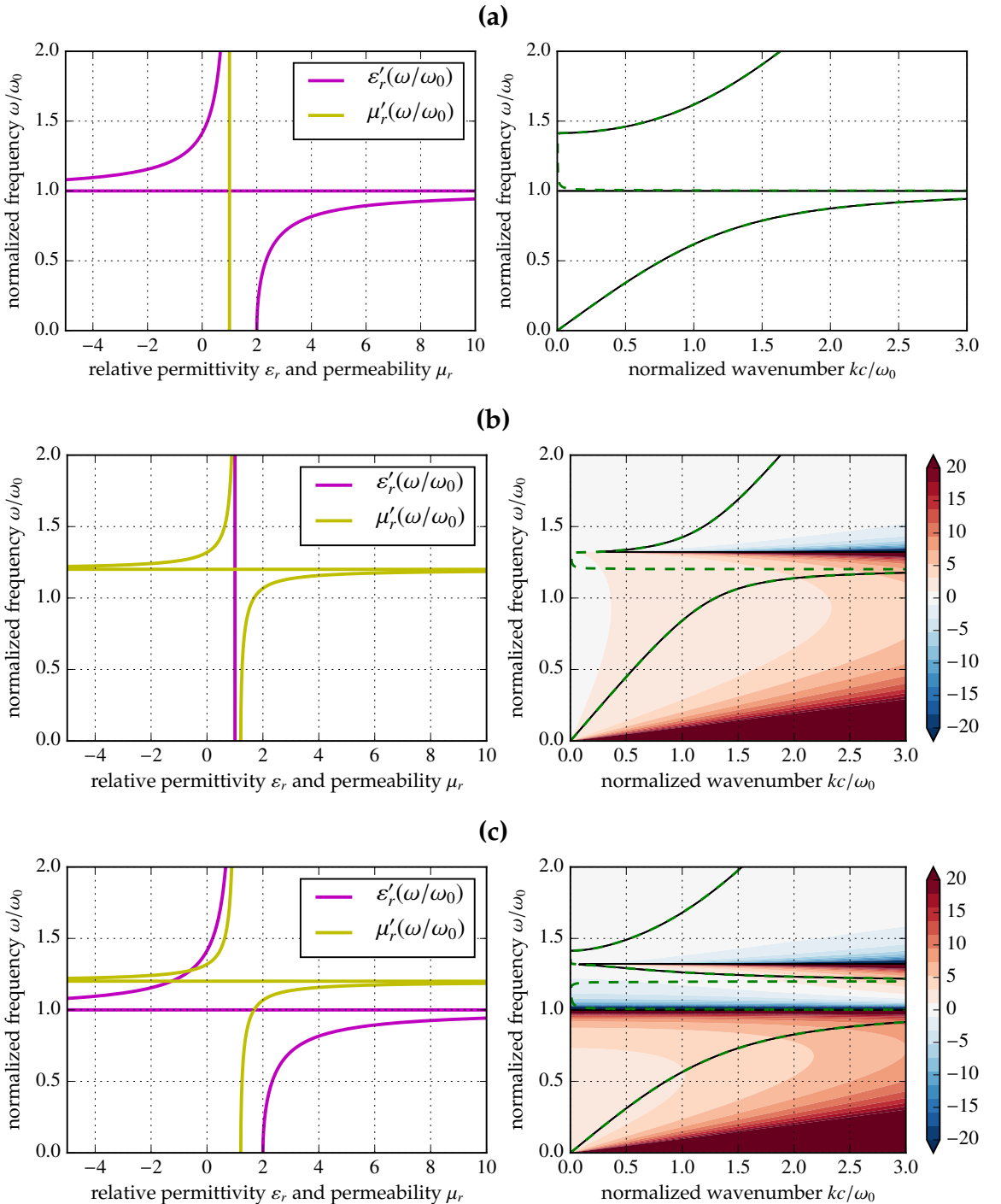
An intrinsic issue of spatial-dispersive media is that the permittivity $\varepsilon_r^{\text{LL}}(\omega, \mathbf{k})$ is a function of the wavevector \mathbf{k} on its own. The dispersion equation then becomes an implicit equation similar to Eq. (2.36), but now with $\varepsilon_r^{\text{LL}}$ dependent on \mathbf{k} :

$$\det \left[\perp_{\mathbf{k}} - \frac{\mu_0 \varepsilon_0 \omega^2}{k^2} \begin{pmatrix} \varepsilon_r^{\text{LL}}_{11}(\omega, \mathbf{k}) & \varepsilon_r^{\text{LL}}_{21}(\omega, \mathbf{k}) & \varepsilon_r^{\text{LL}}_{31}(\omega, \mathbf{k}) \\ \varepsilon_r^{\text{LL}}_{12}(\omega, \mathbf{k}) & \varepsilon_r^{\text{LL}}_{22}(\omega, \mathbf{k}) & \varepsilon_r^{\text{LL}}_{32}(\omega, \mathbf{k}) \\ \varepsilon_r^{\text{LL}}_{13}(\omega, \mathbf{k}) & \varepsilon_r^{\text{LL}}_{23}(\omega, \mathbf{k}) & \varepsilon_r^{\text{LL}}_{33}(\omega, \mathbf{k}) \end{pmatrix} \right] = 0. \quad (2.56)$$

If all tensor elements, $\varepsilon_r^{\text{LL}}_{ij}(\omega, \mathbf{k})$, can be approximated in the form of a polynomial expansion to a low order in \mathbf{k} , the solution can again be found as roots of a characteristic polynomial. The degree of this polynomial may be substantially higher than in Eq. (2.36), the dispersion curves can nonetheless be found by a brute-force numerical search.

Figure 2.10: Dispersion curves for three different types of local media, comparing the local and Landau-Lifshitz representations of constitutive parameters. Three rows show media with (a) a resonance in permittivity, (b) in permeability, and (c) in both parameters simultaneously.

Left column: Local parameters $\varepsilon_r(\omega)$, $\mu_r(\omega)$ as functions of frequency. Right column: Dispersion curves were computed either with the local parameters from Eq. (2.46), plotted as dashed green lines, or with the Landau-Lifshitz parameters from Eq. (2.55), plotted as black line. The Landau-Lifshitz permittivity $\varepsilon_r^{LL}(\omega, \mathbf{k})$ is colour shaded on the background.



Dispersion in a local dielectric in the Landau-Lifshitz model The dispersion curves predicted by the classical and Landau-Lifshitz representations of the constitutive parameters for local media in Eq. (2.55) are mathematically identical. This is illustrated in Fig. 2.10 on three examples: that of a medium with an electric resonance (2.10a), one with a magnetic resonance (2.10b) and with both resonances overlapping (2.10c).

The plots in the left column of Fig. 2.10 show the *local* permittivity $\varepsilon_r(\omega)$ and permeability $\mu_r(\omega)$. Its right column features a thin black contour connecting all points where the dispersion equation (2.56) was found to hold by a numerical search. This is complemented by the Landau-Lifshitz permittivity $\varepsilon_r^{\text{LL}}(\omega, k)$ as a background colour map with blue tone for negative values and red for positive ones. Additionally, the original green dashed dispersion curve as in Fig. 2.4 is retained, as computed using the classical approach based on the Eq. (2.33). It can thus be seen that both models always predict exactly the same dispersion.

For a local isotropic medium with a single electric resonance in Fig. 2.10a, the plotted curves are identical to Fig. 2.4. On the right panel, the Landau-Lifshitz permittivity $\varepsilon_r^{\text{LL}}(\omega, k)$ follows a resonance curve in frequency, but is independent of the wavenumber k (as long as the medium is local). With increasing frequency, the lower polariton branch bends towards higher k , as $\varepsilon_r^{\text{LL}}(\omega, k)$ increases towards the resonance at ω_0 , then a band of frequency follows where no solution of the wave equation [8] exists due to $\varepsilon_r^{\text{LL}}(\omega, k)$ being negative, and finally the upper polariton branch starts when $\varepsilon_r^{\text{LL}}(\omega, k)$ crosses zero and becomes positive again.

A local medium with a single *magnetic* resonance, Fig. 2.10b, is predicted by the symmetric model to exhibit similar dispersion curves. In the right panel of Fig. 2.10b, the magnetic resonance is represented by the contribution that grows proportionally to k^2 :

$$\mathbf{D}^{\text{LL}} = \mathbf{D} + \underbrace{\frac{k^2}{\omega^2 \mu_0} \left(1 - \frac{1}{\mu_r(\omega)} \right)}_{\text{magnetic contribution}} \perp_{\mathbf{k}} \mathbf{E}, \quad (2.54 \text{ again})$$

and unlike the case of the electric resonance, the maximum magnitude of the magnetic contribution is located at the frequency ω_{mp} where $\mu_r(\omega_{mp}) \rightarrow 0$. In the plot 2.10b, this is at $\omega/\omega_0 \approx 1.3$. This shape of $\varepsilon_r^{\text{LL}}(\omega, k)$ causes the lower polariton branch to bend and approach a horizontal asymptote, which is again separated by a band of no allowed wave from the upper polariton branch, starting at ω_{mp} .

Finally, in Fig. 2.10c, both resonances are combined. The main difference from the cases of isolated resonances occurs in the frequency range where originally $\varepsilon_r^{\text{LL}}(\omega, k)$ was negative and no wave could propagate. However, the magnetic resonance increases $\varepsilon_r^{\text{LL}}(\omega, k)$ by a term proportional to k^2 , and consequently a new photonic branch is formed with $d\omega/dk < 0$, that is, with opposite group and phase velocities. IFCs for the new band then appear as sketched in Figs. 2.8b and 2.9b.

Dispersion in nonlocal media Further terms in the permittivity $\varepsilon_r^{\text{LL}}(\omega, k)$ expansion in Eq. (2.55) make the dispersion curves deviate from those predicted for local media. This corresponds to the black contours deviating from the green lines in

Figure 2.11: Dispersion curves for two nonlocal media. They differ by the value of the fourth-order expansion coefficient $\alpha(\omega)$, which was plotted with a thin blue line. The left and right columns of plots show the same information as in Fig. 2.10. The Landau-Lifshitz permittivity $\varepsilon_r^{LL}(\omega, \mathbf{k})$ is colour shaded on the background.

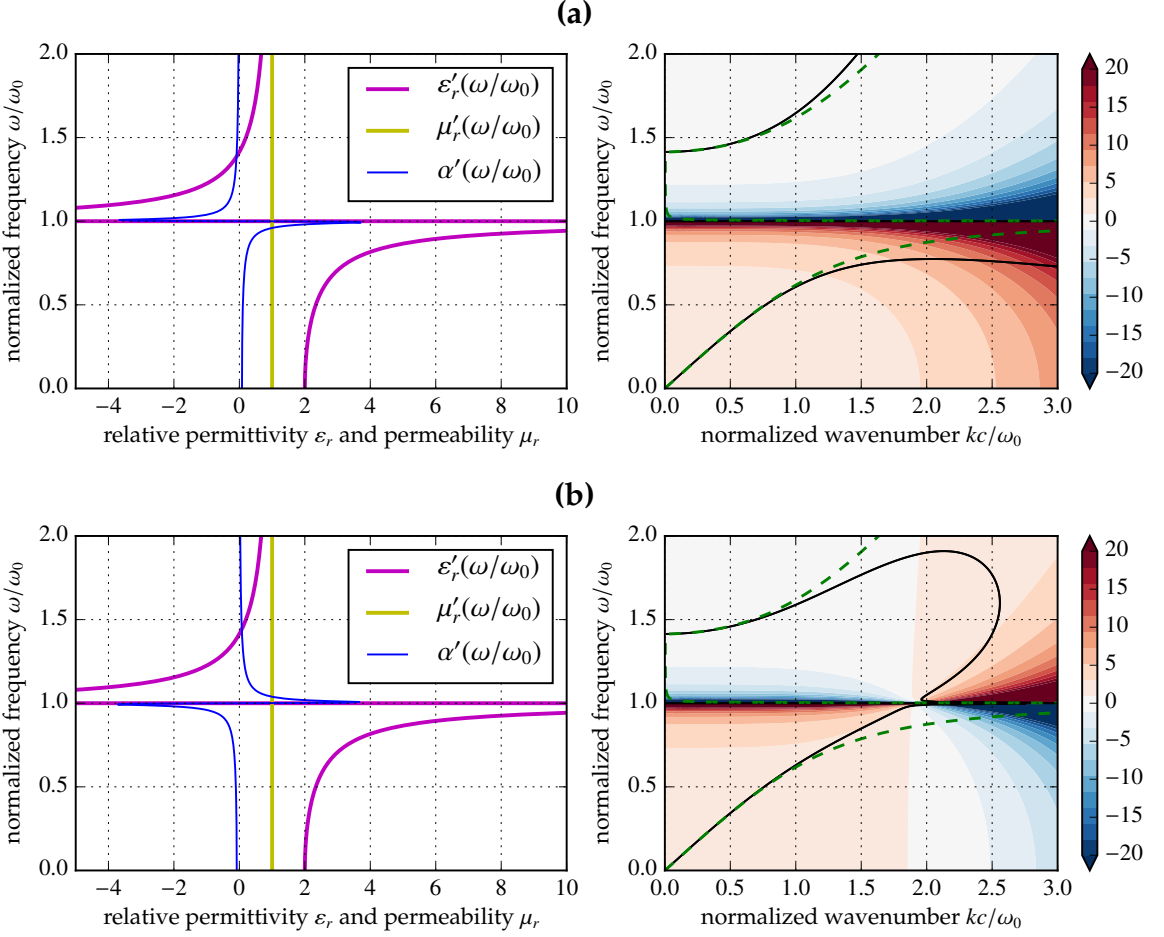


Fig. 2.11. As the simplest example we add one scalar term $\alpha(\omega)k^4$ to $\varepsilon_r^{LL}(\omega, \mathbf{k})$ in Eq. (2.44). The shape of $\alpha(\omega)$ was chosen as a weak Lorentz oscillator at the resonant frequency of the ordinary electric response $\chi_e(\omega)$. This term is shown by adding a thin blue line in the left column of Fig. 2.11.

The choice of the same resonant frequency for $\chi_e(\omega)$ and $\alpha(\omega)$ is not arbitrary; it is assumed that both terms arise from the same resonance mode that has a field shape different from that of a simple dipole. The relation of higher-order expansion terms of the Landau-Lifshitz permittivity to the multipole expansion of the field shape is developed e.g. in Refs. [14], [28] and [26].

The choices of a positive amplitude (Fig. 2.11a) and a negative one (Fig. 2.11b) have typical impacts on the dispersion curves. In the former case, both polariton branches deviate one from another with growing frequency. In the latter case, they come closer to each other with growing k . Eventually, in the upper right corner of the right plot in Fig. 2.11b, they merge into one loop. The author, however, believes this merging may not be observed in nature, and that its occurrence is only due to

unrealistic values of the $\alpha(\omega)$ coefficient or the absence of higher-order expansion terms.

Existence of additional waves For both cases shown in Fig. 2.11, it follows that the dispersion equations can allow multiple solutions with different wavenumbers k at one frequency ω , even when the waves have the same orientation and polarisation. (Note that, conversely, multiple solutions with different ω for a given wavevector \mathbf{k} are commonly present, as a usual consequence of frequency dispersion even in local media.)

The waves propagating with the higher wavenumber k are denoted as *additional* [14, 29, 6, 30]. They were predicted by the works of Pekar et al. and also suggested by experimental data of dispersion near exciton levels, e.g. in cadmium sulphide [31].

The dispersion curves suggest the existence of additional waves around $\omega \sim 0.75\omega_0$ in Fig. 2.11a and $\omega \sim 1.75\omega_0$ in Fig. 2.11b. In both cases, one of the two solutions depicted has opposite signs of the wavevector and the group velocity ($|\mathbf{v}_g| = d\omega/dk < 0$), predicting a negative refraction also in natural homogeneous media.

Odd-power expansion terms and optical activity Returning to the power expansion of $\varepsilon_r^{\text{LL}}(\omega, \mathbf{k})$ in terms of k in Eq. (2.44), we can identify the term constant in k with the electric dipole moment $\chi_e(\omega)$, the term proportional to k^2 with the magnetic dipole moment $\chi_m(\omega)$ (or, also the electric quadrupole moment), and the recently discussed term proportional to k^4 with an electric octupole or magnetic quadrupole ([14, 29, 6]).

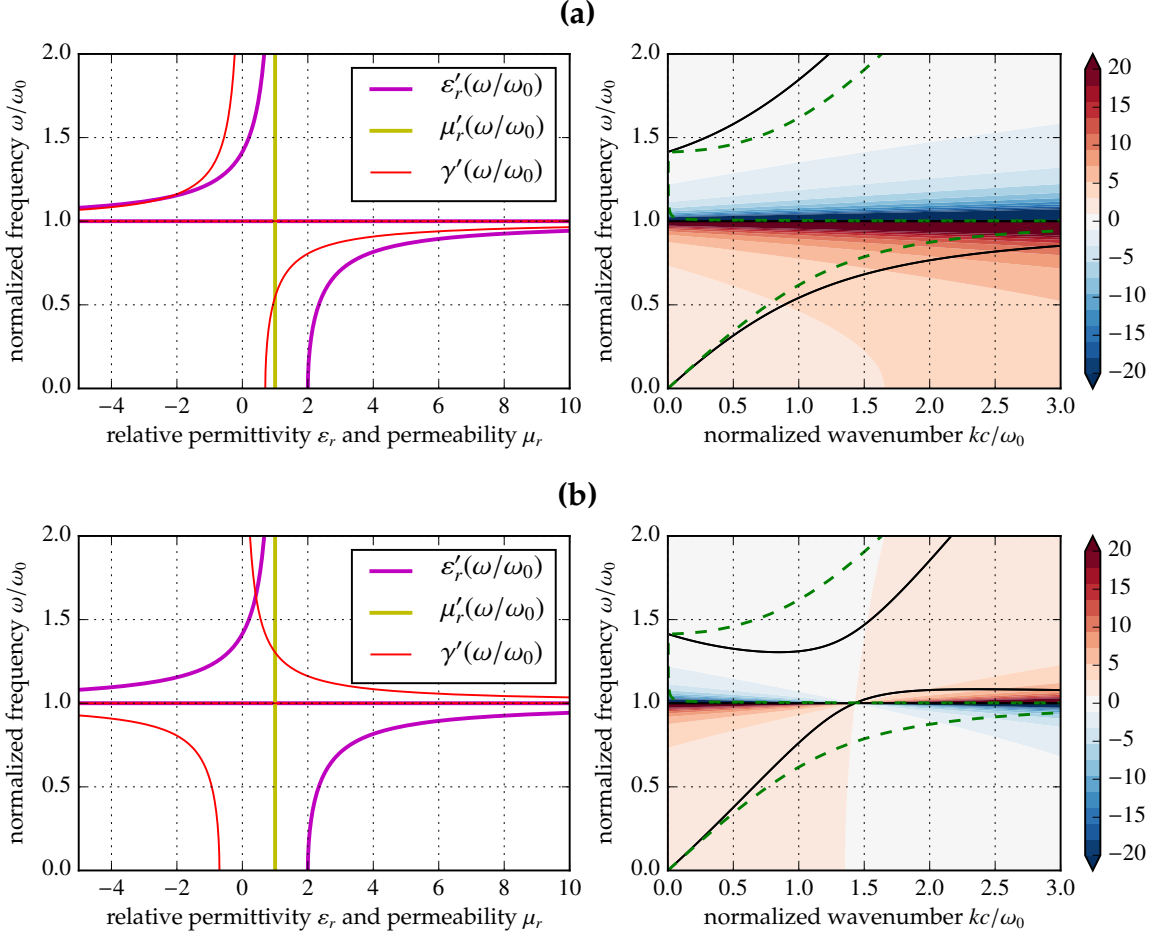
The odd-power expansion terms were not discussed yet, although they have an important physical interpretation – their nonzero values break the spatial inversion symmetry of the medium, and are thus related to optical activity [32]. In media with nonzero odd-power terms, the corresponding eigenwaves are circularly polarized, and they propagate with different velocity depending on the direction. Thus, the two plots in the right column of Fig. 2.12 can also be viewed as the dispersion curves of the same medium, for the left and right circularly polarized waves.

2.2.3 Reflectance and transmittance at an interface of two local media

Continuity requirements In the previous text, only the phase-related phenomena were discussed. The dependence of the dispersion curves and IFCs were computed as a result of the local or nonlocal response of the medium. Geometrical arguments were then used to infer the angle of refraction at the interface of two media, showing e.g. that a positive or negative refraction may occur. It was also shown that the beam may refract in a different direction than the wave vector, and that, in some cases, the notion of index of refraction can be used to simplify the problem to an application of the Snell law.

The conservation of the wave phase at the interface is, however, not the only constraint to the refraction and reflection problem. Assuming there is no surface

Figure 2.12: Dispersion curves for two media with optical activity. The left and right columns of plots show the same information as in Figs. 2.10 and 2.11. The frequency dependence of the function $\gamma_e(\omega)$, which occurs in the term linearly proportional to k in the expansion (2.44), is plotted in the left column as a thin red line.



current nor surface charge, and that both media are local, the components of the fields \mathbf{E} , \mathbf{H} parallel with regard to the interface must be continuous and the *perpendicular* component of the displacements \mathbf{D} , \mathbf{B} is continuous, too. This rule can be derived from the Maxwell equations in Eqs. (2.1–2.4) by integrating them over infinitesimally thin loops or surfaces that are symmetrically placed on the interface [8, pp. 26–29].

Impedance The continuity requirement determines the *amplitudes* of the waves reflected and transmitted at the interface. Corresponding complex *Fresnel coefficients of reflectance r* and *transmittance t* depend on the incidence angle and the polarisation of the wave [11, p. 38]. They are derived in many textbooks with different levels of generalisation.

In the case of isotropic media, the medium is sufficiently described by the ratio of permeability μ_r to permittivity ϵ_r , whose square root is denoted as the *impedance*

of each medium

$$Z = \sqrt{\mu_r/\epsilon_r}. \quad (2.57)$$

It shall be noted that most optics textbooks assume the media not to respond to the magnetic field, $\mu_r = 1$, in which case $Z = 1/N = \sqrt{1/\epsilon_r}$ and the Fresnel coefficients then are expressed as functions of N . This assumption is however not applicable to most structures studied in this thesis.

Perpendicular incidence of two local media In the simplest case where the wave perpendicularly impinges a single interface of two isotropic local media, described by their respective impedances Z_1, Z_2 , the reflectance r and transmittance t of the interface are

$$r = \frac{Z_2 - Z_1}{Z_2 + Z_1}, \quad t = \frac{2Z_2}{Z_2 + Z_1}, \quad (2.58)$$

Refraction on an interface with a nonlocal medium The task to compute the amplitudes of reflectance and transmittance for nonlocal media is substantially more complicated than for the local media. The principal reason is related to the fact that the definition of the medium response (2.41) contains a convolution over an infinite space, which naturally does not account for the interface. For the problem to be better formulated, the integral would have to be modified, either with the nonlocal response of medium to extend also behind the interface, or with the medium response sharply truncated at the interface. For a weak spatial dispersion, different approaches to the problem are discussed in [33]; a similar problem for one example of periodic structures is numerically analyzed in [34].

Strong enough spatial dispersion can also allow the plane wave to refract into a superposition of two independent plane waves, which differ by their component of the wavevector perpendicular to the interface. The respective amplitudes of these components depend on the *additional boundary conditions* [14].

2.2.4 Phase, group, energy and signal velocities

Signs of the phase and group velocities The negative refraction in media shown in Figs. 2.8b,c and 2.9b,c was a result of the requirement for the group velocity v_g to conserve its component perpendicular to the interface, and for the wave vector k to conserve its projection onto the plane of interface.

It was assumed that the group velocity coincides with the energy or information propagation, and therefore that it should always be "positive", that is, it should propagate towards the interface in the first medium and outwards from it in the second one. In the following paragraphs, this assumption will be challenged for special cases of absorbing media, but it will be shown that in media with low losses it is correct and the term of *negative phase* is used when it is opposite to the group velocity. Note that since the phase velocity does not carry energy, it can be also higher than the speed of light in vacuum.

Signs of the group and energy velocities In the discussion of wave refraction on an interface, it was assumed that the envelope (i.e. the modulation, carrying information) of the wave approaches the interface in the first medium, then refracts and propagates away from the interface in the second medium. The envelope propagates with the group velocity v_g as defined by Eq. (2.40). There is another quantity, the *Poynting vector* $\mathbf{S} := \mathbf{E} \times \mathbf{H}$, describing the direction and density of the *power* carried by the optical wave [8, p. 16].

The group velocity usually points in the same direction as the Poynting vector, but this has not necessarily to be always true. A typical counterexample can be found near resonances in lossy (local) media. Such a behaviour can be traced back to Fig. 2.2, where the permittivity drops from high values to negative ones. Since the medium is defined lossy in the figure, the curve of the wavenumber $k(\omega)$ is continuous and smooth, and as a result the magnitude of the group velocity $v_g = d\omega/dk$ is negative for a range of frequencies around the resonance for $\omega \sim 2\pi$,

It follows from this that the group velocity v_g can also point in a direction opposite to the Poynting vector that represents propagation of the light beam energy, \mathbf{S} . This can be observed in narrow parts of the spectrum only, around the resonant frequencies where the media have high losses, and also a strong group velocity dispersion. Assuming passivity and absence of sources in the second medium, it is obviously the Poynting vector that has to conserve its perpendicular component and that the group velocity has inevitably to point towards the interface also in the second medium, which seems contradictory to causality. This result may however be explained by a strong deformation of the envelope shape on a short distance.

A negative group velocity has been experimentally observed in a thin sample. It manifested itself as a negative shift of the light envelope center-of-mass [35], compared to the absence of the medium. Note that the negative group velocity is independent of the sign of the phase velocity, which may be both positive and negative [24].

Signal velocity The notion of *signal* or *information propagation velocity* is sometimes identified with the group velocity, v_g . However, this may be misleading, as the differential definition of the group velocity in Eq. (2.40) enables one to define it for slow-enough modulation only, as long as the span of frequencies is narrow and the second derivative, corresponding to the group velocity dispersion, can be neglected.

Assuming the information is carried by a wave modulation that is limited in time (e. g. presence or absence of an optical pulse), one leaves the comfortable approximation of narrow spectrum: from the convolution-multiplication theorem already used in Eq. (2.30), it can be shown that any information carrying function with a compact support has to span over an infinite spectrum. The simplified version of the proof [36] can be based on the fact that under multiplication by a well chosen compact-supported binary function, e.g.,

$$f(t) \rightarrow f(t) \cdot \text{sign}^2[f(t)],$$

the original function obviously does not change, yet the Fourier transform of this binary function is nonzero over almost all frequencies.

A temporally limited optical pulse will be always more or less distorted upon propagation in a dispersive medium where the dispersion curves are not straight. Then the information velocity becomes a problematic term. If the information could be detected exactly in the first moment when the fields deviate from strict zero, one would come to the surprising conclusion that, even in dispersive media, the information would propagate with the speed of light. In the opposite example of a highly noisy transmission, the pulse may be reliably detected only after most of its energy already arrived, resulting in information propagation even slower than the group velocity.

To conclude, the author is convinced that the notion of *information velocity* is too vague unless its exact definition is provided first, and should not be directly associated with the group velocity.

2.3 Electromagnetic waves in periodic structures

2.3.1 Periodic structures and the Bloch's theorem

Inhomogeneity The previous sections discussed infinite media, with the only deviation from homogeneity at an interface of two media, where refraction of the waves is observed, and it was shown that the resulting orientation of the wave vector and of the group velocity could be easily deduced on a geometrical basis. The amplitudes of the reflected and refracted waves can be also easily computed for local media, whereas their computation for nonlocal media is much less straightforward.

There is a broader class of shapes for which analytical or semianalytical methods have been developed to compute their interactions with electromagnetic waves, such as the Mie theory for scattering on dielectric or metallic spheres and cylinders, propagation through arbitrary stacks of parallel layers, diffraction on narrow apertures, resonances in orthogonal, cylindrical or spherical cavities, or wave guiding in high-symmetry waveguides or optical fibres.

The interactions of electromagnetic waves with most of the possible shapes are too complex to be expressed analytically, and they can only be accessed by numerical methods, some of which are described in Chapter 3.1. However, when these elementary shapes are arranged into an infinite array, any resulting periodic structure behaves in a way typical for the periodicity and its most important traits can again be partially understood on an analytical basis. This chapter focuses on these general properties shared by periodic structures, leaving the particular numerical simulations to the Results section.

Periodicity Under the notion of *periodicity* we understand the existence of discrete translational symmetries. In three dimensions, we can write

$$\varepsilon_r(\omega, \mathbf{r}) = \varepsilon_r(\omega, \mathbf{r} + m_1 \mathbf{a}_1 + m_2 \mathbf{a}_2 + m_3 \mathbf{a}_3) \quad (2.59)$$

where m_1, m_2, m_3 are integers and $\mathbf{a}_1, \mathbf{a}_2, \mathbf{a}_3$ are three linearly independent vectors. The local permittivity, given by Eq. (2.21), was intuitively generalized to a function of the position \mathbf{r} . The constituent media are described by *local* quantities only, to

avoid possible problems at the boundary when computing the spatial convolution in nonlocal media, Eq. (2.43). The same periodicity is also imposed on the permeability $\mu_r(\omega, \mathbf{r})$.

The points generated by all combinations of possible translations of the unit cell center by $m_1\mathbf{a}_1 + m_2\mathbf{a}_2 + m_3\mathbf{a}_3$ form a periodic lattice. The volume defined as a *set of points closest to one given point of the lattice* will be denoted as a *unit cell* (similar to the *Wigner-Seitz cell* in solid-state physics). Obviously, the permittivity or permeability in periodic structures needs only to be specified within one unit cell.

The choice of lattice vectors $\mathbf{a}_{1,2,3}$ limits the set of the rotation or mirror symmetries of the structure. Based on the allowed symmetries, all lattices in three dimensions can be classified into six *crystallographic systems*, namely *cubic*, *tetragonal*, *orthorhombic*, *monoclinic*, *hexagonal-trigonal*, all periodic structures can be classified into 230 *crystallographic space groups*. Numerous crystal optics textbooks (e.g. [11, p. 678]) give more rigorous definitions.

Unless stated otherwise, we will assume that the cubic lattice is used, which allows the highest possible symmetry. In the cubic lattice, the lattice vectors $\mathbf{a}_{1,2,3}$ are of the same magnitude a and mutually orthogonal.

The Bloch's theorem The *Bloch's* (or *Bloch's-Floquet's*) theorem states that while the harmonic wave is no more a solution for the Maxwell equations in a periodic structure that conforms to Eq. (2.59), a solution can always be found as a *Bloch's wave* – a product of a harmonic function and another periodic one:

$$\mathbf{E}(t, \mathbf{r}) = \mathbf{u}_e(\mathbf{r}) e^{i\omega t - i\mathbf{K} \cdot \mathbf{r}}, \text{ where } \mathbf{u}_e(\mathbf{r}) = \mathbf{u}_e(\mathbf{r} + m_1\mathbf{a}_1 + m_2\mathbf{a}_2 + m_3\mathbf{a}_3), \quad (2.60)$$

$$\mathbf{H}(t, \mathbf{r}) = \mathbf{u}_m(\mathbf{r}) e^{i\omega t - i\mathbf{K} \cdot \mathbf{r}}, \text{ where } \mathbf{u}_m(\mathbf{r}) = \mathbf{u}_m(\mathbf{r} + m_1\mathbf{a}_1 + m_2\mathbf{a}_2 + m_3\mathbf{a}_3). \quad (2.61)$$

As a rule, in all linear systems, any sum of Bloch's waves is also a proper solution, but for simplicity we will focus on one Bloch's wave at a time.

The functions $\mathbf{u}_e(\mathbf{r})$ and $\mathbf{u}_m(\mathbf{r})$ have the same periodicity as the structure, and will be denoted as the *mode functions*. They are, in general, complex vector functions, so they not only alter the direction and magnitude of the electric and magnetic fields, but can also introduce a *phase modulation* of the wave in each unit cell.

The remaining term, $e^{i\omega t - i\mathbf{K} \cdot \mathbf{r}}$, is analogous to that of a plane wave

$$\mathbf{E}(t, \mathbf{r}) := \mathbf{E}_0 e^{i\omega t - i\mathbf{k} \cdot \mathbf{r}}, \quad (2.9 \text{ again})$$

except for the capital \mathbf{K} being used to distinguish the wave vector of the Bloch's wave envelope from the wave vector \mathbf{k} in homogeneous media.

Note that the Bloch's theorem does not determine the shape of $\mathbf{u}_e(\mathbf{r})$, $\mathbf{u}_m(\mathbf{r})$, nor the direction and magnitude of \mathbf{K} , it only states a solution in the form of Eqs. (2.60, 2.61) can be found.

Proof of the Bloch's theorem in one dimension This theorem is essential for understanding the electromagnetic behaviour of periodic structures, and it deserves a proof. Originally, it was developed for the electron wave function ψ in crystals on the basis of quantum mechanics. The outline of such a proof in one dimension is based on the following:

1. We assume ψ is an eigenfunction of the Hamiltonian: $\exists h \in \mathbb{C} : \hat{H}\psi = h\psi$.
2. We also assume that the Hamiltonian operator \hat{H} commutes with the operator of discrete translation \hat{T} by the inter-atomic distance: $\forall \psi : \hat{H}\hat{T}\psi = \hat{T}\hat{H}\psi$.
3. Then $(\hat{T}\psi)$ is an eigenfunction of H , because obviously $\hat{H}(\hat{T}\psi) \stackrel{1}{=} \hat{T}\hat{H}\psi \stackrel{2}{=} \hat{T}h\psi = h(\hat{T}\psi)$.
4. From two eigenfunction relations, $\hat{H}\psi \stackrel{2}{=} h\psi$ and $\hat{H}(\hat{T}\psi) \stackrel{3}{=} h(\hat{T}\psi)$, it also follows that ψ and $\hat{T}\psi$ must either represent the very same physical eigenstate of \hat{H} that is uniquely related to its eigenvalue h , or otherwise that there must exist two or more different *degenerate* states $\psi_1 \neq \psi_2$ with the same eigenvalue h .

The latter case of *degeneracy* is proven in many textbooks not to change the conclusion that ψ must be also an eigenfunction of the translation operator, that is,

$$\exists K \in \mathbb{C} : \hat{T}\psi = e^{-iKa}\psi.$$

The physical consequence is that when the Hamiltonian operator is invariant to a discrete translation, its eigenfunctions are also *almost unchanged* upon this particular discrete translation, since they may differ only by a phase shift of $-Ka$. Setting a to be the unit cell size, K becomes the wavenumber of the Bloch's wave envelope.

The Bloch's theorem proof in the electromagnetic formulation The steps can be reformulated replacing the abstract Hamiltonian with an operator derived from the Maxwell equations. In a periodic structure one can no longer assume the solution in the form of a plane wave (2.9), but as long as the structure is time-invariant and linear, the monochromatic electric and magnetic fields can still be decomposed into a product of some complex function of space position, and a harmonic function of time:

$$\begin{aligned} \mathbf{E}(t, \mathbf{r}) &= \mathbf{E}(\mathbf{r})e^{i\omega t}, \\ \mathbf{H}(t, \mathbf{r}) &= \mathbf{H}(\mathbf{r})e^{i\omega t}. \end{aligned} \quad (2.62)$$

One thus only needs to prove the Bloch's theorem for the time-invariant parts of the fields, which will play the same role as the wavefunction ψ in the quantum-mechanical formulation.

1. Assuming $\mathbf{E}(\mathbf{r})$ to be a valid solution of Maxwell equations in the periodic structure at the angular frequency ω , it can be derived from the Maxwell Eqs. (2.3, 2.4), taking into account the local medium response to the fields as defined by Eq. (2.35) to the harmonic wave from Eq. (2.62), that

$$\varepsilon_r^{-1}(\omega, \mathbf{r})\nabla \times [\mu_r^{-1}(\omega, \mathbf{r})\nabla \times \mathbf{E}(\mathbf{r})] = \frac{\omega^2}{c^2}\mathbf{E}(\mathbf{r}), \quad (2.63)$$

In analogy with the quantum-mechanical proof, the left hand side of Eq. (2.63) can be associated with the Hamiltonian $\hat{H}\psi$, and the right hand side with its eigenvalue $h\psi$ [37].

2. The translation operator acts by substitution of the position vector \mathbf{r} in the argument. For example, the translated electric field is

$$\hat{T}\psi \rightarrow \mathbf{E}(\mathbf{r} + \mathbf{a}_1). \quad (2.64)$$

The commutation relation directly follows from the periodicity in Eq. (2.59), thus the right terms in Eqs. (2.65) and (2.66) are identical by definition:

$$\hat{H}\hat{T}\psi \rightarrow \varepsilon_r^{-1}(\omega, \mathbf{r})\nabla \times [\mu_r^{-1}(\omega, \mathbf{r})\nabla \times \mathbf{E}(\mathbf{r} + \mathbf{a}_1)] \quad (2.65)$$

$$\hat{T}\hat{H}\psi \rightarrow \varepsilon_r^{-1}(\omega, \mathbf{r} + \mathbf{a}_1)\nabla \times [\mu_r^{-1}(\omega, \mathbf{r} + \mathbf{a}_1)\nabla \times \mathbf{E}(\mathbf{r} + \mathbf{a}_1)]. \quad (2.66)$$

In three dimensions, this argument is valid for three different translation operators that correspond to the displacements by the different lattice vectors, \mathbf{a}_1 , \mathbf{a}_2 and \mathbf{a}_3 .

3. Then the wave translated by any of the lattice vectors is also a solution of the Maxwell equations:

$$\varepsilon_r^{-1}(\omega, \mathbf{r})\nabla \times [\mu_r^{-1}(\omega, \mathbf{r})\nabla \times \mathbf{E}(\mathbf{r} + \mathbf{a}_{1,2,3})] = \frac{\omega^2}{c^2}\mathbf{E}(\mathbf{r} + \mathbf{a}_{1,2,3}). \quad (2.67)$$

4. In analogy with the fourth step in the Bloch's theorem proof, there exists at least one constant K_1 for which

$$\mathbf{E}(\mathbf{r} + \mathbf{a}_1) = e^{-iK_1 a_1} \mathbf{E}(\mathbf{r}), \quad (2.68)$$

where $K_1 a_1$ represents the phase shift between the adjacent cells along the direction of the lattice vector \mathbf{a}_1 . In a similar manner, constants K_2 and K_3 can be associated with the translations by the \mathbf{a}_2 and \mathbf{a}_3 vectors, respectively.

Bloch's theorem in three dimensions The three constants $K_{1,2,3}$ then define the *Bloch's wave vector* \mathbf{K} in three dimensions:

$$\mathbf{K} := \frac{2\pi K_1(\mathbf{a}_2 \times \mathbf{a}_3)}{\mathbf{a}_1 \cdot (\mathbf{a}_2 \times \mathbf{a}_3)} + \frac{2\pi K_2(\mathbf{a}_3 \times \mathbf{a}_1)}{\mathbf{a}_2 \cdot (\mathbf{a}_3 \times \mathbf{a}_1)} + \frac{2\pi K_3(\mathbf{a}_1 \times \mathbf{a}_2)}{\mathbf{a}_3 \cdot (\mathbf{a}_1 \times \mathbf{a}_2)}. \quad (2.69)$$

Each of three addends in Eq. (2.69) relates to one of the lattice vectors and is orthogonal to the two remaining lattice vectors. If the lattice vectors $\mathbf{a}_{1,2,3}$ form an orthogonal triplet, Eq. (2.69) simplifies to

$$\mathbf{K} := \frac{2\pi K_1 \mathbf{a}_1}{a_1^2} + \frac{2\pi K_2 \mathbf{a}_2}{a_2^2} + \frac{2\pi K_3 \mathbf{a}_3}{a_3^2}. \quad (2.70)$$

Repeating the procedure for the magnetic field, a similar operator can be obtained, where the multiplication by $\varepsilon_r^{-1}(\omega, \mathbf{r})$ and $\mu_r^{-1}(\omega, \mathbf{r})$ occurs in the opposite order. Thus the same arguments, with the identical wave vector \mathbf{K} , have to be valid also for the magnetic field $\mathbf{H}(\mathbf{r})$, where the Hamiltonian is associated with an operator very similar to that of the electric field in Eq. (2.63):

$$\mu_r^{-1}(\omega, \mathbf{r})\nabla \times [\varepsilon_r^{-1}(\omega, \mathbf{r})\nabla \times \mathbf{H}(\mathbf{r})] = \frac{\omega^2}{c^2}\mathbf{H}(\mathbf{r}). \quad (2.71)$$

Virtual periodicity and ambiguity of the mode function Homogeneous media, such as vacuum, naturally fulfill the definition of periodicity in Eq. (2.59). From the principle of correspondence, the Bloch's theorem must predict the already known solution of a harmonic plane wave in vacuum

$$\mathbf{E}(t, \mathbf{r}) := \mathbf{E}_0 e^{i\omega t - i\mathbf{k} \cdot \mathbf{r}}. \quad (2.9 \text{ again})$$

The expected solution of the Bloch's wave in vacuum can be directly found as a formal modification of the dispersion relation,

$$\mathbf{E}(t, \mathbf{r}) = \mathbf{u}_e(\mathbf{r}) e^{i\omega t - i\mathbf{K} \cdot \mathbf{r}}, \text{ where } \mathbf{u}_e(\mathbf{r}) := \mathbf{E}_0 \text{ and } \mathbf{K} := \mathbf{k}. \quad (2.72)$$

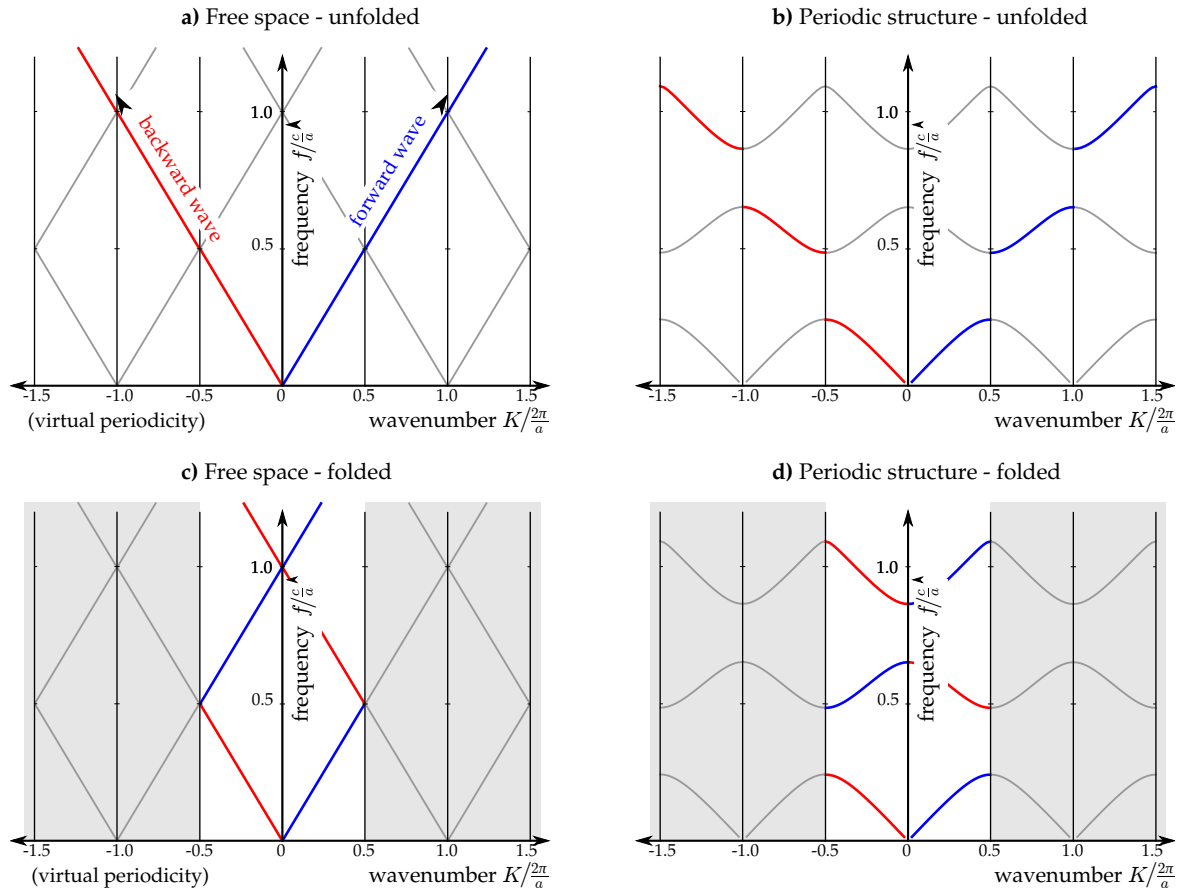
However, this is not the only possible representation of a plane wave as the Bloch's wave, as the Eqs. (2.60, 2.61) are mathematically ambiguous. For illustration, using the fact that any lattice of periodic unit cells may be imagined in vacuum, one can choose a cubic lattice with an arbitrary unit cell size a , for which the plane wave in vacuum can be simultaneously represented by any of infinitely many other combinations of

$$\mathbf{u}_e(\mathbf{r}) := \mathbf{E}_0 e^{2\pi i \left(\frac{m_1}{\mathbf{a}_1 \cdot \mathbf{r}} + \frac{m_2}{\mathbf{a}_2 \cdot \mathbf{r}} + \frac{m_3}{\mathbf{a}_3 \cdot \mathbf{r}} \right)} \quad \left. \right\} \quad \forall m_{1,2,3} \in \mathbb{Z} \quad (2.73)$$

which all give the exactly same resulting plane wave.

Figure 2.13: Folded and unfolded dispersion curves for free space and a periodic structure viewed along one of its axes. The phase difference across a unit cell can be expressed either by the wavenumber K , as it is in the unfolded plots (a) and (b), or it can be predominantly absorbed into the periodic mode function $\mathbf{u}(\mathbf{r})$ as in the folded plots (c) and (d) with inaccessible K -values greyed out.

The lattice periodicity allows one to draw the dispersion curves of periodic structures using natural scale-invariant units, with the Bloch's wave number K divided by the spatial frequency of the lattice $2\pi/a$, and the angular frequency ω multiplied by the time needed for the light to traverse the unit cell.



2.3.2 Dispersion in periodic structures

Folding of the dispersion curves All possible dispersion curves for a *Bloch's wave in vacuum* with the \mathbf{K} vector oriented along one lattice axis in vacuum are plotted in Fig. 2.13a. The dispersion curve for the original forward wave from Eq. (2.72) is plotted in blue; another solution exists for a wave propagating in the opposite direction which is plotted in red. All other solutions generated by Eq. (2.73) are plotted in gray, for both forward and backward waves. Note that the actual physical shape of the fields in space, $\mathbf{E}(\mathbf{r})$ and $\mathbf{H}(\mathbf{r})$, cannot be deduced from the dispersion curve. To fully determine the fields, the dispersion curves would have to be complemented by the mode functions $\mathbf{u}_e(\mathbf{r})$ and $\mathbf{u}_m(\mathbf{r})$, which depend on the frequency.

The inherent ambiguity of the description on the basis of the Bloch's wave can be used to save space in the plot by showing the dispersion curves only for $K \in \langle -\pi/a, \pi/a \rangle$, as shown in Fig. 2.13c. Plotting any other interval of equal width would be equivalent [38, p. 177].

The space of the plot can be further halved, since all forward and backward propagating solutions are symmetrical with respect to the vertical $K = 0$ axis, except for structures with optical activity (cf. Fig. 2.12) or those breaking the time-reversal symmetry (cf. Ref. [39]), which are not discussed in this thesis.

In many papers on periodic structures, all dispersion curves are plotted as *folded* into the $K \in \langle -\pi/a, \pi/a \rangle$ region only [40, 41, 42], while some employ the symmetry to fold all curves further into the $K \in \langle 0, \pi/a \rangle$ range. In some other references, such as [43] or [44], unfolded dispersion curves are used.

The mathematical interpretation of folding the dispersion curves in vacuum can be found from Eq. (2.73):

1. For $\omega \in \langle 0, \pi c/a \rangle$, the mode function is constant in space, $\mathbf{u}_e(\mathbf{r}) := E_0$, and $K := \omega/c$.
2. At the first point of folding for $K = \pi/a$, the mode function changes to $\mathbf{u}_e(\mathbf{r}) := E_0 e^{2\pi i r/a}$ and the formal solution of the *backward* wave is used with $K := 2\pi r/a - \omega r/c$. The phase increase across one unit cell remains positive, since the phase decrease of the backward-wave envelope is less than the phase contribution of the mode function.
3. When the dispersion curve touches the $K = 0$ axis at the frequency $\omega = 2\pi c/a$, the mode function is not changed, but the dispersion curve continues again along with the *forward* wave $K := -2\pi r/a + \omega r/c$.

In vacuum, this process repeats with higher orders of the mode function: $\mathbf{u}_e(\mathbf{r}) := E_0 e^{4\pi i r/a}$, $\mathbf{u}_e(\mathbf{r}) := E_0 e^{6\pi i r/a}$, etc.

We will show in the Results section on a particular example that some numerical approaches provide rules for the selection of one particular dispersion curve in the unfolded plot. The Results section also contains a physical interpretation of this finding.

Fourier expansion of the mode function If the periodic structure is not homogeneous, that is, $\varepsilon_r(\omega, \mathbf{r})$ or $\mu_r(\omega, \mathbf{r})$ depends on \mathbf{r} , the mode functions $\mathbf{u}_{em}(\mathbf{r})$ acquires

more complex, anharmonic shape than assumed in Eq. (2.73). They however still show the periodicity of the lattice, as dictated by the Bloch's theorem in Eq. (2.60), and their exact shapes can thus be decomposed into Fourier series, characteristic for the structure and the frequency of operation, defining nonzero amplitudes for all branches. The grey lines plotted in Fig. 2.13 then are no more hypothetical solutions to be chosen from, but they all have real amplitudes, and are present simultaneously. Note this does not contradict the ambiguity of choice of the Bloch's wavevector \mathbf{K} , which stems from the mathematical representation of the Bloch's wave.

Brillouin zones in the reciprocal space The periodically repeating interval of $K \in \langle -\pi/a, \pi/a \rangle$ can be viewed as the unit cell in the space of wave vectors, i.e. in the *reciprocal space*. This unit cell is then denoted as the first *Brillouin zone*.

In two or three dimensions, any m -th Brillouin zone is defined as the set of all points for which the center point $K = 0$ is the m -th closest point from the regular lattice of all points where $\mathbf{K} = (2\pi m_1/a, 2\pi m_2/a, \dots)$ for $m_1, m_2, \dots \in \mathbb{Z}$. All Brillouin zones have equal measure (i.e. length, area or volume), and moreover, they can be transformed into the first one by simple translation.

In the 1-D case, the definition of higher Brillouin zones trivially consists in dividing the axis symmetrically into equal intervals, such as

$$K \in \langle -2\pi/a, -\pi/a \rangle \cup \langle \pi/a, 2\pi/a \rangle$$

for the second one etc.

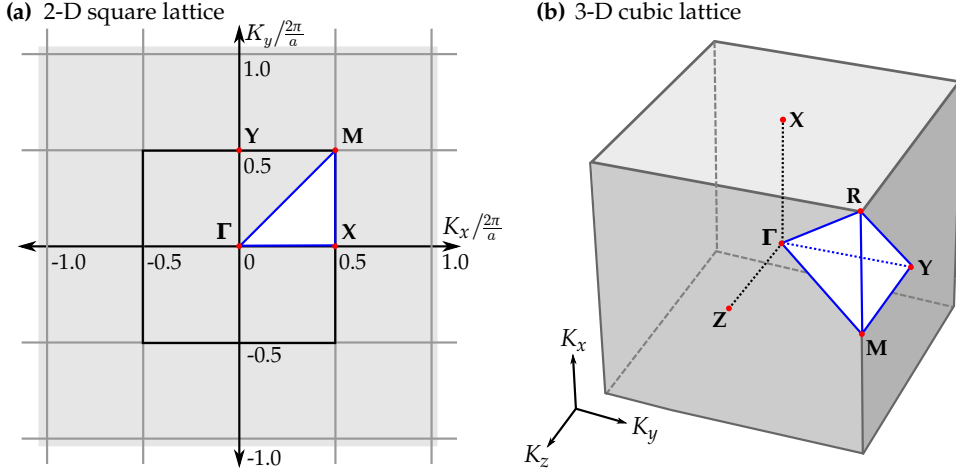
In two or three dimensions the shapes of higher Brillouin zones become much more complex, and are unlike to each other [8, pp. 134–135]: in two dimensions, all Brillouin zones are composed of polygons that are connected in their vertices to enclose the previous Brillouin zone [38, p. 126]. Similarly, in three dimensions, they are composed of polyhedra connected by their edges, and their shape roughly resembles sphere shells.

The above illustration of how the plot space can be saved by folding the dispersion curves into the first Brillouin zone also applies to two- or three-dimensional structures. The exact shapes of the Brillouin zones are determined by the crystal family of the real-space lattice and its set of lattice vectors $\mathbf{a}_{1,2,3}$. As noted above, the space occupied by the plot can be further reduced thanks to the symmetry of the dispersion curves. This applies naturally to higher dimensions as well; the minimum part of the Brillouin zone that contains all necessary information is denoted as the *irreducible Brillouin zone* and is determined by the crystallographic point group of the lattice.

A more detailed listing and comparison of Brillouin zone shapes is beyond the scope of this thesis, but can be found in numerous solid-state textbooks, e.g. [8, pp. 96–99].

High-symmetry points of the Brillouin zones The fundamental difference between plotting one dispersion curve and the isofrequency contours (IFCs) is that IFCs provide information about the dispersion for a two-dimensional subspace of

Figure 2.14: High-symmetry points in the reciprocal \mathbf{K} -space and the Brillouin zones for (a) a two-dimensional square lattice and (b) a three-dimensional cubic lattice. For these lattices, the first Brillouin zones have square and cubic shapes, respectively. In each figure, one of the irreducible Brillouin zones is highlighted.



the wave vector \mathbf{K} , whereas the dispersion curve is limited to a 1-D scan along some line in the \mathbf{K} -space (cf. Fig. 2.5). The limitation is even more significant in the case of three dimensions, where it is virtually impossible to visualize the frequency $\omega(\mathbf{K})$ as a function of three components of \mathbf{K} .

A hybrid approach can be taken, however, that maintains most of the physical information about the dispersion in the two- or three-dimensional structures. It consists in plotting the dispersion curves around the boundary or edges of one selected irreducible Brillouin zone. It is expected that no important information is lost by leaving out its inner surface.

The notation of high-symmetry points in the \mathbf{K} -space is standardized. For the square lattice in two dimensions, four high-symmetry points are named as follows: "Gamma" corresponds to the center, $K = 0$. Provided that the first lattice vector \mathbf{a}_1 is parallel to the x -axis of the coordinate system, the point where $\mathbf{K} = (\pi/a, 0)$ is denoted as "X" and the point $\mathbf{K} = (0, \pi/a)$ as "Y". Finally, the diagonal point of $\mathbf{K} = (\pi/a, \pi/a)$ is known as "M". In a two-dimensional case, the dispersion curves are typically plotted along the triangle encircling the irreducible Brillouin zone: $\Gamma - X - M - \Gamma$.

In three-dimensional cubic lattice, these points maintain their meaning in the plane perpendicular to the z -axis [8, p. 99]. Additionally, "R" denotes the spatial diagonal of $\mathbf{K} = (\pi/a, \pi/a, \pi/a)$. Other lattices introduce more complex sets of the high-symmetry points and the paths along which the dispersion curves are plotted do not seem to be standardized.

Tight-binding model for the dispersion curves The notation of the high-symmetry points in the Brillouin zone can outline a different way [45] of understanding the origin of the dispersion, which can be drawn in analogy with the *tight-binding*, or also *hopping*, model in solid-state physics.

Analyzing one unit cell isolated in free space, one obtains its natural resonant frequency. When the cell is surrounded by other cells in the periodic lattice, their mutual coupling alters the resonant frequency [8, p. 75]; the actual sign of the coupling effect does not seem to be determined by any simple general rule, however.

For a steady oscillatory solution to be obtained, the electromagnetic fields in the surrounding cells must have the same modulus of oscillation amplitude, but they do not need to share the phase. This is equivalent to a single Bloch's wave propagating in the structure.

Identical phase in all cells corresponds to a zero Bloch's wave vector, $\mathbf{K} = 0$, and to the point Γ in the center of the Brillouin zone. Under the basic assumption that the fields \mathbf{E}, \mathbf{H} are continuous and smooth vector functions, the requirement of an identical phase of adjacent cells translates into

$$\frac{\partial \mathbf{E}}{\partial \mathbf{n}} = \frac{\partial \mathbf{H}}{\partial \mathbf{n}} = 0 \quad (\text{Neumann boundary conditions}). \quad (2.74)$$

Here, the operator $\partial/\partial\mathbf{n}$ denotes the derivative along the normal to the boundaries.

Other special cases are observed when \mathbf{K} corresponds to some of the high-symmetry points of the Brillouin zone. For the simple case of a two-dimensional square lattice, the M-point corresponds to the adjacent cells having exactly opposite phase of the fields. This requires that the field amplitudes at the boundary are zero:

$$\mathbf{E} = \mathbf{H} = 0 \quad (\text{Dirichlet boundary conditions}). \quad (2.75)$$

The X and Y points are combination of the Dirichlet and Neumann boundary conditions for two different directions. As a generalization of the above mentioned criteria, the boundary conditions can be found for any point in the Brillouin zone, provided that a correct phase difference between all opposite faces is conserved.

The stronger the coupling between the neighbouring cells, the bigger the difference between the resonant frequencies for the Γ and X points. Returning to the definition of the group velocity in Eq. (2.40), one comes to the already expected fact that the energy transfer is proportional to the strength of the inter-cell coupling.

2.3.3 Band gaps

Properties of band gaps In the plots of dispersion curves, one can identify ranges of frequencies which are not associated with any dispersion curve. They can be observed for a local dielectric (Figs. 2.4 and 2.10), for nonlocal dielectrics (Figs. 2.11, 2.12), as well as for periodic structures in Fig. 2.13. Such regions are denoted as (electromagnetic) *band gaps*, or sometimes also *stop-bands*. They are a very common phenomenon both in dispersive homogeneous media and periodic structures. While the wave propagation received due attention in the above, also the wave "non-propagation" deserves to be commented.

The band-gap behaviour is the simplest to be described in isotropic media, analogously to the one-dimensional case: for a frequency within the band gap, no wavevector \mathbf{K} can be found with which the electromagnetic wave would propagate, or more precisely, there is no real wavevector for which the (Bloch's) wave would be a solution of Maxwell equations.

In the more complicated cases of a harmonic plane wave in anisotropic homogeneous media, or of a Bloch's wave in any periodic structure, the band-gap properties depend on the field polarisation and on the direction in which the wave propagates. Many such media, for example, exhibit a band gap for one polarisation and only in some set of wave vector orientations.

Reflection from an interface with a band-gap medium A familiar scenario is that a wave propagates through a transparent medium (e.g. glass) and impinges upon an interface with a band-gap medium (e.g. metal). In the latter, it is not allowed to propagate, and all its energy reflects back into the first medium. The Maxwell equations however require that the fields do not end abruptly at the interface; in particular, it follows from the linearity of the medium that a so-called *evanescent* wave amplitude decays in the second medium in an exponential manner with the distance below the interface.

If losses are present, a part of the impinging wave energy may be also dissipated. Nonetheless, the exponential decay of the evanescent wave should not be confused with the exponential nature of the Lambert-Beer law in absorbing media.

Radiating dipole inside a band-gap medium A less usual, but equally instructive, scenario is when a dipole source is embedded in an infinite medium and is forced by some external mechanism to oscillate at some frequency inside the band gap. Intuitively, one could expect such a forced dipole must inevitably radiate energy into the medium. In reality, the effect of the medium surrounding the dipole will make the dipole act, with regard to the driving force, as a purely elastic or inertial load.

In particular, if the dipole is realized as an antenna driven by a high-frequency circuit, it will appear to the circuit as purely capacitive or inductive load. Thus, for continuous oscillations, all energy will be returned to the driving mechanism. This way, the environment can enhance or suppress the radiation from an excited atom or molecule, which is known as the *Purcell effect*.

Band gaps stemming from individual resonances One common class of band gaps is based on *individual resonances* in the medium or structure. These band gaps are often observed in realistic natural media, where the resonances arise from vibrations of electrons, atoms or molecules, as described above. Although realistic crystalline media are composed of a lattice of individual atoms, which would suggest that even here the wave has to be described in the Bloch's form of Eqs. (2.60) and (2.61), the optical wavelengths are roughly 10^4 times larger than the inter-atomic distances, and in Eq. (2.9) the electromagnetic wave can be satisfactorily approximated as a harmonic wave with a well-defined wavelength. To make this harmonic approximation, it is important that these particles be small and close to each other compared to the wavelength.

Periodic structures can similarly exhibit a resonance confined in the unit cell. To the author's knowledge, every possible shape formed from a dielectric or metal has multiple resonance modes, characterized by a relatively high localisation of energy close to the structure. Arranging such resonant elements with a translational

symmetry is a fundamental step in building a periodic structure with resonant behaviour. When such a structure is viewed as a homogeneous medium, its dispersion for the Bloch's wave follows a resonance curve similar (but not exactly the same) to that in Fig. 2.2. Sometimes the behaviour of the Bloch's wave is described as *macroscopic*, while the fields localized in the resonant elements as *mesoscopic* [46] and finally the word *microscopic* is left for the much finer field in the constituent atoms or molecules.

Another important characteristic of individual resonances consists in a *qualitative* change in the field shape between the lower and upper edge of the band gap. This is true for natural media as well as for lattices of individual resonators. Stipulated by Eq. 2.19 for a harmonic oscillator, the dipoles are in a phase with the wave at the lower band-gap edge, whereas they are in opposite phase at the upper edge. The actual resonant frequency is located at some point inside the bandgap, as will be shown on the examples of simple individual resonators, e.g. in Fig. 5.8c.

Yet another characteristic is whether the resonant-field shape in the structure unit cell can be approximated as a point dipole or multipole, or their combination. Further, the dipole moment may be electric, magnetic, zero or both simultaneously, as given by symmetry of the field. Most types of structures exhibit multiple resonances at different frequencies, each of them having usually either an electric or a magnetic dipole. In structures of lower symmetry, one resonant mode may have both nonzero dipole moments simultaneously; this leads to optical activity.

Other resonances have both dipole moments zero, due to higher-order rotational symmetry of the fields. Their interaction with the electromagnetic waves is mediated by the electric or magnetic *quadrupole* (or even higher *multipole* [47]) moment. This interaction is usually weak, however it grows with the wavenumber k . Such multipole moments often complement dipole resonances, and are responsible for the spatial dispersion, see Chapter 2.2.2.

Bragg band gaps Band gaps of a different type, denoted as *Bragg band gaps* or also as *photonic band gaps* (PBG), are observed exclusively in periodic structures when an integer number of half-waves fits into the unit cell. In the above mentioned periodic lattice of isolated particles, the Bragg band gap can therefore be understood as a resonance of the electromagnetic wave in the space *between* the particles, in contrast with the individual resonances where most of the energy is localised *inside* the particles – or at least very close to them.

The first Bragg band gap is observed in a periodic structure when the wavenumber K reaches the X, Y or Z points of the Brillouin zone. For a wave propagating parallel to any axis of a square or cubic lattice with unit cell size a , the rule for a band gap is particularly simple:

$$K = \frac{\pi m}{a}, \quad m \in \mathbb{Z}. \quad (2.76)$$

The Bragg band gaps exhibit a constant m over the whole band gap, without any resonance-like shape of the $N_{\text{eff}}(f)$ curve observed for individual resonances.

In analogy with the solid-state physics the Bragg band gaps can be called *direct* if the dispersion curves at the lower and upper band gap edges have the same

wavenumber K . In contrast, the individual resonances are analogous to the *indirect* band gaps, as the phase increase over an unit cell is different for frequencies below and above the individual resonance.

The width of the band gap depends on the scattering strength of the particles; it can be described by the transfer-matrix formalism and analytically computed for a one-dimensional layered system [48]. In the Results section, it is also shown that for a particular choice of parameters the width of the Bragg band gap can vanish.

2.4 Historical notes on metamaterials and photonic crystals

2.4.1 One history of three paradigms

The scientific progress rarely follows a straightforward, efficient way. Making a brief historical review and following the development is therefore important to understand the current state of research, and possibly also the actual physical theory.

Moreover, the field covered by this thesis is also burdened by confusion due to the used terminology: objects falling under the definition of *periodic structures* have been denoted in the literature also as *metamaterials*, *photonic crystals*, *nanostructured electromagnetic materials* or *composites*, *photonic band-gap materials*, *artificial dielectrics* etc. Typically, these terms are used without a proper definition, and may and need not [49] overlap in their meaning.

The split in terminology is apparently not only a formal issue, as it psychologically divides the scientific community and thus directs the future research. Physics, and the field under discussion in particular, has developed rapidly in the recent decades. Some of the seemingly novel concepts were in fact conceived much longer ago, as indicated in the following. Sometimes a mere change in terminology seems to have lead the community to disregard, and later re-invent concepts that were already known [50],[8, p. 5].

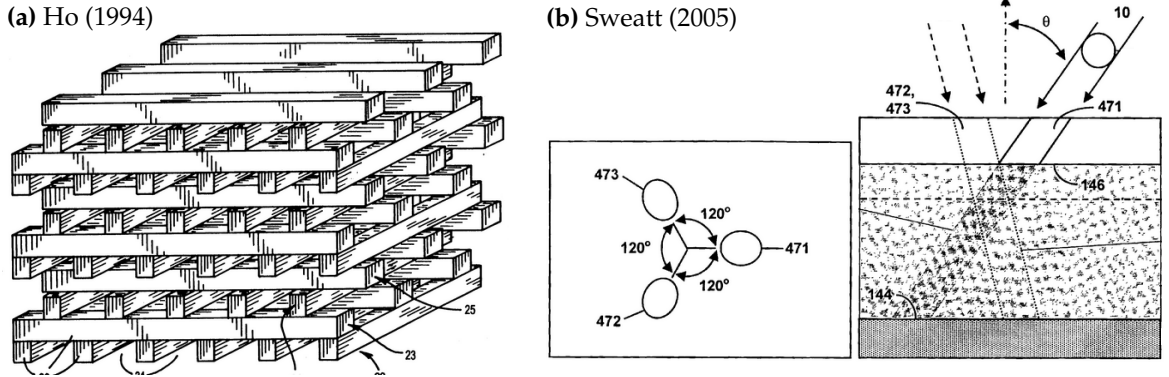
Following the author's personal view, the historical notes on metamaterials and photonic crystals below are organized into three independent paradigms that developed in parallel, and only later they were unified. Each of them, on its own, once might seem to already have given their fruits, but their *unification* appears to have renewed the scientific interest and pushed the research further.

This chapter can in no way cover all relevant papers and ideas over the last century; much better resources on the history of the field are in [51, 52, 53], at the web pages of Moroz [54] etc. Also the actual designs of the periodic structures are mentioned very briefly, since they will be the subject of the Results section.

2.4.2 Photonic band-gap structures

One-dimensional band gaps and dielectric mirrors In 1887, Lord Rayleigh [37] noticed the light reflecting in the volume of a transparent crystal composed of thin periodic layers of slightly different optical properties. X-ray scattering on crystals was observed by Max von Laue [55] and explained by W. H. and W. L. Braggs in

Figure 2.15: Two approaches for efficient fabrication of a photonic crystal: (a) dielectric rods stacking into a woodpile structure, (b) top view and side view of soft X-ray lithography inscribing a yablonovite-like hole lattice into a negative photoresist. Both drawings adapted from patent applications [58] and [59], respectively.



the 1910s [56]. Both effects are enabled by the constructive interference of the waves reflected from the macroscopic interfaces in the Rayleigh's crystal, or directly from the atomic layers in the X-ray case. This phenomenon became known as the *Bragg band gap*.

The very same principle was later employed for the design and fabrication of *dielectric mirrors*, which are made by stacking multiple layers of two alternating dielectrics with different wave impedances and quarter-wavelength thicknesses. They find a wide variety of applications, owing to their advantages over classical metallic mirrors such as higher reflectance and angular and spectral selectivity.

Embedding one layer different from the others, a *defect*, into the middle of a dielectric mirror can introduce a narrow transmittance window within its photonic band gap. The corresponding *defect mode* is characterized by a strong concentration of the electric field E in the defect, enabling one to construct narrow-band photonic filters that can be tuned by the defect properties [57].

Photonic crystals The success in prohibiting the light to propagate along one direction inspired the design of two- and three-dimensional *photonic crystals*, named in analogy with the band gaps for the electron wave in natural crystals [16]. A non-trivial accomplishment of manufacturing the first three-dimensional structure with a delimited range of frequencies for which there exists no propagating wave in any direction, a *complete band gap*, is attributed to Yablonovitch [60] in 1987.

The structure, known as *yablonovite*, was designed for microwaves, since it was made by precise mechanical drilling into a plastic cube. Different technologies were developed in the 1990s in attempts to fabricate photonic crystals operating efficiently in the optical range, e.g. a similar approach based on X-ray nanolithography (see Fig. 2.15a), stacking of structured layers (Fig. 2.15b), direct laser writing in a resin or self-assembly of dielectric spheres into opal-like lattice.

The demands for achieving a complete three-dimensional band gap can be reduced when a singly or doubly periodic modulation is etched into an index-guiding dielectric slab, as was developed by Zengerle in the 1970s and 1980s [61]. Planar

structures are also much easier to fabricate using existing technologies such as photolithography.

Band gap used in fibres and waveguides Embedding a linear defect into a photonic crystal with a complete band gap forms a waveguide from which the wave cannot escape, even when it is bent under sharp angles. Likewise, the *planar band-gap waveguide* can be formed by a linear defect in a photonic crystal slab, which restricts the light by the total internal reflection horizontally and by a means of the two-dimensional band gap vertically. Such structures can form waveguides, beam-splitters and filters in integrated optics.

The *photonic-crystal fibre* (PCF), conceived by Russel in 1991 [62], differs from the standard index-guiding fibres in that the light is confined to its core by a photonic band gap in both lateral directions. Its special feature is the strong guiding of waves even if its core is hollow, that is, with refractive index lower than the cladding. Broad-band single mode operation can be achieved, and the high field concentration can lead to very strong nonlinear interaction.

As a complementary concept, a one-dimensional photonic band-gap structure can be inscribed into conventional index-guiding fibres, forming a *distributed Bragg reflector*. Its filtering capabilities can be made extremely narrowband, which is employed in fibre lasers, telecommunication, sensing, etc.

Within the sole paradigm of band-gap engineering, new concepts emerge even in the last decades: Obviously, a minor shift of the band gap has a strong impact on whether the light can propagate. Such a shift can be introduced e.g. by static magnetic field in low symmetry PhCs, resulting in enhanced magneto-optic interaction for one-dimensional light propagation [39].

2.4.3 Homogeneous media with uncommon parameters

Negative parameters By *negative parameters* we understand either a negative real value of permittivity $\varepsilon_r(\omega)$, permeability $\mu_r(\omega)$, or a negative index of refraction. In transparent media without spatial dispersion, negative index of refraction $N'_{\text{eff}}(\omega)$ requires $\varepsilon_r(\omega)$ and $\mu_r(\omega)$ to be negative simultaneously, at least if its imaginary part is supposed to be small [63]. Note that all theoretical papers cited in this subsection used the electrodynamics of a *homogeneous* medium, without imposing its microscopic periodicity nor any other technical way how such a medium should be obtained.

Media with *negative permittivity* are in fact very common in the nature, including metals, doped semiconductors and plasmas; additionally, negative permittivity also results from lattice or electronic vibrations, forming the so called *reststrahlen* bands. Reflection from metals has been explained as the opposite signs of $\varepsilon_r(\omega)$ and $\mu_r(\omega)$ causing the wave to become *evanescent* and rapidly decaying under the surface. The same mechanism causing the radio wave reflection from the dilute plasma in the Earth's ionosphere was predicted as early as in 1839 by Gauss; its application for over-the-horizon communication was suggested in 1901-1902 by Heaviside and Kennelly.

Negative permeability manifests itself similarly to the electrodynamic point of view, but is observed much less often, typically above magnetic resonances, *magnons*.

Theoretical investigation of electrodynamics in media with a *negative index of refraction*, or slightly more generally, those with antiparallel group and phase velocities (cf. Chapter 2.2.4), can be traced back [14] to early discussions of anomalous dispersion near resonances by Lamb or in a 1904 book from Schuster [64, 23]. Mandelshtam's lectures on optics illustrated negative refraction of light in the 1940s [65] and were further complemented, among others, in 1957 by Sivukhin's discussion of energy concerns [66] and Pafomov's notes about reversed Čerenkov radiation [67].

It was Veselago's review of the negative-index homogeneous media from 1968 that received later significantly wider attention in the literature [10]. Veselago used the term of *left-handed media* and speculated to what extent they might exist in the nature, but he did not discuss the way of realizing such media, nor the more general theory of the spatial dispersion which may also lead to natural negative refraction.

Terminology of media with unusual parameters In the literature, different terms are used for a similar class of media. In most cases it appears [21] that it is a result of disunited terminology rather than a need to distinguish fine nuances.

1. The most general term is *negative-refraction* media. However, negative refraction can occur due to a range of phenomena, for example, in the anisotropic crystal of calcite under well-chosen incidence angle [14].
2. The aforementioned term is most probably supposed to mean *negative-refractive-index*, or simply *negative-index* media, which by definition behave as (approximately) isotropic at least in a limited range of incidence angles, and therefore their index of refraction can be defined as it is discussed in Sect. 2.1.3.

Isotropy also implies the phase and group velocities are parallel or anti-parallel, which legitimates to call the latter group as *backward-wave* [21].

3. Yet a narrower group is defined by the terms of *left-handed* [10] or *doubly-negative* media. Their etymology is based on the spatial orientation of the vector triplet (\mathbf{E} , \mathbf{H} , \mathbf{K}). In ordinary media with $\varepsilon_r > 0$, $\mu_r > 0$, the pseudovector \mathbf{H} is chosen so that the triplet can be associated to the thumb, index and middle finger of the right hand, in this order.

By simultaneous reversal the sign of both ε_r and μ_r , the electric and magnetic induction change their sign to be antiparallel to the fields. The wavevector \mathbf{K} is reversed, associating the triplet with the left hand.

In the author's view, both terms can therefore be associated exclusively with a subset of the *negative-index* media, for which the local *effective permittivity* $\varepsilon_{\text{eff}}(f)$ and *effective permeability* $\mu_{\text{eff}}(f)$ make physical sense.

Prediction of focusing effects by a negative-index slab As also discussed by Veselago [10, p. 511] and a decade later by Silin [68], a plane-parallel slab with an isotropic negative index of refraction and sufficient thickness would refract waves emanated from a point source towards a new focus in its volume, and similar negative refraction forms a second focus behind the slab. It is thus often referred to as a *negative-index lens*, although neither its focal point nor optical axis are defined as in classical lenses.

Clearly, a negative-index slab would be free of spherical aberrations, allowing a wide-angle and high numerical aperture for the imaging. To the knowledge of the author, the papers from this time did not discuss its application for overcoming the diffraction limit nor of amplification of evanescent waves.

Media with parameters close to zero Media where $\varepsilon_r(\omega)$ or $\mu_r(\omega)$ have very low values compared to vacuum form another class uncommon in nature. They are often denoted as *epsilon-near-zero* (ENZ) and *mu-near-zero* (MNZ). The result of $\varepsilon_r(\omega) \sim 0$ or $\mu_r(\omega) \sim 0$ is also the index of refraction being close to zero, $N(\omega) \sim 0$, particularly when both conditions are satisfied simultaneously.

Although e.g. the physics of the ionosphere involves regions where the permittivity transits from negative to positive values, the scientific interest in designing such media significantly grew after the merging of the paradigm with metamaterials, and therefore such media are often denoted syncretically as *zero-index metamaterials*. This is a somewhat confusing term, as the papers focusing on their peculiar macroscopic properties [69] usually do not discuss any structuration and are thus also applicable to fully homogeneous media of such properties.

A feature typical of this class of media is a very small wavevector $K \sim 0$, which can be approximated as the whole $N \sim 0$ region oscillating in phase. The wave entering from air into a $N \sim 0$ medium at near-normal incidence refracts under large angles from the normal; for angles higher than a small critical angle, the wave undergoes the *total external reflection* [70].

Transformation optics and electromagnetic cloaks Slow spatial changes in the refractive index cause the electromagnetic wave to follow a curved path, which can be alternatively viewed as propagation through a particularly curved (transformed) space filled with homogeneous medium. This is the basis of *transformation optics*.

The *electromagnetic cloak* is a hollow structure that guides the electromagnetic waves around its core and reconstructs the wavefront behind it, so that it casts no shadow, independent of the wave direction and of an obstacle present inside the cloak. The curved path used to evade the obstacle is always longer than a line segment, however, so typically a medium with continuously varying $N_{\text{eff}} \in \langle 0, 1 \rangle$ must be properly designed by transformation-optics calculations [52]. Electromagnetic cloaking was considered in 1961 by Dollin [71] and later by Kerker [72].

The concept of cloaking was realized [73] in 2006 using a microwave metamaterial, and followed by many others. All reported electromagnetic cloaks based on $N < 1$ media are inevitably dispersive, which limits their band width; they are also usually polarisation sensitive. The presence of any macroscopic cloak made

of known materials is also revealed by its losses, at least at the infrared or optical frequencies. Obviously a great conceptual breakthrough would be needed to overcome these issues.

A simplified task is to construct the *carpet cloak* which conceals the obstacle near a surface [74]. The carpet cloak can be built with $N < 1$ media as in full-angle cloaks, however for a single light polarisation, it can also be made of virtually lossless anisotropic dielectrics with quite usual values of parameters [75].

2.4.4 Artificial dielectrics and metamaterials

Analysis of nonresonant sub-wavelength structures The third independent paradigm was based on arranging sub-wavelength particles into an optically dense lattice to obtain some desired macroscopic behaviour of the light.

Its original source of inspiration can be traced to the late 19th century, when the scientific community resolved the question of how the dipoles of individual atoms in matter affect the macroscopic permittivity and permeability. The atomic size is negligible compared to the optical wavelengths, so all optically transparent natural media can be easily approximated as homogeneous. The explanation of the diamagnetic behaviour of some materials was proposed in the form of each atom behaving as a microscopic conductive loop in 1853 [76]. However, the inter-atomic electric dipole interactions are not negligible, and except for gases they preclude simple dipole averaging, so the explanation of the permittivity was formulated two decades later using the Lorentz-Lorenz (or, Clausius-Mossotti) formula.

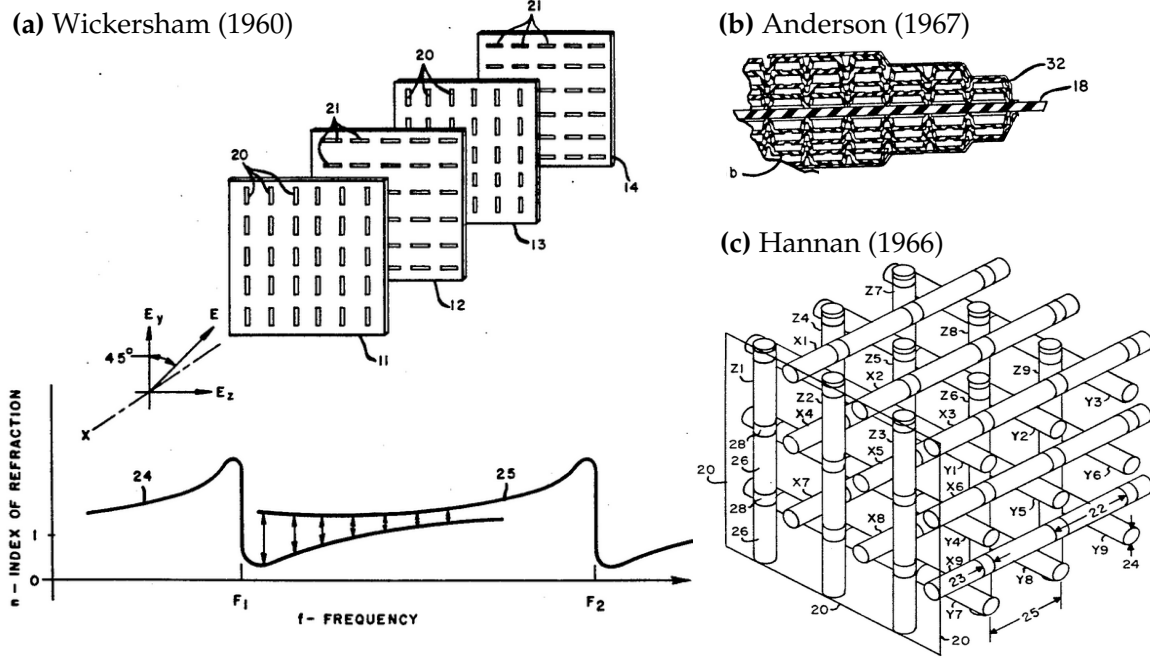
Theories of dielectric behaviour of composites having inhomogeneities larger than the atomic scale have been developed throughout the 20th century, among which the Maxwell-Garnett (1904) and Bruggemann (1935) are most known among multiple approaches. Their common assumption is that the wavelength is much larger than the particles; furthermore, they suppose there are no internal resonances in the embedded particles. More elaborate theories are needed when the particle have unusual shapes, particularly near the so-called percolation threshold when they become connected.

Synthesis of nonresonant sub-wavelength structures The design of inhomogeneous structures that could be treated as homogeneous with some desired properties has also a surprisingly long history. Inspired by the Lorentz-Lorenz formula, Lord Rayleigh theoretically elaborated the wave propagation through a rectangular lattice of cylindrical or spherical particles in 1892. He also noted the analogy between electromagnetic and acoustic waves [80, p. 498]. His thoughtful analysis was however still limited to the *static limit* of frequencies well below any resonant frequency of the particle, and to the *long-wavelength limit* well below the first photonic band gap.

Subwavelength wire arrays have been experimentally used at least since 1898 as microwave polarisers. The concept of assembling a microwave polarisation rotator from organic or metallic helices comes from that era, too [81, 82].

Periodic structures denoted as *artificial dielectrics* [83] found their use since the 1940s to engineer the broad-band permittivity tensor for the applications in light-

Figure 2.16: Three examples of artificial dielectrics designs patented half a century ago: (a) sheets containing cut wires of alternating orientation and resonant frequency, enabling one to manipulate the microwave polarisation, (b) cross-section through a lightweight lens of 3 m diameter designed for 50-500 MHz radio waves, made of partially metallized plastic layers, (c) artificial dielectric made of non-resonant cut wires arranged into a nearly isotropic 3-D lattice. Drawings adapted from patent applications [77], [78] and [79], respectively.



weight lenses for microwave frequencies [84]. Initially, they were operated in the static limit below any resonance. Usually the particles consisted of hollow metal waveguides or spheres/disks which increased or reduced the wave phase velocity, respectively.

2.4.5 First unification: metamaterials with uncommon parameters

Negative effective permittivity The 1950s brought the first step towards achieving negative effective parameters from man-made periodic structures: The geometry of the wire antennas was chosen to put the fundamental resonance of the electric dipole *below* the frequency of operation [85, 23]. The spectrum of *effective permittivity* $\varepsilon_{\text{eff}}(\omega)$ of this structure had the shape similar to the Lorentz oscillator shown in Fig. 2.2. It formed a frequency range of values that were negative or at least lower than one. This feature lead to the occasional use of the term *artificial plasma* [86].

In all cases of $\varepsilon_{\text{eff}}(\omega) < 1$, the effective refractive index $N_{\text{eff}}(\omega)$ was also lower than that of vacuum [87], but, as follows from

$$N(\omega) := k(\omega) \frac{c}{\omega} \equiv \sqrt{\varepsilon_r(\omega)\mu_r(\omega)}, \quad (2.37 \text{ again})$$

it could not become negative, since the effective permeability $\mu'_{\text{eff}}(\omega) > 0$ was still positive and its imaginary part $\mu''_{\text{eff}}(\omega)$ was negligible. The unit cell size was kept

much smaller than the wavelength, so the problem of *homogenisation* appeared as settled and the nonlocal effects apparently did not cause much concern.

Negative effective permeability and negative refractive index The literature is somewhat ambiguous, but a thorough search shows that the term *metamaterial* (MM) was first used on conference by Walser in 1999. Although apparently redundant to *artificial dielectrics*, which was used for decades before¹, the new term of *metamaterial* can be viewed as more fortunate as it does not imply whether the structure is man made or not, nor whether its effective parameters mimic a dielectric or, e.g., a metal.

It remains unclear whether there was an objective cause, or a semantic bias from the term *artificial dielectrics* only, that the periodic structures with magnetic effects received less attention than those with electric ones. Apparently the first theoretical studies thereof by Lewin [88] and Schelkunoff [89] date back to the 1940s, but the first realisations of split-ring resonator arrays and other magnetically resonant structures seem to have been published no earlier than in the 1980s. Further details can be found in the Results chapter on pp. 135 and 150.

The research of artificial dielectrics, or newly, metamaterials, gained on significant popularity after the papers from 1999 by Pendry [90] and from 2000 by Smith [91]. The former outlined how a negative index of refraction can be obtained in a structure composed of metallic wires introducing $\epsilon_{\text{eff}} < 0$ and of small metallic loops, known as *split-ring resonators* (SRR), introducing $\mu_{\text{eff}} < 0$. The latter paper described the experimental verification of negative refraction in the microwave range. Thousands of papers followed suite which covered different spectral ranges, demonstrated other MM designs, discussed theoretically when and how the metamaterial can be viewed as homogeneous, and sought for new applications.

Imaging beyond diffraction limit with metamaterials Arguably the most intense excitement was caused by another Pendry's paper [92] from 2000. It stated that a flat lens made of a lossless local medium with a negative refractive index can not only enable imaging, but it should do so with a resolution better than is allowed by the diffraction limit, theoretically down to infinitely small details. This device for *subdiffraction imaging*, denoted as the *superlens*, acquires this extraordinary feature through the formation of high-amplitude evanescent waves at its rear surface. The resulting extremely sharp image in some distance behind the superlens would then be composed not only of negatively refracted propagating waves, but also of the evanescent waves.

If a metamaterial is used as a negative-index medium, subwavelength imaging requires the unit cells being *finer* than the finest details to be imaged. The requirement is in fact even stricter, as also the spatial dispersion has to be negligible for all wavenumbers needed for the desired resolution. For the formation of highly concentrated evanescent waves at the rear surface, the small energy flow-through and

¹An interesting search into the terminology usage by means of the *Google Books Ngram Viewer* shows that the notion of *artificial dielectrics* has been the most used in the 1950s and early 1960s, and then its usage declined, to be greatly exceeded by the usage of *metamaterial* in early 2000s. Simultaneously, the usage of *photonic crystal* has rose an order of magnitude higher.

simultaneous high energy concentration require extremely low losses. In contrast, down-scaling of the unit cells inherently requires a higher energy localisation, and this is usually at the expense of the losses growing.

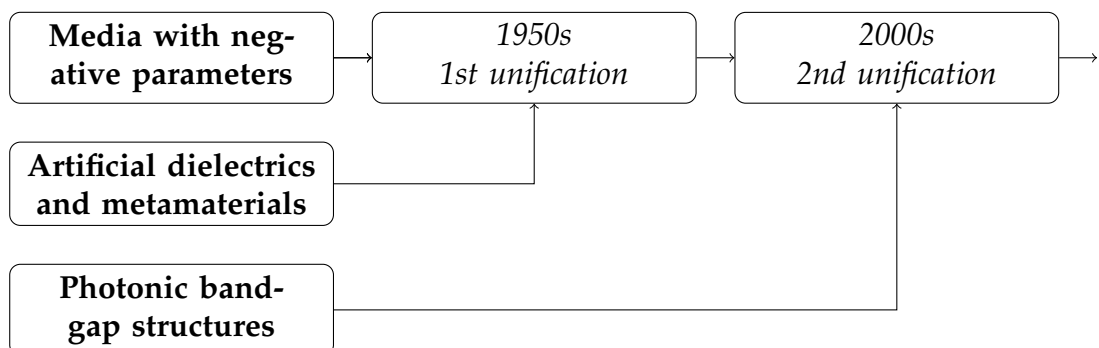
A related concept is the *hyperlens*, an inhomogeneous structure which employs anisotropic negative-index media to couple near fields to waves radiated in the air, thus enabling subdiffractive imaging in the far field. Again, the ultimate resolution of the hyperlens is determined by the spatial dispersion of the metamaterial used.

The problems of dissipative losses in resonant periodic structures were not sufficiently overcome yet. Some quantitative improvements can be easily done, namely thickening the metallic structures and increasing the inductance-to-capacitance ratios of the split-ring resonators (SRR) [93]. At the near-infrared and optical wavelengths, SRRs are overcome by perforated metallic sheets, so called *fishnets*, and it may be favorable to substitute metals with certain types of oxides with metallic-like permittivity in the optical range [94]. To the author's knowledge, all demonstrations of metamaterial sub-wavelength imaging were so far either only proof-of-concept, microscopic devices, or were limited to the easier accessible microwave region.

Metamaterials without unusual parameters and metasurfaces In spite of the metamaterials being the most often associated with superlenses and cloaks, many MM applications [95] do not involve negative or close-to-zero effective parameters [50, p. 15]. Among these are novel antenna designs, sensors, light modulators or devices making use of the enhanced nonlinear interaction. Strong interaction of resonant structures with electromagnetic waves enables one to efficiently manipulate the surface impedance by two-dimensional periodic layers, so called *metasurfaces*.

A recently published paper [96], even if it is somewhat controversial [97], presents a metamaterial application where a strong chirality leads to reversing the Casimir force between two close metamaterial surfaces, which then becomes repulsive.

Figure 2.17: Author's view of the development in the metamaterial and photonic crystal research over the past century



2.4.6 Second unification: metamaterials with photonic crystals

Experimental research Over the 20th century, the paradigms of metamaterials (MM) and photonic crystals (PhC) apparently developed independent of each other. The situation started to change in 2000s, when the metamaterial structures were realized to operate at near-infrared or optical frequencies. As already stated, increasing the operation frequency is intricate; not only is the contemporary three-dimensional submicroscopic fabrication technology somewhat limited in its resolution, but even more importantly, with any choice of available materials the dissipative losses become a major issue at the optical frequencies, particularly when the tight confinement of the field is required.

For both reasons, a compromise is usually made at the near-infrared and optical frequencies: the particle size is chosen only few times smaller than the wavelength of operation. Realized metamaterial structures can no more be viewed as deeply subwavelength [98], and classifies at the boundary of metamaterials and photonic crystals. This second unification of paradigms is sketched in Fig. 2.17.

Theoretical investigation of the structures on the MM-PhC boundary Along with experiments, the interplay between the individual and Bragg-type resonances was also studied on a theoretical basis. The former type of resonances is typical for metamaterials, while the latter for photonic crystals. Typically, one either scans the relative cell spacing (this can be done in simulations [45, 99] as well as in experiments [100]), or tunes the individual resonant frequency keeping the lattice parameters unchanged (e.g. [42]). The frequencies of the individual and Bragg resonances have different sensitivities to these parameters, and can thus be identified in the spectra. One such study of a typical structure, the array of dielectric rods, is elaborated in the Results section of this thesis.

In more abstract studies, the structure of the unit cell with its full electrodynamic behaviour is substituted by a flat homogeneous layer characterized only by its effective parameters which may be negative at certain frequencies. This approach is only an approximation, since usually the unit cell behaviour involves its coupling with nonradiative fields, which can no more be taken into account when they are replaced by a layer. The advantage is however in the possibility to use analytic means for understanding of the factors forming the band diagram.

Such an unusual photonic crystal can exhibit a specific *zero-order photonic band gap* [101, 102, 103] when the phase advance through the layer stack is zero, as has been confirmed also on an experimental basis [104]. In contrast, the typical photonic band gaps in positive-index dielectric layers occur when the phase advance is πM , $M \in \mathbb{N}$ [16]. The characteristic property of the *zero-order* band gap lies in its insensitivity to the structure scaling. The band gap can thus be observed even when the spacing of the hypothetical PhC is deeply subwavelength.

Another type of a band gap with a different field pattern was predicted [105] for a case when layers with $\varepsilon_r > 0, \mu_r < 0$ and $\varepsilon_r < 0, \mu_r > 0$ are stacked.

The common property of structures operating at Bloch's wavelengths of comparable magnitude to the cell spacing (i.e. $2\pi a/K \gtrsim 0.2$) is the strong manifestation of the spatial dispersion. The effective index of refraction then forms a typical reso-

nance curve clipped by the closest pair of Brillouin zone boundaries. In most such cases, the use of the local effective parameters $\varepsilon_{\text{eff}}(\omega)$ and $\mu_{\text{eff}}(\omega)$ hinders the possibility to obtain physical insight. On the contrary, it leads to a deviation from the expected Lorentz oscillator curves in $\varepsilon_{\text{eff}}(\omega)$ and $\mu_{\text{eff}}(\omega)$ and formation of *antiresonances* [106, 107] and complex values of ε_{eff} and μ_{eff} even in lossless media [101]. These problems, however, appear to be only artifacts of using the local theory outside its applicability. Instead it is necessary to adopt the full theory of spatially dispersive media, as sketched in Chapter 2.2 of this thesis.

2.5 The boundary between photonic crystals and metamaterials

In the light of the previous historical review, it appears that the notions of MMs and PhCs developed, for historical reasons, as different paradigms during the 20th century. It was however argued above that these paradigms and research communities are undergoing a process of unification, which raises the question whether there are any objective rules to tell apart MMs and PhCs.

The wavelength criterion Originally, the determining parameter was surely the ratio of the unit cell size to the wavelength of the electromagnetic wave (at the given frequency of operation). Even some recent papers [108] define MMs as

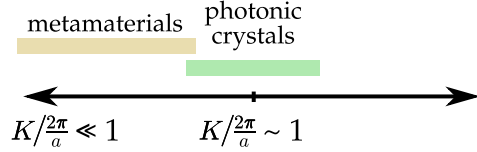
(...) *artificial periodic structures with features smaller than the vacuum wavelength.*

Studies of MMs and PhCs were both inspired by a wave propagating through the lattice of a natural crystal. The difference was however that in the case of MMs, it was an *optical* wave, whereas in the case of PhCs the inspiration came from the *electron wavefunction*. The wavelength of the valence-band electrons is similar to the inter-atomic distance ($\approx 10^{-10}$ m), always requiring the description by the Bloch's theorem, whereas the wavelength of light is roughly four orders of magnitude larger, enabling one to approximate the crystal as a homogeneous medium.

Analogously, the earlier metamaterials (or, artificial dielectrics) were mostly viewed as deeply subwavelength, which provided a clear and easy distinction from all PhCs. It also allowed to neglect spatial dispersion for the wave. The situation however appears to change with realistic MMs scaling to the optical range, since the wavelength becomes of the same order of magnitude as the unit cell size and both regions start to overlap as illustrated in Fig. 2.18. Besides, the PhC-MM boundary then becomes also frequency dependent.

The energy criterion The time-averaged energy of a plane wave in vacuum is constant, but any sort of interaction of MMs or PhCs with the wave is inherently connected to an uneven distribution of the electromagnetic energy in the structure. This may become the rationale for a new criterion: In the waves in MMs near a resonance, the energy is highly concentrated inside a part of the unit cell, typically

Figure 2.18: Rough illustration of the ratio of the Bloch's wavelength ($2\pi/K$) to the unit cell size a in metamaterials and photonic crystals



close to sharp edges of metals or within a particle of high-permittivity dielectric. On the contrary, the resonances in typical PhCs do not concentrate the energy, and instead there is a moderately high intensity of the field in the majority of the space between the scattering structure elements.

As a result, one can easily understand that the Bragg band gaps typical of a PhC are more sensitive to the unit-cell spacing. By contrast, the high concentration of the energy within a small part of the structure reduces the sensitivity of the parameters to a moderate disorder in the cell position, which has also been viewed as a trait of metamaterials, [109]:

(the fact that) the randomized positions do not influence significantly the left-handed properties indicates that such composite is different from (...) photonic crystals

The phase criterion The above criteria are somewhat vague, but there exists a well-defined, rigorous criterion dividing the periodic structures clearly into two groups at a given frequency: When a metamaterial is excited above its resonant frequency, and the resonant energy is well localized, the part of the unit cell volume contains field with the sign opposite to that in the excitation wave. This is similar to the behaviour of the Lorentz oscillator illustrated in Fig. 2.2. This opposite-field domain is delimited by a surface where either the electric or magnetic field is constantly zero, which will be denoted as the *nodal plane*. For the individual resonance, the nodal plane is closed and there exists some path through the unit cell which does not cross it. The Bragg band gap leads to open nodal surfaces delimiting the opposite-field domain which traverse the unit cell boundaries.

The difference between the topologies of localized and delocalized pair of nodal planes can be interpreted as the boundary between MMs and PhCs. In practice, this well-defined difference manifests itself in the change of the phase along each unit cell, without any obvious impact on the propagation of energy. In more details this is demonstrated in the Chapter 5.8 by numerical studies of the transition cases in dielectric rod arrays.

Less fortunate criteria Some sources include the requirement of unusual parameters into the MM definition, but this is hardly acceptable since it would obviously exclude some established MMs from the definition; the previous historical chapter attempts to give several examples. It also mentions that even some natural materials can exhibit unusual parameters.

Also the demand for "artificiality" in some other definitions appears to be somewhat artificial on its own, provided that one is interested in the actual structure properties rather than in its origin:

Metamaterial is an arrangement of artificial structural elements, designed to achieve advantageous and unusual electromagnetic properties [110]

Some confusion may arise from the fact that some authors seem to overly broaden the applicability of the popular term of metamaterials. For example, two-dimensionally periodic structures, in which a wave interacts with a single layer of unit cells only, have substantially different behaviour and applications, and in the author's view should be denoted as *metasurfaces*.

It is even more unfortunate to associate the concept of MMs with one iconic design of a unit cell. Under no thinkable definition can a metamaterial be made by attaching a single split-ring resonator to a microwave transmission line.

Some of other definitions realize an important trait of metamaterials, which is *emergence* [50]. While the complexity of the electromagnetic field grows proportionally to the number of unit cells stacked together, new kinds of relatively simple and understandable behaviour can be observed for a large enough system. The introduction of effective parameters, a behaviour emergent from the structure of each unit cell, is one of the best examples.

A metamaterial is a (...) substance whose properties depend on its inter-atomic structure rather than on the composition of atoms themselves, (whatis.com)

or, in more words,

metamaterials are artificially structured materials used to control light, sound and many other physical phenomena. The properties of metamaterials are derived from the inherent properties of their constituent materials, as well as from the geometrical arrangement of these (...) (website of the Duke university)

In the author's view, such quotes represent brilliant observations of emergence in physics, but they cannot be used as a distinction between metamaterials and photonic crystals. In fact, they apply to both classes of structures.

Metamaterials as all structures subject to homogenisation The criteria of wavelength or energy localisation leave many structures on the indefinite boundary. The phase-advance criterion is rigorous, but of little practical use. There are other criteria proposed that appear to fail in some way. This leads the author to the personal view that the difference in one's decision on how each structure is characterized.

The unifying concept of virtually all MM studies is to describe *how* the wave propagates through them. Their overwhelmingly complicated electromagnetic interaction is approximated by *homogenisation*, i.e. by finding such properties of a homogeneous medium that would behave in similar way.

In contrast, the PhC research focuses on *whether* the wave can propagate at all. When a mirror, filter, waveguide cladding or other structure with a band gap is designed, it is important to prevent or allow the light propagation rather than to achieve some desired effective parameters for the Bloch's wave.

This also justifies denoting MMs and PhCs as two different *paradigms* rather than two distinct *classes* of periodic structures, and it is the reason why the neutral term of *periodic structure* is used in this thesis.

With this in mind, the author believes that there is no need for a strict rule for classification. Some structures are then more useful to be subject to homogenisation, and with some other it is more interesting to focus on their band and band-gap structure.

Chapter 3

Numerical methods

“Computers are useless. They can only give you answers.” — P. Picasso (1968)

3.1 Numerical simulation algorithms

This section describes the numerical methods used for preparation of this thesis. Major accent is put on the finite-difference time-domain method, since it was used for most simulations. Several important observations are discussed which are probably not found elsewhere. At its end, this chapter briefly mentions the plane-wave expansion method.

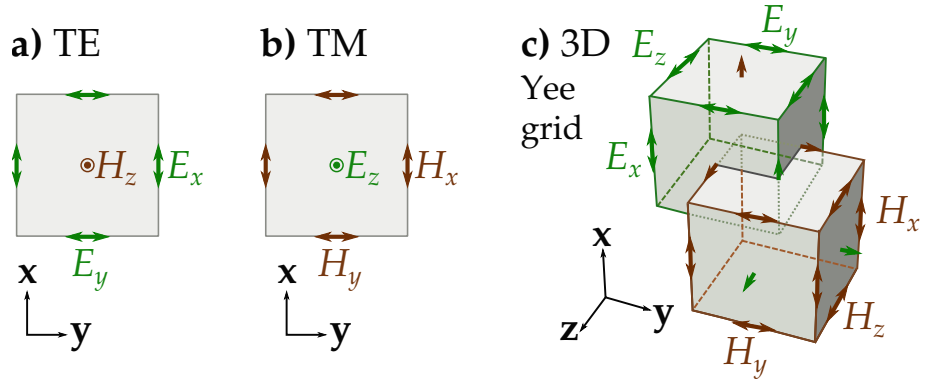
3.1.1 Finite-difference time-domain method

Algorithm description Finite-difference time-domain (FDTD) simulations rank among the simplest methods for solving partial differential equations. The simulation volume is initialized as an array in the computer memory, each element of which corresponds to a so called *voxel* in an orthogonal grid. When the FDTD method is applied to solve the Maxwell equations in three dimensions, six complex numbers per voxel describe the electric and magnetic vector fields, other static scalar arrays describe the permittivity and permeability of the structure and additional arrays may be used to store other physical quantities, such as material conductivity, polarizabilities and polarisations etc.

The actual computation is realized in consecutive time steps as an explicit arithmetic operation on each voxel, taking into account only the field values in the neighbouring voxels and in the previous time step [111]. This corresponds to iterating equations (2.3), (2.4) and (2.5). Most of the computational time is thus occupied by a simple and unconditional loop repeatedly updating all voxels, which allows to fully employ the processor cache and facilitates multi-processor parallelisation. FDTD is applicable to (possibly non-linear) problems where either the temporal evolution of the fields is being determined, or for linear systems where a frequency-domain response function can be found by Fourier-transforming the time-domain response.

The time-stepping routine needs the same computing power in empty vacuum as inside a complex structure. Grid-based methods such as FDTD are therefore the

Figure 3.1: (a), (b) Different two-dimensional grids are used for different polarisations of the fields. (c) The three-dimensional Yee grid. The electric field components are related to the centres of the green cube edges which they are parallel to, whereas the magnetic components are expressed in the centres of the green cube which they are perpendicular to. Note the electric and magnetic fields are completely equal in this scheme; the description in terms of edges and faces could be interchanged if the lower, brown-edged cube was taken as the elementary one.



most efficient when a structure has a relatively complex shape, but its smallest features are no more than two or three orders of magnitude smaller than the simulation size. In contrast, an accurate-enough simulation of a structure that has some very fine features surrounded by big empty space would require an excessively high resolution, often resulting in the great majority of the voxels being inefficiently used in space where the high resolution is not needed. Other methods, such as the finite-element method (FEM) or boundary-element method (BEM), would be preferable for such cases.

As widely used in the later chapters, simulations of waves propagating in any periodic structure can make use of the periodic boundaries of the simulated volume, so that only one unit cell has to be taken into account in order to derive the response of the whole structure. The unit cells of periodic structures discussed in this thesis have their finest features no less than two orders of magnitude smaller than the unit cell size, and most of the simulations were aimed at obtaining a broad-band spectrum, so the FDTD approach was an optimal for this task.

Spatial discretisation The discretisation of the grid and the time stepping introduce errors that manifest themselves by an imprecise description of the structure being simulated, known as *staircasing* errors. Other errors arise due to an appreciable deviation of the light velocity from the correct values at higher frequencies, the so-called *numerical dispersion* [111]. In most of the FDTD implementations, the error due to the numerical dispersion is reduced from first to second order ($\propto \Delta x^{-2}$ with regard to the voxel size Δx) by using a *staggered grid*, which, in three dimensions, is also known as Yee grid [112]. All six field components are expressed in different points within the voxel, as is illustrated in Fig. 3.1c. Likewise, the updates of electric and magnetic fields have to be interlaced also in time (a so-called *leapfrog* process). When accessing the field values at a given position and time, each field

component has to be properly averaged between the nearest points in the grid, and between the nearest update times.

Spatial discretisation By adequate averaging of permittivity on the boundaries of materials, this error can likewise be reduced to the quadratic order with regard to Δx . Various averaging approaches have been studied in the literature [2]. Arithmetic averaging of permittivity with a weight proportional to the voxel volume occupied by the material is perhaps the most intuitive one, but it often leads to wrong results, and sometimes it is even worse than no averaging at all [113, 114].

In case of a single planar interface between two different materials under a general orientation, the arithmetic average of the permittivities ε_r is correct only for the electric field component *parallel* with the interface, whereas the component *perpendicular* to the interface requires to apply this weighted averaging to the reciprocal value of permittivity, ε_r^{-1} , instead. Such an approach is extremely accurate for all interfaces with low curvature, but it requires the FDTD simulations to define the permittivity as a 3×3 tensor array [115]. This is needed even in the case of isotropic materials.

The situation gets even more complicated for materials with a dispersive permittivity, where also the weighting coefficients of both media need to be frequency-dependent, and another sophisticated approach has to be employed [114, 116]. Such a level of elaboration easily leads to computation requirements that may outweigh the benefits of averaging, and accordingly, no averaging was used for the simulations presented in this thesis.

In general, the effect of discretisation in FDTD simulations can be easily identified by comparing results from two simulations that differ by the grid resolution only. It is a good practice to verify that such an error is negligible whenever a new simulation is tested.

Temporal discretisation While the spatial resolution Δx can be set relatively freely depending on the accuracy expected by the user, the *temporal resolution* Δt is related to Δx . Generally, if the time interval Δt is set too high, the simulation will get numerically unstable, yielding unrealistic or even infinite values.

In the literature, one often encounters that the *Courant factor* s is used instead of the description in terms of Δt ,

$$s = \frac{c\Delta t}{\Delta x}, \quad (3.1)$$

In words, the Courant factor s denotes what part of a FDTD cell the light can travel within one time step. The reason for introducing this quantity consists in the Maxwell equations [Eq. (2.1-2.4)] being scale invariant, which holds also for the field update routine in FDTD when materials with frequency-independent permittivity are used. Therefore, when the resolution Δx is changed, s can be a well-chosen built-in constant and the time resolution given by Eq. (3.1) ensures that the simulation does not go unstable. The convenient values of the Courant factor, leading to correct results, are discussed below.

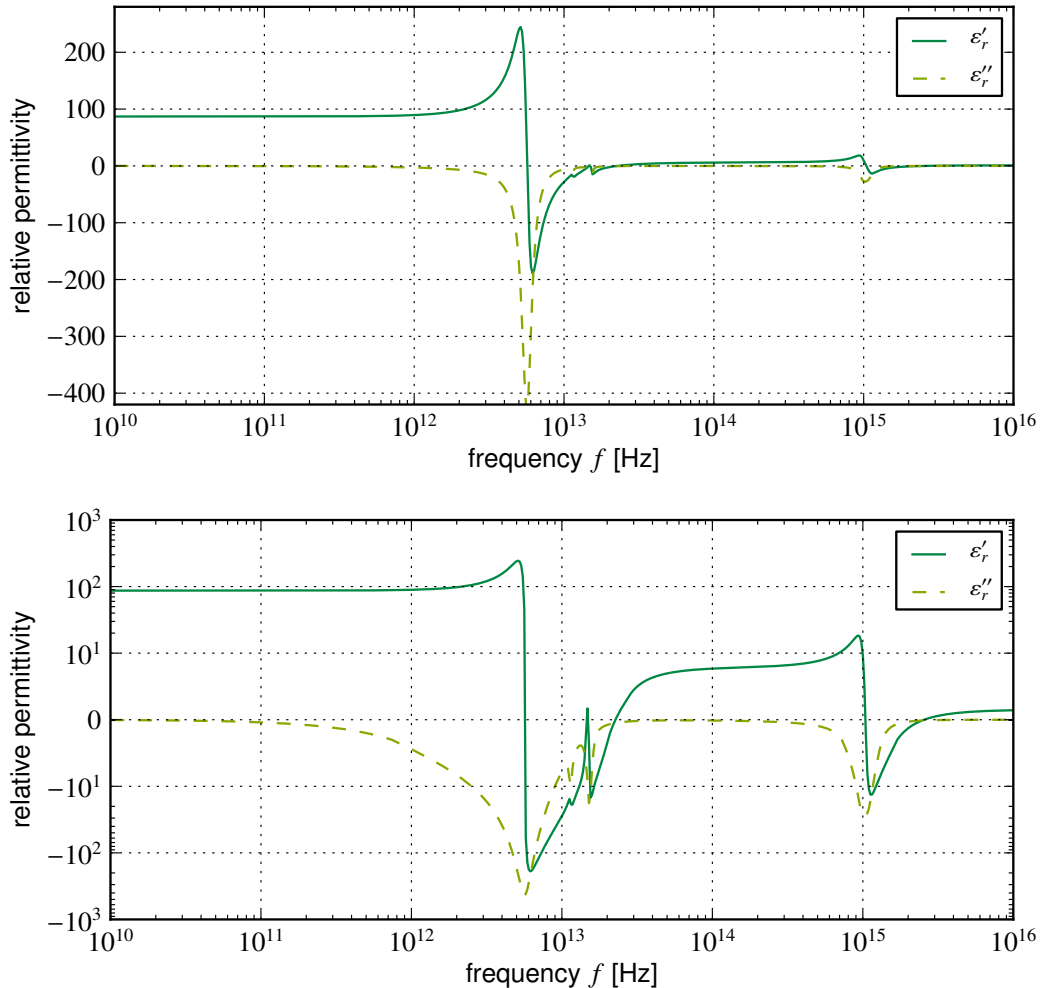
FDTD obviously ceases to be scale-invariant whenever the properties of the materials depend on the frequency, which is needed for many realistic simulations.

Then it appears more convenient to formally introduce yet another quantity, a *critical frequency* f_c :

$$f_c := \frac{1}{\pi \Delta t} \equiv \frac{c}{\pi s \Delta x} \quad (3.2)$$

Note that this frequency is only $1/\pi$ of the frequency of time-stepping cycles. From our observations, it is the value of f_c , and its relation to the model of materials used, that are of key importance for assessing the numerical stability of simulation.

Figure 3.2: Plots of complex permittivity $\varepsilon_{ro}(\omega)$ of titanium dioxide (rutile), for an ordinary ray, as defined in the simulation scripts [117]. The above plot has a linear vertical scale, while the bottom plot displays the same quantity using the scale that is $-\log(-\varepsilon_r)$ for $\varepsilon_r < -1$; linear for $-10 < \varepsilon_r < 10$ and $\log(\varepsilon_r)$ for $\varepsilon_r > 1$. The second approach better shows different orders of magnitude in the permittivity function. Similarly to other figures in this thesis, the solid line denotes the real component, while the dashed line denotes the imaginary one.



Definition of materials for the FDTD method As described in Chapter 2.1.2, Eqs. (2.21, 2.24), the local response of many usual media to electromagnetic waves can

be well approximated by a set of Lorentz oscillators, each of which is defined by three positive real numbers: its resonance angular frequency ω_0 , damping rate γ and oscillator strength F .

FDTD, being a time-domain method, uses a computationally efficient description of the media in a similar form, with the difference that the non-dispersive part of relative permittivity $\varepsilon_{r\infty}$ can be additionally defined as a real number.

$$\varepsilon_r(\omega) = \varepsilon_{r\infty} + \sum_{m=1}^M \frac{F_m}{\omega_{0m}^2 - \omega^2 + i\omega\gamma_m} \quad (3.3)$$

An illustration of a complex permittivity spectrum for titanium dioxide in its rutile allotrope is shown in Fig. 3.2. As the crystal is birefringent, only one permittivity component, denoted as *ordinary*, from the tensor in Eq. (2.35) was selected.

Conditions of stability in FDTD The author has observed that f_c determines the constraints for the simulation stability simultaneously in two ways:

1. The resonant frequencies of all Lorentzians must be lower than the critical frequency,

$$\frac{\omega_{0m}}{2\pi} < f_c, \text{ for all oscillators,} \quad (3.4)$$

regardless of the strength F_m of the oscillator or its damping rate γ_m .

2. For all frequencies higher than the critical frequency f_c , the real part of the permittivity given by Eq. (3.3) must exceed a minimum value given by the Courant factor s ,

$$\varepsilon'_r(2\pi f) > 3s^2 \equiv 3 \left(\frac{c\Delta t}{\Delta x} \right)^2 \text{ for } \forall f \geq f_c. \quad (3.5)$$

A geometrical interpretation of this rule is that an instability is introduced when any wave with a frequency above f_c can travel more than $1/\sqrt{3}$ of one FDTD voxel distance within one time step. Note that in a nonmagnetic medium, the travelled distance is

$$\frac{c\Delta t}{\sqrt{\varepsilon'_r}}.$$

Both these rules were observed to hold in media with $\mu_r = 1$ only; in media with magnetic response they would probably become more complex. The FDTD simulation will become unstable if one of these rules is broken. The instability error initially arises from inevitable numerical noise at the boundary of the problematic material and it grows exponentially. It can be identified as a pixel-wise checkerboard pattern on the early field snapshots. Later, the field visualisation usually returns black images as the numerical infinity is reached within several tens of FDTD steps.

Choice of the Courant factor Provided that a part of the simulation volume is empty vacuum ($\varepsilon'_r = 1$), Eq. (3.5) clearly determines the *maximum value of the Courant factor*:

$$s_{max} = 3^{-1/2} \approx 0.577.$$

In practice, a slightly more conservative choice is made that provides a safe margin for the numerical imprecision:

$$s := 0.500 \quad \rightarrow \quad \varepsilon'_r(2\pi f) > 0.75, \quad \forall f \geq f_c. \quad (3.6)$$

For any material with a problematic high-frequency permittivity, $\varepsilon'_r(\omega = 2\pi f_c) \in (0, 1)$, some low value of s can be found that makes the simulation stable against the second rule described on p. 74. Simultaneously, the critical frequency shifts up, so potential problems with the first rule may be alleviated, too. This is done, however, at the price of scaling up the number of required FDTD steps, so usually a reasonable change of the material definition is made instead of reducing s .

Practical aspects of material definition In all realistic media, the frequencies of different oscillators span over many orders of magnitude, and an accurate medium model would need to determine the parameters of too many oscillators. Not all oscillators should be accounted for in a given FDTD simulation, though.

First of all, high-frequency oscillators would make the simulation unstable. Aside from this, adding unduly many oscillators is also inefficient, because each oscillator term increases the computing difficulty of FDTD computations. It is therefore advisable to keep the oscillator number to an acceptable necessary minimum, and to describe the material within some frequency range of interest (FRoI) only:

1. The upper bound of the FRoI is limited by the numerical stability as stated above. Mostly, a more strict limit is imposed by the spatial resolution of the simulation: in a high-permittivity material, too high frequencies correspond to wavelengths similar to the voxel size or even smaller, leading to a significant inaccuracy.

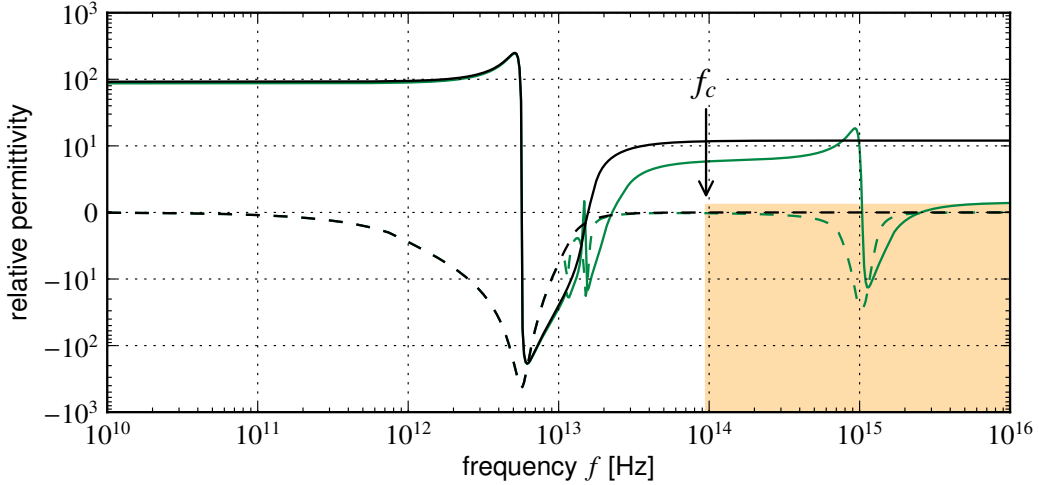
Each oscillator far above the frequency of interest shall be expressed only as a real constant added to the non-dispersive part of permittivity $\varepsilon_{r\infty}$. The contribution of an m -th oscillator is given by Eq. (2.22) as

$$(\Delta\varepsilon_r)_m = \frac{F_m}{\omega_{0m}^2}.$$

If some of the high-frequency oscillators introduces significant dispersion or losses in the FRoI, it should not be eliminated in this way. This usually concerns the oscillator that is the closest to the FRoI, and it usually can be kept without causing instability.

2. Very low frequencies, corresponding to wavelengths much larger than the whole simulation volume, are theoretically accessible with a long-enough FDTD simulation, but it would not be practical to extend the FRoI close to

Figure 3.3: Permittivity plot for titanium dioxide, similar to Fig. 3.2. The region forbidden by the stability rules is yellow shaded (above $f_c = 95$ THz and below $\varepsilon_r < 0.75$). The exact model for TiO_2 (green line, from Ref. [117]) would be definitely unstable due to violating both stability conditions. The numerically stable model for the frequency range of interest up to ca. 10 THz (black line) has all high-frequency oscillators substituted by an increased value of $\varepsilon_{r\infty}$. Solid and dashed lines denote the real and imaginary parts, respectively.



the zero frequency. If needed, the low-frequency phenomena can often be computed more efficiently in a separate simulation with a lower resolution or even with different numerical methods.

The oscillators at too low frequencies can therefore be omitted without any change to the behaviour within the FRoI. One important exception is the low-frequency oscillator that stands for the Drude term and defines the conductive behaviour, as described below.

Drude model for conductive media The Drude model, describing the response of free charge carriers, assumes a zero resonance frequency, i.e., the relative permittivity in the form

$$\varepsilon_r(\omega) = 1 + \frac{\omega_p^2}{0 - \omega^2 + i\gamma\omega} = 1 - \frac{\omega_p^2}{\omega^2 - i\gamma\omega}, \quad (3.7)$$

where ω_p and γ are two independent parameters that describe the metal:

- ω_p is the *plasma frequency*, at which the real part of permittivity crosses zero. The physical consequence is that for $\omega > \omega_p$ the medium allows the transverse electromagnetic waves to propagate.
- γ is the momentum *scattering frequency*, which can be understood as the *rate of exponential decay* of the medium response to an impulse, similar to the Lorentz model. The Drude model was conceived in the early 20th century, with the simplified hypothesis that electrons are freely propagating particles that undergo collisions with the atoms at an average frequency γ . Upon the collisions,

their velocity vector would be randomized. The Drude model often provides a very good approximation of the metallic-like response.

The Drude model can thus be considered a specific case of a Lorentz oscillator with $\omega_0 = 0$, and oscillator strength given by $F = \omega_p^2$. Obviously, using Eq. (2.22) to compute the contribution of the Drude term to the real part of permittivity would give infinite values, as a static electric field can displace an unlimited amount of charge in a conductor.

If γ is nonzero, the permittivity is a complex function and it can be separated into its real and imaginary part $\varepsilon_r = \varepsilon'_r + i\varepsilon''_r$ by expanding the fraction in (3.7) by the complex conjugate of its denominator:

$$\varepsilon_r = 1 - \omega_p^2 \cdot \frac{\omega^2 + i\gamma\omega}{\omega^4 + \gamma^2\omega^2} = \underbrace{\left(1 - \frac{\omega_p^2}{\omega^2 + \gamma^2}\right)}_{\text{real part } \varepsilon'_r} + i\underbrace{\left(\frac{-\omega_p^2\gamma}{\omega^3 + \gamma^2\omega}\right)}_{\text{imaginary part } \varepsilon''_r}. \quad (3.8)$$

The low- and high-frequency limits of the permittivity given by the Drude model are:

$$\lim_{\omega \rightarrow 0} \varepsilon'_r = 1 - \frac{\omega_p^2}{\gamma^2}, \quad \lim_{\omega \rightarrow 0} (\varepsilon''_r \cdot \omega) = -\frac{\omega_p^2}{\gamma}, \quad (3.9)$$

$$\lim_{\omega \rightarrow +\infty} \varepsilon'_r = 1, \quad \lim_{\omega \rightarrow +\infty} (\varepsilon''_r \cdot \omega^3) = -\omega_p^2\gamma. \quad (3.10)$$

We can see that in the low-frequency limit, the imaginary part of permittivity diverges (while its real part has a finite value). In the high-frequency limit, the metal permittivity approaches that of vacuum, i.e. $1 + 0i$.

Low- and high-frequency limits of conductivity in the Drude model The notion of *conductivity* is widely used to describe metals and doped semiconductors, i.e. media where the response to the electric field is characteristic by the motion of free charge carriers. Generally, both permittivity $\varepsilon_r(\omega)$ and conductivity $\sigma(\omega)$ are complex functions of the angular frequency ω . As long as the approximation of a negligible spatial dispersion is used, each of them is fully determined by the other function. For clarity, we avoid using the conductivity in the rest of the thesis except this chapter.

The relation between $\varepsilon_r(\omega)$ and $\sigma(\omega)$ can be derived by realizing that the current in a material is always caused by movement of charges with a density j and average velocity $\mathbf{v}(t)$. The conduction and polarisation currents are not distinguished here, as their density is given as $j\mathbf{v}(t)$ in both cases. When the current is excited by a harmonic electric field $E(t) = e^{i\omega t}$:

$$j\mathbf{v}(t) = \sigma(\omega)E(t) = \sigma(\omega)e^{i\omega t}, \quad (\text{conduction approach - Ohm law}) \quad (3.11)$$

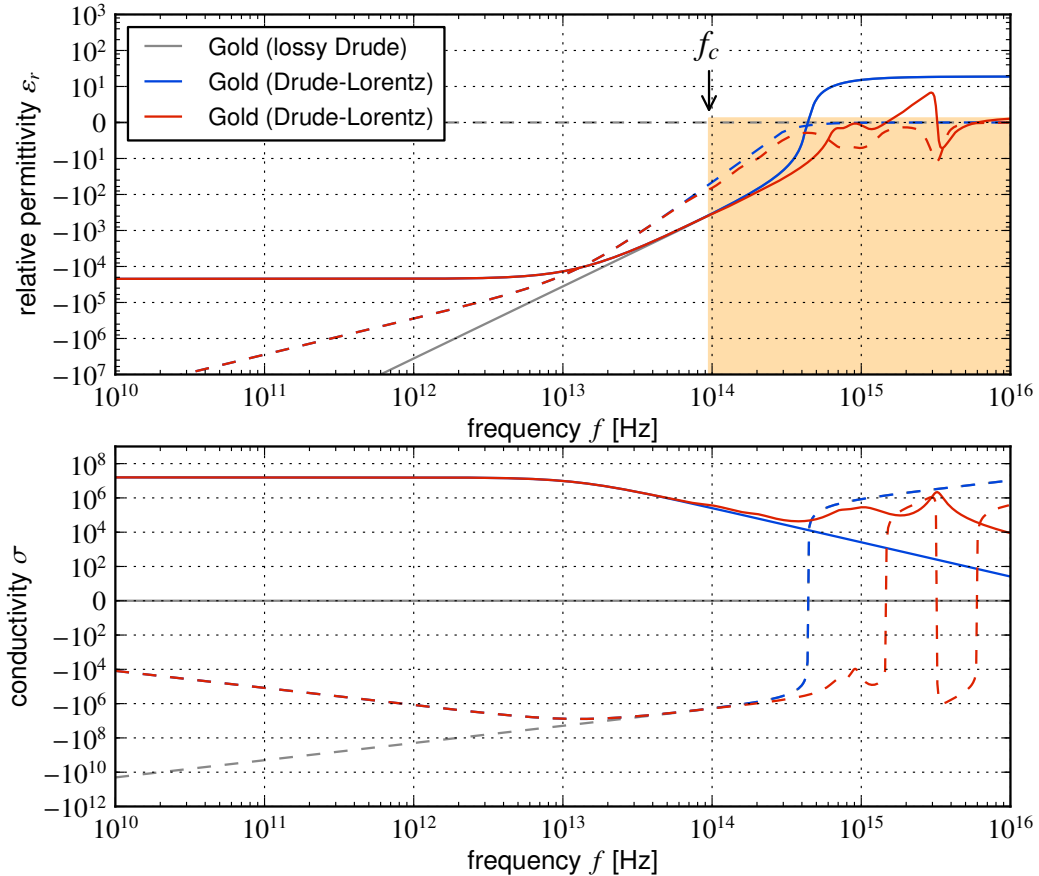
$$j\mathbf{v}(t) = \varepsilon_0\varepsilon_r(\omega)\frac{\partial E(t)}{\partial t} = i\omega\varepsilon_0\varepsilon_r(\omega)e^{i\omega t}. \quad (\text{displacement current approach}) \quad (3.12)$$

Both these equations describe the same quantity, so

$$\sigma(\omega) = i\omega\varepsilon_0\varepsilon_r(\omega), \quad \text{and} \quad \varepsilon_r(\omega) = \frac{\sigma(\omega)}{i\omega\varepsilon_0}. \quad (3.13)$$

Figure 3.4: Permittivity and conductivity plot for gold; the yellow region, forbidden by the stability rules, is the same as in Fig. 3.3. The exact model of gold [118] (red) is compared to the lossy Drude model with Lorentz oscillators substituted by ε_r (blue), and for illustration, also to the lossless Drude model with scattering frequency set to zero (grey). Obviously, none of these models is numerically stable if $f_c = 95$ THz.

The bottom plot shows the conductivity of these three models as given by Eq. (3.13).



Thus, a dielectric medium with a real constant permittivity has a purely *imaginary* conductivity, the magnitude of which grows with frequency (cf. the admittance of a capacitor). A conductor with a real constant conductivity has a complex permittivity, whose imaginary part diverges in the low-frequency limit.

Using the above relation (3.13) to convert the metal permittivity $\varepsilon_r(\omega)$ into conductivity $\sigma(\omega)$, and substituting the Drude-model permittivity (3.8), we obtain

$$\sigma(\omega) = i\omega\varepsilon_0\varepsilon_r(\omega) = i\omega\varepsilon_0\varepsilon'_r(\omega) - \omega\varepsilon_0\varepsilon''_r(\omega) = i\varepsilon_0 \underbrace{\left(\omega - \frac{\omega_p^2\omega}{\omega^2 + \gamma^2}\right)}_{\text{imaginary part } \sigma''} + \varepsilon_0 \underbrace{\frac{\omega_p^2\gamma}{\omega^2 + \gamma^2}}_{\text{real part } \sigma'}. \quad (3.14)$$

We may now express the low- and high-frequency limits also for conductivity:

$$\sigma_{LF} := \lim_{\omega \rightarrow 0} \sigma' = \frac{\omega_p^2\varepsilon_0}{\gamma}, \quad \lim_{\omega \rightarrow 0} (\sigma''/\omega) = \varepsilon_0 - \frac{\omega_p^2\varepsilon_0}{\gamma^2}, \quad (3.15)$$

$$\lim_{\omega \rightarrow +\infty} (\sigma' \cdot \omega^2) = \varepsilon_0 \omega_p^2 \gamma, \quad \lim_{\omega \rightarrow +\infty} (\sigma''/\omega) = \varepsilon_0. \quad (3.16)$$

Let us note again that in the literature that uses the negative phase convention $e^{-i\omega t}$, the resulting $\varepsilon_r(\omega)$ and $\sigma(\omega)$ are complex conjugated to the above results.

Defining resistive metals for stable low-resolution simulations Simulations in the optical range are relatively safe in terms of numerical stability. From Eq. (3.2) it follows that the resolution of $\Delta x = 50$ nm, suitable for the near infrared or visible spectrum, yields a critical frequency of $f_c = 3.82 \cdot 10^{15}$ Hz ($\lambda = c/f_c \approx 78$ nm), which is far above the plasma frequency of metals and other conductors. Accordingly, no changes to the Drude model are usually required, although the simulation may run faster if one or more Lorentz terms outside the FROI can be omitted.

Realistic simulations of metals at lower resolutions, however, require taking measures to ensure stability, as the critical frequency f_c is reduced below the plasma frequency of most metals when $\Delta x \gtrsim 200$ nm. A trivial approach consists in drastically reducing the Courant factor s so that f_c remains above the plasma frequency. Although this should reliably avoid the instability, it would be at the expense of scaling the computational time. As a general rule, a lower resolution is typically chosen for larger structures, where also all investigated processes accordingly happen on a longer timescale.

For simulations with a lower resolution, it is much more efficient to replace the exact Drude model with its approximation that maintains the same low-frequency limit of conductivity σ_{LF} , but has a positive permittivity around the critical frequency and above. This formally inverts the relations that describe the material:

- For *high-resolution simulations* typically in optical range, ω_p and γ are given as experimental properties of the metal, which determine the lower limit $\sigma_{LF} = \omega_p^2 \varepsilon_0 \gamma^{-1}$ and the non-dispersive part of permittivity $\varepsilon_{r\infty} = 1$ is fixed to that of vacuum.
- For *low-resolution simulations* typically in microwave range, the situation is the opposite: σ_{LF} is given as an experimental property, $\gamma < 2\pi f_c$ is given by the critical frequency, whereas $\varepsilon_{r\infty}$ and ω_p are to be determined from the previous two input parameters.

Debye media in FDTD The Lorentz model can be also employed to define over-damped oscillators, corresponding to the processes where $\gamma \gg \omega_0$, i.e. the inertia is negligible. A typical example is the reorientation of polar molecules in liquids or solids.

It can be shown that for $\gamma \gg \omega_0$, the peak in $\varepsilon_r''(\omega)$ lies approximately at the frequency ω_p^2/γ . The spectral width of such a peak is proportional to its central frequency.

3.1.2 Finite-difference frequency-domain method

Principle When the procedure for one time-step in FDTD is defined, it can play the role of the linear operator \mathcal{L} in the generic formulation the eigenfunction prob-

Table 3.1: Comparison of Lorentzian types and the corresponding physical phenomena

| Charges are | | Charge inertia is | Phenomenon | Example |
|-------------|-------------|-------------------|--------------------------------|---|
| Bound | Significant | | Lorentz oscillator | optical phonons, electronic levels, molecular vibration or rotation in gases |
| Bound | Negligible | | Debye relaxation | molecular rotation in solids or liquids |
| Free | Significant | | Reactive (plasmonic) medium | collisionless plasma, metals (from mid-infrared to optical range) |
| Free | Negligible | | Resistive medium | doped semiconductors, metals (in far-infrared range and below) |

lem:

$$\mathcal{L}\psi = e^{i\omega t}\psi,$$

where the function ψ represents either of the electric or magnetic fields.

Both time- and frequency-domain simulations used in this thesis use complex numbers to represent all field components. The whole frequency-domain problem can thus be expressed as a simultaneous optimisation of the $\mathbf{E}(\mathbf{r})$, $\mathbf{H}(\mathbf{r})$ fields, so that one time-step of FDTD is as similar as possible to the phase rotation of the functions. The angle of the phase rotation is given by the user-defined angular frequency ω . For the optimisation to be as efficient as possible, the *stabilized biconjugate gradient* algorithm [2] is used. More information on the frequency-domain solver is on the project's website [119].

The modes obtained by a frequency-domain simulation can be retrieved with an unknown phase offset; sometimes the real part of either electric or magnetic field can be nearly zero. In such a case, the imaginary part thereof always gives a sufficient amplitude to be plotted accurately.

Comparison to the time-domain computation To verify their reliability, the results of multiple finite-difference frequency domain (FDFD) simulations, with their frequency being scanned over a desired range of values, were compared against the results from the time-domain simulation to evince an acceptable match.

The advantage of the frequency-domain (FDFD) method over the time-domain (FDTD) is a better efficiency of the field shape computation at a single given frequency, where the computational time of the time-domain methods grows proportionally to the desired spectral resolution. Having both algorithms packed in one library enables extremely easy switching between them.

While the spectra of all material properties in FDTD have to conform to the Kramers-Kronig relations, in FDFD the permittivity and conductivity of each medium can be chosen without any limitations. A frequency scan of multiple FDFD simulations can thus be more efficient for simulation of materials with unusually complex spectral response, such as superconductors.

It was observed by the author that the FDFD solver in the MEEP program often fails to converge when plasmonic effects at the optical frequencies occur. In such cases, one has to replace it by the FDTD algorithm with a narrow frequency source.

3.1.3 Plane-wave expansion method

Description Another algorithm used in this thesis is the *plane-wave expansion method* (PWEM). Whereas FDTD and FDFD are very general algorithms that can be applied with different choices of simulation set-ups and for virtually any structure, PWEM is specialised for periodic structures only.

Each PWEM computation is always performed for one given value of the wavevector \mathbf{K} . PWEM resolves one or more frequencies which lie on the dispersion curve of the Bloch's wave $\omega(\mathbf{K})$. For each of them, it can also provide the shape of the mode function $\mathbf{u}_{e,m}(\mathbf{r})$. The algorithm is described in detail, e.g., in Ref. [63, pp. 24-28].

As a convenient implementation of PWEM, we used the freely available program *MPB*[3], provided as open-source project by the same group [119] as MEEP. The graphical presentation of the results was prepared using a custom script published on-line [120].

Comparison to FDTD and FDFD The shapes of the electric and magnetic field at the edges of each photonic band are important for understanding the physics of periodic structures. Note that in accordance with the Bloch's theorem, when \mathbf{K} does not lie in any high-symmetry point of the Brillouin zone, the electric and magnetic field differ by their phase between adjacent unit cells. Thus, their shapes do not share the periodicity with the lattice, which makes them harder to be interpreted from a field visualisation. Finding the band edges is an intrinsic feature of PWEM, whereas the same task is only approximate in FDTD and requires a previous search for the band edge frequencies.

Scaling of the computational time with the resolution may present a disadvantage compared with FDTD/FDFD, since in a simple implementation it scales with the second power of the resolution for one-dimensional problems, fourth power in 2-D problems and ninth power for 3-D problems. Application of more sophisticated algebra of sparse matrices can, however, partially remedy this.

Perhaps the most important limitation of the MPB program is that it cannot cope with negative permittivity values. Its applicability is thus restricted to fully dielectric structures only.

3.2 Simulation set-ups for metamaterial homogenisation

The general electromagnetic algorithms, such as FDTD, FDFD or FEM, can be employed to find the electromagnetic field behaviour in a wide variety of problems. These algorithms, however, tell nothing about the effective parameters of a metamaterial, unless they are employed in a particular simulation set-up.

This section describes two different approaches to the homogenisation we have implemented, the retrieval of scattering parameters and the current-driven homogenisation. Other approaches can be found in the literature, which are briefly mentioned at the end of this section.

3.2.1 Retrieval of the scattering parameters

Principle The retrieval based on scattering parameters, also known as the *s-parameter*, *distributed impedance* or *Nicolson-Ross-Weir* (NRW) method [121, 122], has been used since the 1970s to retrieve experimentally the index of refraction N and wave impedance Z of a homogeneous material sample.

The first step to its derivation is that by means of the Fresnel-Airy formulas [11, p. 329], one can easily compute the transmittance $t(f)$ and reflectance $r(f)$ spectra of a slab of any material, provided its thickness d , index of refraction N and wave impedance Z are known. If r, t are known instead, the Fresnel-Airy formulas can be inverted to yield N and Z of the material of the slab. The actual computation is therefore also denoted as *Fresnel inversion*.

Mathematically, this can always be done. When a homogeneous sample is replaced by an inhomogeneous structure, such as a layer of a metamaterial unit cells, this method still yields some *effective* parameters, $N_{\text{eff}}(f)$ and $Z_{\text{eff}}(f)$, the relevance of which is discussed later.

As a great advantage of this approach, there is no requirement to inspect the fields inside the tested structure, as the retrieval is based only on the amplitude and phase of the $r(f)$ and $t(f)$ outside the material. It has become a popular way to retrieve the effective metamaterial parameters thanks to its ease to realize both experimentally and numerically, with FDTD or other algorithms [123].

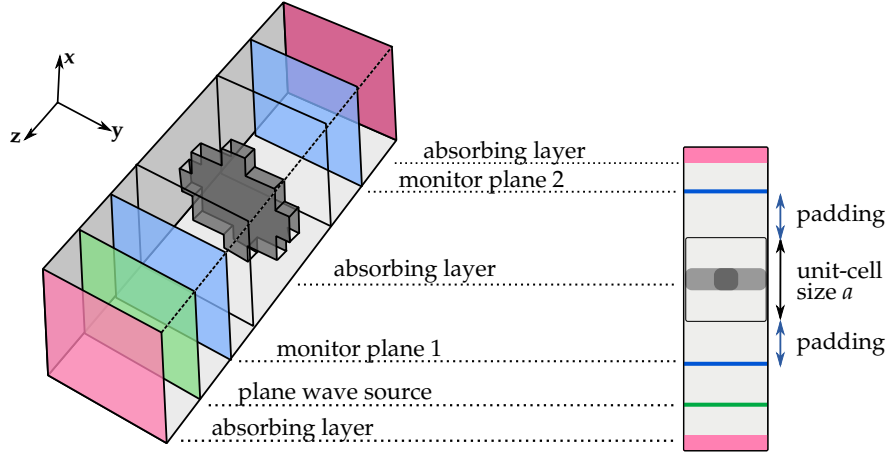
The most-often mentioned downside of this method is that its solutions have infinitely many branches, and it is necessary to establish which one should be chosen, and why. In this section we describe that this can, in fact, be solved by a relatively simple extension of the algorithm, and in the Results chapter it is shown that there exist well-defined rules for the choice of the branch.

Aside from yielding multiple branches, the physical interpretation of the data can get even more intricate when effective parameters are to be assigned to an inhomogeneous slab of a metamaterial. Due attention has to be paid to minimize the intrinsic imprecision of this method, as well as to establish the limits of its applicability.

Simulation set-up The set-up for the scattering parameter method is depicted in Fig. 3.5. The wave is emitted from the source plane (green rectangle) in a direction parallel to the z -axis. The temporal shape of the waves was not critical for the simulation; a very short pulse, with a spectrum spanning from the GHz range to ca. 5 THz was used.

Periodic boundary conditions along the x - and y -axes were set, so that effectively an infinite metamaterial slab was simulated. On both faces perpendicular to the z axis we added regions denoted as *perfectly matched layers* [124] to absorb all

Figure 3.5: The simulation set-up for the scattering parameter method. All simulation elements are described in the text.



radiation (pink areas in Fig. 3.5). The implementation is based on gradually introducing imaginary part into the voxel dimensions [2] to prevent reflections with an arbitrary incidence angle, polarisation or frequency of the wave. The average electric and magnetic fields in each of the monitor planes (blue rectangles) were recorded in each simulation step.

Passing through the first monitor plane, the wave enters the volume of the unit cell (delimited by empty rectangles) and interacts with the structure. A part of its energy is reflected back, a part passes through and the rest may be dissipated if the structure is lossy. The fields that pass through the structure are recorded at the second monitor plane. After the energy stored in the structure drops to a small enough level, the FDTD simulation terminates and the recorded fields are processed to obtain the complex-valued reflectance $r(f)$ and transmittance $t(f)$ as functions of frequency f .

Avoiding the near-field response in monitor planes With the obvious exception of an effectively one-dimensional structure of layers perpendicular to the wave vector, all other structures will change also the orientation of the electric and magnetic fields. Such a perturbation of the field will be localized around the structure, and exponentially decaying with the distance in the form of an *evanescent wave*.

An evanescent wave does not transport energy out of the structure into free space. However, some energy is stored in it, which can be transmitted to another structure if it approaches the zone of the evanescent wave. Even if no energy is transferred by this means, the electromagnetic behaviour of a structure is always slightly influenced by its surroundings, which manifests itself most often by the resonances shifting up or down in frequency.

The impact of the evanescent waves partially reaching the unit cell boundaries in the s-parameters method is twofold:

1. First, computing a single layer of a metamaterial unit cells, with free space in front and behind it, obviously more or less changes its behaviour compared

to the periodic lattice.

This issue is inherent to the simulation set-up, but its impact can be assessed by simulating more than one unit cell, since the retrieved values will change slightly with the number of layers being simulated: a single-cell simulation suffers the most from the absence of adjacent layers, whereas in a two-cell simulation the effect should be halved. Simulations of three (or more) cells suffer from different behaviours of the cells at the surface and inside, which possibly broadens the resonance frequency and can yield confusing results unsuitable to the retrieval method.

2. Second, the monitor planes cannot distinguish between the evanescent or radiated electromagnetic field, but only the radiated waves are relevant for the s-parameter computations. At very low frequencies or at frequencies close to resonances, it was observed that the near field can significantly distort the retrieved parameters.

This can be resolved by shifting both monitor planes away from the metamaterial cell by a distance denoted as *padding*. As the evanescent field decays exponentially, padding of less than half of the unit cell size is often sufficient to suppress all artefacts due to near-field components. In contrast, propagating waves only gain an additional phase offset that can be easily compensated after the simulation.

To the knowledge of the author, such a shift of monitor planes has not been employed in any related paper. It efficiently resolves the issue, and it does so at an acceptable expense of moderately extending the simulation volume.

Scattering-parameter retrieval procedure The averaged electric and magnetic fields recorded at the first monitor plane will be denoted as $E_x^{(1)}(t), H_y^{(1)}(t)$. Likewise, those at the second monitor plane will be denoted as $E_x^{(2)}(t), H_y^{(2)}(t)$. The amplitudes of typical time records are shown and commented in Fig. 3.6.

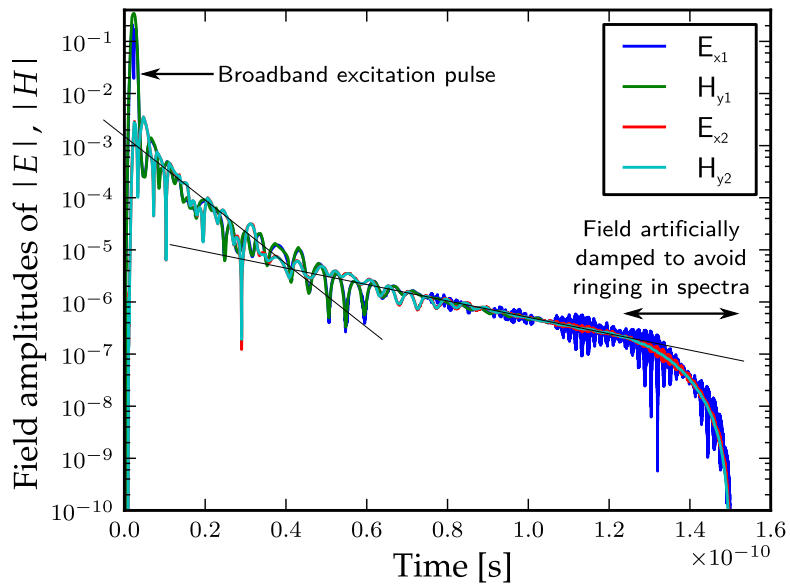
The spectral resolution is determined by the length of the time record. The higher quality of resonance, the sharper its spectral features. From the *Fourier-Plancherel theorem* it follows that the part of the electromagnetic energy that was coupled to the structure, but was not radiated back until the end of the time record, will be also missing in the spectra in the frequency domain. When the time record is too short and significantly truncates a resonance ring-down, characteristic artefacts in the spectra occur which are very detrimental to further visual and numerical evaluation.

Using the convolution theorem (see Sect. 2.1.2), it can be deduced that clipping the recorded fields by a rectangular window in time domain introduces artefacts equivalent to convolution with the $\sin(f)/f$ function in the frequency domain. Multiplication of the records with a smooth window function, known also as *apodisation*, does not improve spectral resolution, but it suppresses the visually distracting *ringing artefacts*, which are apparent for the quadrupole resonances (see, e.g., Fig. 5.44).

Figure 3.6: Time-domain records of the fields in the s-parameter-based retrieval method; absolute values of the complex recorded fields at the first $E_x^{(1)}(t), H_y^{(1)}(t)$ and second $E_x^{(2)}(t), H_y^{(2)}(t)$ monitor plane.

The impinging pulse (ca. 2 ps long) excited two distinct resonances in the structure, that both decayed exponentially in time with different decay rates, as outlined by the thin line segments. About 35 ps after the source was switched off, the stronger resonance reduces its intensity below that of the higher quality resonance, which can be clearly seen as a change of the decaying amplitude slope. The simulation duration was $t_{sim} = 150$ ps.

After 80 % of the time record length, the field is multiplied by the smooth envelope function described by Eq. (3.17).



To this end, all four time records were multiplied by the envelope function $g(t)$ before further processing:

$$g(t) = 1 \text{ for } t < 0.8t_{sim}$$

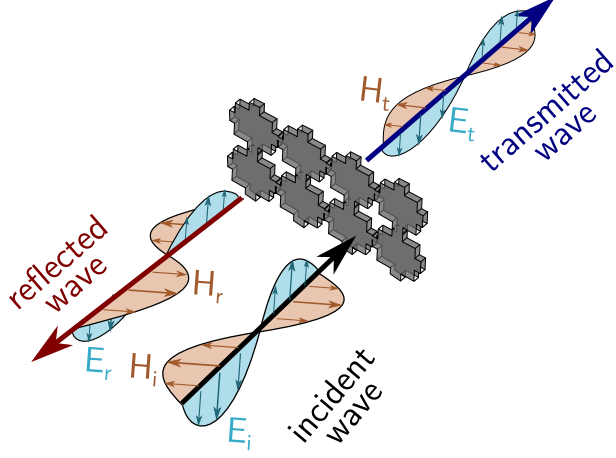
$$g(t) = \frac{1 + \cos\left(\pi \frac{t/t_{sim}-0.8}{1-0.8}\right)}{2} \text{ for } t > 0.8t_{sim}, \quad (3.17)$$

which ensured that after 80 % of the overall simulation duration t_{sim} the field starts dropping smoothly to zero, introducing a temporal envelope similar to the *Hann window* function often used in digital signal processing.

By means of the Fourier transform, the fields were converted to the frequency domain. This operation is simply denoted as $E_x^{(1)}(t) \rightarrow E_x^{(1)}(f)$, and so on.

The monitor planes are assumed to be located in vacuum, and at a distance sufficient to eliminate the evanescent waves of the simulated structure. It follows that the vectors of the electric field \mathbf{E} , magnetic field \mathbf{H} and the wave vector \mathbf{k} must form a right-handed triplet. At both monitor planes, the forward and backward waves are linearly superposed as illustrated in Fig. 3.7. Therefore they can be separated

Figure 3.7: An illustration of orientations of the electric field \mathbf{E} (blue), magnetic field \mathbf{H} (light brown) and wave vector \mathbf{k} (thick arrow) for the waves registered in the simulation.



by using the following relations:

$$\begin{aligned} A^{(\text{in}1)}(f) &:= \frac{E_x^{(1)}(f) + Z_0 H_y^{(1)}(f)}{2}, & A^{(\text{out}1)}(f) &:= \frac{E_x^{(1)}(f) - Z_0 H_y^{(1)}(f)}{2} \\ A^{(\text{out}2)}(f) &:= \frac{E_x^{(2)}(f) + Z_0 H_y^{(2)}(f)}{2}, & A^{(\text{in}2)}(f) &:= \frac{E_x^{(2)}(f) - Z_0 H_y^{(2)}(f)}{2}. \end{aligned} \quad (3.18)$$

The constant Z_0 stands for the *vacuum impedance*, i.e. the ratio of the electric and magnetic fields of a freely propagating wave. Its universal value in SI units is $Z_0 = \sqrt{\mu_0/\epsilon_0} = 4\pi c \cdot 10^{-7} \approx 376.7 \Omega$, but in the actual FDTD simulations, the built-in convention of $Z_0 = 1$ was used. An example of the wave separation result is plotted in Fig. 3.8.

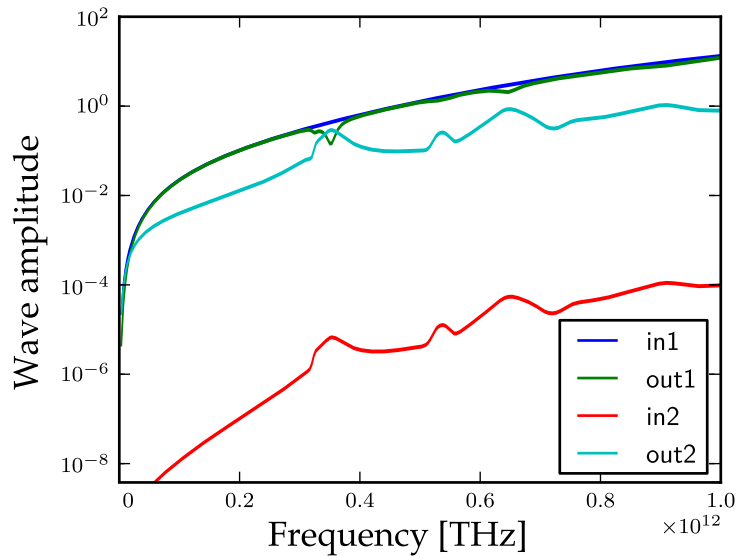
Finally, one can easily compute the complex scattering parameters $r(f)$ and $t(f)$ as the ratios of the reflected and transmitted wave amplitudes to that of the incident wave, respectively:

$$\begin{aligned} s_{11}(f) \equiv r(f) &:= \frac{A^{(\text{out}1)}(f)}{A^{(\text{in}1)}(f)}, \\ s_{12}(f) \equiv t(f) &:= \frac{A^{(\text{out}2)}(f)}{A^{(\text{in}1)}(f)}. \end{aligned} \quad (3.19)$$

Figure 3.8: Separated amplitudes of the forward and backward waves at the first and second monitor planes allow to assess the validity of the simulation results.

The incident wave $A^{(in1)}(f)$ should have a smooth spectrum (blue curve), as it is directly generated by a broadband source. The reflected wave $A^{(out1)}(f)$ (green curve) and the transmitted one $A^{(out2)}(f)$ (light-blue curve) appear to be somewhat complementary to each other, since squares of their amplitudes should approximately sum up to the square of the incident wave amplitude, or less in case of losses.

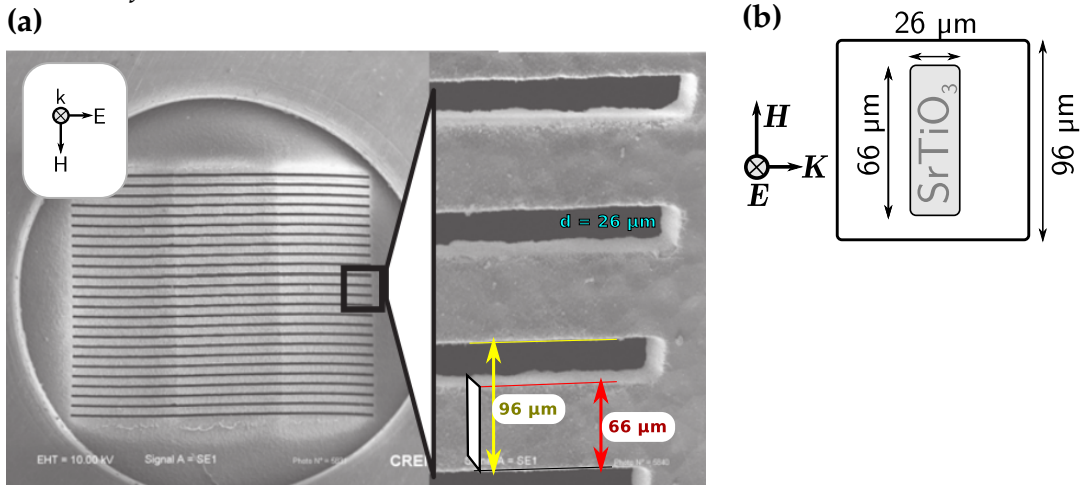
The fourth wave $A^{(in2)}(f)$ should be negligible, as almost all the wave energy is expected to be absorbed by the perfectly matched layers at the z -faces of the simulation volume. In practice it is nonzero, also due to numerical imprecision and remaining near-field components of the structure. This relative error in amplitude is usually less than 10^{-3} .



Comparison of simulated and experimental spectra To verify the simulation results against experimental data, we computed $r(f)$ and $t(f)$ for a structure that had been measured in our terahertz laboratory. It consisted of an array of high-permittivity dielectric bars, cut using a femtosecond laser from a $26\text{ }\mu\text{m}$ thick strontium titanate (STO) slab [125]. The periodicity was $96\text{ }\mu\text{m}$ and the laser cut width $30\text{ }\mu\text{m}$, resulting in the width of $66\text{ }\mu\text{m}$ for each rectangular bar as shown in Fig. 3.9.

The permittivity of STO strongly depends on the temperature, and was not known a priori, so it was chosen as $\varepsilon_r(1\text{ THz}) = 365 + 62i$ for the simulation to match the experimental spectra.

Figure 3.9: (a) Electron microphotograph of the STO array (from [125]), front view, (b) dimensions of one unit cell, drawn as the side view



In Fig. 3.10, the curves computed using the FDTD simulations are compared with the experimental ones, showing very good match in three well-resolved resonance peaks, and high reflectance ($|r| > 0.9$) in most of the spectrum which is caused by strong impedance mismatch between the dielectric and the surrounding air.

Figure 3.10: Experimental transmission $t_{exp}(f)$, compared with numerical reflectance $r(f)$ and transmittance $t(f)$ for strontium titanate bars with a rectangular cross-section $26 \times 66 \mu\text{m}^2$, oriented parallel with the electric field.

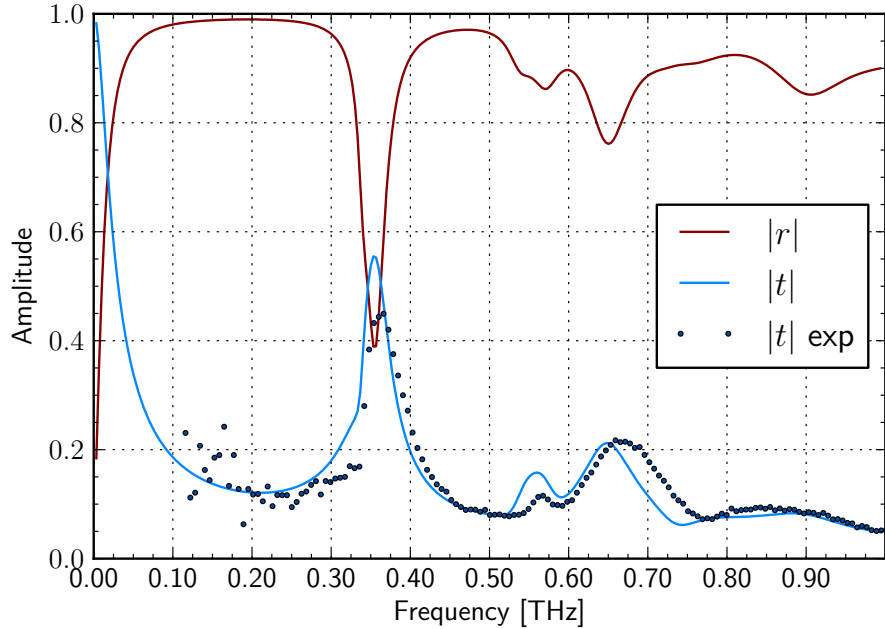
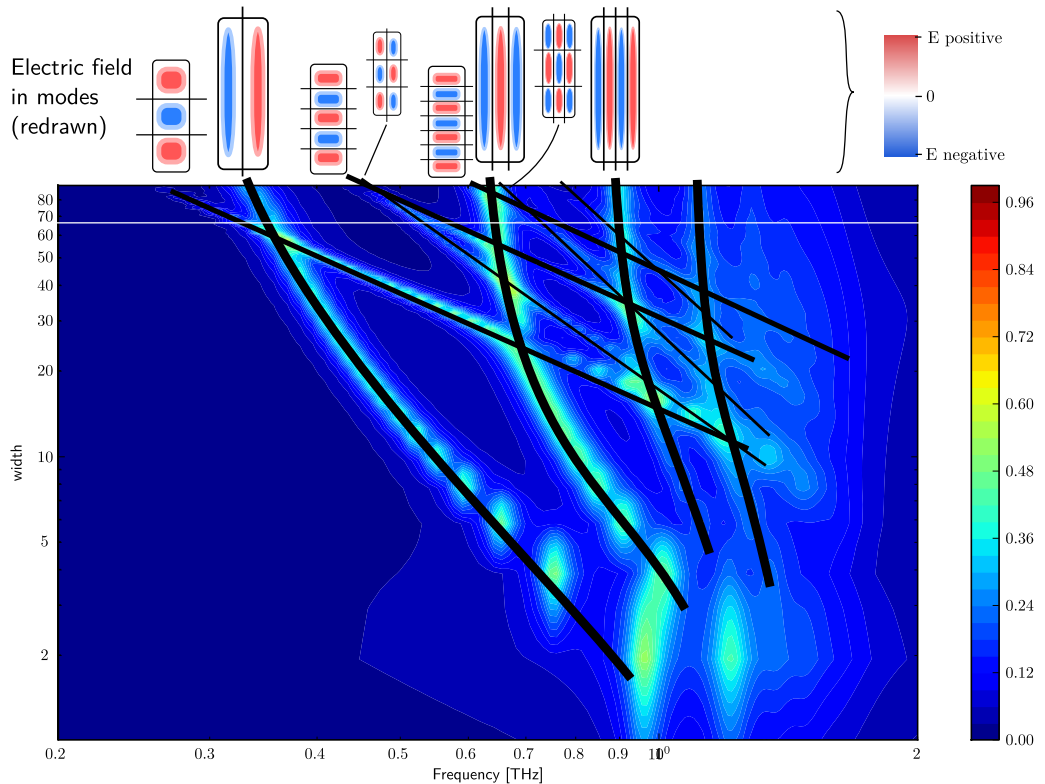


Figure 3.11: Set of simulated absorption spectra, computed as $1 - |r^2| - |t^2|$, for different widths of the strontium titanate bar (in micrometers). The experimental bar width of $66 \mu\text{m}$ is denoted by the white line. Different modes are marked by the black curves and the cross-sections of their approximate electric field shapes are drawn above the plot.



Example of a parametric scan with FDTD simulations To briefly illustrate further possibilities of the numerical simulations, in Fig. 3.11 we scanned the relative width of the STO bar, and computed the relative energetic loss in the structure given by $1 - |r^2| - |t^2|$. Each loss peak can be clearly associated with one resonant mode in the dielectric. Only modes with a mirror symmetry in the direction transverse to the wave propagation couple to the wave; the remaining antisymmetric modes would manifest themselves at oblique incidence only.

The two-dimensional scan can provide further information about the underlying physics. Most importantly, it is clear that the resonance frequencies of the modes have different sensitivities to the bar width. Note that both the vertical and horizontal axes are logarithmic, so the power dependence can be directly estimated from the slope of each line.

It can also be seen from Fig. 3.11 that for the bar width close to 66 μm , which is indicated by the horizontal white line, two modes cross-over in frequency. Namely, one of these is a narrow mode with nodal planes almost parallel to the wave propagation, while the other one is much broader one with one nodal plane centered inside the dielectric slab volume. This explains why the first resonance in Fig. 3.10 has an obviously asymmetric shape, both in the simulated and experimental spectra.

The overlap of two modes differing by the spectral widths and the resonance frequencies forms a typical *Fano resonance* shape, which would be probably observed experimentally if the losses were lower. A more elaborate discussion on periodic structures composed of dielectric bars/rods oriented either along the electric or the magnetic field will follow in the Sections 5.7 and 5.8.

Retrieval of the effective parameters Complemented with the cell thickness d , the spectra of the frequency-dependent reflectance $r(f)$ and transmittance $t(f)$ can serve as inputs for the s-parameter method, [126, 127] [22, pp. 51-55]. The expression for the effective index of refraction is

$$N_{\text{eff}} = \frac{\pm \arccos\left(\frac{1-r^2+t^2}{2t}\right) + 2\pi m}{kd}, \quad (3.20)$$

where neither the integer-valued branch index $m \in \mathbb{Z}$, nor the sign of the solution are known a priori. For the effective impedance, the sign is also ambiguous:

$$Z_{\text{eff}} = \pm \sqrt{\frac{(1+r)^2 - t^2}{(1-r)^2 - t^2}}. \quad (3.21)$$

Search for the correct solution From Eqs. (3.20) and (3.21) it follows that the correct solution depends on three discrete-valued functions of frequency, i.e. the sign of $N_{\text{eff}}(f)$, its branch index $m(f)$, and the sign of $Z_{\text{eff}}(f)$, which have to be determined during computation. We identified the following criteria for selecting exactly one of infinitely many solutions:

1. Passivity, i.e., inability to supply energy to the wave propagating through the structure, requires the *imaginary* part of refractive index be non-positive:

$$N''_{\text{eff}}(f) \leq 0 \quad \forall f \in \mathbb{R} \quad (3.22)$$

2. Passivity with regard to the wave reflected from the structure interface requires the *real* part of refractive index be non-positive, too:

$$Z'_{\text{eff}}(f) \leq 0 \quad \forall f \in \mathbb{R} \quad (3.23)$$

3. A causal response of the sample requires a specific relationship between the real and imaginary parts of $r(f)$, $t(f)$ and of effective parameters $N_{\text{eff}}(f)$ and $Z_{\text{eff}}(f)$, when substituted for the function $F(\omega)$:

$$F'(\omega) = \int_{-\infty}^{+\infty} \frac{-2i}{\omega - \Omega} F''(\omega) d\Omega \equiv \left[\frac{-2i}{\omega} \right] * F''(\omega). \quad (2.30 \text{ again})$$

Perhaps the most familiar consequence of this criterion is the requirement of continuity for $N_{\text{eff}}(f)$ in all structures with nonzero losses.

Note that in the papers that use the other complex convention, i.e. $e^{-i\omega t}$, both passivity conditions use the opposite sign. This does not apply to the kernels of the Fourier nor Hilbert transforms.

Retrieval of effective N'_{eff} based on unambiguous complex arccosine We wrote a custom procedure to select the correct solution automatically on pure mathematical basis. To our knowledge, such an approach was not addressed in any of previously published papers. Alternative approaches are briefly discussed in the following section.

The ambiguity in Eqs. (3.20, 3.21) results from the fact that the inverse functions of arccosine and square root are not injective mappings [128]:

$$\cos x = \cos(-x) = \cos(x + 2\pi) \quad \forall x \in \mathbb{C}, \quad (3.24)$$

$$x^2 = (-x)^2 \quad \forall x \in \mathbb{C}. \quad (3.25)$$

Since the temporal records of the fields are exponentially decaying functions, the reflectance $r(f)$ and transmittance spectra $t(f)$ must be continuous. It is assumed that for any realistic structure with nonzero losses, the transmission never passes exactly through the complex zero, and the arccosine argument from Eq. (3.20)

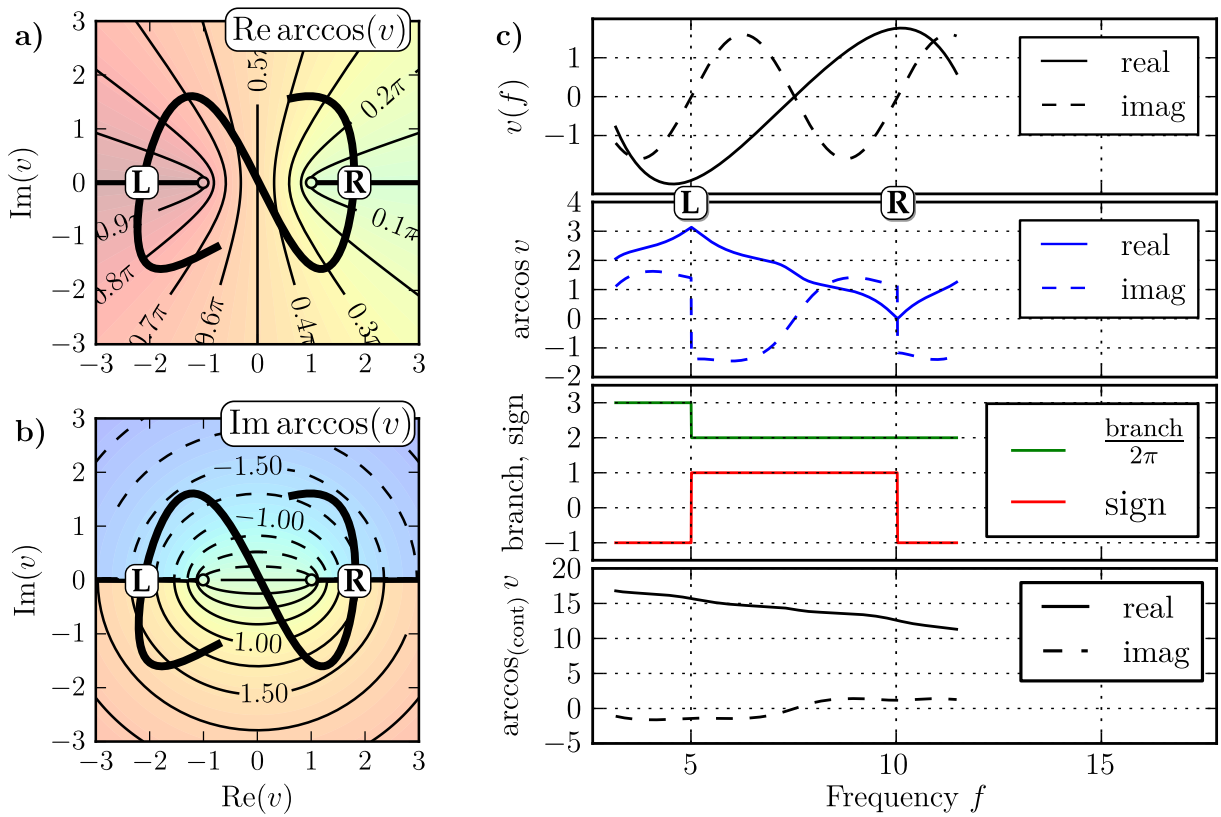
$$v(f) = \frac{1 - r^2 + t^2}{2t}, \quad (3.26)$$

is also a continuous complex function. Any discontinuities in the retrieved spectra of $N'_{\text{eff}}(f)$ may therefore arise exclusively from discontinuities of the arccosine function in the complex plane.

To ensure the overall continuity of N_{eff} in Eq. (3.20), it is therefore necessary to identify the two *branch cuts* of arccosine in the complex plane, as illustrated in Figs. 3.12a,b. Different measures must be taken for the sign and branch index $m(f)$ to ensure continuity:

1. If, by increasing the frequency, the arccos argument v passes through the right branch cut at $v' > 1, v'' = 0$ (point "R" in Fig. 3.12c), the real part of $\text{arccos}(v)$ touches zero, whereas its imaginary part is non-zero and changes its sign. The direction given by the sign of dv'/df does not play any role. The continuity is achieved if, from this frequency on, one reverses the sign of the arccos term .

Figure 3.12: (a) Real and (b) imaginary parts of the arccosine of complex argument v . Branch cuts are denoted with thick lines. The thick curve shows a possible trajectory of $v(f)$ (upon a frequency variation), which intersects the branch cuts in points marked as R, L. (c) From top to bottom: an example function $v(f)$, its ordinary arccosine, example branch and sign choices ensuring the continuity of the arccosine function, and the continuous version of $\text{arccos}_c(v)$, as determined by the algorithm described.



- At the left branch cut (the "L" point in Fig. 3.12c), i.e., for $v' < -1, v'' = 0$, where the imaginary part of $\arccos(v)$ experiences again a step-like change of the sign and the real part touches the value of π . To restore the continuity, the sign reversal must be also accompanied by a change of the branch index. .

Effective impedance retrieval The sign of the square root function is similarly chosen so as to ensure that Z is a continuous function of frequency. Probably the simplest approach is to express the square root argument in Eq. (3.21) in the polar notation, i.e., as its real-valued modulus and its angle in the complex plane. The angle can be easily ensured to be a continuous function by shifting it by $\pm 2\pi$ at any discontinuity.

Using the *Moivre theorem*, the square root is then computed by halving the angle of the argument, and computing the square root of its real-valued modulus. Both operations are safe in terms of maintaining the continuity.

A particular implementation of this algorithm for continuous arccosine and square root retrieval can be found online in Ref. [117, `effparam.py` file].

Initial branch and sign choices Next, it is necessary to establish the sign and branch index of N_{eff} and the sign of Z_{eff} at the starting point of the spectrum. One can assume that for very low frequencies below any individual resonance, also the Bloch's wave vector tends to zero, $K \rightarrow 0$. In case of conductive structures, the spectrum starts with a plasma-like band gap at low frequencies, leading to an evanescent wave with vanishing wavenumber as well.

Whenever the spectra of $r(f)$ and $t(f)$ are computed using the Fourier transform, they are known also for very low frequencies and the selection of the initial branch is thus easy.

The remaining step is to establish the signs of N_{eff} and Z_{eff} , using the aforementioned rules requiring the metamaterial passivity.

Computing effective parameters of a 1-D photonic crystal The above described algorithm was proven to work reliably with most structures. However, it is sensitive to numerical errors when the arccosine argument $v(f)$ in Eqs. (3.20, 3.26) passes near the points $(-1 + 0i)$ and $(1 + 0i)$, that is, near the ends of the branch cuts of the complex arccosine.

Unfortunately, it was observed that $v(f)$ comes excessively close to these points in the spectra of planar slabs of lossless dielectrics, particularly when the spectral resolution is low. A correct retrieval of effective parameter spectra for this particular structure requires that even in these points, the curve is processed as if it had crossed the branch cuts.

Otherwise, the retrieved spectrum of $N_{\text{eff}}(f)$ remains continuous, but at higher frequencies it ceases to make physical sense. Its imaginary part acquires the wrong sign in the band gaps, breaking the passivity criterion. Simultaneously, in the next photonic band its real part decreases with frequency, which would break the Kramers-Kronig relations [see Eq. (2.30)] and would be a sign of negative group velocity occurring without significant dispersion. For these reasons, this error can

be easily notified, and with further programming it can be combined with the verification against the Kramers-Kronig relations.

This is the only issue known to the author which arises from the described effective-index retrieval algorithm. This problem has proven to be efficiently resolved by introducing moderate losses into the structure and/or artificially shifting the branch-cut detection points to be slightly closer to the complex zero, e.g. to $(-0.999+0i)$ and $(0.999+0i)$. In many cases, the wrong detection of the branch was resolved simply by multiplying the recorded fields by the smooth window function from Eq. (3.17).

Summary of the scattering-parameter method The scattering-parameter method is the most widely used one for the effective parameter retrieval. It stands out among other methods by relying on the amplitudes of the reflected and transmitted waves only, without any inspection of the fields inside the unit cell. It is also efficient, since it requires a single time-domain simulation to retrieve the full spectrum of effective parameters. The wave is let to propagate freely through the structure, and then the retrieval algorithm determines the wavenumber at each frequency component of the incident wide-band pulse. The frequency ω represents the input, and the wavenumber $K(\omega)$ is one of the outputs.

However, the scattering-parameter method also has its weaknesses. Perhaps the worst one is that it does not fail explicitly in cases it is not appropriate for; or, as stated in Ref. [129]:

Of course, a refractive index per se (generally, tensorial and dependent on the direction of the Bloch's wave vector) can always be formally introduced for a Bloch's wave.

One has to be careful to verify whether the retrieved values of effective parameters make any physical sense whatsoever, or are just a confusing output of an algorithm used outside its scope. The majority of the possible issues was mentioned above:

1. The method is intrinsically imprecise, because the evanescent fields of most structures are influenced by the free space in front of the unit cell and behind it. This issue can be neglected if nearly all the energy is transferred by the radiated wave, in which case the metamaterial is sometimes described as a *Bloch's lattice* [130, 131]. In other cases, usually in dense or metallic structures, a significant amount of energy is transferred by the near-field coupling, and it can be demonstrated that the effective parameters retrieved by this method strongly depend on the number of layers [132, 133] which renders the approach invalid.
2. Another source of errors is the fact that the monitor planes detect also the near field, requiring one to increase the distance between the structure and the monitor planes.
3. Although we devised a relatively robust computation of effective parameters, the current implementation is still sensitive to numerical errors when spectra of lossless dielectric slabs are computed.

4. The method requires the structure to be symmetric with regard to the wavevector \mathbf{K} , since it attempts to approximate it by effective parameters that leave no degree of freedom for possible asymmetry. An example of an asymmetric structure was discussed in Ref. [127], where it was concluded that

...so different are the two solutions for Z_{eff} for the asymmetric structure that in general the assignment of values of ε_{eff} and μ_{eff} to the composite becomes counterproductive.

In the view of the author of this thesis, also the retrieved N_{eff} in Fig. 7c of Ref. [127, p. 036617-9] can be reasonably interpreted if and only if the structure is symmetric.

5. Perhaps the most fundamental limitation of this method comes from its principle of retrieving the wavenumber at a given frequency. For a periodic structure which exhibits a strong enough spatial dispersion, more than one wavenumber exist at a single frequency as shown in Figs. 2.11. For any frequency from such a problematic range, the retrieved effective parameters depend on the unknown ratio of the energy coupled to either of the waves. Therefore, the method is inapplicable for structures with a strong spatial dispersion. This effect is illustrated in the Results section (e.g. in Fig. 5.21).

3.2.2 Current-driven homogenisation

Principle When more than one wavevector \mathbf{K} corresponds to a given frequency, a different approach to the effective-parameter retrieval must be used, for which the wavevector \mathbf{K} becomes the input, and the corresponding frequencies $\omega_{1\dots\infty}(K)$ at the dispersion curves are returned as the output. This section describes the *current-driven homogenisation* (CDH), in which the whole simulation is computed exclusively with a single wavevector \mathbf{K} , and the dispersion curves are reconstructed from multiple simulations differing by the wavevector.

In this thesis, the method is described in its simplest form. More elaborate implementation is discussed in Refs. [134], [135] and [26], which would enable to recover all 36 parameters that describe the influence of the fields ($E_x, E_y, E_z, H_x, H_y, H_z$) to the displacements ($D_x, D_y, D_z, B_x, B_y, B_z$), taking into account also possible anisotropy and bianisotropy.

Bloch-periodic boundaries for arbitrary wave vector In CDH, the unit cell is simulated as being placed in an infinite lattice, neighbouring with the same cells of size a in all three dimensions. To emulate such a lattice in a simulation of a single cell, all the faces of the unit cell have to be set Bloch-periodic, i.e., set to copy the field from the opposite face.

Exact copying of the fields from one side to another would require the wavevector of the Bloch's wave to be strictly $K_{xyz} \in 2\pi m/a_{xyz}$, which is, however, the known condition for a photonic band gap. Since we are mostly interested in computing the wavenumber inside photonic bands, the periodic boundaries have to allow for an

arbitrary phase shift before the fields are copied:

$$E(\mathbf{r} + a_x \mathbf{x}/2) \rightarrow e^{-iK_x a_x} E(\mathbf{r} - a_x \mathbf{x}/2), \quad (3.27)$$

where \mathbf{x} is the unit vector along the x -axis, and a_x are the unit cell size along this axis. The unit cell is assumed to be centered around the $x = 0$ point, thus $x = \pm a_x/2$ denotes the point at the boundary, and similarly for other axes.

Positive phase advance proportional to K_x is applied when copying the fields parallel to the x -axis, and negative phase retardation is applied when simultaneously copying the fields in the opposite direction:

$$E(\mathbf{r} - a_x \mathbf{x}/2) \rightarrow e^{+iK_x a_x} E(\mathbf{r} + a_x \mathbf{x}/2). \quad (3.28)$$

A similar field-copying procedure is repeated in each simulation step for all remaining axes, y and z , in the case of a 3-D simulation.

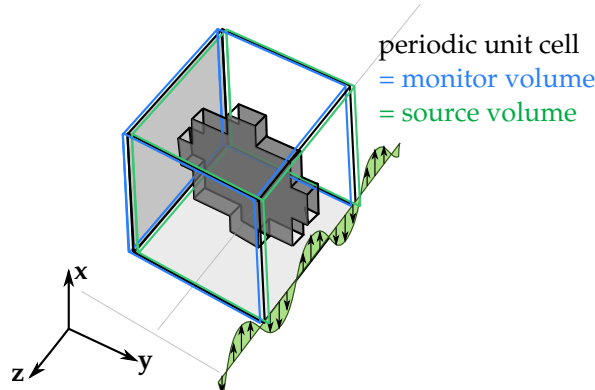
Single-wavevector source In order to excite the simulation volume with a single wavevector \mathbf{K} which complies to the Bloch-periodic boundary conditions imposed, the source volume must expand over the whole unit cell and acquire a correct harmonic modulation of its complex amplitude. While this task appears impossible by experimental techniques, it is straightforward in the FDTD simulation. The source is typically designed to be a complex-valued electric current with a given amplitude:

$$\mathbf{J}(\mathbf{r}, t) := \mathbf{x} e^{-i\mathbf{K} \cdot \mathbf{r}} j(t), \quad (3.29)$$

where \mathbf{x} determines the default polarisation of the electric field and $j(t)$ is the temporal profile of the source.

Excitation of the structure with this kind of the source gave the current-driven homogenisation its name. Unlike the scattering-parameters method, in CDH the source volume coincides with the entire unit cell volume. An attempt of visualisation of this minimalistic simulation set-up is in Fig. 3.13.

Figure 3.13: Current-driven homogenisation set-up consists of a single unit cell with all faces set to be Bloch-periodic, with appropriate phase shift between the corresponding pair of faces. One example of the real part of the spatially varied source amplitude is sketched along the unit cell edge as the green-filled curve.



Temporal profile of the source With the wavevector restricted to a single given value, it is necessary to excite and detect as many corresponding modes of the structure as possible. Therefore, a short and broadband temporal source profile could be reused from the scattering parameter method.

Unlike the scattering-parameters method, CDH cannot detect easily the spectral profile of the exciting field, and the retrieved fields cannot be normalized against it. To maintain an approximately constant source amplitude over a wide part of the spectrum, a nontrivial temporal shape of the source was designed, tested and finally also submitted to the MEEP simulation developers:

$$j(t) := w_{BN}(t) [\text{Si}(2\pi f_1 t) - \text{Si}(2\pi f_2 t)] \quad (3.30)$$

where the transcendent sine-integral function introduces the flat-top rectangular spectrum of the wave radiated from the source:

$$\text{Si}(t) = \int_0^t \frac{\sin \tau}{\tau} d\tau, \quad (3.31)$$

The electric field radiated by a source is proportional to the temporal derivative of the current $j(t)$ [119], therefore the sine-integral must be used to obtain the field shape of $E_x \propto \sin(t)/t$, which is known to have a rectangular flat-top spectrum.

If the source amplitude had an infinite duration in time, its spectrum would form a perfect rectangular function. However, clipping the temporal duration of the source results in spectral artefacts, as was already described on the page 84. The artefacts can be very efficiently suppressed by multiplying the source by the *Blackmann-Nuttall window* function

$$\begin{aligned} w_{BN}(t) := & 0.3635819 + \\ & + 0.4891775 \cos \frac{2\pi(t - t_c/2)}{t_c} + \\ & + 0.1365995 \cos \frac{4\pi(t - t_c/2)}{t_c} + \\ & + 0.0106411 \cos \frac{6\pi(t - t_c/2)}{t_c} \quad \text{for } t \in \langle 0, t_c \rangle, \end{aligned} \quad (3.32)$$

$$w_{BN}(t) := 0 \quad \text{otherwise.}$$

Since $w_{BN}(t)$ has finite support in time, but particularly fast decaying wings in its spectrum, it ensures relatively steep edges of the nearly rectangular spectrum of the source.

Field monitor and identification of the dispersion curves The detection of the fields is defined in a way similar to the definition of the source. In each timestep, the electric field $E_x(\mathbf{r}, t)$ is sampled in multiple points through the unit cell. As each of the points could have a different phase, the values are divided by $e^{-i\mathbf{K}\cdot\mathbf{r}}$ before they are averaged.

After the simulation ends, the single record of cell-averaged E_x is processed to identify the set of frequencies $\omega_m(\mathbf{K})$ at which E_x exhibited a ringdown. For example, if the cell is empty vacuum, the source with wavevector \mathbf{K} can only excite

a wave at the frequency $\omega = Kc$. All other combinations of (ω, \mathbf{K}) are off the dispersion curve (known also as the light line in vacuum) and no solution of Maxwell equation exists for them. Although the source can create temporary evanescent fields even at such "off-shell" combinations, the evanescent-field energy is immediately returned back to the source.

The same holds for any kind of structure placed in the unit cell: the energy persists to the end of the simulation only at frequencies $\omega_m(\mathbf{K})$ that lie at one of corresponding dispersion curves. An intuitive way of detecting such frequencies would be to compute the Fourier transform of the recorded averaged field E_x and identify the peaks in the resulting spectrum. The resolution of the Fourier transform is nonetheless proportional to the time record, and it is inefficient for the task of accurately recognizing the frequencies of a small number of damped oscillations.

A more advantageous algorithm for recognition of oscillations is the *filter diagonalisation method* (FDM), originally developed in 1990 for analysis of experimental spectra and the nuclear magnetic resonance waveforms in particular [136, 137]. Unlike Fourier transform, FDM does not require the oscillators to decay before the temporal record ends; on the contrary, it appears to work even more reliably when supplied with several tens of the oscillation periods at most. Using FDM, the simulation time could be shortened several times.

Advantages over the scattering-parameters method Using CDH resolves some of the issues of the s-parameters method, namely

1. It simulates the unit cell embedded from all sides in the lattice, and there is no problem with the evanescent fields sensing free space as it was in the s-parameter method.
2. Retrieval of the dispersion curves is not much sensitive to the actual field amplitude, but rather to the frequencies detected in its ringdown. The shape of dispersion curves is less distorted by any possible error during the scattered field detection.
3. Since the wavevector is given before each simulation, no issues with wrong branch detection can flip or otherwise distort the dispersion curves.
4. Also the requirements to the structure symmetry are weaker. In general, the structure is not required to have any symmetry plane perpendicular to the wavevector. Other kinds of lower symmetry may lead to bianisotropic behaviour, which would require more sophisticated detection of the waves, though.
5. Last but not least, CDH inherently takes into account even very strong spatial dispersion, which is not the case of the s-parameters method. All additional waves are detected correctly.

CDH also has more general applicability. It can operate with arbitrary orientation of the wavevector \mathbf{K} ; it can even excite longitudinal waves in the structure and retrieve their dispersion curves.

Weaknesses compared to the scattering-parameters method The downside of CDH, as implemented in this thesis, is mainly in the fact that it provides less information than the s-parameter method:

1. It does not compute the effective impedance Z_{eff} at all, and it is questionable whether Z_{eff} could be computed if also the averaged magnetic field $H_y(\mathbf{r}, t)$ was recorded.
2. On the one hand, CDH reliably computes the dispersion curves, and the corresponding set of $\omega_m(\mathbf{K})$ functions could be inverted into $\mathbf{K}(\omega)$ and, for propagation along an optical axis (cf. page 27), also into $N_{\text{eff}}(\omega)$. On the other hand, it does not give any information on the topology of nodal planes, nor which branch of $N_{\text{eff}}(\omega)$ would be selected by the s-parameter method.
3. We failed to obtain any useful information related to the imaginary part of N_{eff} – about the structure losses, field decay in photonic band gaps, and its behaviour outside the dispersion curves in general.

Other downsides relate to the practical implementation, and arguably are the reason for its rarer use in the literature.

1. A comparable task in CDH is more computationally intensive than in the s-parameters method. For a single set of dispersion curves, several tens of simulations with different \mathbf{K} are needed. After they are run, a postprocessing script must analyse all recorded fields and assemble the dispersion curves.
2. Naturally, CDH can hardly be employed in an experiment, since it inspects the field in multiple points inside the structure simultaneously.

In spite of these limitations, the simplified implementation of CDH for this thesis remains an important complement to the s-parameter method.

3.2.3 Other effective parameter retrieval methods

Extensions of the scattering parameters method Various modifications to the scattering parameters method were proposed, in particular with connection to the homogenisation of metamaterials. One modification makes it robust against the experimental error in the reflectance phase [138]. Another solution to the issues connected with experimental measurement of the reflectance was employed during the preparation of this thesis [139]. It involved a slight modification to the experimental set-up, and thus it is described in the experimental chapter (pp. 110–112).

Some of the modifications apply to the effective parameters retrieval only, and no change is made to the way how the scattering parameters $r(f)$ and $t(f)$ are measured. Not knowing the correct branch of the index of refraction is equivalent to using the folded dispersion curves (cf. Par. 2.3.2), so the post-processing of FDTD data can also be viewed as a specific, non-trivial way of *unfolding* the dispersion curves. This task appears to have been often done manually, particularly in earlier papers [126]. An approach based on iterative fitting which avoids abrupt discontinuities in $N'_{\text{eff}}(f)$ has been published [140], but the author conjectures that, from

its very nature, it would become unstable whenever a localized resonance introduces fast changes of $N'_{\text{eff}}(f)$, which can be found e.g. in Fig. 5.8. Manually assisted approaches present the risk of affecting the resulting effective parameters with unjustified subjective expectations.

A more elegant method was published in 2010 by Szabó et al. [141] and relies on the inherently unambiguous knowledge of $N''_{\text{eff}}(f)$. It uses the Hilbert transform introduced in Eq. (2.30) to recover $N'_{\text{eff}}(f)$ from $N''_{\text{eff}}(f)$. However, from our own experience, applying this integral transform to a finite part of spectrum introduces not only an arbitrary constant offset, but also slow continuous distortion of the $N'_{\text{eff}}(f)$ curves, which would require a complicated compensation.

The discussion in this thesis is restricted to the near-perpendicular wave propagation, since it is assumed the optical axis is also perpendicular to the interface. In Ref. [142], Eqs. (3.20, 3.21) were generalized also for oblique incidence. Note that for retrieving the effective index of refraction one must establish whether it makes any physical sense at all, i.e., whether the structure is either isotropic, or at least whether the angle of refraction is parallel to its optical axis (see page 27).

In Ref. [143], the scattering parameter method was extended also to the biaxial-isotropic behaviour of structures with reduced symmetry, and other approaches can be found [133] in the recent literature.

Averaging of the fields With the scattering parameters method, $N_{\text{eff}}(f)$ and $Z_{\text{eff}}(f)$ are retrieved first using the amplitudes of the reflectance and transmittance. The local effective permittivity $\varepsilon_{\text{eff}}(f)$ and permeability $\mu_{\text{eff}}(f)$ can be computed using Eqs. (2.37) and (2.57), but are considered valid only when $|N'_{\text{eff}}| \ll 2\pi/a$, i.e., when the unit cell size a is much less than the Bloch's wavelength.

The effective parameters $\varepsilon_{\text{eff}}(f)$ and $\mu_{\text{eff}}(f)$ can however be computed directly by exciting a unit cell of the structure, averaging both the fields (\mathbf{E} , \mathbf{H}) and the displacements (\mathbf{D} and \mathbf{B}), and dividing the respective displacement by the field. The method is described in Ref. [49], where also numerical examples are given.

Bloch-mode analysis A *single-interface* method has been proposed [144] that analyses only the field behaviour at the interface of a semi-infinite structure. The fields in the structure are computed and decomposed into discrete modes of the Bloch's wave. The method attempts to recognize a dominant Bloch's mode for which the wavevector $\mathbf{K}(\omega)$ is deduced. [145] [146]

When no mode is clearly dominant, this method naturally cannot be used. In such a case, even the scattering parameter method fails, but its limitations of applicability are less obvious than with the *single-interface* method. Failure of the scattering parameter method can be observed as contradictory results [132] from simulations of different numbers of unit cells. In Ref. [98] it is argued that the existence of one dominant mode is the prerequisite for the structure to be viewed as homogeneous. Refs. [98, 131] apply the Bloch-mode analysis approach to selected structures. A direct numeric evaluation of amplitudes of the different modes in 1-D photonic crystals can be found in [43].

Wave phenomena In the *Wave propagation retrieval method*, proposed in Ref. [133], the wave impinges a thick, ideally semi-infinite, volume of the periodic structure. Since there are no repeated reflections from the second interface, the averaged field amplitude is assumed to have exponential nature: $E(z) \propto e^{-2\pi ifN_{\text{eff}}/c}$, and thus N_{eff} can be reconstructed using a complex logarithm.

Like in the s-parameters method, the function of $K(\omega)$ can be resolved in a single run by using a broad band pulse. Like in the current-driven homogenisation, the fields need to be sampled inside the structure.

Concluding remarks Other homogenisation methods include the *multipole expansion* [18, 147], *quasimode theory* [148], or other advanced approaches as discussed by Simovski [130, 128, 149, 108]. Without much exaggeration it can be concluded that there are roughly as many homogenisation methods as authors involved in the research of periodic structures. All such methods work reliably in the easy cases:

Homogenisation theories are typically valid when the unit-cell size is insignificant with respect to the wavelength (the zero-frequency limit) and thus might be expected to result in a poor description of metamaterials. [49]

Indeed, in most practically encountered metamaterials today, the wavelength is not more than an order of magnitude smaller than the unit cell.

Most homogenisation methods attempt to describe the structure using local effective parameters, $\varepsilon_{\text{eff}}(f)$ and $\mu_{\text{eff}}(f)$, which do not provide enough degrees of freedom to fully express the interaction between the medium and fields. The homogenisation methods differ by the shapes of excitation fields the structure is probed with, by the boundary conditions that may be either partially or fully periodic, and also by the way the field is analysed. Thus, it should not be surprising that also the results strongly deviate between the methods [49, Fig. 5] and that they even seem to break fundamental physical postulates [106], even when no mistake was made during the application of the method.

As a matter of fact, the mistake might have been made already during the *selection* of the method.

From the literature available, one can conjecture that systematic homogenisation in terms of the spatially dispersive (Landau-Lifshitz) permittivity $\varepsilon_r^{\text{LL}}(\omega, \mathbf{K})$ should prevent most striking quirks arising in the local homogenisation methods. All problems involving an interface then also need to be complemented by the additional boundary conditions [14]. However, computations and the application are more complex for the medium described by the spatially-dispersive effective parameter, than for a medium described by local parameters. This is the price that would have to be paid for its more general validity.

In this thesis, we restrict the discussion mostly to the scattering parameters method, pointing out where it is applicable, and where its results cease to make any sense. The current-driven homogenisation then remains as a good reference to compare the results with.

Chapter 4

Experimental methods

4.1 Short review of the terahertz technology

The terahertz range of the electromagnetic spectrum, spanning roughly from 100 GHz to 10 THz, has met a relatively small application potential in science and technology as yet, compared to the development in the microwave (< 100 GHz) and near-infrared (> 100 THz) or optical ranges. The reason can be traced down both to the limited choice and high cost of suitable terahertz sources and detectors, and to their usually small efficiency or sensitivity. The technology and science, however, develop fast in this field, and the number of terahertz-related papers has doubled every 3.2 years [150] between 1975 and 2010.

There is a great number of books and papers that describe different terahertz sources and detectors in detail [151, pp. 155-158][152, 150] and many of them are also, with more or less detail, discussed in previous doctoral theses written in our group ([153, pp. 2-30], [154, pp. 19-25], [155, pp. 7-26], [156, pp. 11-21], [157, pp. 31-45], [158, pp. 33-38], [159, pp. 25-33], etc.).

Electromagnetic waves in the terahertz range are radiated whenever charged particles are subject to fast-enough acceleration at the picosecond scale. The generation processes may be sorted with regard to the medium in which the emission occurs and to the origin of the force causing the acceleration. In the following paragraphs, we try to review the terahertz technology in a systematic manner.

Although they are widely used at higher frequencies, thermal sources are rarely used in the THz range. The black body radiation is governed by the Planck law [8, p. 23]

$$I(f, T) = \frac{2h}{\pi^2 c^2} \frac{f^3}{e^{\frac{hf}{kT}} - 1} \text{ W sr}^{-1} \text{ Hz}^{-1} \text{ m}^{-2}, \quad (4.1)$$

from which it follows that the luminosity I in the terahertz range is always very small: Integrating over frequencies from 300 GHz to 3 THz, one obtains roughly 0.6 W sr⁻¹ m⁻² at the room temperature ($T = 300$ K). Furthermore, all Planck oscillators at the frequency of e.g. $f = 1$ THz are already fully saturated:

$$k_B T \approx 1.38 \cdot 10^{-26} \text{ J K}^{-1} \cdot 300 \text{ K} \approx 25.8 \text{ meV} \quad \gg \quad hf \approx 4.13 \text{ meV},$$

and therefore the power radiated in the THz range cannot be significantly improved by increasing the black body temperature. Thus, it can be shown that in this part of

the spectrum the luminosity scales only linearly with the temperature T ; in contrast, the total power scales as T^4 as follows from the Stefan-Bolzmann law. Therefore, sources other than thermal are preferred for measurements in the THz range.

4.1.1 Terahertz sources

Kinetic energy of an electron beam One class of devices uses the kinetic energy of an electron beam propagating in the vacuum. In devices accelerating a circulating electron beam, such as cyclotrons or synchrotrons, radiation is emitted when electrons are passing through the bends in the particle path, the deflection of the electrons being caused by a static transverse magnetic field. If the electrons are packed in a short bunch, it results in an efficient emission of a coherent broadband pulse. Another example is the free electron laser with the electron bunches passing through a device with a periodically poled magnets, called *wiggler*. Both types of devices provide an excellent brightness and tunability, but they are rather large-scale facilities often with a dedicated building.

Tabletop sources of radiation covering a part of the THz range are the microwave vacuum tubes: *gyrotron*, travelling-wave and backward wave oscillators (BWO, also known as *carcinotrons*, of the O- and M-types), and *klystron*. The unifying principle of these devices is that the electron beam speed, position or density can be modulated by the electric field, and the modulation in turn radiates amplified electromagnetic waves. Backward-wave oscillators are tunable monochromatic sources used for continuous-wave spectroscopy, but the tunability of one device is typically limited to tens of percent and the power drops with the frequency [150].

Terahertz solid-state oscillators Reducing the size of the active regions of well-established microwave devices, such as microwave diodes, transistors and vacuum tubes, usually enables scaling down the wavelength of the emitted radiation proportionally with the dimensions. The fundamental issue lies in that the power drops very fast when the device is miniaturized. If the total emitted power is limited by cooling, i.e. by the surface of the active region, it drops with the second power of the device size. If the volume power density is the determining factor, the power drops even faster. As a solution, either substantial changes in the device geometry, constituent materials, or even new physical principles have been introduced for efficient THz sources [152, pp. 8-12].

If a relatively low power is required, principles used in microwave engineering can be extended to the lower part of the terahertz spectrum. The frequency range of operation of high electron mobility transistors (HEMT) has been extended in this way up to 1 THz.

An oscillator may be formed by placing an element with a negative differential resistance (NDR) into a resonant cavity or circuit. In *Gunn diodes*, widely used in microwave technology, the NDR is due to the electron's effective mass abruptly increasing with their velocity in certain direct-gap semiconductors. In *resonant tunneling diodes* (RTDs) [160, 161], NDR is achieved by a heterostructure quantum

well, where, upon an increase of the voltage, the electron energy is detuned from the resonance of the quantum well, and the current is reduced.

Yet another principle is employed in the *impact ionization avalanche transit-time* (IMPATT) diodes, where a non-destructive breakdown of a reverse-biased p-n junction follows the voltage with a delay which again enables oscillations if the junction is surrounded by a cavity. In contrast, in the *tunneling transit-time* (TUNNETT) diodes, the NDR is achieved by changing the transit time of carriers through the semiconductor volume.

Nonlinear up-conversion of microwaves A nonlinear response of semiconductor devices to microwaves can be used for up-conversion into the terahertz range. Starting from a relatively powerful and widely available semiconductor source operating in the 100 GHz range, frequency multiplying stages are often cascaded to reach frequencies several times higher [162].

Harmonic frequency multipliers and mixers often employ varactor diodes or Schottky diodes embedded in a waveguide. They, however, still suffer from a significant power drop above 1 THz.

Nonlinear down-conversion of optical waves The opposite approach, also known as *optical rectification*, generates THz radiation as the difference frequency between two or more detuned optical waves. The radiation may come from two lasers or laser modes, mutually detuned by a frequency that is to be generated. Other possibility is to use the *terahertz parametric generation* where a single wave enters the nonlinear crystal as the *pump* and the second wave, *idler*, is generated during the nonlinear process. The *idler* wave is kept in an optical resonator; the terahertz output can be tuned by changing parameters of the resonator. For nonlinear generation of pulses in the THz range, usually a mode-locked laser is used that emits pulses that intrinsically cover a broad spectrum of frequencies (e.g. typically over 360–390 THz for a titanium-sapphire laser). The difference frequencies are generated from all optical frequency components simultaneously, which results in a terahertz pulse with a very broad spectrum given by the type of nonlinear medium.

The classical process of nonlinear optical conversion involves transparent electro-optic crystals, where some measures are taken to account for the generally different velocity of all interacting waves.

- For the difference-frequency generation between optical waves of close frequency, the classical condition of *phase synchronization* is equivalent to ensure similar group velocity at the optical and terahertz frequencies. Among the materials satisfying these requirements, zinc telluride (ZnTe), gallium selenide (GaSe), and lithium niobate (LiNbO_3) found their widest applications in the frequency ranges up to 3–5 THz.
- The *quasi-phase-matching* technique allows to compensate the difference of the group velocity of the optical wave and the terahertz wave by periodically altering the nonlinear coefficients of a crystal so that the nonlinear contribution to the resulting wave never reverses its sign. Crystals of *periodically poled*

lithium niobate (PPLN) are often used for this, with the possibility of shaping the poled regions as wedges (*fanned-out PPLN*), which allows to change the effective poling pitch. This method is suitable for continuous-wave or narrow-band pulse terahertz generation.

- A sufficiently strong nonlinear interaction, on a length scale smaller than the coherence length, alleviates the requirements of both phase matching and low absorption of the waves [163]. Organic crystals, e.g. those of DAST,¹ have been reported [164] to have their electrooptic coefficients two orders of magnitude higher than the materials usual in nonlinear optics, making them suitable for operation up to 20 THz.

Nonlinear interactions in semiconductors are enhanced when the incident photon energy is above their band gap. Common crystals used for *resonant THz emission* are GaAs, InP or CdTe (with band-gaps of 1.42, 1.34 and 1.5 eV, respectively), which can be illuminated by a titanium-sapphire laser (with an average photon energy $hc/\lambda \approx 1.5$ eV).

- With a proper spatio-temporal optical pulse geometry and choice of materials, THz pulses can be generated in the form of Čerenkov cone [165] even if the optical group velocity is higher than the terahertz one.
- Finally, plasma generated in gases by high optical intensity of optical pulses can serve as a nonlinear medium, with low dispersion and thus a very broad bandwidth of tens of THz [166, 167, 168].

Photoconductive sources Terahertz waves can be generated by *photoconductivity*, i.e. by transient acceleration of charges upon optical illumination. In the photoconductive devices, the major part of the energy is supplied by the external quasi-static electric field, which reduces the requirements for the laser illumination intensity. The light sources can be again two detuned lasers or laser modes [169], or pulses from a mode-locked laser oscillator. Obviously, this method requires the photon energy to exceed the band gap of the selected semiconductor.

The photoconductive emitter is usually a slab of a suitable semiconductor with an antenna structure, deposited on the illuminated side [170]. Earlier antenna designs use two metallic segments of different shapes, such as split-H shape or a spiral. The gap between the electrodes may vary; the *large-aperture* emitters with gaps of several millimetres allow to increase the energy and directivity of the THz radiation in the pulsed regime, however they require a high-voltage power supply. The optical beams (continuous or pulsed) are always more or less tightly focused to the gap between the electrodes.

The *interdigitated emitters* [171, 172] provide a large-aperture and relatively high-energy THz pulses even with low voltage in the range of tens of volts. The metallisation on its front side forms a dense array of narrow metallic wires; every second gap between them is covered with opaque paint. The odd and even wires are connected to two terminals of a voltage source. Upon pulsed illumination, all charge

¹DAST is a shortcut for 4-dimethylamino-N-methylstilbazolium tosylate

stored in the interdigitated electrodes discharges through the illuminated parts of the semiconductor surface, emitting THz waves polarized perpendicular to the wire grid.

The emission efficiency can be improved when the sharp current rise is followed by a similarly sharp falling edge of the current, again in the order of one picosecond. For this purpose one needs to select a material with a very short lifetime of carriers, but a relatively high mobility thereof. Radiation-damaged silicon films on sapphire, or gallium arsenide slabs with lattice disordered either by (Be or Cr) doping, or by growing at low temperature, are used to this purpose.

A weaker THz emission can also be observed from semiconductors even with no static bias voltage, owing to the surface electric field, photo-Dember and other phenomena [173, 174].

Terahertz lasers Continuous gas terahertz lasers use stimulated emission from quantum transitions between discrete rotation levels of small organic molecules [175]. Although they represent high-brightness continuous sources at multiple lines in the terahertz range, they are rather expensive and their quantum efficiency is poor, as they usually have to be pumped by a powerful carbon dioxide laser at 33 THz.

Solid-state terahertz lasers are represented by the p-doped germanium laser, where the quantum transition occurs between energy levels of light and heavy holes in a strong magnetic field and at cryogenic temperatures. The transition frequency can be continuously tuned by the magnetic field.

Quantum cascade lasers (QCL) are composed of hundreds of semiconductor layers [176], which create multiple closely-spaced quantum levels. Each electron or hole travelling across the structure thus undergoes multiple transitions. Such devices are compact and efficient sources of continuous and slightly tunable radiation in the mid-IR region. The extension of their operation under 2 THz oftentimes requires cryogenic cooling and is subject to intense research.

Other THz sources Although a complete list of all physical phenomena that lead to possibly useful emission of terahertz waves is beyond the scope of this thesis, we try to point out some most notable examples of these.

Earlier in our laboratory it was observed that an oblique impact of femtosecond optical pulse on a 50-150 nm thick gold layer on glass emits a THz pulse of similar energy as those from an interdigitated emitter [177, 178]. Other experiments, e.g. with thin organic layers [179], suggest the process may be intensified by surface plasmons.

Tunable terahertz continuous-wave emission was observed in multiple stacked Josephson junctions [4], where the oscillation frequency is determined by the junction voltage $f(U) = 2e/h$, thus 2 mV correspond to roughly 1 THz. This method however requires cryogenic temperatures as a superconductor structure is used, and is still subject to primary research.

The *Smith-Purcell* effect is observed when a relativistic electron beam passes close to a corrugated surface, e.g., that of an optical grating. The emitted coherent radiation can be obtained also in the THz region [180] (as determined by the

grating pitch). A similar effect was later observed from a direct current flowing through a graphene monolayer placed over a photonic crystal [181].

4.1.2 Terahertz detectors

Thermal detection A broad class of detectors, applicable also to the terahertz range, measure the energy of the radiation. Classical bolometers use thermistors or thermocouples, resistivity of which will change when they are heated by radiation. Pyroelectric detectors convert the heat directly to the electric signal by means of a crystal that changes its polarisation with temperature. In the Golay cells, an incident terahertz pulse heats the air and its thermal expansion is detected. Such devices usually operate at room temperature.

The concept of a bolometer can be greatly improved, in terms of sensitivity or speed, at cryogenic temperatures when a superconductor near its critical temperature or a doped semiconductor are used as the temperature detector. In the *hot-electron* bolometers, the superconductor forms a narrow bridge between two contacts so that the changes in resistance are more pronounced. The changes in the superconductor behaviour can also be detected by a superconducting quantum interference device (SQUID).

Heterodyne mixing A continuous-wave terahertz signal can be mixed with the signal from a local terahertz oscillator, producing a difference frequency in the microwave spectral range which can be processed easily using an oscilloscope or a spectral analyzer. The nonlinear components often used up to 1 THz are Schottky diodes or superconducting Josephson junctions [182]. Fast enough thermal detectors, such as hot-electron bolometers based on Nb or NbN superconducting transition, can also be used, offering higher sensitivity [151].

Time-resolved field sampling Another class of terahertz detectors enables measuring the electric field $E(t)$, or magnetic field $H(t)$, as a function of time. An important advantage of such devices is the possibility to recover the instantaneous amplitude of the field, i.e., both its modulus and phase in the frequency domain). It also allows to synchronize the detection with the pulsed source to record short terahertz transients. It should be noted that the measurement of the transmittance phase can be accomplished with a continuous tunable source, too, using a Mach-Zender interferometer. Pulsed measurement is however vital for transient dynamics investigation.

Most of such detectors require a simultaneous incidence of the terahertz pulse and of a *sampling* (or, *gating*) optical pulse. The mutual timing of the pulses can be scanned using an optical delay line, thus the terahertz waveform can be recovered over repeated measurements [183]. Alternatively, various single-shot detection schemes have been also implemented, usually being based on the temporal dilation (chirp) of the sampling optical pulse and subsequent spectral analysis of the output. The physical process of the optical sampling is in most cases analogous to one of the above described mechanisms of terahertz pulse generation:

1. Photoconductive receiving antennas use a short optical pulse to introduce a subpicosecond time window to short-circuit the antenna segments. The instantaneous THz field at the time of the optical pulse arrival moves a charge across a semiconductor gap between two metallic stripes. The charge amount is proportional to the THz field and can be amplified and measured by relatively slow electronics.
2. Electrooptic sampling uses the nonlinear interaction between the optical and THz electric fields in an electrooptic crystal, typically a thin plate of ZnTe. To discriminate between the sampling optical pulse and the weaker component added to it by the nonlinear interaction, usually a change of optical polarization is detected.
3. Magnetooptic sampling was also demonstrated [184], based on the Faraday rotation induced by the magnetic component of a transient THz wave.

Similar to all cases of the pulsed terahertz sources, the temporal resolution of sampling terahertz detectors is generally limited by the duration of the sampling optical pulse, and more often, by the limited speed of the photoconductive antenna or by the group velocity dispersion of the nonlinear crystal. The detection bandwidth can be improved using the approaches used in the terahertz pulsed sources such as the use of thin plates of organic crystals (DAST) or nonlinear detection in plasma.

4.2 Terahertz time-domain spectroscopy

Overview of the method The numerical data presented in this thesis could be in some cases corroborated by experimental measurements using the *time-domain terahertz spectroscopy* (TDTS) in our laboratory.

The basic principle of the measurement is similar to the scattering-parameter retrieval in FDTD simulations presented in Chapter 3.2.1. A short, broadband pulse impinged the sample, one part of its energy was transmitted, another reflected and the rest was dissipated in the sample. The transmitted pulse was then recorded by the time-domain sampling setup, and processed to obtain the transmittance amplitude and phase as functions of frequency.

The reflectance could not be directly measured in the setup described, but at the end of this section an indirect method is described that allows to compute the equivalent sample properties from the subsequent echoes that arise when the sample is surrounded by thick transparent slabs of sapphire. In the following, we give details on the optical and terahertz experimental setup.

Terahertz pulse generation As the source of ultrashort optical pulses, we used the commercial *Coherent Mira* titanium-sapphire femtosecond oscillator with a mean power of 0.5 W, central wavelength 810 nm, repetition rate of 76 MHz and pulse duration not exceeding 70 fs.

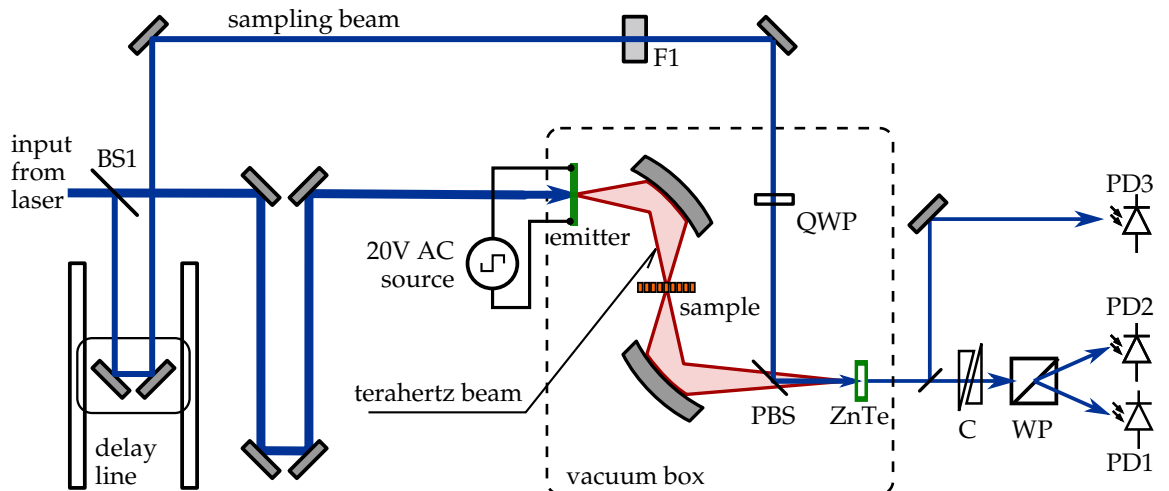
The laser output was split into two branches at the beamsplitter (BS1 in Fig. 4.1), one of which was used for the electrooptical sampling setup. The major part of the

energy passing through BS1 was converted to terahertz pulses using an *TeraSED* interdigitated photoconductive emitter, described in the previous section. The voltage at the emitter was 15-20 V, and its polarity was modulated at the frequency of 91-92 kHz. This enabled us to use synchronous lock-in detection to increase the signal-to-noise ratio of the detection system.

Vacuum chamber and sample holder The diameter of the active region on the *TeraSED* emitter was comparable with the longer-wavelength components of the THz pulses, so the beam diffraction led to a broad angle of the terahertz emission, of the order of 0.5 radian. Therefore, the waves were reflected at an ellipsoidal mirror and refocused at the sample. Upon passing through it, they diffracted again and were collected by an identical ellipsoidal mirror and focused at the detector. To allow enough clearance for a bigger instrumentation surrounding a sample, such as a liquid-helium cryostat or a heating furnace, the ellipsoidal mirrors were separated by 0.3 m and the whole beam path approached 0.6 m.

Propagation of terahertz waves in air over such a distance is impeded by absorption of water vapour, which is the only polar molecule found in the air in a significant concentration. The absorption forms clear notches in the terahertz transmittance spectra, for instance around 0.62, 0.75, 1.07 and 1.41 THz, which can be traced down to discrete rotational levels of the water molecules [185]. In the time domain, the absorption manifests itself as an exponentially decaying ringdown. In order to avoid such a signal deformation, the whole terahertz wave path has to be in an environment free of water vapour, and the fastest way to achieve this reliably was to enclose the emitter, mirrors, sample and detector in a vacuum chamber evacuated by a two-stage rotary pump.

Figure 4.1: Experimental setup for the terahertz time-domain spectroscopy. BS1 is the beam splitter separating the pump and sampling branches, F1 a focusing lens, QWP a quarter-wave plate, PBS a pellicle beam splitter. ZnTe denotes the optoelectric crystal, C is the Babinet compensator, WP is the Wollaston polarizer and PD1, PD2 and PD3 are photodiodes.



Terahertz detection setup Before the laser pulse entered the vacuum chamber to induce the photoexcitation of the THz emitter, a small part of its energy was separated by a reflection from a beam splitter (BS1 in Fig. 4.1) into the *sampling* branch.

The pulse in the *sampling* branch reflected from a pair of mirrors on a delay line, acquiring a precisely controlled relative delay against the terahertz pulse. Then it was attenuated at a filter (F1) and its polarisation was converted from linear to the circular one on a quarter-wave plate (QWP). The pellicle beamsplitter (PBS) directed the optical beam along the axis of the terahertz beam.

We used the electrooptic sampling mentioned in the previous chapter: The electric field of the terahertz pulse induced a slight transient change in the permittivity tensor of the zinc telluride crystal (ZnTe). The much weaker and shorter optical pulse was modified by this change, acquiring diagonal ellipticity that could be fine tuned for zero signal with the Babinet compensator (C). The Wollaston prism (WP) was used to separate the two diagonal components of the resulting elliptic-polarized light. The difference between these two signals, if a small modulation is assumed, is proportional to the amplitude of the electric field. This allowed us to sample the electric field with a theoretical temporal resolution given by the duration of the optical pulse, but using a standard intensity detection using a pair of silicon diodes.

Signal processing and acquisition To reduce the noise, synchronous detection with the *Stanford SRS360* lock-in amplifier was used and the polarity of THz waveforms was modulated by the voltage at the TeraSED emitter. The difference signal at the two photodiodes, PD1 and PD2, was first fed to an analogue filter (with center frequency 91.3 kHz and 3 dB drop at ± 7 kHz), sampled by the lock-in amplifier and digitally normalized against the signal measured by the auxiliary photodiode PD3. The normalisation was necessary due to the fact that the difference signal is proportional not only to the terahertz field, but also to the laser intensity which may fluctuate over time.

The spectral response of both the emitter and electrooptic sampling substantially influenced the measured sample spectra. Moreover, the phase of the recorded waves was modulated, too, as a beam passing through a focus acquires additional phase due to the Gouy shift [186]. Every transmittance measurement was therefore normalized in frequency domain against a corresponding free-space reference, so that both the amplitude and phase artifacts cancelled out.

4.2.1 Simultaneous reflectance and transmittance measurement

Principle With rearrangement of optics, it would be possible to measure the *reflectance spectrum*, similarly as the transmittance was measured. However, due to the complexity of such a setup and its very high sensitivity to the sample displacement, we did not use a second sampling branch for detecting the reflected signal. Instead of using two sampling schemes, we recovered the amplitude and phase reflectance of the sample by stacking it between a pair of thick (3 and 6 mm) sapphire slabs [139]. Thanks to the relatively high refractive index of sapphire in the terahertz

range along the optical axis, $N \approx 3.068$, these slabs introduce several time-delayed pulse reflections, also called echoes, into the transmitted signal.

If the beam divergence is neglected, each optical element can be characterised by its complex transfer function in the resulting spectrum. One needs to define three intrinsic transmittance functions: that for the beam passing through the volume of the thin sapphire $A(f)$, the one of the thick sapphire $B(f)$ and one through the thin sample $t_S(f)$; all of these are without the effect of reflection at interfaces.

The reflection is described by two reflectance functions for the beam reflected on sapphire-air interface $r_A(f)$ and on the sapphire-sample interface $r_S(f)$.

By measuring the references of the thin and thick sapphires separately, the spectra of $A(f)$ and $B(f)$ as well as $r_A(f)$ can be established [139].

To retrieve the characteristics of the sample, i.e. $t(f)$ and $r_S(f)$, the overall transmitted time-domain waveform of the sapphire-sample-sapphire structure has to be split into two parts that correspond to the direct pass, and the first echo arising from the pulse reflecting back and forth in the thin sapphire. The double propagation delay through 3 mm of the thinner sapphire is roughly 70 ps, which limits the spectral resolution to 14 GHz. All spectral features in the sample transmittance must be significantly broader than this value. Otherwise they could not be resolved, and even more importantly, their temporal ringdown would overlap in the time domain with the following echo and produce spurious results. Using a thicker sapphire could improve spectral resolution of this method, however it conflicts with the requirements of the terahertz beam fitting into the area of the sample [125] and of reducing the error caused by beam diffraction as noted in the following paragraph.

Limitations of the scheme In the experiment, we observed substantial deviation from the numerically predicted results, which were moreover sensitive to subtle changes in the parameters. We propose several independent explanations for the experimental errors:

1. The geometrical beam divergence cannot be fully compensated by the transfer functions of separate sapphire slabs, $A(f)$ and $B(f)$. The terahertz beam is relatively tightly focused, and the focus of the echoes is longitudinally displaced compared to the focus of the first pulse. The deconvolution algorithm can compensate for slight focus displacement by changing the amplitude of different frequency components, or shifting them in phase.

However, due to the hyperbolic shape of the Gaussian beam, with its Rayleigh length z_R being similar to the sapphire thickness², the overall effect of two sapphires cannot be linearly compensated from two separate measurements of each of them.

2. The possible asymmetry of the sample with regard to the beam axis can substantially bias the measured reflectance. This happened during the characterisation of the dielectric spheres, when the sapphire distance was defined by a

²As an approximate example, for the main frequency component $f = 1.5$ THz with wavelength $\lambda = c/f \approx 200$ μm, for $\vartheta \lesssim 0.15$ rad as an estimated divergence of the beam from its axis, the Rayleigh half-length of a Gaussian beam would be $z_R = \frac{\lambda}{\pi\vartheta^2} \gtrsim 2.8$ mm, i.e. roughly the thickness of the thinner sapphire.

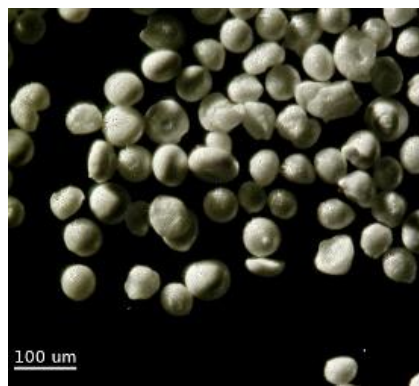
$\approx 60\mu\text{m}$ teflon spacer. The nonuniform size of the resonators required us to attach them to one of the sapphire windows. While the spheres with the $60\mu\text{m}$ diameter were placed symmetrically in the gap, the smaller spheres had an asymmetric position. Since the latter have higher resonant frequencies, the effect of asymmetry was probably also frequency dependent.

3. The sapphire slabs can influence the near field of resonances in some samples, cf. Sect. 3.2.1. This error should not be significant in transversally homogeneous samples (i.e. slabs), nor in samples that are made of dielectrics with much higher permittivity than that of sapphire. However for some samples, such as metallic resonators, the spectra are completely changed in the vicinity of a dielectric (see its application on a fishnet sample in Fig. 4.19 in Ref. [157]).
4. Finally, it follows from Eq. (3.20) that reliable reflection data can only be retrieved at frequencies where also the transmittance amplitude is strong enough for the signal not to be dominated by noise.

4.3 Preparation of the titanium dioxide microspheres

Fabrication through the spray-dry technique The collaborating laboratory of Dr. Patrick Mounaix in France provided us with high-permittivity TiO_2 spheres with the sizes from 30 to $100\mu\text{m}$, which were examined by the terahertz spectroscopy as dielectric resonators, and as possible constituents of a metamaterial with negative effective permeability.

Figure 4.2: Microphotograph of the TiO_2 spheres after preliminary sieving



Compared to most metamaterial designs, the fabrication of the dielectric spheres can be extremely simplified by the *spray-drying* technique. In contrast with the expensive and time consuming *top-down* processes such as laser cutting, lithography or polishing, this is a typical *bottom-up* process, where the particles are formed all within one procedure, though certain postprocessing is needed.

As a first step, rutile (TiO_2) was ground to a sub-microscopic powder [157, pp. 91-93]. A suspension of this powder in ethanol was sprayed into flame. It immediately formed spherical droplets, which dried up and sintered in the hot air. Rutile

concentration in the suspension, feed rate and gas flow in the flame determined the average size of the sintered particles.

The resulting particles were annealed in a furnace to further solidify. The degree of recrystallization could be controlled by the temperature of the furnace from 1200 to 1400 °C from microscopic grains to few large crystalline domains in one microsphere. Note these temperatures used are still far below the melting temperature of rutile, which exceeds 1800 °C. Similar TiO₂ microspheres are also available commercially (e.g. from Brace, GmbH), and they were likely made with a similar process.

The annealed spheres were further treated with the aim to break or eliminate clusters, by means of light milling with agathe mortar, which was separated afterwards by ultrasound bath cleaning in ethanol. Pre-sieving was performed on commercial sieves with 100, 53, 50, 40 and 38 µm size of the square hole, though these nominal parameters of sieves should be in no way understood as hard limits for the particle sizes. The procedure of milling, cleaning and sieving was repeated 2-3 times, according personal communication with Dr. Patrick Mounaix and Dr. U-Chan Chung.

Only the low-temperature annealed samples were measured by the terahertz spectroscopy in this thesis. The fine-grained rutile was assumed to represent a nearly isotropic dielectric. We estimated the size of the constituent crystalline grains by grinding one microsphere and observing it under a polarizing microscope: unlike polycrystalline aggregates, small rutile monocrystals appear as coloured particles due to their inherent birefringence. In this way, the sizes of crystalline grains were assessed to be in the order of few micrometres or smaller.

Theory of anisotropic sieves Triple sieving on commercial sieves, weaved from stainless steel wire, did not provide narrow enough size distribution, which is however essential for obtaining a narrow resonance peak of the sample. We therefore developed a more exact method for very fine sample sieving and characterisation.

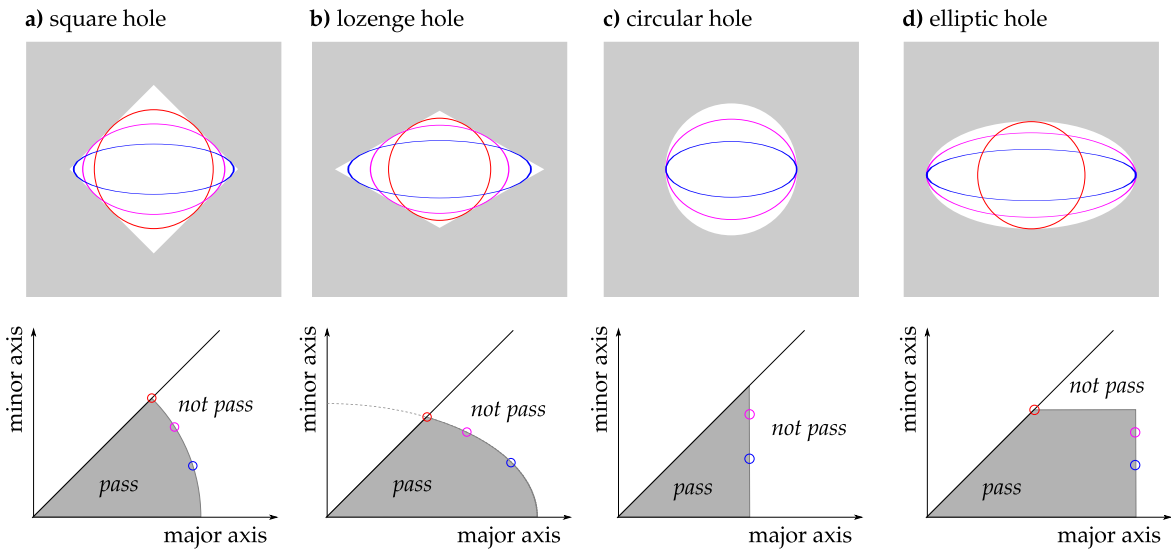
In the following, the dielectric particles are approximated by ellipsoids with three (generally different) half-axes

$$\rho_a \leq \rho_b \leq \rho_c.$$

For the purpose of sieving, only the values of the shortest two half-axes, ρ_a and ρ_b , decide whether the particle can pass through the sieve. The longest ellipsoid half-axis ρ_c does not affect this, although it may influence the sieving speed. Therefore we can represent each three-dimensional particle with its projection on the smallest possible ellipse, which is described by its *minor axis* $\equiv 2\rho_a$, and by its *major axis* $\equiv 2\rho_b$ (which is, in fact, the *medium axis* of the ellipsoid). For a given shape of a hole in a homogeneous flat sieve, it is easy to determine which values of minor and major ellipse axes allow a particle to pass through, and which not. For a square sieve such area in the parameter space forms a disk around the center of origin (Fig. 4.3a). It can be shown that when the sieve is diagonally stretched, forming a lozenge-shaped hole, the area of spheres allowed to pass transforms into an ellipse (Fig. 4.3b). When the hole shape is circular or elliptical, it is obvious that the area forms a part of a square or of a rectangle, respectively (Fig. 4.3c,d).

Figure 4.3: Correspondence between the hole shape (above) and the set of ellipsoids that can pass through the hole (below), determined by their medium and minor axes. Somewhat surprisingly, the (a) square and (b) lozenge holes result in circular/elliptic set of passing particles, whereas the (c) circular and (d) elliptic holes result in the square/rectangular shape of such an region.

For clarity, some limiting-case examples of the ellipsoid projection and the equivalent position on the minor-major ellipse axis plot are drawn in blue, violet and red.



The resonant frequency of a dielectric resonator depends on all three half-axes, $\rho_a \leq \rho_b \leq \rho_c$. In order to select a size fraction as narrow as possible, one has to use double sieving: the above sieve not allowing the fraction of particles too big, the bottom sieve removing the fraction of particles too small. This is where the anisotropic hole shapes become useful – the bottom sieve can exclude also all oblong particles with the difference of $\rho_a \leq \rho_b$ too big. This effect is illustrated in Fig. 4.4, which also presents a comparison between using more usual sieves with square/lozenge holes and the approach with a pair of sieves with micromachined square/elliptical holes. Obviously, the latter approach better discriminates between the *shapes* of the ellipsoids. This advantage further gains on importance when the anisotropy of the sieve is low.

It shall be noted that although we plotted a binary (pass/not pass) function in Figs. 4.3 and 4.4, the sieving speed continuously drops when the particle dimensions approach those of the sieve holes. However, this particular fraction of particles is exactly what one is interested in during the high-accuracy sieving. The process must therefore be run for a long enough time, of the order of days, and with as high a sieving speed as possible.

First sieving apparatus Employing the idea of anisotropic sieves from Fig. 4.4a, the author assembled a first prototype based on nylon sieves, as depicted in Fig. 4.5. Two glass containers, 6 mm high and 11 mm in diameter, were cut on a lathe from a glass tube. On their bottom, the sieves were glued and carefully clipped. The side of the sieve holes was $60 \pm 5 \mu\text{m}$.

Figure 4.4: Application of the effect from Fig. 4.3 for separating a narrow fraction of ellipsoids between the sieves. Both combinations of (a) square-rectangular and (b) circular-elliptic sieves can be used, with the latter one promising better selectivity also in terms of the particle aspect ratio.

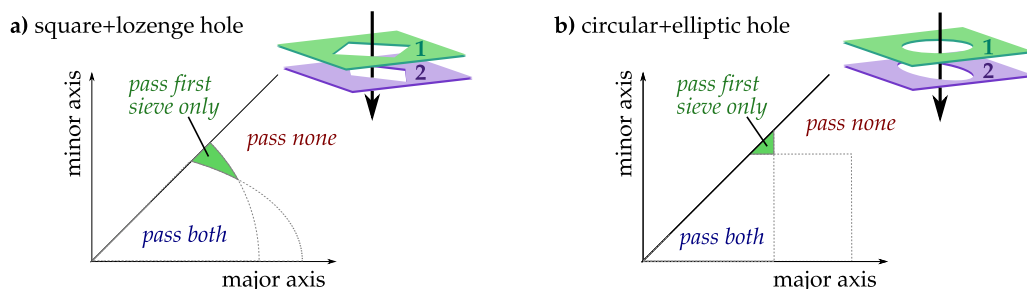
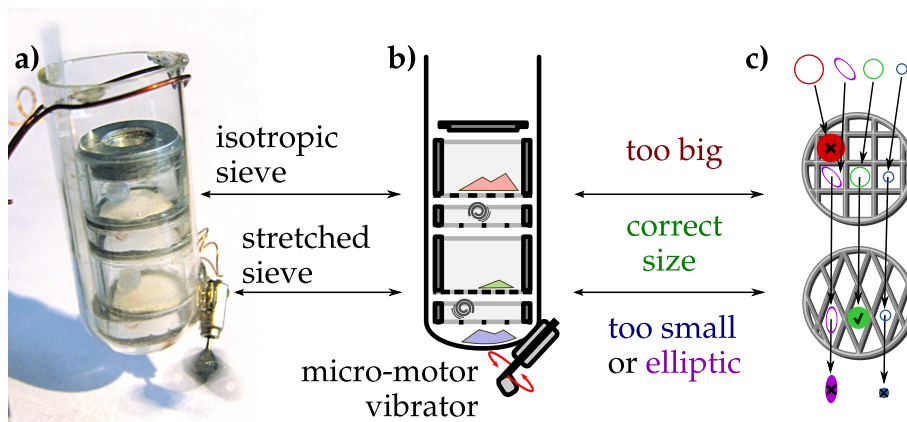


Figure 4.5: (a) Photograph and (b) scheme of the first sieving apparatus based on square-lozenge sieve pair, with a schematic out-of-scale illustration of its operation for an input of four different microspheres (c)

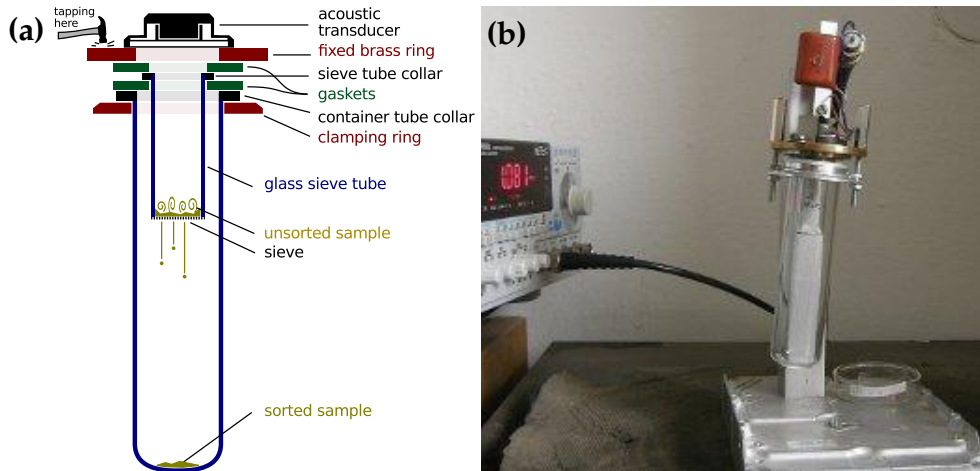


The mesh was woven of nylon threads, so the bottom sieve could easily be stretched by ca. 20-25 % in the diagonal direction. The above sieve was kept isotropic.

This property however proved to be also detrimental for precise sieving, as the threads easily bent aside under only a small force, thus allowing oversized particles either to pass or to get stuck permanently and to block the sieve within few minutes. To help resolving the latter problem, two additional narrow glass rings were cut from the glass tube, supporting much coarser sieves with 150 μm pitch glued on the bottom, to allow little spherical springs bounce beneath the sieves and to loosen the particles that got stuck in the holes. For the same purpose, 2mm plastic balls were added to the microsphere samples.

A cover on top prevented the particles to jump out of the above container. The whole stack was carefully lowered into a test tube with a larger diameter, and vibrated by a tiny electric motor glued on the bottom.

Figure 4.6: (a) A sketch of the acoustic sieving device, and (b) a photograph thereof



Second sieving apparatus The partially promising results and, more importantly, obvious deficiencies of the previous apparatus motivated the construction of a second one depicted in Fig. 4.6. Different from any other sieving apparatus known to the author, this one made use of vertical acoustic waves for the movement of particles. It consisted of two coaxial glass tubes: The inner tube, with outer diameter of 13 mm, had a round metallic sieve glued to its bottom, and on its upper end it was covered by a small acoustic transducer. The outer tube (90 mm long, outer diameter 26 mm) surrounded the inner one and had a round bottom, where the particles were collected.

The gaskets ensured that the whole apparatus was tightly closed, preventing both sieved particles and the sound from escaping. The brass ring with the transducer was fixed to a massive aluminum stand, and the rest of the structure was held by two accessible screws that allowed easy disassembling.

The key advantages of this novel approach are the following:

1. The speed of sieving is expected to grow with the frequency at which the particles hit the sieve. The acoustic frequency of 1 kHz is roughly two orders of magnitude higher than in usual commercially available devices. Moreover, the spheres are continuously stirred, so it is ensured that a layer of over-sized particles does not occupy the sieve.
2. The upward air pressure pulls out particles that got stuck in the sieve in every period of acoustic vibration. This resolves the major issue of clogging inherent for the previous prototype.
3. Avoiding macroscopic vibrating parts, except the membrane of a small acoustic transducer, allows the device to operate over multiple days with reduced risk of mechanical failure.

The outer tube acted as an acoustic resonator, greatly enhancing the effect of the sound when tuned to resonance around 750-900 Hz. These frequencies obviously correspond to the fundamental acoustic resonance, as the corresponding quarter-

wavelength is close to the 10 cm length of the outer tube. The electrical input power of the sine wave feeding the device was in the order of 1 W.

Sieving challenges A practical deficiency of this setup was that the upper opening of the transducer radiated relatively intense sound during operation. We resolved this potential issue by covering the whole apparatus by a robust glass bell jar.

With the acoustic power and frequency correctly adjusted, the particles formed a cloud 5–10 mm high. One difficulty arose from that the small particles tend to attach to the surface of glass or metal, probably due to electrostatic charges on their surface. While at an average particle radius $\rho = 50 \mu\text{m}$ this effect was rather marginal and transient, it took only few seconds of sieving for $\rho = 20 \mu\text{m}$ particles to immobilize permanently on any surface. It has however proven efficient to tap the upper brass ring, as the mechanical shock released most spheres and renewed the sieving process. To ensure unattended sieving for a timespan in order of days, we added a little motorized hammer with a timing circuit (Fig. 4.6a).

The amount of particles in one batch was limited to ca. $10\text{--}20 \text{ mm}^3$, otherwise the sieve would be covered with a layer too thick, which could not be efficiently lifted by the acoustic pressure. This problem could however be slightly mitigated by tilting the apparatus. With a tilt of 5–10 degrees, the bulk of particles then accumulated near one side, leaving most of the sieve surface free for sieving the moving particles. Given the small amount of particles required for the terahertz spectroscopy measurements, it is however advisable to sort a batch in order of $1\text{--}3 \text{ mm}^3$.

4.4 Optical determination of microparticle statistics

Image preparation An accurate characterisation of the particle statistics was necessary not only to assess the efficacy of sieving, but also to explain possible differences between the measured terahertz spectra and the computed ones on a quantitative basis. To obtain reliable statistics, thousands of particles needed to be evaluated, repeatedly for every sample. This, along with the small dimensions of particles, indicated that the most viable way to do so would be the optical microphotography with computer image processing automatically resolving each particle.

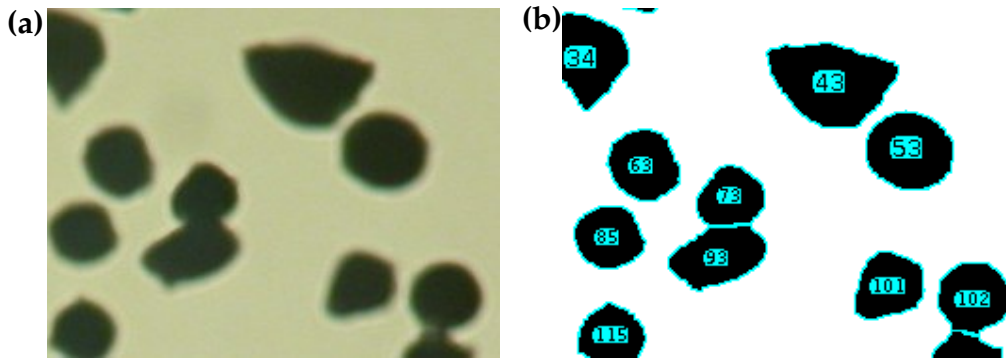
Computer *granulometry*, identification and measurement of photographed particles from a digital image, is a well-established technique. It is implemented in several advanced image processing programs, of which *ImageJ* was selected [187] since it is free of charge and allows its use for large batches of images through the use of macros.

The transmission microphotographs were acquired either with the lowest magnification on a laboratory microscope, or with a portable microscopic digital camera on its highest magnification, yielding similar results.

The first processing step, applied at the somewhat blurred photographs, as shown in Fig. 4.7a, was to establish the intermediate brightness level between the image's bright and dark areas, and apply a threshold so that the image was a binary function. Then the *ImageJ*'s *watershed* algorithm was applied to resolve two

or more touching particles relatively reliably, and a particle outline was found. An example is depicted as cyan lines in Fig. 4.7b. Finally, the particle outlines were approximated by best matching ellipses, and the major and minor axes of the ellipse were added into the statistics. We complemented the *ImageJ* macro with a

Figure 4.7: (a) A small section of a microphotograph of a pre-sieved sample before applying the described double-sieve method, (b) the corresponding identification of particles in ImageJ



Python script enabling us to process multiple photographs in a batch, and to plot the resulting histograms of the ellipse axes distribution. The script has also been published online [188]. The scale for each batch of images had to be determined from a separate photograph of a ruler.

Imprecision of the method An intrinsic deficiency of this method is that it was not possible to resolve the third dimension of particles. It can be however estimated that when ellipsoidal particles were randomly sprinkled on the glass, they would lie mostly on their flat side – i.e. their orientation would enable to measure the *medium* ρ_b and *major* axes ρ_c of the ellipsoid. This is in contrast with the process of sieving, as described above, where the particles were sorted according to their *minor* ρ_a and *medium* ρ_b axes.

This source of error is probably similarly important as another one, arising from rough shapes of the particles which could not always be well approximated by an ellipsoid.

4.5 Laser cutting

Fabrication of dielectric bars Dielectric or metallic structures can be made by cutting a thin polished slab of the given material. Electromagnetic waves with a frequency of 1 THz have a free-space wavelength of 0.3 mm. Periodic structures designed to operate in this range have their unit cells of a similar size or less, and their finest features are usually in the order of 10–20 μm .

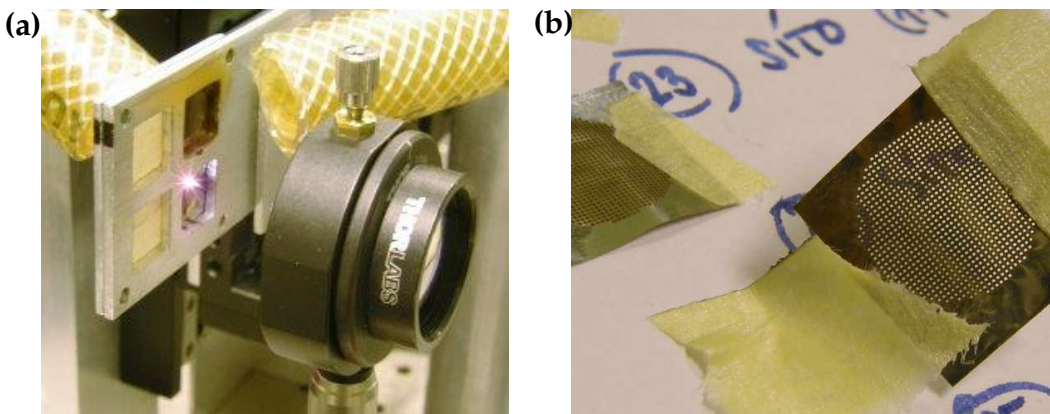
The sample already shown in Fig. 3.10 consisted of bars from strontium titanate (SrTiO_3) with a rectangular cross-section (see Fig. 3.9), where a structure with 10–30 μm lateral bar dimensions was engraved into a thin slab of the dielectric of a similar thickness [189].

If the slab consists of a monocrystal or a ceramic, it is usually extremely brittle and also sensitive to breaking due to thermal stresses. Femtosecond laser cutting (or, micro-machining) is suitable for such a task because it delivers the energy so fast that most of the heated material evaporates before the heat can diffuse into the rest of the structure. The strontium titanate bars were fabricated by the *Alphanov* facility in France.

Fabrication of sieves and fishnets Femtosecond cutting of metallic sheets into two-dimensional meshes is relatively easy, compared to the dielectrics, and was implemented in our laboratory. To achieve the required precision, we used 20 or 30 μm thick high-quality stainless steel foils.

The femtosecond laser used was different from that serving as the femtosecond source for terahertz spectroscopy (Sect. 4.2). A largely sufficient power was provided by the *Spectra Physics Spitfire Ace* multipass titanium-sapphire amplifier, with 1 mJ of energy per impulse, duration of \sim 50 fs, and 5 kHz repetition rate. Its output beam had to be attenuated to obtain finer cut at the expense of a slightly slower rate. The mechanical part consisted of two crossed *Owis* stepper-motor controlled linear stages, and a fast mechanical shutter allowed us to control the beam with a sufficient resolution of ca. 100 ms.

Figure 4.8: (a) Laser cutting the steel foil with a moving holder for four samples, metal vapour ventilation, and the focusing lens. A bright plasma spot is visible at the focus. *(b)* The resulting sieves made from 30 μm stainless steel foil with 10 mm overall diameter.



The 3 mm wide beam was focused by a lens with a focal length of 10 mm or 50 mm (Fig. 4.8a). The tighter focusing lead to a better resolution, but had stricter requirements for accurate focusing of the beam. To facilitate the task of optimal focusing, we devised a focusing-collimating setup which used the fact that the steel foil reflected the light like from a point source only when it was exactly in the lens focus. Then the reflected light would be collimated again by the very same lens into a beam returning to the laser. A part of the beam energy reflected from the metal sheet was separated sideways by a skewed glass in front of the lens, so that one could finely align the lens seeking for the smallest spot diameter on a distant screen.

A compact stepper-motor controller of a custom design [190] facilitated to automate the sample movement by means of computer control operated by a Python script. The sequences of shutter opening, sample movement and shutter closing could be assembled into a program for fabrication of a whole mesh sample of ca. 10 mm diameter, which took about 30 minutes to finish. Multiple different meshes with different parameters could be cut out from one steel foil in a batch, without user interaction.

Laser cutting issues The metal evaporated during the laser cutting immediately oxidises in the air. Although in total only few milligrams of the stainless steel foil were removed, the microscopic particles would pose a risk of damaging optical components. We built a miniature ventilation and filtering system out of a tube filled with cotton wool and fine synthetic fibres. After few meshes were cut, the cotton changed its colour from white to pale brown, indicating that at least a part of the particles were filtered out.

A greater challenge arose from thermal expansion of the foil. In order to fully utilise the valuable laser beam time, one would wish to set the cutting speed as high as possible. However, the speed of cutting was rather limited by the speed of stepper motors. The heat remaining in the steel foild was high enough to cause its thermal expansion and bending out of the plane of its holder. Even though the resulting displacement was less than 1 mm, the sheet moved significantly out of the beam focus. We assume this was the reason for slight variations between the hole sizes in Fig. 5.42. The effect would be diminished through slower cutting speed or by gluing the foil to a sacrificed rigid substrate.

Cutting the foil into free-standing wire array was however not successful since the resulting thin wires bent out of their original plane due to the thermal expansion. Their spacing was so uneven that no usable sample of wires was made.

Difference between sieves and fishnets The meshes were made for two purposes – either as sieves used in the second sieving apparatus described above, or as meta-material samples known as *fishnets*, which are predicted to exhibit a negative index of refraction (see Sect. 5.10). The difference between these applications is subtle; the meshes intended as sieves would surely exhibit a resonance in the terahertz range.

The optimum size range for the titanium dioxide spheres resonating around 1 THz is around 30–60 μm , which determined the hole diameter of sieves. To maintain mechanical robustness, the periodicity in sieves was kept much larger than the hole diameter, usually $300 \times 300 \mu\text{m}$, and the thickness was chosen as 20 or 30 μm . The fishnets had the same periodicity as sieves, and the hole dimensions were chosen between 150 and 280 μm . For cleaner cutting, a thinner stainless foil was used, with a thickness of 5 μm .

Chapter 5

Results

“The purpose of computing is insight, not numbers.” — R. W. Hamming

5.1 Dielectric slab

Dispersion curves of a one-dimensional photonic crystal One-dimensional photonic crystals (1-D PhC) were investigated thoroughly in the previous century and they found their major application in dielectric mirrors. This represents the simplest example of periodic structures, exhibiting only a subset of different phenomena that can be observed in other periodic structures. This is due to a continuous translational symmetry in the transverse direction that excludes all phenomena with a lower symmetry.

Most importantly, no *individual resonances* can occur in a 1-D PhC; all interactions with the waves occur through partial reflections of the electromagnetic waves on the interfaces of the layers. The only type of the band gap observed is of the Bragg type.

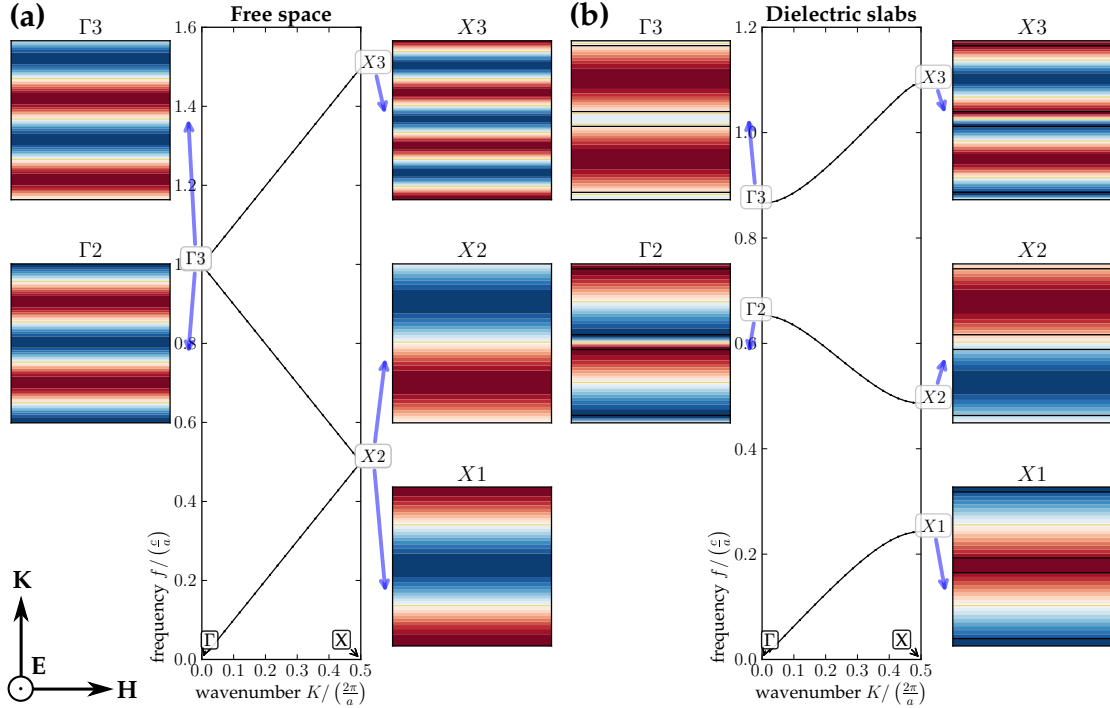
Dispersion curves for two examples of one-dimensional photonic crystals computed using PWEM are shown in Fig. 5.1. Its left panel shows the folded dispersion curves for a plane wave propagating in vacuum on which we imposed virtual periodicity. To save space, the dispersion curves were plotted as *folded*, but one can easily imagine how the curve unfolds into a linear dispersion of vacuum, known as the *light line*. No scattering occurs for homogeneous vacuum, hence for any frequency f , there exists a real wavenumber k corresponding to a propagating wave and there are no band gaps of nonzero width.

The right panel, Fig. 5.1b, is obtained by introducing periodic layers of a dielectric with a permittivity of 12% and a 15% filling fraction. In the field plots, the dielectric is outlined by thin black lines. The band gaps of nonzero width correspond to frequency ranges where the waves cannot propagate through the structure.

Characteristics of Bragg-type band gaps The lower and upper edge of the photonic bands are located in high-symmetry points of the Brillouin zone, such as Γ or X , which are equivalent to the wavenumber $K = m\pi/a$ for $m \in \mathbb{Z}$ in the discussed one-dimensional case. Whenever K corresponds to one of these points, the electric

Figure 5.1: Dispersion curves (a) in free space with virtual periodicity a , (b) in dielectric layers with permittivity $\varepsilon = 12$ and 15 % filling fraction.

Side plots show the electric field in 2×2 unit cells, with dielectric outlined by thin black lines. The triplet of the electric \mathbf{E} and magnetic \mathbf{H} fields and the wave vector \mathbf{K} for the incident wave is indicated in the lower left. The electric field is plotted as a blue-white-red color map. In the left panel, corresponding to vacuum propagation, the fields acquire pure harmonic shape.



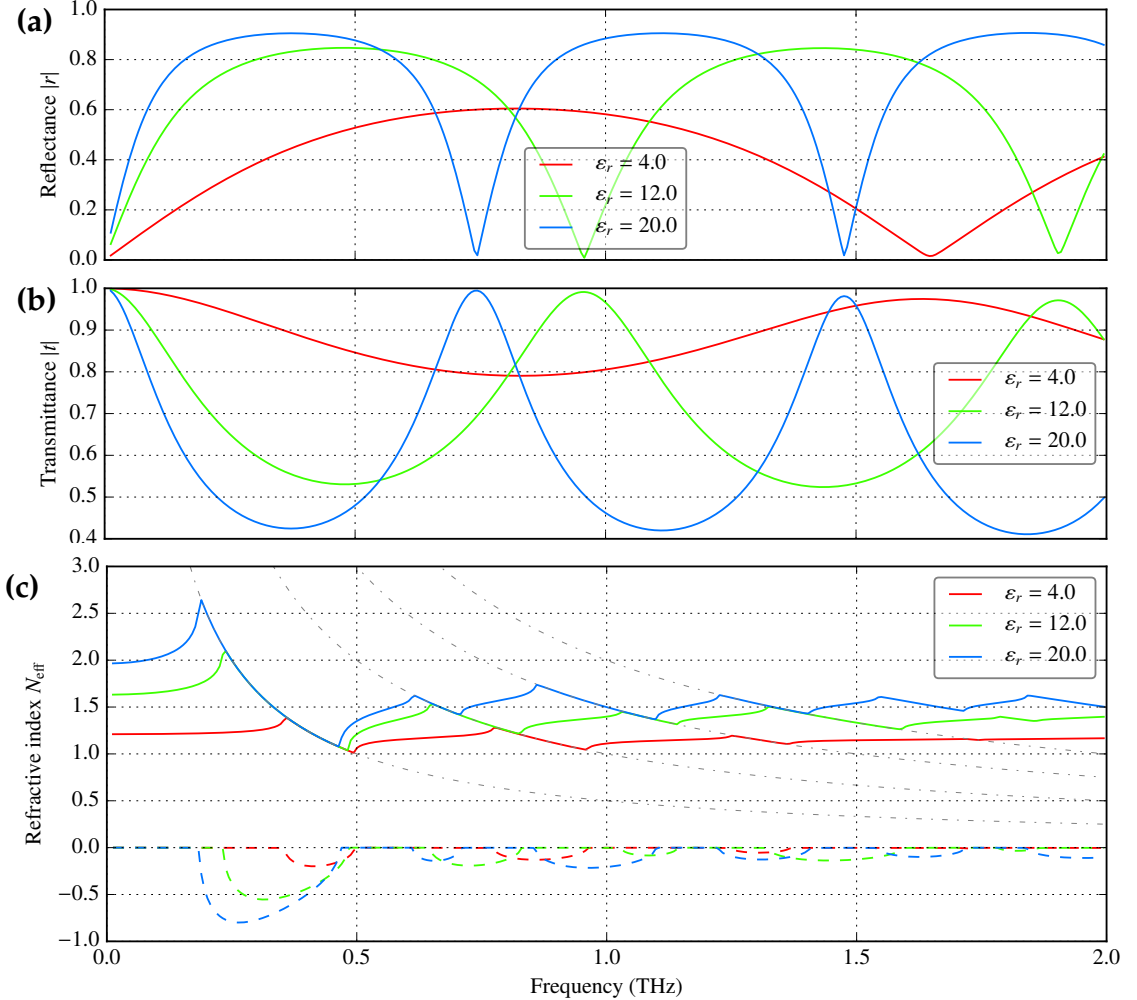
and magnetic fields are periodic in space, and can be easily visualized. The side plots in Fig. 5.1 show the shapes of the electric field E_x in the (y, z) plane at respective frequencies of the band edges. To stress the fact that the field is periodic even in the X point, each of the side plots spans over 2×2 unit cells.

An important characteristic of each field pattern is the set of all points where the field amplitude remains zero at any time. Such sets will be denoted as *nodal planes*, or also, more accurately, *nodal surfaces*.

From all pairs of field plots that are connected by a photonic band (i.e. $X_2-\Gamma_2$, Γ_3-X_3 etc.), it can be deduced that one nodal plane dividing the unit cell in perpendicular orientation to the wave vector is always added when the frequency increases from the lower band edge to the upper one. This rule is more general and is satisfied by other structures, too.

A feature typical for all Bragg band gaps (i.e. X_1-X_2 , $\Gamma_2-\Gamma_3$, etc. in 5.1) is that between the lower and upper edges of each band gap, the phase increase across an unit cell does not change and thus K remains constant, as does the number of the nodal planes. The field does change between these points, however, and the change is in the location of the *nodal planes* such that the upper band-gap edge concentrates the field energy in mostly lower-permittivity regions.

Figure 5.2: Amplitude of (a) reflectance, (b) transmittance and (c) effective index of refraction N_{eff} (real part solid, imaginary part dashed) for a dielectric slab with a 15% filling fraction in a 300 μm unit cell, and various values of permittivity of the dielectric $\epsilon_r \in \{4, 12, 20\}$. The dashed black lines in panel (c) denote the boundaries between the first, second and further Brillouin zones.



Bragg and Fabry-Pérot resonances The *Bragg condition* for the formation of a band gap in a periodic structure is that an integer number of half waves must fit into the unit cell; i.e. that the phase difference ϕ_{1+2} of the wave along the unit cell is

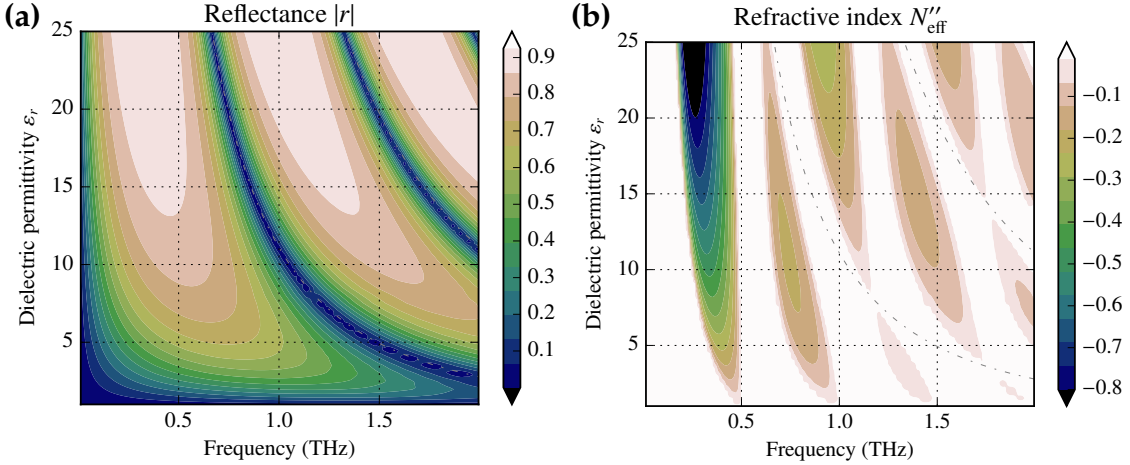
$$\phi_{1+2} = d_1 n_1 \frac{\omega}{c} + d_2 n_2 \frac{\omega}{c} = \pi m, \text{ where } m \in \mathbb{Z}. \quad (5.1)$$

Here $d_{1,2}$ are the thicknesses and $n_{1,2}$ are the refractive indices of the two layers.

The width of the band gap grows with the amplitude of the wave scattered from the unit cell. This amplitude, however, also depends on frequency and, in the case of a lossless dielectric slab, it vanishes whenever an integer number of the half-waves fits into either of the dielectric layers. For comparison with Eq. (5.1), this condition is

$$\phi_1 = d_1 n_1 \frac{\omega}{c} = \pi m \quad \text{or} \quad \phi_2 = d_2 n_2 \frac{\omega}{c} = \pi m, \text{ where } m \in \mathbb{Z}. \quad (5.2)$$

Figure 5.3: (a) Reflectance and (b) the imaginary part of the retrieved refractive index for a 1-D PhC, with filling fraction of 15 % in a $300 \mu\text{m}$ unit cell, as a function of frequency and dielectric permittivity. On the right panel, the Fabry-Pérot condition from Eq. (5.2) are marked by a thin dash-dotted line.



Note that unlike the Bragg resonance, this effect can be observed even in a single isolated unit cell; in fact it is the well known *Fabry-Pérot resonance*.

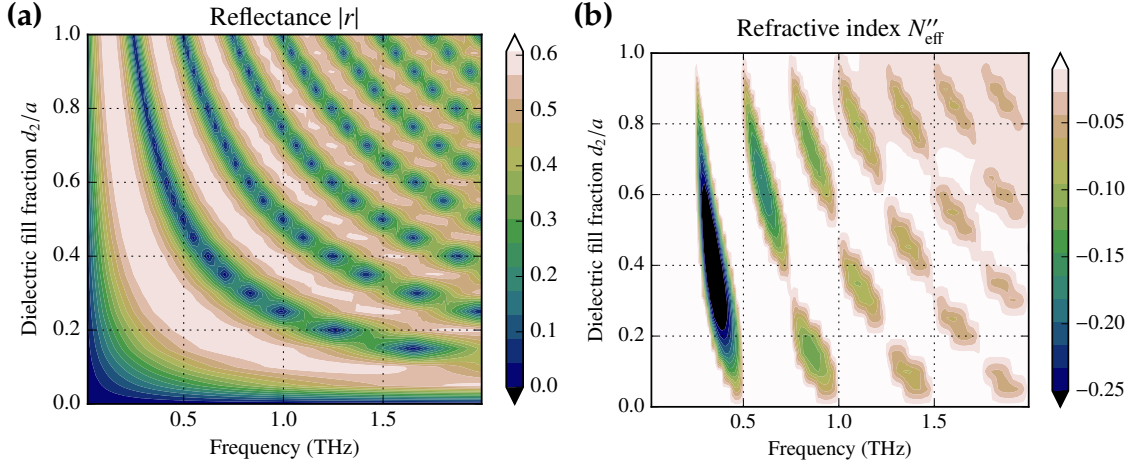
The vicinity of a Fabry-Pérot resonance influences the position and width the neighbouring band gap, which can be found for different values of dielectric permittivity of the slab $\epsilon_r \in \{4, 12, 20\}$ in Fig. 5.2.

As a special case, the conditions for both Bragg and Fabry-Pérot resonances can be fulfilled simultaneously: a *zero-width band gap* results and two photonic bands are adjacent to each other in the same way as they were in vacuum (cf. Fig. 5.1a). In all cases of zero-width PBGs, the dispersion curves appear to approach the boundary of photonic bands (located in a high-symmetry point in the Brillouin zone) as lines with nonzero slope. In analogy with the dispersion of electrons in a solid, this can be viewed as a *Dirac point for photons-polaritons*, where the photons-polaritons have zero effective mass. The corresponding isofrequency contour may have a cusp in this point, invalidating even the generalised notion of the refractive index as elaborated in Section 2.1.3.

An example of a structure that exhibits multiple zero-width band gaps is the 1-D PhC with equal optical thicknesses of both slabs ($d_1 n_1 = d_2 n_2$), but multiple such points exist when the dielectric permittivity or the dielectric filling fraction is changed, as depicted in Figs. 5.3 and 5.4, respectively. These plots are also the simplest examples showing the interplay between the resonances contained in the dielectric structure and the overall band-gap structure, a topic that will be discussed later in more detail.

Local effective parameters of a 1-D PhC Employing the *s-parameter* method based on FDTD simulation, as described in Chapter 3.2.1, one can obtain the scattering parameters (i.e. complex reflectance and transmittance) of a finite layer of the periodic structure, and eventually retrieve its local effective parameters: the index of refrac-

Figure 5.4: (a) Reflectance and (b) the imaginary part of the retrieved refractive index for a 1-D PhC, with a relative dielectric permittivity of 4, as a function of frequency and filling fraction in a $300 \mu\text{m}$ unit cell



tion $N_{\text{eff}}(f)$, impedance $Z_{\text{eff}}(f)$, permittivity $\varepsilon_{\text{eff}}(f)$ and permeability $\mu_{\text{eff}}(f)$. The first one is plotted in Fig. 5.2c, allowing one to clearly identify the Bragg band gaps as regions where N'_{eff} follows one of the Brillouin zone boundaries and $N''_{\text{eff}} < 0$.

To what extent the three remaining local parameters, Z_{eff} , ε_{eff} and μ_{eff} , have any physical meaning? As a generally accepted approach, they will be considered meaningful only for the long wavelength limit, i.e. if K is close to the Γ point in center of the Brillouin zone where the effects of the spatial dispersion should be negligible [191]. According to Fig. 5.2c, this is true for frequencies up to 100 or 200 GHz only.

In the low frequency limit of a 1-D PhC, it was always observed that

1. $Z_{\text{eff}} \approx 1/N_{\text{eff}}$, thus the effective permeability is $\mu_{\text{eff}} = \sqrt{N_{\text{eff}} Z_{\text{eff}}} \approx 1$, corresponding to our expectations for a dielectric structure without internal resonances.
2. The effective permittivity ε_{eff} is the weighted average of the constituent media, which determines the low-frequency limit for the refractive index:

$$N_{\text{eff}}|_{K \ll 2\pi/a} = \sqrt{\varepsilon_{\text{eff}}}|_{K \ll 2\pi/a} \approx \sqrt{\frac{d_1 n_1^2 + d_2 n_2^2}{d_1 + d_2}} \quad (5.3)$$

Notice in Fig. 5.2c that N_{eff} at higher frequencies converges towards its asymptotic value $N_{\text{eff}}|_{K \rightarrow +\infty}$, which differs from the value obtained by Eq. (5.3):

$$N_{\text{eff}}|_{K \rightarrow +\infty} \approx \frac{d_1 n_1 + d_2 n_2}{d_1 + d_2} \quad (5.4)$$

The difference comes from the fact that in the low-frequency limit, the electromagnetic energy concentration is the highest in the areas of higher permittivity, whereas in the high-frequency limit it appears to be distributed evenly. Note that with the

correct branch retrieval procedure, the index of refraction never drops with frequency except for the photonic band gaps. A negative derivative of $N_{\text{eff}}(f)$ would otherwise imply the group velocity to be higher than the phase velocity [24], which was never observed in a 1-D PhC.

5.2 Wire medium

High-frequency behaviour The structure consisting of a regular square lattice of conductive wires exhibits more interesting properties when the electric field is parallel to the wires, and this polarisation will be assumed in the following (Fig. 5.6a). The lattice of wires perpendicular to the electric field does not appreciably interact with the electromagnetic waves, until the wire width is of similar magnitude to their spacing; such a case is discussed in Section 5.9.

In the high-frequency part of the spectrum above the first photonic band, the array of metallic rods in the lattice allows the light to pass through. Each layer scatters a part of the wave in a similar way to that one discussed in the previous section. Thus, the high-frequency interaction of the waves consists of photonic bands alternating with Bragg band gaps. In contrast with the dielectric PhC described above, no Fabry-Pérot resonances are observed and the scattering strength of the wire layers reduces monotonously with growing frequency.

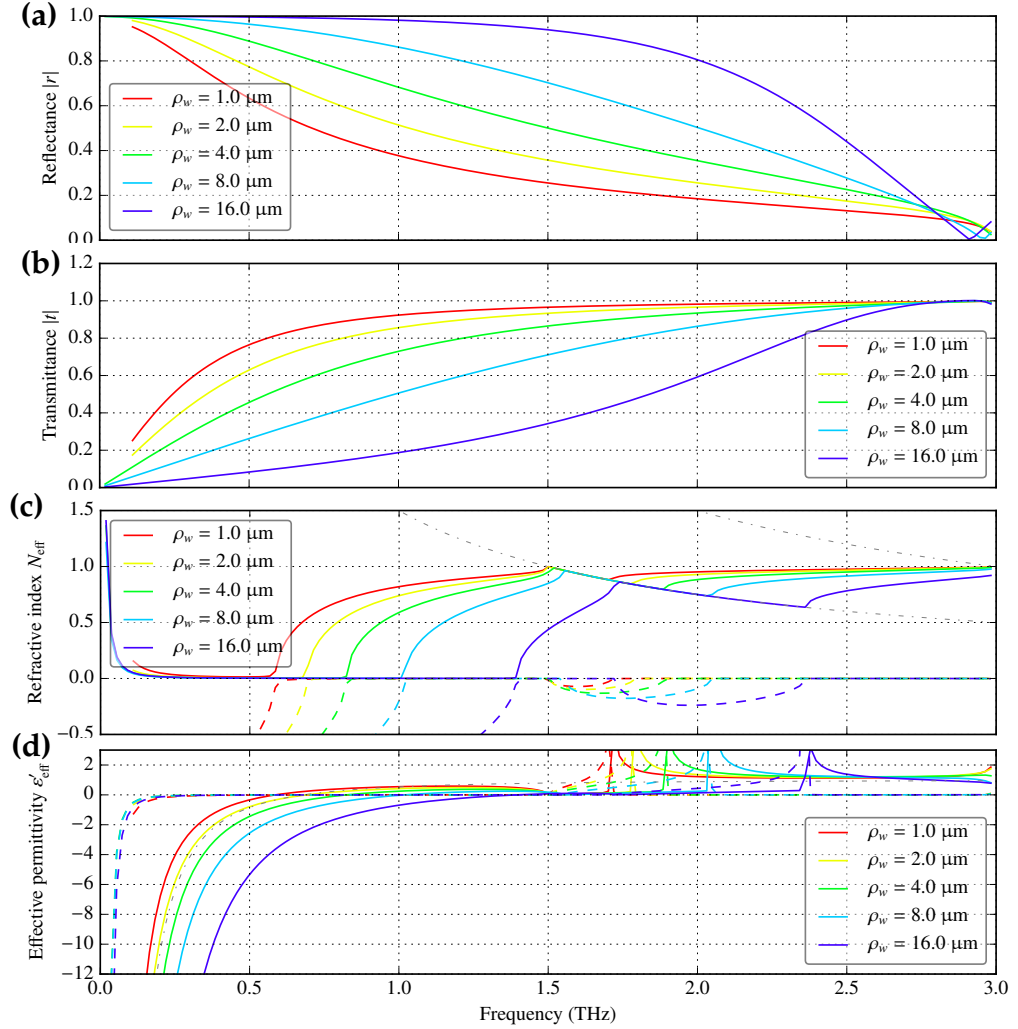
Inductive behaviour at low frequencies At low frequencies, in contrast, the interaction of the conductive wires with the electromagnetic wave becomes very strong and leads to a behaviour completely different from that described above. For a frequency range from zero up to the *effective plasma frequency* f_p , the array exhibits a band gap where N_{eff} is pure imaginary. Therefore, in the low-frequency part of the spectrum, the local effective permittivity ε_{eff} is a physically meaningful quantity and it follows the law typical for inductive media:

$$\varepsilon_{\text{eff}}(f) = 1 - \frac{f^2}{f_p^2} \quad (5.5)$$

Such a dependence of ε_r was already used in the Drude model in Eq. (3.7), and plotted in Fig. 3.4. Owing to this similarity to metals or plasma, wire arrays are denoted also as *diluted metal* or *artificial plasma* since the 1950s [86, 85], or as *metallic delay dielectrics*, owing to the possibility to manipulate the phase and group velocities [87, p. 54].

The physical origin of $\varepsilon_{\text{eff}} < 0$ is different from that in homogeneous metals or plasmas, where it is of *kinetic* origin, i.e., due to the effective mass of electrons [192]. In contrast, the negative effective permittivity in wire arrays is the result of the *self inductance* due to the magnetic field circulating around the conductor. As a result, except for optical frequencies, f_p does not substantially depend on the internal plasma frequency of the constituent metal, and the above described behaviour can be obtained even if the wires are thought to be made of a perfect electric conductor (PEC). The effective plasma frequency f_p does, however, depend on the geometry described by two parameters, the wire radius ρ_w and the unit cell size a .

Figure 5.5: Amplitude of (a) reflectance, (b) transmittance (c) effective index of refraction N_{eff} and (d) effective permittivity ϵ'_{eff} for an array of wires made of gold, depending on the wire radius $\rho_w \in \{1, 2, 4, 8, 16\} \mu\text{m}$ with a fixed unit cell size $a = 100 \mu\text{m}$. The results were obtained by FDTD simulations with a grid resolution of $1 \mu\text{m}$. The results for the effective permittivity have no physical value above the first band gap, in the right half of the plots.



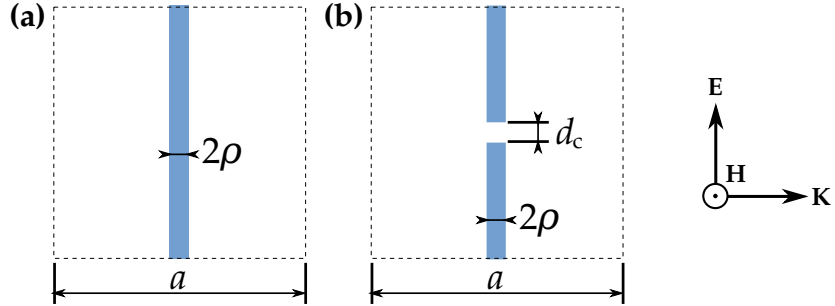
The wires may also be arranged parallel to all three axes, forming a nearly isotropic plasma. Somewhat surprisingly, its behaviour differs depending on whether the wires are interconnected or not [191].

Behaviour close to the effective plasma frequency The dependence of f_p on the wire radius $\rho_w \in \{1, 2, 4, 8, 16\} \mu\text{m}$ is illustrated by the spectra of reflectance, transmittance, refractive index and effective permittivity in Fig. 5.5. The effective plasma frequency f_p can be easily determined as the point where $\epsilon'_{\text{eff}}(f)$ crosses zero in the plot 5.5d. This coincides with the lower edge of the first photonic band in Fig. 5.5c.

At frequencies close to f_p , but slightly higher, the *phase velocity* in nonmagnetic media

$$v_p = \frac{c}{n} = \frac{c}{\sqrt{\epsilon_{\text{eff}}(f)}} \quad (5.6)$$

Figure 5.6: Drawings of one unit cell of (a) the wire array, (b) of the cut wire array. The unit cell is outlined by a dashed line.



is proportional to $(f - f_p)^{-1/2}$ and thus very high. Conversely, the *group velocity* [24]

$$v_g = \frac{c}{n + f \frac{\partial n}{\partial f}} \quad (5.7)$$

vanishes, being proportional to $(f - f_p)^{+1/2}$. Hence the product of the phase and group velocities close to f_p remains nearly constant c^2 , which is a phenomenon commonly encountered also near the *cut-off frequency* of metallic waveguides.

Exactly at $f = f_p$, the wire array medium can support the longitudinal oscillations of the charges, oriented parallel to the wires. They bear a close resemblance to plasmons in bulk media [193].

Notice that for a single cell, the transition from negative to positive permittivity is not accompanied by any obvious spectral feature on the reflectance/transmittance plot. Except for the zero frequency, a layer of wires has always a nonzero transmittance that increases with frequency. Independent of the wire conductivity, it is not possible to build a 100% efficient wire polarizer.

Plasma frequency as a function of wire radius and unit cell size From Fig. 5.5, it can be also deduced that f_p is approximately proportional to the logarithm of ρ_w if $\rho_w \ll a$. This is related to the fact that thicker wires should have a lower self-inductance per unit length. The effect of wire spacing a is the opposite; with a growing, the magnetic field has more space to circulate around the wire and f_p reduces.

Different analytical models were proposed for the description of both effects. The early model by Pendry *et al.* from 1996 [193] works well for thin wires:

$$f_p(\rho_w, a) \approx \sqrt{\frac{c^2}{2\pi a^2 \ln\left(\frac{a}{\rho_w}\right)}}. \quad (5.8)$$

Its refinement by Maslovski *et al.* from 2003 [194] should be valid also for wires with a relatively high filling fraction:

$$f_p(\rho_w, a) \approx \sqrt{\frac{c^2}{2\pi a^2 \ln\left(\frac{a^2}{4\rho_w(a-\rho_w)}\right)}} \quad (5.9)$$

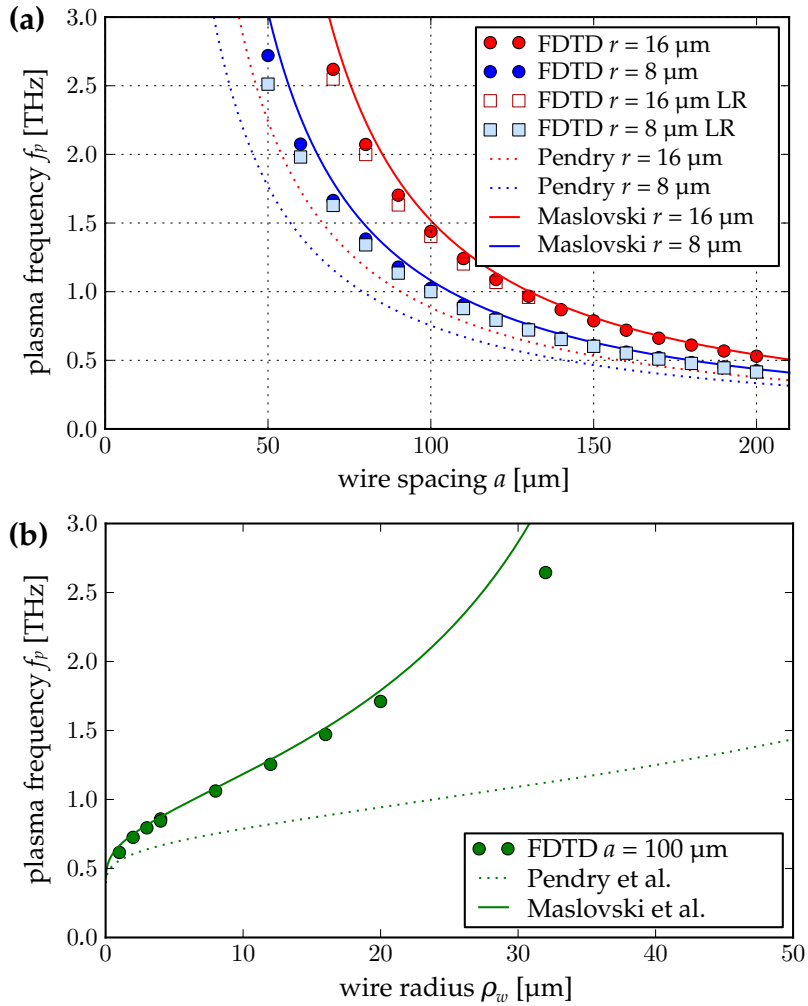


Figure 5.7: Comparison of numerical results (dots) and two analytical models (solid and dotted lines) for plasma frequency f_p of a wire medium: (a) f_p as a function of wire spacing for two different wire radii of $16 \mu m$ and $8 \mu m$ (red and blue curves/dots, respectively). Added for comparison are the empty symbols, correspond to FDTD simulations with significantly reduced resolution (hence marked as "LR"). (b) f_p as a function of wire radius ρ_w .

We ran two series of wire array simulations as a simple verification of the FDTD algorithm against the mentioned analytical models. In the first series plotted in Fig. 5.7a, we kept the wire radius constant $\rho_w = 16 \mu m$, or changed the wire spacing a (red points). We changed the radius to $\rho_w = 8 \mu m$ in the second batch, marked by blue points. For comparison, we plotted the plasma frequency predicted by both analytical models from Eqs. (5.9, 5.8) as full and dotted lines with the color corresponding to the simulation parameters, respectively.

To test the possible error introduced by the FDTD algorithm, we ran the simulation with a different resolution - results with a fine ($1 \mu m$) grid are denoted by full circles, results "LR" with a coarse ($4 \mu m$) grid by empty squares which are located relatively close to the respective high-resolution results.

In the second series of simulations plotted in Fig. 5.7b, we kept the spacing constant as $a = 100 \mu m$ and changed the wire radius r . The analytical model and FDTD simulations give similar results (within 5 %) even for wire radii approaching roughly $a/4$. For thicker wires, the analytical model predicts higher plasma frequency than FDTD. To conclude, the results of the model presented by Maslovski match the FDTD simulations with good accuracy for thin wires (where $r \lesssim a/5$). One possible application of the wire media is in constructing of negative-refractive-

index metamaterials, where a small negative real value of the effective permittivity is desired.

5.3 Cut wires

Individual resonances The low-frequency behaviour of a wire array is determined by the distributed inductance of the wires, which introduces a negative effective permittivity up to the plasma frequency f_p . When the wires are cut in each unit cell as shown in Fig. 5.6b, a three-dimensional periodic lattice of wire segments is formed. Its important parameters are not only the inductance along each antenna, but also the capacitance across the gap between wires. In a direct analogy with a series LC (coil-capacitor) circuit, such antennas exhibit *individual resonances* at some nonzero resonant frequency $0 < f_r < f_p$ when the cut distance d_c is small compared to the unit cell size a .

These resonances couple to the electromagnetic field by means of their electric dipole moments, so they are denoted shortly as *electric resonances*. Still, the magnetic field is essential for the resonance; in fact, the energy is exchanged between the resonant electric and magnetic fields during each quarter-period. The situation partially changes when the unit cell dimensions decrease; at optical frequencies, the energy is exchanged between the electric field and the kinetic energy of the electrons, while the magnetic field circulating around the metallic particle plays a minor role only. Such a regime is known as *plasmonic resonances* and was described by Mie in 1908 [195].

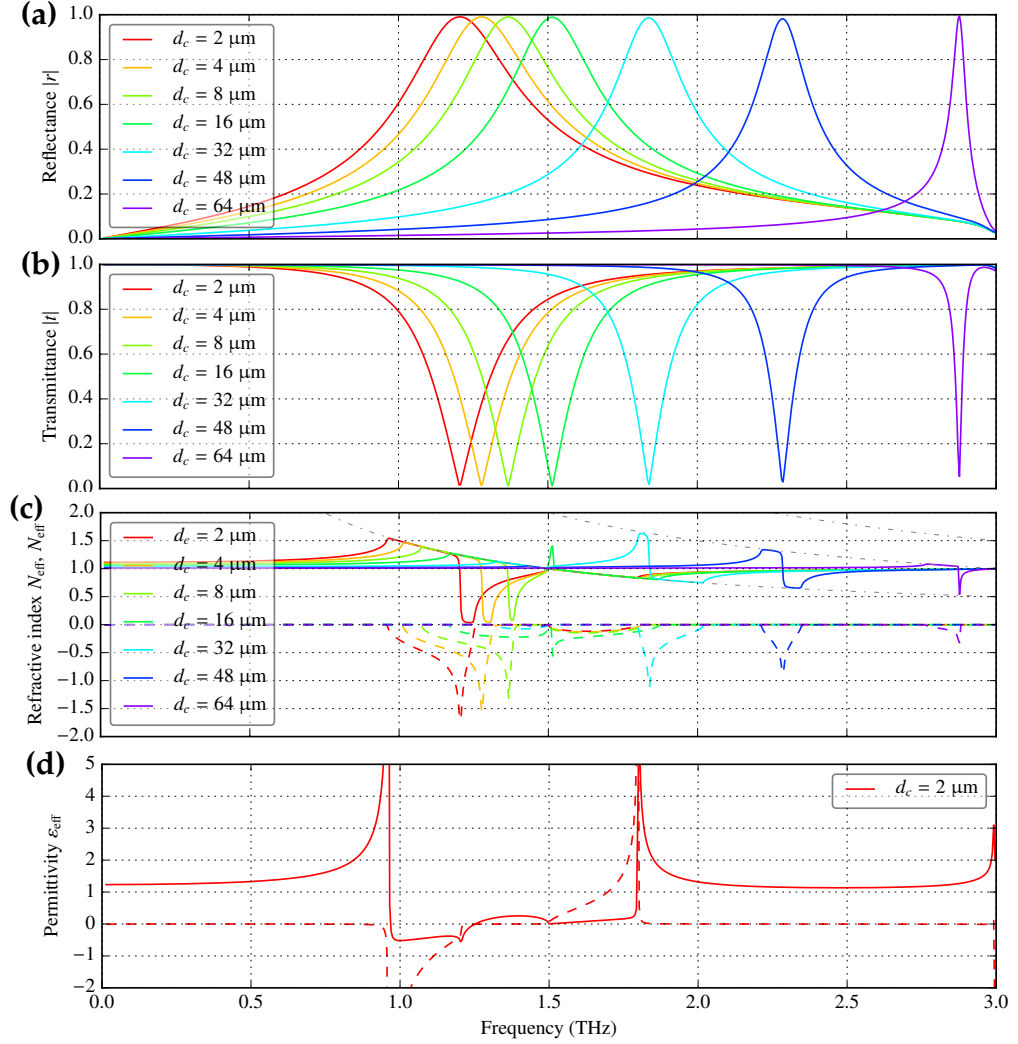
The spectra of cut-wire structures for different cut distances d_c are depicted in Fig. 5.8. Starting with the thinnest wires of $\rho_w = 2 \mu\text{m}$ (red curves), we can identify the individual resonance at frequency close to 1200 GHz where even a single layer of unit cells reflects the whole wave amplitude and the transmittance drops to zero. Towards higher or lower frequencies from the resonance, the transmittance is relatively high.

Dispersion near individual resonances Each individual resonance in a periodic structure forms a characteristic shape in the spectrum of effective index of refraction $N_{\text{eff}}(f)$. The following description will therefore be applicable to individual resonances in other resonant structures, as well.

1. At frequencies under the resonance, the electric dipole of the antenna oscillates in phase with the driving field and the resonance contributes to the effective index of refraction $N'_{\text{eff}}(f)$. The spectrum of a periodic structure with an individual resonance differs from that of a homogeneous medium which was already described by the Lorentzian resonance curve in Fig. 2.2b. At some frequency below the resonance $f \lesssim f_r$, the index of refraction $N'_{\text{eff}}(f)$ becomes high enough to join the closest Brillouin zone boundary which was above it. From this point up to the resonant frequency f_r , $N_{\text{eff}}(f)$ has a nonzero imaginary part, and the medium exhibits a band gap.

Figure 5.8: Amplitude of (a) reflectance, (b) transmittance, (c) effective index of refraction $N_{\text{eff}} = N'_{\text{eff}} + iN''_{\text{eff}}$ for the arrays of cut wires of radius $\rho_w = 1 \mu\text{m}$ made of gold, depending on the cut distance $d_c \in \{2, 4, 8, 16, 32, 64\} \mu\text{m}$. The unit cell is cubic and its size is $a = 100 \mu\text{m}$.

In plot (d), the effective permittivity is illustrated for the thinnest cut distance $d_c = 2 \mu\text{m}$. Although retrieved for the entire spectrum, the local effective parameters have physical meaning only when the wavelength is much larger than a , i.e. roughly from 0 to 500 GHz and from 1220 to 1280 GHz.



- Exactly at the resonant frequency, the interaction of the dipole with the field changes its sign, since above the resonance, the dipole starts to be oriented opposite to the driving field. The real part of the refractive index $N'_{\text{eff}}(f)$ ceases to follow one Brillouin zone and it traverses to another Brillouin zone below it. In local media, individual resonances appear to be the only occasions for $N'_{\text{eff}}(f)$ to traverse downwards.

The imaginary part of the refractive index, $N''_{\text{eff}}(f)$, is required by the Kramers-Kronig relations to exhibit a sharp peak at the resonant frequency, which is superposed over the broader background stemming from the band gap (see Fig. 5.8c).

The spectral width of the transition and peak is inversely proportional to the quality of the resonance. Whenever the structure is built from realistic materials with nonzero losses and its spatial dispersion can be neglected, $N_{\text{eff}}(f)$ is a continuous complex function.

3. The band gap continues up to some frequency $f > f_r$, where another photonic band begins between the same pair of Brillouin zones.

The most important observation is that the resonance curves of $N_{\text{eff}}(f)$ in periodic structures are constrained between the closest two Brillouin zone boundaries, which can be understood as the "floor" and "ceiling" for the dispersion curve. Apparently a single individual resonance cannot shift the transmittance phase by more than π per each layer of unit cells. It can therefore introduce a band of imaginary N_{eff} , but this is not sufficient for N_{eff} to reach negative values. For this, elements with both electric and magnetic dipoles opposite to the driving field have to be combined.

Another observation is that two resonances of the same type, i.e. either both with an electric dipole, or both with a magnetic dipole, cannot be combined into a single wide region of negative effective parameter. This is due to the dipole changing its sign below and above the resonant frequency. Combination of multiple elements of different resonant frequencies thus leads either to multiple separate bands, or to a wide spectral region of high losses.

Effects of the cut distance d_c An increase in the cut distance d_c clearly increases the resonant frequency f_c (see Fig. 5.8). The reason is twofold: for a cut width small relative to the unit cell size, $d_c \ll a$, it is mostly due to a reduced capacitive coupling between the cut wires; for a cut width comparable to unit cell size, $d_c \gtrsim a$, reduction of the cut-wire inductance is more important.

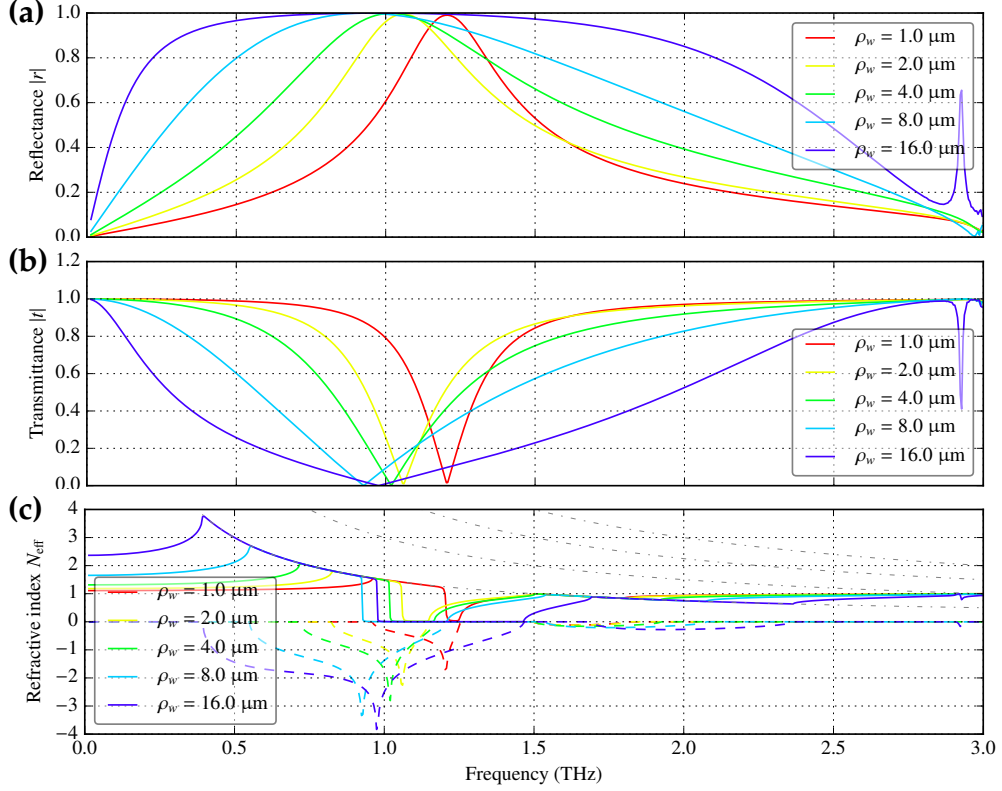
Both the individual and Bragg-type resonances can be identified in the plot for different d_c in Fig. 5.8c. When $d_c \sim 16 \mu\text{m}$, the individual resonance shifts above 1.5 THz and exchanges its order with the Bragg band gap. For $d_c \gtrsim 32 \mu\text{m}$ on, the individual resonances are similar to those for $d_c \sim 2 \mu\text{m}$, but are shifted by one Brillouin zone up.

Effects of the wire radius ρ_w The dependence of the resonant frequency f_c on the wire radius, Fig. 5.9, is somewhat more complicated: For thin enough wires in the $a = 100 \mu\text{m}$ unit cell, the resonant frequency decreases with growing ρ_w , since the inter-wire capacity increases. For high enough ρ_w the opposite mechanism prevails; $f_c(\rho_w)$ then starts growing as a result of reduction of the wire inductance.

While the changes in the cut-wire radius ρ_w relatively weakly influence the resonant frequency, they have a major impact on the *strength* of the individual resonances. Thick wires lead to a stronger reflectance out of resonances, which also reflects itself in the wider band gap in Fig. 5.9c.

Experimental measurement of cut wire spectra Although we did not fabricate any cut-wire metamaterial, we used the terahertz time-domain spectroscopy to

Figure 5.9: Amplitude of (a) reflectance, (b) transmittance and (c) effective index of refraction $N_{\text{eff}} = N'_{\text{eff}} + iN''_{\text{eff}}$ for a metamaterial made of cut wires with radius ρ_w . Cut distance $d_c = 2 \mu\text{m}$, unit cell size $a = 100 \mu\text{m}$ (see Fig. 5.6).

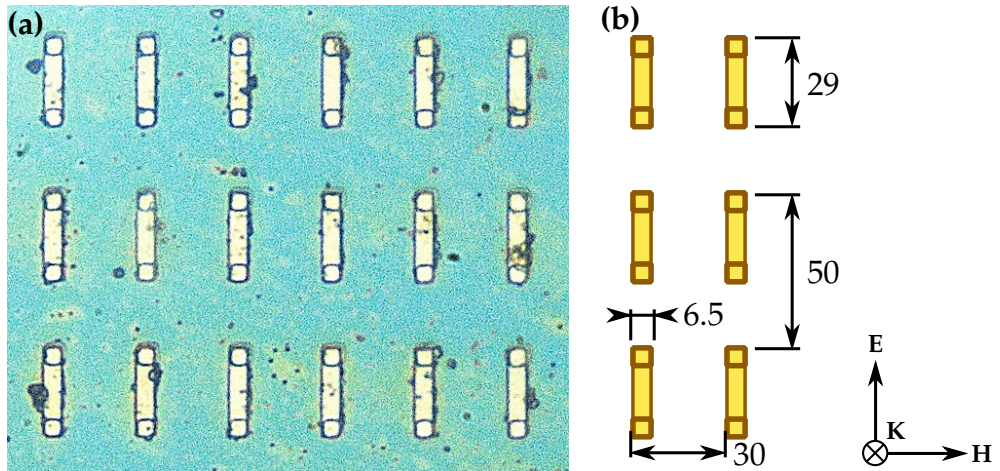


characterise cut-wire-on-silicon structures, one representative of which is photographed and sketched in Fig. 5.10. The metallic wires were deposited on a silicon substrate, and at their ends, the silicon was doped to form diode-like transitions.

This kind of structure was designed to operate as a switch for the terahertz radiation, controlled by the current that flows along the orientation of the wires and modulates the conductivity of semiconductor transitions at the ends of each cut wire. For an unknown reason, the modulation of the terahertz signal was very weak, if any, in all of 7 supplied samples. The only observed kind of systematic modulation manifested itself as a 2.2% drop in amplitude of the transmitted terahertz waveform, and its temporal advance by no more than 18 fs. These values required to feed the structure with a strong modulation signal, dissipating roughly 10 watt peak thermal power.

The sample presented above in Fig. 5.10, though not applicable as a modulator, exhibits a clear electric resonance around 1550 GHz. This resonance is substantially broadened and weakened by the losses of the structure (red line in Fig. 5.11). A FDTD simulation of thin metallic stripes 30 μm long and 6.5 μm wide on a silicon substrate did not match the experimental spectra quite well (green line in Fig. 5.11). A much better match was obtained by simple elongation of the conductive stripes to 40 μm (blue line in Fig. 5.11). This may reflect the fact that the wires were surrounded by highly doped, conductive zones of silicon. Although not taking into

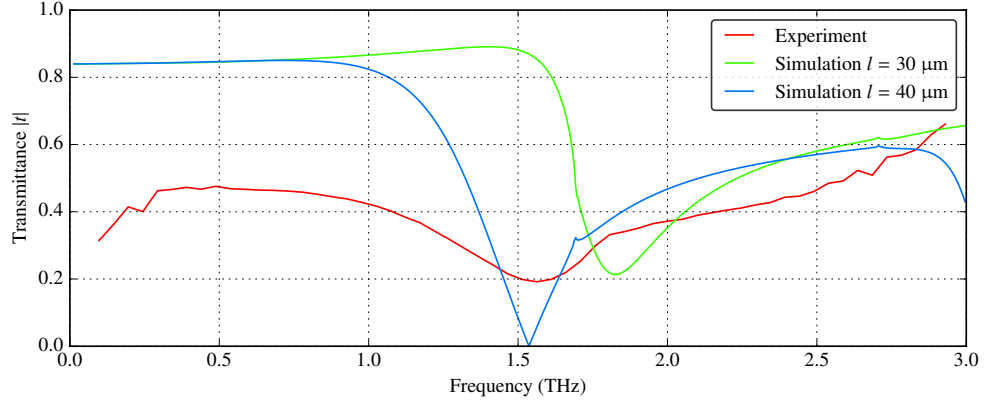
Figure 5.10: The sample of cut wires (pale yellow) on silicon (cyan) substrate. (a) Natural-colour photograph from an optical microscope, (b) Geometry of the wires in micrometres. They were measured to be 6.5 μm wide and 30 μm long. The periodicity of cut-wires was $30 \times 50 \mu\text{m}$.



account the dissipative losses, such a simulation identifies correctly the resonance frequency of the stripes. It also, at least quantitatively, matches the asymmetric spectral shape, which is caused by the onset of diffraction into the silicon substrate at $f_c = c/(50 \mu\text{m})/N_{\text{Si}} \approx 1730 \text{ GHz}$.

The presented simulations were not optimized for the dissipative losses in silicon, which could be modelled with more detailed knowledge of the structure preparation.

Figure 5.11: Comparison of experimental (red line) and simulated transmittance spectra (green and blue lines) of the cut-wire array on a silicon substrate. The green line corresponds to the original geometry from Fig. 5.10b; a better match with the experiment is obtained by changing the length of stripes from 30 to 40 μm (blue line).



5.4 Split-ring resonator

Resonances with magnetic dipole moment The fundamental resonance in a cut wire has an electric dipole moment only. The resonant magnetic field circulates around the wire and due to its rotational symmetry along the x -axis, the magnetic dipole moment is zero. Other structures can support resonances without symmetry with regard to the x -axis, thus having a magnetic dipole moment.

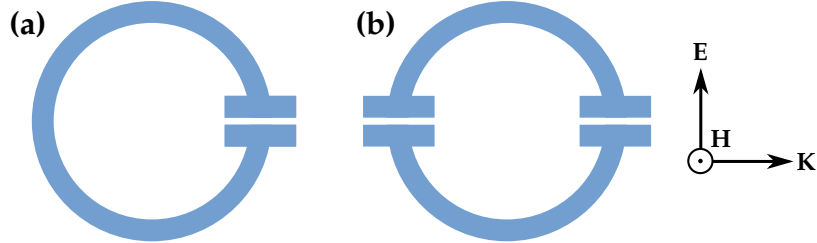
One of the simplest examples is formed by bending a wire into a "C"-shaped *split-ring resonator* (SRR). To reduce the resonant frequency without changing the SRR diameter, capacitor pads can be added to the cut, as shown in a side view in Fig. 5.12a. The first resonance in its spectrum has a dominant magnetic dipole moment, and it will be denoted simply as the *magnetic resonance*. The electric current flows through the wire along a circular path, while the magnetic field has a toroidal shape around the wire.

The very concept of SRR is at least as old as the Hertz's experiments with the spark-gap transmitter from the 1880s. As described in the historical review of Ref. [196, pp. 120–126], first SRR arrays were built in the early 1980s with the aim to build an effective medium with highly lossy complex permeability; a decade later asymmetric SRRs were used to achieve strong bianisotropy. Many publications cite Refs. [90, 92] from Pendry et al. as the first application of SRR array for achieving negative effective permeability and index of refraction, respectively. Since then, the number of SRR-related publications has grown rapidly.

Symmetry of the split ring resonator The orientation of the splitting in the SRR determines the possible coupling between its electric and magnetic dipoles. In particular, when the splitting is on the front or rear side of the ring relative to the direction of wave propagation, the predominantly magnetic resonance creates also a weak electric dipole, leading to optical activity [197].

Simultaneously, it precludes to use the common homogenisation approaches,

Figure 5.12: Variants of the split-ring resonators, viewed from the side perpendicular to the magnetic field: (a) classical SRR with low symmetry, (b) symmetric SRR with two splits.



since the scattering parameters retrieval method assumes that the structure is symmetric along the axis of wave propagation, i.e., that its reflectance is equal from both sides. Asymmetric structures therefore have properties that cannot be matched by any (reciprocal) homogeneous medium.

The symmetry is restored again by considering a *symmetric split ring resonator* (sSRR), depicted in Fig. 5.12b, which has two splittings at opposing position on the ring. This is documented by the results in Fig. 5.14. The SRR with a single splitting is represented by red lines; while its magnitude of reflectance and transmittance in the plots 5.14a,b appear similar to these of a cut wire, the computation of the refractive index yields a spectrum (in panel 5.14c) which has no reasonable interpretation near the resonance at 500 GHz and above it.

The symmetric resonator is represented by green curves. In Fig. 5.14c, the refractive index follows a resonance pattern that was already described on the example of the cut wires: the curve rises up to the upper Brillouin zone boundary, follows it for a span of frequencies, drops to the Brillouin zone boundary below, follows it again and then a next band starts.

At higher frequencies, outside the range of Fig. 5.14, the SRR exhibits also an electric resonance where the current flows symmetrically along both its arms. It is assumed that any structure should support an infinite number of resonances, of which only the lowest few are usually of practical interest.

Antiresonances in local effective parameters In the case of symmetric split-ring resonators, the first resonance possesses only the magnetic dipole moment, as follows from the symmetry of the resonant fields. This fact implies a strong resonant behaviour of the permeability $\mu_{\text{eff}}(f)$ (green curve in Fig. 5.14e, between 600 and 700 GHz).

The permittivity spectrum $\varepsilon_{\text{eff}}(f)$ is, however, also affected by the magnetic dipole resonance (Fig. 5.14d). The impact of the magnetic resonance on $\varepsilon_{\text{eff}}(f)$ is several times weaker than on $\mu_{\text{eff}}(f)$, and more importantly, it has the opposite sign: The real part of $\varepsilon'_{\text{eff}}(f)$ is reduced at frequencies below the resonance, and enhanced above it. Simultaneously, in the chosen $e^{i\omega t}$ convention, the positive sign of the imaginary part $\varepsilon''_{\text{eff}}(f)$ would imply an amplification of the electric field oscillating around 650 GHz, which is impossible in a structure composed of lossy materials only. This feature in the spectrum is sometimes described as an *antiresonance* and

has incited much discussion in the literature [106, 107].

Physical relevance of effective parameters in their local approximation We believe that the influence of a magnetic resonance on $\varepsilon_{\text{eff}}(f)$, or conversely, of an electric resonance of $\mu_{\text{eff}}(f)$, is a mere artifact of approximating a strongly nonlocal structure with a concept of local effective parameters. It can be shown that antiresonances become stronger at higher frequencies, as the wavelength $2\pi/K$ becomes similar to the unit cell size a . In Ref. [107], it is argued that

the periodicity cannot . . . be the only explanation since qualitatively similar antiresonances have been reported using the measured data for a disordered high permittivity composite.

The true origin of antiresonances and other deviations of $\varepsilon_{\text{eff}}(f)$ and $\mu_{\text{eff}}(f)$ from the Lorentzian resonance curve can however be attributed to the presence of photonic band gaps and nonlocal response of the structure. These effects are, to some extent, maintained also under randomizing the unit cell positions [109], and there is probably no need to seek for another explanation.

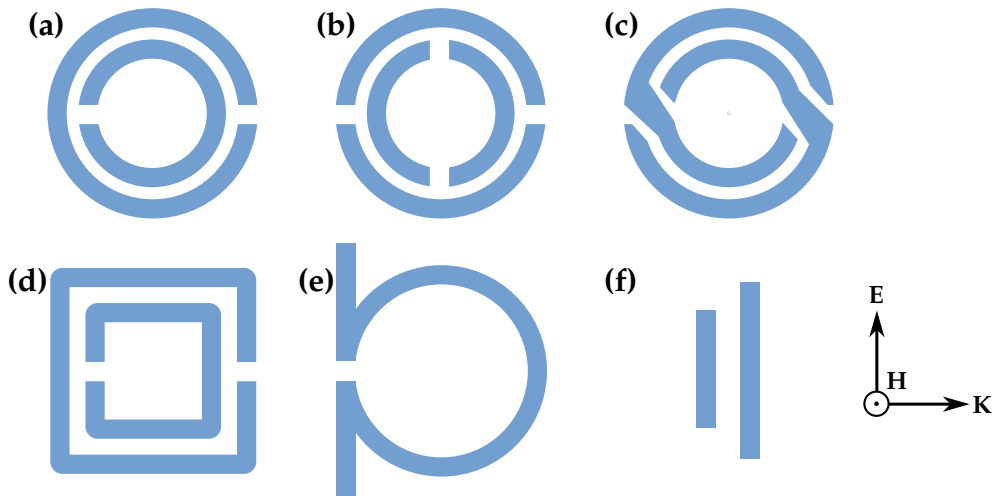
Comparison of the s-parameters method and current-driven homogenisation With local effective parameters $\varepsilon_{\text{eff}}(f)$ and $\mu_{\text{eff}}(f)$ appearing to lose their physical meaning in a frequency range near a resonance, the question remains to what extent the dispersion curves, or equivalently, the spectrum of effective index of refraction $N_{\text{eff}}(f)$ are applicable. While the Bloch's theorem in Eq. (2.60) suggests that the dispersion curves for the Bloch's wavevector \mathbf{K} can be determined for any periodic structure, the s-parameter method might return invalid values.

Dispersion curves obtained by the s-parameters method and by the current-driven homogenisation (CDH) are compared in Fig. 5.15. Although these methods are fundamentally different, their results overlap, and thus one can assume that the array of symmetric split-ring resonators can be treated as homogeneous with a well-defined index of refraction $N_{\text{eff}}(f)$ for the Bloch's wave over the whole spectrum. Its local effective parameters $\varepsilon_{\text{eff}}(f)$ and $\mu_{\text{eff}}(f)$, however, seem to have no useful physical interpretation near the resonances, where the Bloch's wavelength is similar to the unit cell size. They remain useful farther from the resonance, though.

Variants of split-ring resonators Diverse metamaterial designs based on the SRR principle were developed. Many SRR designs involve a smaller ring nested inside the original one, as shown in Fig. 5.13a,b in the asymmetric and symmetric variants. The long narrow gap between the inner and outer split rings enhances their capacitive coupling. In this way, the frequency of the magnetic resonance can be reduced without increasing the overall SRR dimensions. Such designs usually do not need capacitor pads, and can be made by etching or microlithography.

A modification of this *double split-ring* design includes a cross-connection between the inner and outer conductors as in Fig. 5.13c; this version breaks the mirror symmetry, but restores the central symmetry. Such resonators can be attached to each side of the unit cell, forming a nearly-isotropic, three-dimensional metamaterial [197]. However, some highly symmetric structures that eliminate anisotropy

Figure 5.13: Other variants of split-ring resonators: (a) double SRR, (b) symmetric version thereof, (c) double SRR with cross-connection between the inner and outer rings, (d) illustration of a square variant of the double SRR, (e) "omega" structure aimed to introduce $N'_{\text{eff}} < 0$, (f) cut-wire pair



still enable near-field coupling between the electric and magnetic fields; this effect is sometimes denoted as *bi-isotropy* [198].

The square "ring" resonator (Fig. 5.13d) is also widely used, without any substantial difference from the round SRR.

The *omega structure* was designed to emulate the operation of a SRR and a wire simultaneously [199, pp. 62–72], by interconnecting the ends of a SRR along the x -axis (Fig. 5.13e).

All SRR structures in Fig. 5.13 can be made flat in the plane perpendicular to the magnetic field, which facilitates their fabrication. At terahertz and higher frequencies, using a thin metal film should not be much detrimental to the SRR conductivity, since the skin depth caused by eddy currents is often submicroscopic [200].

A similar way of operation is achieved by structures which extend infinitely in the direction of the magnetic field of the incident wave. This allows one to fabricate magnetic resonators by rolling stripes of a semi-metallised plastic foil, producing a *swiss-roll* metamaterial [200], or by partially sputter-coating a polymer fibre by a metal [201]. Such structures however seem to exhibit relatively high losses when applied above the microwave range.

The metallic *cut-wire pair*, or also *strip pair*, metamaterial depicted in Fig. 5.13f, was designed for operation in the infrared or optical range. It can be understood as a split-ring resonator flattened along the direction of the wave vector. The geometry is tuned so that the electric and magnetic resonances overlap.

At the radio frequency range up to 100s MHz, each split-ring resonator can be connected to a small electric circuit which may provide gain [202] in the metamaterial. The effective parameter spectra of such an active metamaterial do not have to conform to the Kramers-Kronig relations anymore, since the spectrum of the medium response may acquire any sign of its imaginary part.

SRR in a wire array The analysis of the wire arrays has shown that at low frequencies, their effective permittivity is physically valid and has a negative value. Likewise, the symmetric SRRs have a region in the spectrum above its magnetic resonance where the effective permeability is negative, too.

A combination of these two structures yields a region of negative index of refraction, probably the first [92] and most prominent metamaterial design to achieve this. The possibility of combining structures that interact exclusively with magnetic and electric field is nontrivial, discussed in more detail e.g. Refs. [203, 204].

The resulting effective parameters are represented by the blue line in Fig. 5.14. Its spectrum of the effective index of refraction resembles that of the wire array up to 630 GHz, where it drops by one Brillouin zone down at the resonant frequency. As a rule, a single individual resonance always causes $N'_{\text{eff}}(f)$ to drop from one Brillouin zone boundary to another, which should be observed in all correctly retrieved spectra.

Notice that the magnetic resonances cause a drop in $N'_{\text{eff}}(f)$ even without the wire array (green curve in Fig. 5.14c), but in such a case it happens between the first Brillouin zone boundary and zero. Without wires, N'_{eff} does not reach negative values.

By contrast, a magnetic resonance in the combined SRR-wire structure introduces a narrow region, still within the photonic band gap, where the index of refraction follows the *minus-first* Brillouin zone boundary:

$$N_{\text{eff}}(f) = - \frac{c}{2af}, \quad (5.10)$$

with a being the unit cell size. This means that the whole photonic band spanning from 635 to 670 GHz has $N'_{\text{eff}} < 0$. The effective permittivity and permeability with physical meaning can be retrieved only when N'_{eff} comes close to zero, roughly from 650 to 670 GHz. Then they are correctly retrieved as both negative, as can be indeed seen in Figs. 5.14d,e (blue lines).

Fano resonance The spectrum of reflectance magnitude $|r(f)|$ for the sSRR-wire structure (blue line in Fig. 5.14a) has a relatively complex shape – starting from a high reflectance introduced by the wire array, it rises below the magnetic resonance, then it drops to zero around 660 GHz, and it rises until its local maximum on 750 GHz is reached. The resonance profile differs significantly from the arguably simpler spectrum of the cut wires (Figs. 5.8a and 5.9a), where the resonance was accompanied by a single peak in reflectance. The reason is in that with the sSRR-wire structure, $|r(f)|$ is a linear superposition of the wave scattered by the interaction of the structure with the electric dipole, which has a relatively large amplitude $r_1(f)$ over broad spectral range, and another wave $r_2(f)$ scattered by the magnetic dipole of the split-ring which is prominent only close to its magnetic resonance, between 550 and 750 GHz.

Both scattered components, $r_1(f)$ and $r_2(f)$, are complex functions. The phase of the wave scattered by a resonant element differs almost by π when f is below and above the resonance. The impact on the plot of the overall reflectance is in a change from a constructive to destructive interference between the two components.

Such typical spectral features, observed whenever a narrower resonance overlaps with another broader one, are known as *Fano resonances*, and can be found on most following plots of $|r(f)|$ or $|t(f)|$. The Fano spectral profile comes from a natural interference between waves scattered by different mechanisms: whenever the spectrum of a structure close to a magnetic dipole resonance does not fall into the class of possible Fano resonance profiles, it suggests the homogenisation has failed. For an example of such an error, see the spectra of the asymmetric SRR in Fig. 5.14.

Figure 5.14: Spectra obtained by simulations of THz waves incident on three different structures: the asymmetric SRR with split width $d = 4 \mu\text{m}$ (red curves), its symmetric variant sSRR (double split width $d = 2 \mu\text{m}$) and the same sSRR with wire grid added (blue curves). (a) Amplitude of reflectance, (b) amplitude of transmittance, (c) effective index of refraction, (d) effective permittivity ϵ_{eff} and (e) effective permeability μ_{eff} . Note that in panels (c)-(e), the dispersion curves nor effective parameters for the asymmetric SRR could not be determined by the scattering parameters method. In all cases, the outer ring radius was $\rho = 30 \mu\text{m}$, conductor cross-section $\Delta\rho = 6 \mu\text{m}$ and unit cell size $a = 100 \mu\text{m}$.

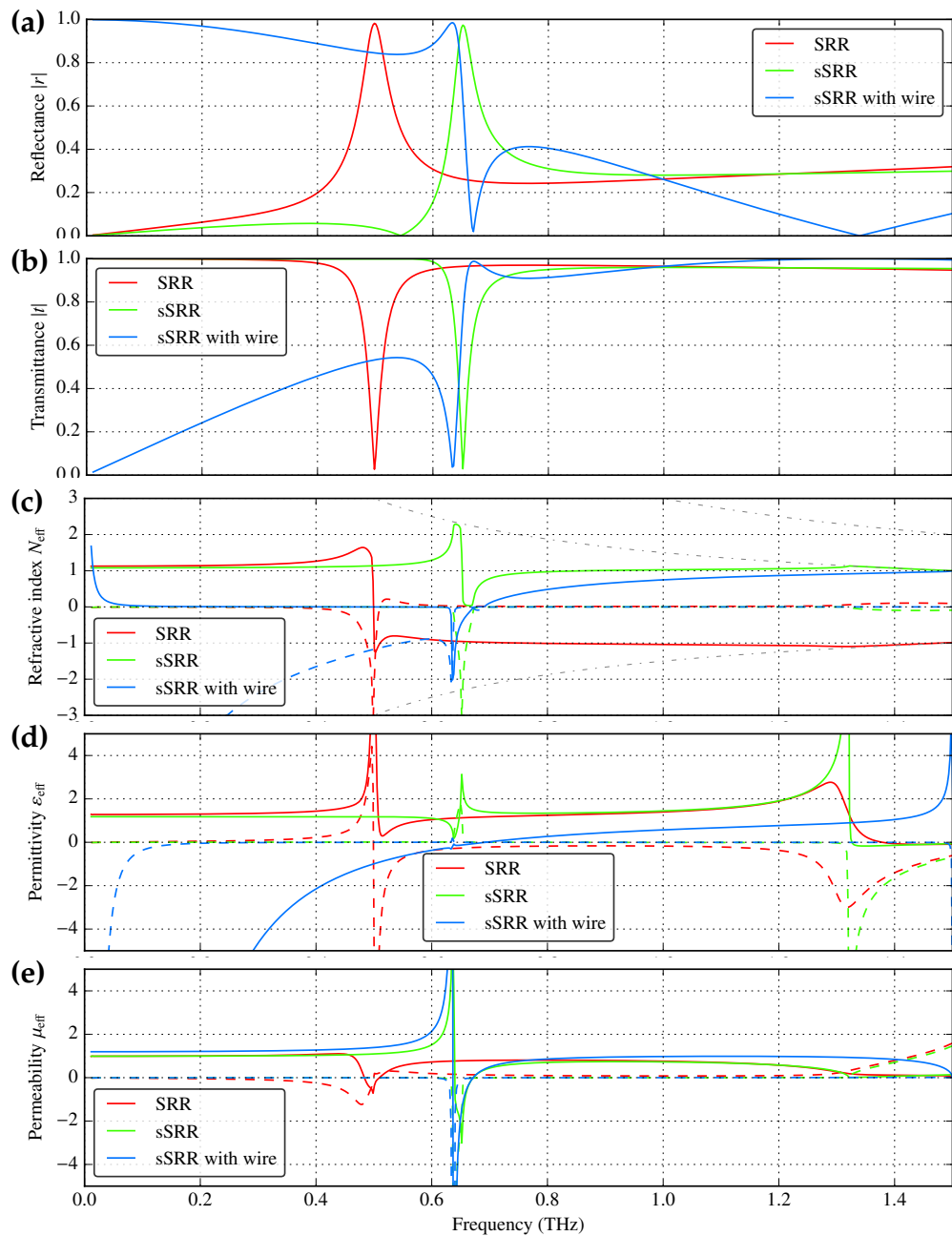
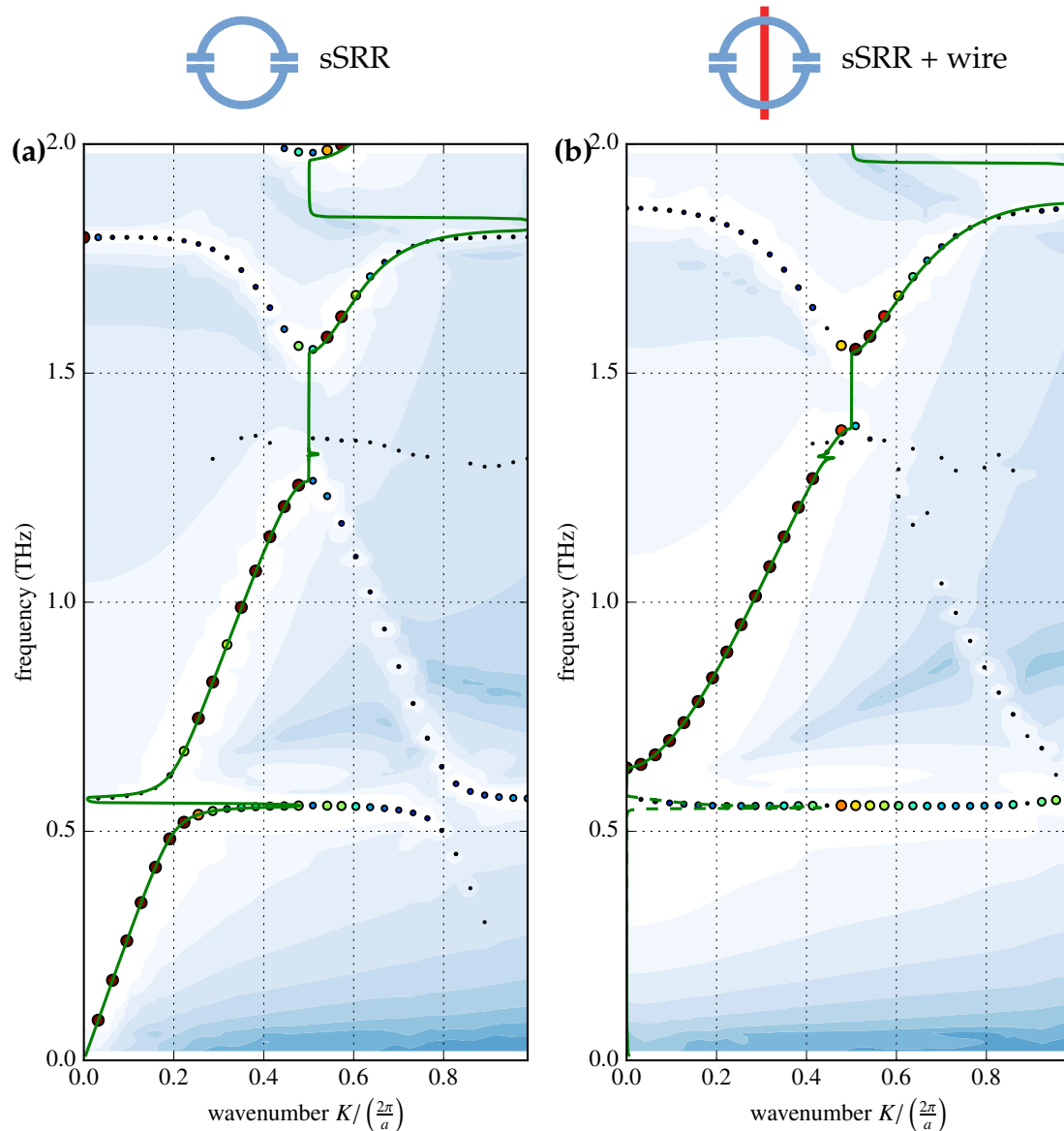


Figure 5.15: Current-driven homogenisation results, shown as bubbles, indicating the dispersion curves for (a) a symmetric split-ring resonator and (b) the same with a wire mesh. The area of each bubble corresponds to the relative amplitude of the respective harmonic component at the given frequency, as detected by the FDM algorithm; the blue shading on the background denotes the amplitude of the excited electric field as computed directly by Fourier transform.

The results of the scattering-parameters method are overlaid as green lines; these show the same data as the green and blue solid lines from Fig. 5.14c.

To save plotting space, in the right panel, the negative-index range of frequencies between 630 and 670 GHz was mirrored against the $K = 0$ vertical axis and plotted by a dashed green line.

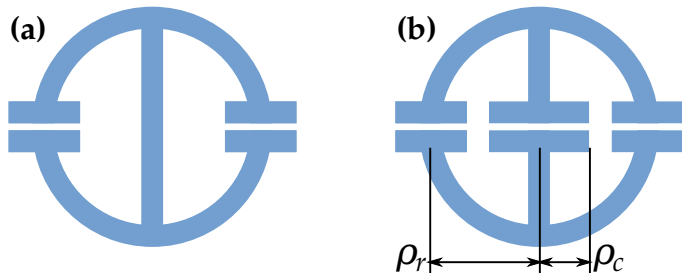


5.5 Combined electric and magnetic resonator

Effect of the central bar in SRR In contrast to all previously discussed structures, the fundamental resonance of a split-ring resonator (SRR) couples to the field through a magnetic dipole and the electric current flows around the circumference of the SRR. Therefore, the frequency of the magnetic resonance does not change significantly even when central bar parallel to the incident electric field is added (see Fig. 5.16a). From the symmetry of the resonant fields it follows that in the magnetic resonance zero current flows through the central bar.

However, a new electric resonance (Fig. 5.17b) is introduced by adding the bar, characterized by a current flowing through the central bar antiparallel to that conducted through the outer SRR arms. Simulations have shown that the corresponding frequency is lower compared to the original parallel electric resonance (Fig. 5.17c), and similar to the frequency of the magnetic resonance (Fig. 5.17a).

Figure 5.16: (a) A modification of a split-ring resonator with a central bar, (b) a similar structure where the central bar was split by another circular capacitor with a radius ρ_c , allowing to tune the antiparallel electric resonance



Tuning the frequency of the antiparallel electric resonance The spectra of cut wires (Fig. 5.8) suggest that each electric resonance, unless it is preceded by a Bragg band gap, or excessively lossy, introduces a region in the spectrum where the local effective permittivity has a physically meaningful and negative value. Under the same conditions, the magnetic resonance introduces a region of $\mu_{\text{eff}}(f) < 0$.

Figure 5.17: Three low-frequency resonances in the combined SRRs: (a) magnetic resonance, (b) antiparallel electric resonance, (c) parallel electric resonance.

The actual order of the first two resonances in the spectrum is determined by the inner capacitor radius ρ_c and other parameters of the resonator.

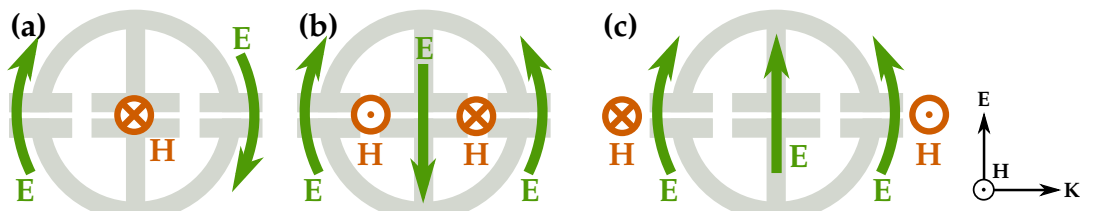
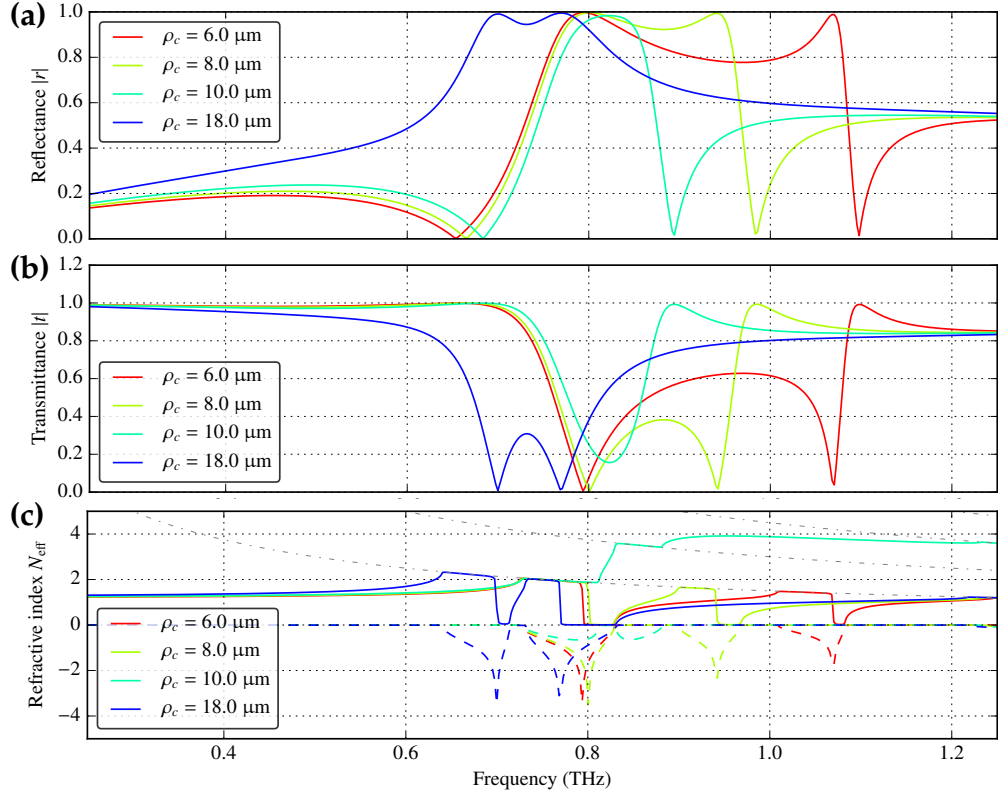


Figure 5.18: Simulated spectra of the electric-magnetic resonators shown in Fig. 5.16: amplitude of (a) reflectance, (b) transmittance and (c) effective index of refraction $N_{\text{eff}} = N'_{\text{eff}} + iN''_{\text{eff}}$. The frequency of the electric resonance is tuned by the series capacitor radius ρ_c on the central bar.

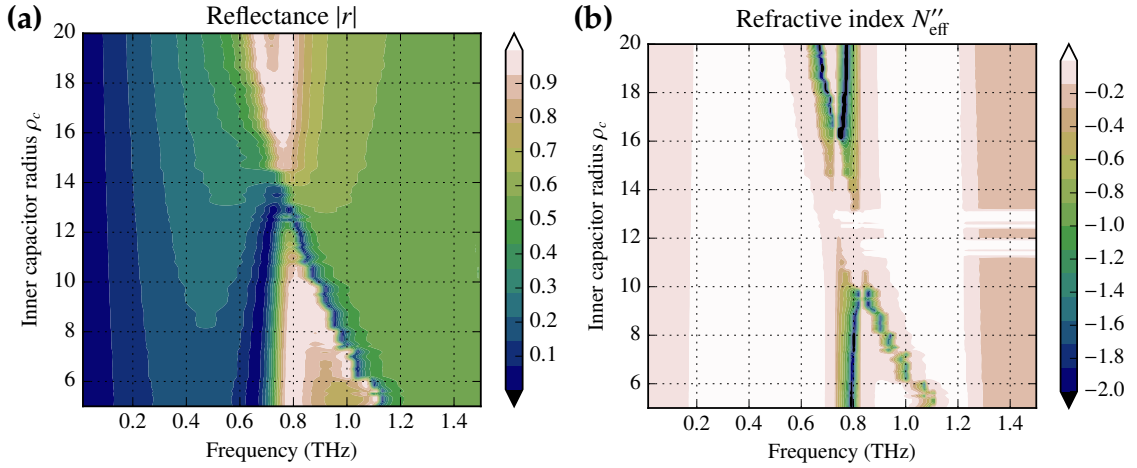


By optimizing the structure geometry, the resonances can be tuned against each other so that the regions of $\varepsilon_{\text{eff}}(f) < 0$ and $\mu_{\text{eff}}(f) < 0$ overlap. This is the conventional approach to design a metamaterial with a negative index of refraction; applying it to the electro-magnetic resonator leads to an array of independent, separate elements, which may be an advantage over embedding SRRs in a wire array. One of the means of tuning the frequency of the antiparallel electric resonance is to divide the central bar by an *inner* capacitor as shown in Fig. 5.16b.

If the inner capacitor is relatively small, with inner capacitor radius $\rho_c = 6 \mu\text{m}$, the electric resonance is located around 1150 GHz, and it shifts down to 940 GHz when ρ_c is increased to 8 μm. By contrast, the magnetic resonance is virtually independent of ρ_c and remains close to 800 GHz. Both individual resonances can be identified clearly in the spectra by the points of zero transmittance and by the corresponding steep, but still continuous, drops in the refractive index (red and light green curves in Fig. 5.18). For $\rho_c \leq 8 \mu\text{m}$, the resonances are separated by a photonic band, indicating that the regions of $\varepsilon_{\text{eff}}(f) < 0$ and $\mu_{\text{eff}}(f) < 0$ do not overlap.

However an attempt to reduce the frequency of the electric resonance further, in order to obtain negative index of refraction $N'_{\text{eff}} < 0$ in the region of overlap, leads to confusing results (cyan curves in Fig. 5.18). For $\rho_c \in \langle 10, 16 \rangle \mu\text{m}$, the scattering parameters method retrieves apparently erroneous spectra with two distinct band gaps, but without any individual resonance. A more detailed parametric scan

Figure 5.19: (a) Reflectance and (b) the imaginary part of the refractive index of the electromagnetic split-ring resonator, retrieved by the scattering parameters method,



through these problematic values of ρ_c can be found in Fig. 5.19.

The effective parameters retrieved by the s-parameters method become easy to interpret for $\rho_c \geq 18 \mu\text{m}$. The antiparallel resonance at 690 GHz is again well separated from the magnetic one, which remains near its original frequency (dark blue curves in Fig. 5.18). Further explanation of these results is beyond the capabilities of the scattering parameters method, and it necessitates the more expensive computational approach using the current-driven homogenisation (CDH) method.

Current-driven homogenisation and spatial dispersion CDH results for the same structure parameters, $\rho_c \in \{6, 8, 10, 18\} \mu\text{m}$ are presented in Figs. 5.20 and 5.21. For comparison, the dispersion curves corresponding to the $N'_{\text{eff}}(f)$ retrieved by the scattering parameters method are shown by green lines.

For $\rho_c = 6 \mu\text{m}$, both retrieval methods yield relatively similar results, and they identify correctly two indirect band gaps, the first of which corresponds to the magnetic resonance, and the second to the antiparallel electric one. The match is not as good as in Fig. 5.15, though. Namely the magnetic resonance around 800 GHz appears somewhat wider when retrieved by the s-parameters method, compared to CDH. The deviation can be attributed to the structure being surrounded by vacuum instead of sensing the near fields of the surrounding cells (cf. page 98).

The value of $\rho_c = 8 \mu\text{m}$ used for the right panel of Fig. 5.20 was not chosen randomly, since for this inner capacitor radius, the spatial dispersion starts to affect substantially the dispersion curve of the second photonic band. It starts in the Γ point at 794 GHz with a positive group velocity and reaches its maximum of 890 GHz, but with growing K , the group velocity changes its sign and the band ends in the X point at ca. 887 GHz. At a given frequency between 887 and 890 GHz, two solutions of the wave equation exist that differ merely by the wavevector. The s-parameters method has no means of distinguishing them, and accordingly, the retrieved dispersion curve deviates from that retrieved by CDH.

The spatial dispersion is even more evident in Fig. 5.21, where the frequen-

cies of the second photonic band in the Γ and X points come close to each other, amounting to 784 and 795 GHz, respectively. The central maximum of the band is on 828 GHz, which explains why the s-parameters method no longer correctly determines the dispersion curve shape, nor it identifies any of the resonances.

These issues persist until $\rho_c \geq 18 \mu\text{m}$, when the second photonic band becomes a relatively flat function of the wavenumber K . Both resonances are then retrieved correctly again, except for a systematic error in the frequency determination which may arise from the already discussed difference in the simulation geometry used by the s-parameters method.

Is this a negative-refraction structure? The electro-magnetic resonator was examined as an example structure which, particularly in its magnetic resonance, exhibits a strong electric quadrupole moment, leading to a prominent spatial dispersion. Figures 5.20 and 5.21 illustrated that not only the s-parameters retrieval algorithm fails, but also the very idea of describing the structure behaviour in terms of refractive index $N_{\text{eff}}(f)$ cannot describe all dispersion curves observed the physical reality. A similar failure of the s-parameters method in homogenisation of an array of SRRs in a wire lattice was reported previously, [132], showing that $N_{\text{eff}}(f)$ can be determined only for a relatively big spacing between the metallic elements.

For particular values of the inner capacitor radius $\rho_c \in \langle 8, 16 \rangle \mu\text{m}$, the second photonic band supports simultaneously a wave of group velocity collinear with the phase velocity, and an *additional wave* with a higher wavenumber and opposite direction of these velocities.

The interface of this metamaterial with vacuum should exhibit negative refraction, provided the auxiliary boundary conditions are arranged to couple all energy exclusively to the described additional wave with a relatively high Bloch's wavevector. In any other case, the single-valued index of refraction is not sufficient for description of this kind of metamaterial – even for propagation nearly parallel to the optical axis.

Figure 5.20: Current-driven homogenisation results for the combined electric-magnetic resonator, differing by the inner capacitor radius (a) $\rho_c = 6 \mu\text{m}$, (b) $\rho_c = 8 \mu\text{m}$.

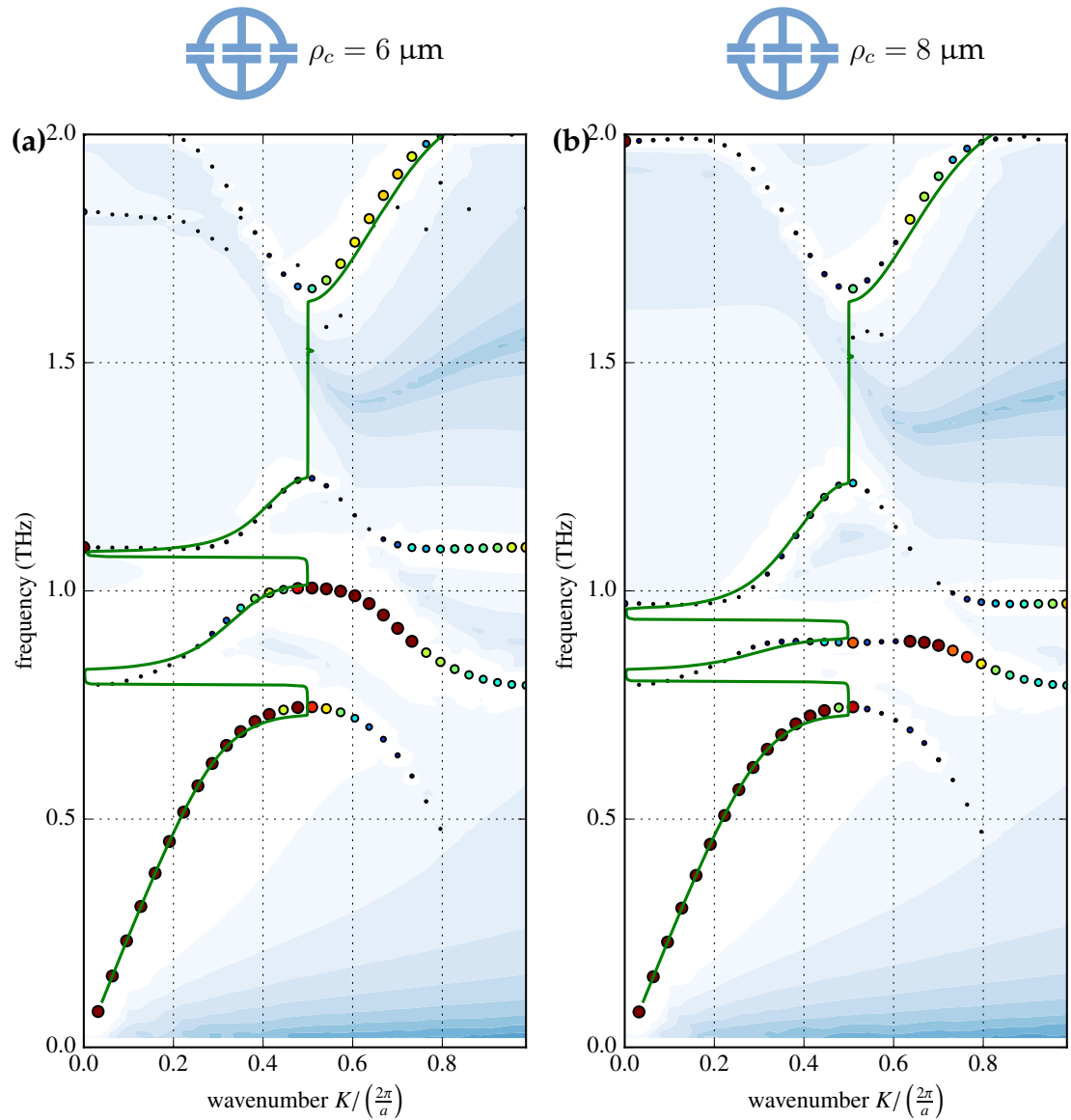
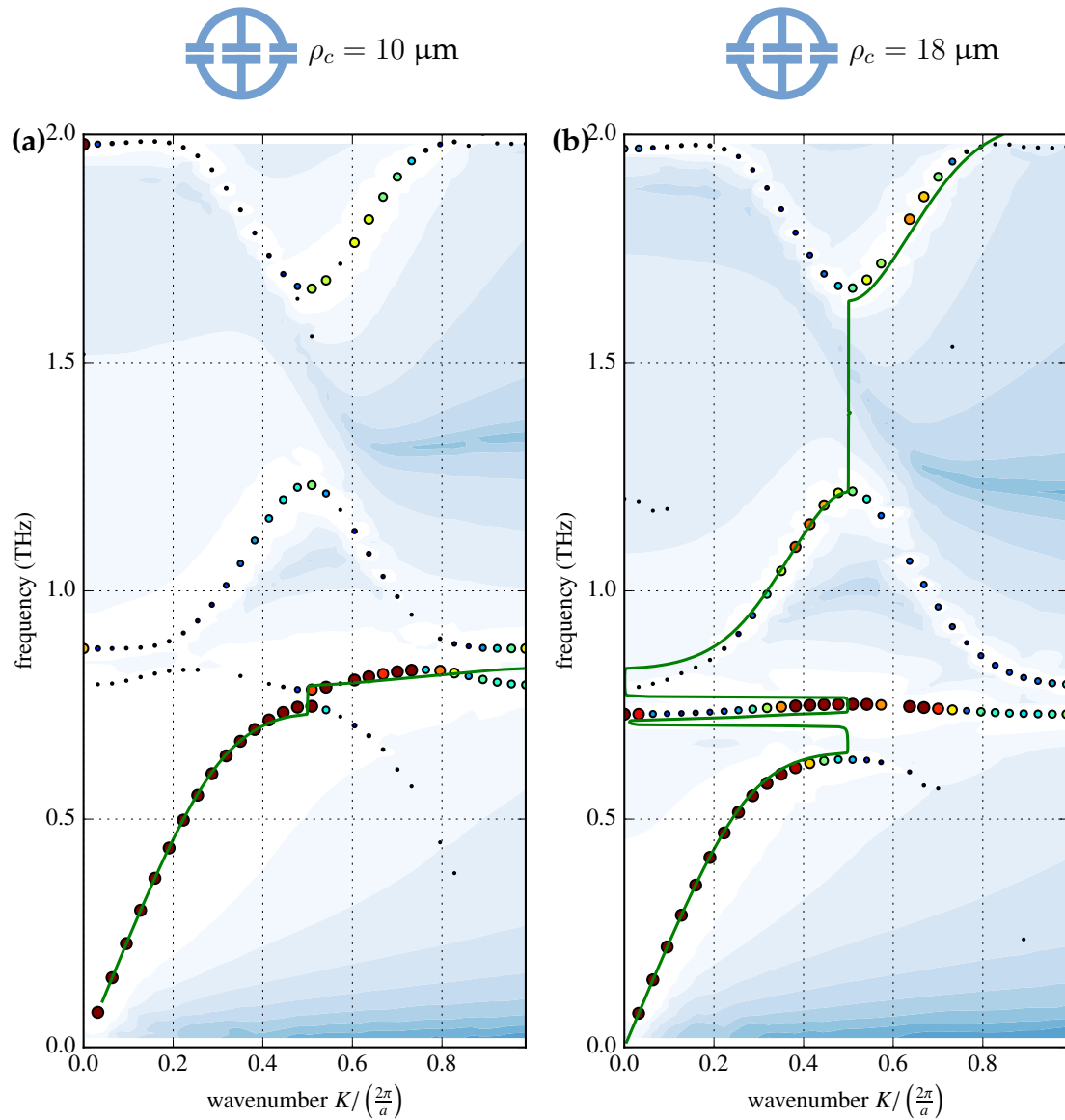


Figure 5.21: Current-driven homogenisation results for the combined electric-magnetic resonator, differing by the inner capacitor radius (a) $\rho_c = 10 \mu\text{m}$, (b) $\rho_c = 18 \mu\text{m}$.

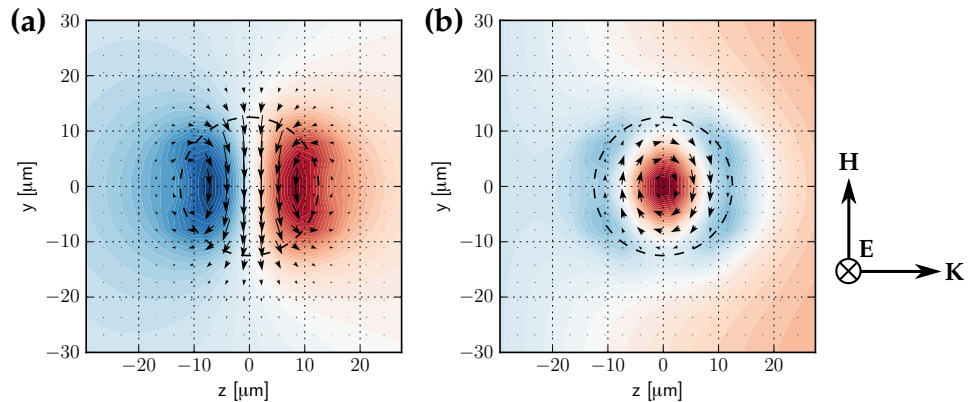


5.6 Dielectric spheres

Mie resonances Already in Eqs. (3.11, 3.12) it was assumed that at higher frequencies, there is no difference between the effect of conduction and the polarisation currents. The current flowing around a split-ring resonator has a direct analogy in the polarisation current circulating in a dielectric particle, be it a torus of dielectric [205], or a sphere [40]. The capacitor of the SRR is then replaced by the distributed capacitance of the whole dielectric. For the first resonance in spherical dielectric particles, the magnetic dipole moment induced by the polarisation current points through the sphere center, as can be found from the resonant field shape in Fig. 5.22a. The resonant frequency is inversely proportional to the radius ρ of the sphere and it decreases monotonously with the growth of the dielectric permittivity ϵ_r .

The second resonance (Fig. 5.22b) has an electric dipole moment. It is similar to the magnetic one, but the electric and magnetic fields exchange their topology: The magnetic field circulates around the axis of the sphere, and the polarisation current forms the electric dipole. In spite of the similarity of both resonances, the frequency of the magnetic resonance is lower, since it allows the electric field to be more localized in the dielectric volume. In contrast, for the electric resonance, most of the streamlines of the electric field have to pass through the surrounding air (see Fig 5.22a,b).

Figure 5.22: The electric field component E_x (shaded in blue-white-red) and magnetic field components H_y, H_z (plotted as vectors) for (a) the magnetic and (b) electric Mie resonances in a dielectric sphere. The figure is in the y - z plane of mirror symmetry, so the fields have no other nonzero components than those shown here. On the right side, the vectors depict the right-hand vector triplet of the incident plane wave.



An analytical theory of electromagnetic resonances in dielectric spheres (or rods) was developed by Mie in 1908 [195], and correspondingly they are denoted as *Mie resonances*. Dielectric resonators operate in a similar way to a series L-C circuit, as was noticed by Richtmyer in 1939 [206]. Few decades later, the dielectric resonator found its use in the developing microwave technology; usually it takes the form of a millimetre-sized ceramic disc glued to a microstrip circuits.

The Mie theory describes the scattering from a single particle surrounded by vacuum, but for high-permittivity dielectrics, the resonant fields are well confined

in the dielectric volume and are not appreciably affected by the presence of the neighbouring cells, so the Mie theory remains applicable.

An artificial dielectric consisting of dielectric particles with effective permeability differing from unity was considered by Lewin in 1947 [88]; apparently it was not until 2002 when O'Brien et al. computed [40] that the effective permeability of such a structure may be negative.

Infinite number of the higher-order resonances exist [195, pp. 407-408], resembling the set of single-electron orbitals around an atomic nucleus. Many of these, e.g. most *d*-type orbitals, have zero electric or magnetic dipole moments. Dipole moments of many others are nonzero, but are not oriented parallel to the fields of the incident wave, and do not couple to the electromagnetic wave. In the spectrum of an array of dielectric spheres, one can identify clearly an alternating series of electric and magnetic resonances, of which the first three are easy to identify in Fig. 5.23. Each of them manifests itself as a peak in reflectance, and as a pair of resonance in $\mu_{\text{eff}}(f)$ and antiresonance in $\varepsilon_{\text{eff}}(f)$, or vice versa.

Dielectric losses Unlike split-ring resonators, where the high-frequency dissipative losses depend on many factors such as the metal surface, eddy currents and fine details in the geometry, the losses in dielectric resonators can be more accurately modelled and their effect can be computed reliably by the FDTD simulation.

We used a realistic model [207] of permittivity of polycrystalline rutile (TiO_2), which was already plotted in Fig. 3.2. In the terahertz range it counts among high-permittivity dielectrics with relatively low losses compared to similar materials:

$$\varepsilon_r(f = 1 \text{ THz}) = 94.2 - 2.43i. \quad (5.11)$$

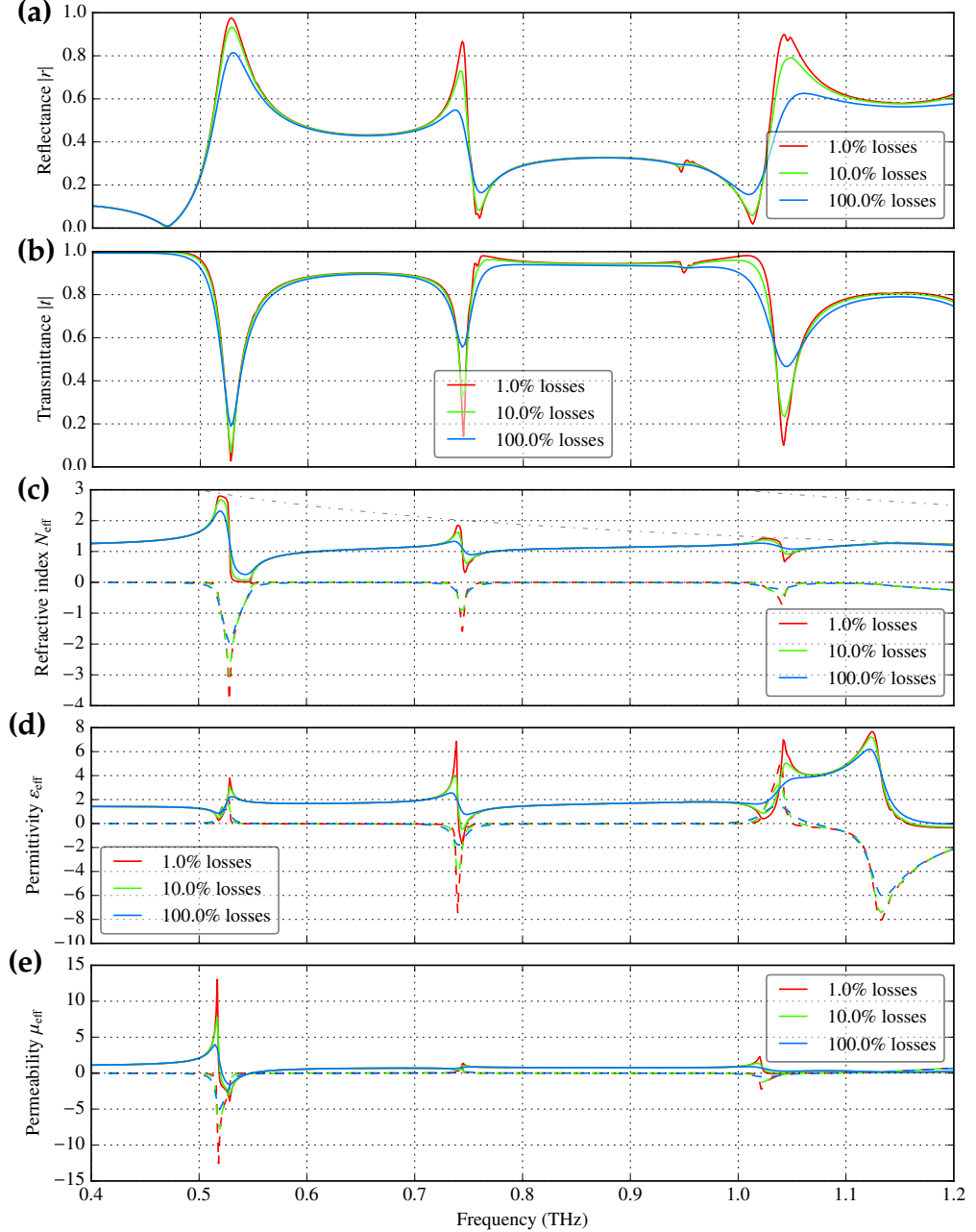
The actual permittivity of the experimentally measured samples depends on their preparation, in particular the volume fraction of microscopic voids. For such composites, Ref. [207] gives only the ratio of $\varepsilon''_r/\varepsilon'_r$, but since ε'_r could be determined from the resonant frequencies in the experimental spectra, also the imaginary part could be inferred.

The reflectance, transmittance and effective parameters of rutile spheres with radius $\rho = 15 \mu\text{m}$ are compared in Fig. 5.23. Three different levels of losses were considered. The realistic value was denoted as 100 %, and it was accompanied with hypothetic low-loss dielectrics with the same real part of ε'_r , but the imaginary part ε''_r artificially reduced to 10 % and 1 %.

In all three cases, the magnetic resonance is located at 530 GHz and the electric one at 790 GHz, the second magnetic resonance follows at 1040 GHz. As a natural result of the Lorentzian model, the dielectric losses grow proportional to the frequency. Notice that around the resonant frequencies, the transmittance is higher in the case with high losses.

When the realistic losses are taken into account, the curves of the effective parameters in Figs. 5.23c,d,e become smoother and approach the familiar curve of the damped oscillator in Fig. 2.2. Strong enough losses can even prevent the formation of regions with negative effective parameters. Note, however, that formally N'_{eff} can become negative [63, pp. 12–15] even when either $\varepsilon'_{\text{eff}} > 0$ or $\mu'_{\text{eff}} > 0$. Such

Figure 5.23: (a) Amplitude of reflectance, (b) amplitude of transmittance, (c) effective index of refraction $N_{\text{eff}} = N'_{\text{eff}} + iN''_{\text{eff}}$, (d) effective permittivity $\varepsilon_{\text{eff}} = \varepsilon'_{\text{eff}} + i\varepsilon''_{\text{eff}}$ and (e) effective permeability $\mu_{\text{eff}} = \mu'_{\text{eff}} + i\mu''_{\text{eff}}$ of TiO_2 spheres with varied loss compared to the natural one from Ref. [207]; sphere radius $\rho = 30 \mu\text{m}$, unit cell size $a = 100 \mu\text{m}$.



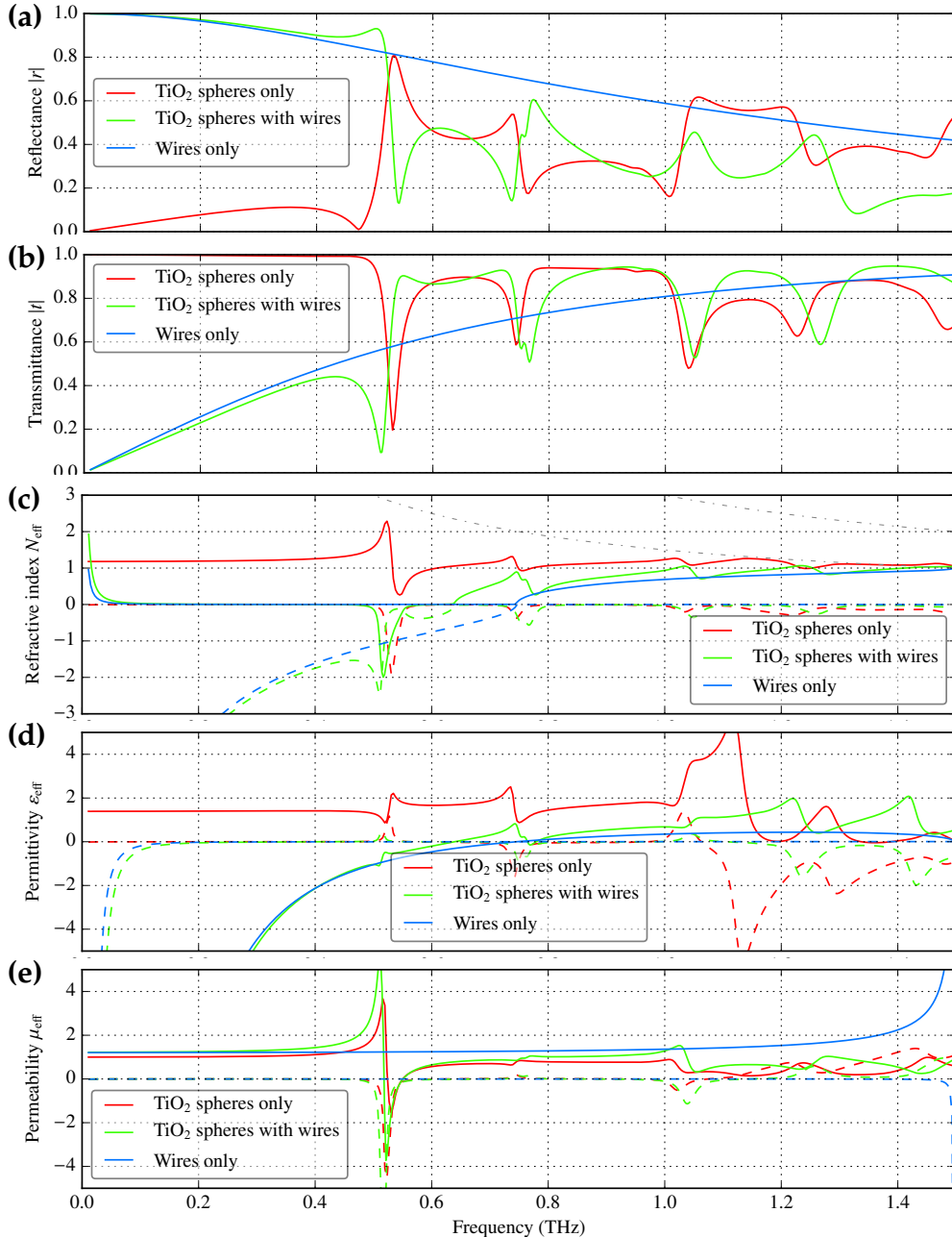
a negative-index medium is however inevitably extremely lossy, which is represented by its *figure of merit*

$$\text{FOM} := \frac{N'_{\text{eff}}(f)}{N''_{\text{eff}}(f)} \lesssim 10. \quad (5.12)$$

At the right hand side of the plot, for $f \sim a/(2c) \approx 1.5 \text{ THz}$, the structure reaches a Bragg band gap. This kind of resonance is not appreciably affected by the losses,

since most of the field energy in the Bragg resonance is concentrated in free space between the particles.

Figure 5.24: Amplitude of (a) reflectance, (b) transmittance, (c) effective index of refraction $N_{\text{eff}} = N'_{\text{eff}} + iN''_{\text{eff}}$, (d) effective permittivity $\varepsilon_{\text{eff}} = \varepsilon'_{\text{eff}} + i\varepsilon''_{\text{eff}}$ and (e) effective permeability $\mu_{\text{eff}} = \mu'_{\text{eff}} + i\mu''_{\text{eff}}$ of TiO_2 spheres, wire grid array, a combined negative-index structure and its modification with varied loss compared to the natural one from Ref. [207]; sphere radius $\rho = 30 \mu\text{m}$, unit cell size $a = 100 \mu\text{m}$.



Negative-index metamaterial based on dielectric spheres An important property of the periodic sphere array is its nearly *isotropic* electromagnetic behaviour, i.e. independence of its behaviour on the wave polarisation, which is approximately

maintained at low frequencies even when the spheres are arranged into a periodic lattice, provided that the spheres are not too close.

Following the approach used to build a metamaterial with a negative refractive index from SRRs, it is possible to combine the sphere array with an array of wires to introduce negative permittivity and permeability simultaneously. In order to maintain the approximate isotropy of the resulting structure, the wires may form a two- or three-dimensional mesh. This modification does not make any appreciable change in the low-frequency behaviour.

Fig. 5.24 compares the already commented spectra for the sphere lattice (red line), and wire grid (blue line) with the spectra for the compound structure, which is sketched in Fig. 5.25a,c. At $f > 0$, the wire grid does not reflect all energy, leading again to formation of the Fano resonance profile.

Notice in 5.24 that the Fano resonances of structures with and without the wire mesh have a peculiar complementary shape. The wave reflected from the electric dipole of the wire mesh has the opposite sign than that reflected from the electric dipole of dielectric particles. Its sign determines whether the interference with the second component, scattered by the Mie resonances, would be constructive, or destructive.

A band of negative index of refraction is formed above the magnetic Mie resonance, between 510 and 550 GHz. When the realistic model of losses in TiO_2 is used, the maximum figure of merit $N'_{\text{eff}}/N''_{\text{eff}} \approx 6$ is reached around the centre of the photonic band. This means that the metamaterial, in the optimum of the negative-index band, reduces the wave amplitude to $e^{1/6} \approx 0.84$ within one wavelength λ . When a wave propagates over a distance of ca. 40λ in the metamaterial, the amplitude drops to 10^{-3} and the wave energy to 10^{-6} of the incident value. The applicability of such a metamaterial for building a macroscopic optical device is questionable.

Effect of elliptic shape For a spherical dielectric particle, the frequencies of the magnetic and electric resonances, f_{M1} and f_{E1} , respectively, scale inversely proportional to the radius ρ :

$$f_{M1} \propto \rho^{-1}, \quad f_{E1} \propto \rho^{-1}. \quad (5.13)$$

A deviation from this rule may result from the inter-particle coupling in a very dense lattice, or from dispersion of the constituent dielectric.

When the particle is an ellipsoid with three independent semiaxes ρ_x , ρ_y and ρ_z aligned parallel to the x -, y - and z -axes, the resonant frequencies f_{M1} and f_{E1} become certain functions of these three ellipsoid parameters. For a nearly spherical shape,

$$\rho_x \sim \rho_y \sim \rho_z,$$

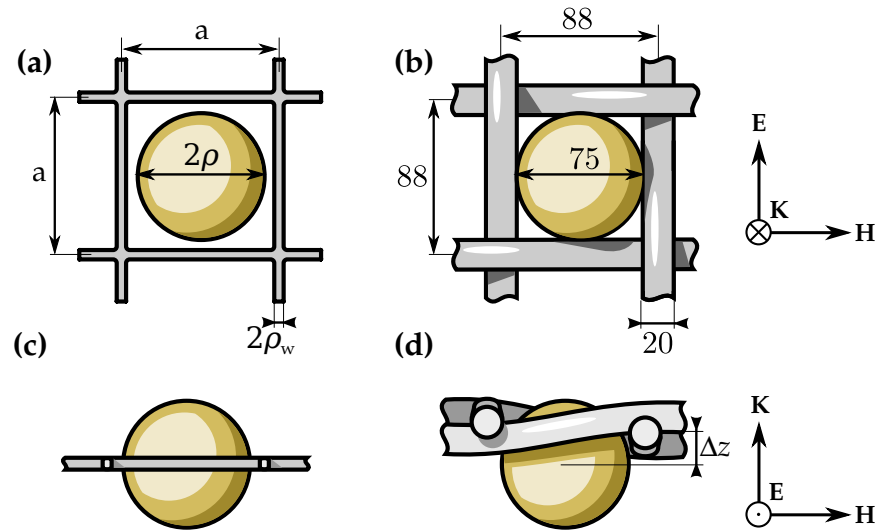
we observed that both frequencies can be approximated as

$$f_{M1} \propto \rho_x^{-0.4} \rho_y^{-0.2} \rho_z^{-0.4}, \quad (5.14)$$

$$f_{E1} \propto \rho_x^{-0.15} \rho_y^{-0.15} \rho_z^{-0.7}. \quad (5.15)$$

Obviously, in both Eqs. (5.14) and (5.15), all three exponents must sum exactly to -1 so that they are compatible with the scaling rule for a sphere in Eq. (5.13). Their

Figure 5.25: Sketch of the sphere array embedded in the wire grid. (a) Front view of the simulated structure, (b) the experimental structure used in Ref. [208], measures are in micrometres. (c) and (d) top views of the corresponding structures



values are approximate only, as they were interpolated from batches of simulations which scanned through the ellipsoid parameters.

When the ellipsoid axes have a general orientation with regard to their cubic lattice, the resonant frequencies remain almost the same. In such a case, an incident wave polarized along the x -axis can excite multiple magnetic or electric Mie resonances of the same topology but of different orientation, which differ slightly by their frequencies. The structure then may change the polarisation state of the wave, which is beyond the scope of this analysis.

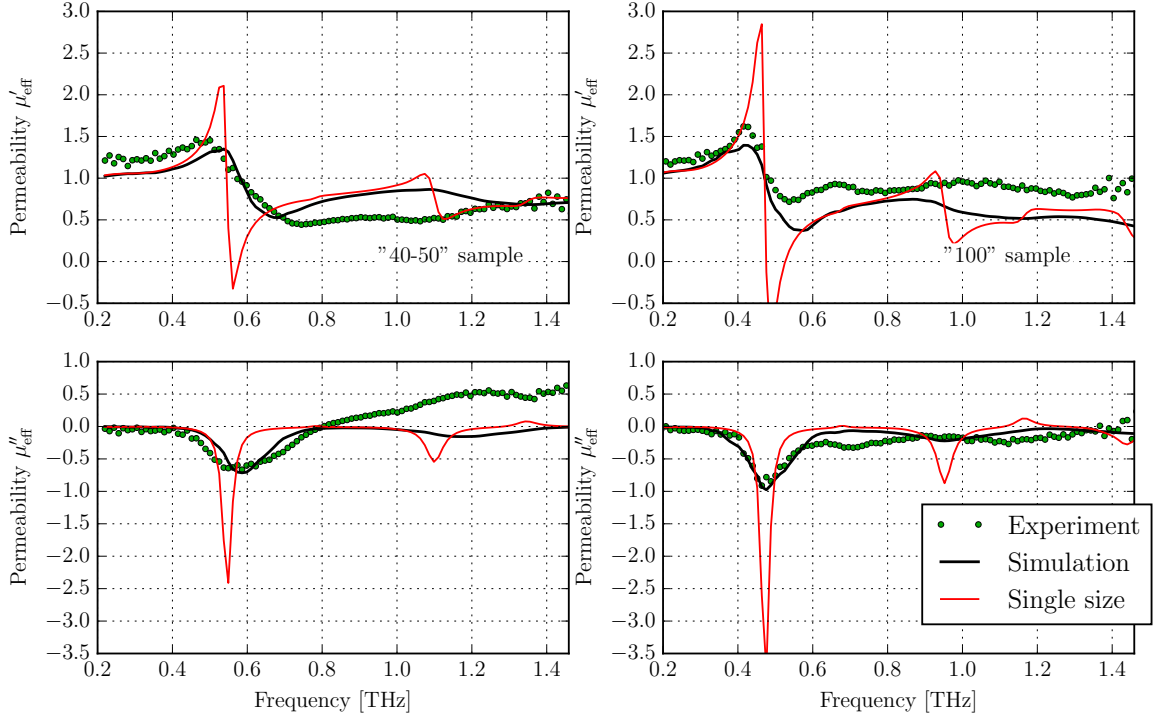
Experimental spectra of spheres We measured series of spectra of titanium microsphere samples using the terahertz time-domain spectroscopy. We used the scheme described on pages 110–112 to retrieve not only the transmittance of the single-layered sample, but also the reflectance, which enabled us to approximately compute the effective parameters of a metamaterial which would be made by arranging the spheres into a lattice.

The first magnetic Mie resonance was easy to identify in the spectra. The exact quantitative comparison of the results was also possible, but of lesser physical meaning, since two most important quantities, the resonant frequency and the oscillator strength (i.e. amplitude of the resonant waveform) could not be characterised reliably.

In particular, the exact dielectric permittivity of the polycrystalline rutile samples was not known, and over multiple measurements, our group established a consensus of $\epsilon'_r \approx 94$ as in Eq. (5.11), which provided the best match with most experimental data.

Second, the oscillator strength of the first Mie resonance does not allow for a direct comparison with the experiment. While it could be determined reliably in the

Figure 5.26: Comparison of the effective permeability $\mu_{\text{eff}}(f)$ of an ideal monodisperse sphere array (dashed red line), weighted average according to the size distribution (solid black line) and experimental data (green dots). (a) Real part of effective permeability for a sample denoted as having the "40-50" μm diameter, (b) for another sample with slightly larger average diameter, also depicted in Fig. 4.2. (c), (d) corresponding imaginary parts of $\mu_{\text{eff}}(f)$



simulations with a given unit-cell size a , the exact density of the microspheres was very hard to determine exactly. They were attached to one of the sapphires by static electricity, and their position was random. Upon manipulation with the samples, part of the spheres fell off the sapphire surface. Moreover, we had no reliable way of determining through which part of the sample the probing THz beam passed.

Comparison of experimental and simulated spectra The effective permeability of two samples having different average sphere sizes is represented by dots in Fig. 5.26. The FDTD simulations for an array of identical TiO_2 spheres yielded much narrower resonant spectra of $\mu_{\text{eff}}(f)$, which are represented by dashed red lines. To enable a direct comparison, we used the granulometric data obtained by digital processing of the microscopic images. Using the granulometric data,, the effective radius of a sphere ρ_{eff} was estimated for each particle from the minor ρ_a and major axes ρ_b :

$$\rho_{\text{eff}}^{(m)} := \left[\frac{2}{3(\rho_a^{(m)})^2} + \frac{1}{3(\rho_b^{(m)})^2} \right]^{-0.5} \quad (5.16)$$

This expression is based on the assumption that the ellipsoids will orient horizontally when sprinkled on the microscope slide, thus making the shortest axis verti-

cal and hidden from the statistical processing. Obviously, it is arbitrary to assume the shortest and medium ellipsoid axis will be both equal to ρ_b , but this approach yielded a relatively good match with experiment. The most accurate procedure would be to determine all three axes of the particle and predict its resonance spectra by means of Eqs. (5.14), (5.15). Without the knowledge of all three ellipsoid axes, the spherical approximation using Eq. (5.16) however appears as an acceptable approach.

From the FDTD simulations, we deduced that the resonant frequency of a TiO_2 sphere is inversely proportional to its effective radius $\rho_{\text{eff}}^{(m)}$, and its scattering cross-section to the square thereof. Once a reference permeability spectrum $\mu_{\text{eff}}^{(\text{ref})}(f)$ was computed for a reference radius ρ^{ref} , the experimental spectra could be estimated as the following weighted sum over all M particles processed:

$$\mu_{\text{eff}}^{(\text{simulated})}(f) := 1 + \frac{\sum_{m=0}^M \left(\rho_{\text{eff}}^{(m)}\right)^2 \left[\mu_{\text{eff}}^{(\text{ref})} \left(\frac{f \rho_{\text{eff}}^{(m)}}{\rho^{\text{ref}}} \right) - 1 \right]}{\sum_{m=0}^M \left(\rho_{\text{eff}}^{(m)}\right)^2}. \quad (5.17)$$

The result, plotted by thick black curves in Fig. 5.26, corresponds to a weighted average through the particle statistics, with the weight proportional to the scattering cross-section of each particle. The averaged simulation results are relatively close to the experimental data at frequencies around the first magnetic Mie resonance (around 600 and 480 GHz, respectively).

At higher frequencies, the experimental data deviate substantially from the predictions. This can be attributed to one or more sources of error in the experimental setup for effective-parameter retrieval.

Narrowing the resonance by sieving The broad dispersion of the microsphere sizes leads to a broadening of the Mie resonance, which is detrimental to the meta-material performance. In the samples measured, it precludes $\mu'_{\text{eff}}(f)$ from reaching negative values. It also spreads the very strong dissipative losses, introduced by a resonance, over a broader spectral range, including the region where the FDTD simulations in Fig. 5.23 would otherwise predict relatively low losses and $\mu'_{\text{eff}}(f) < 0$.

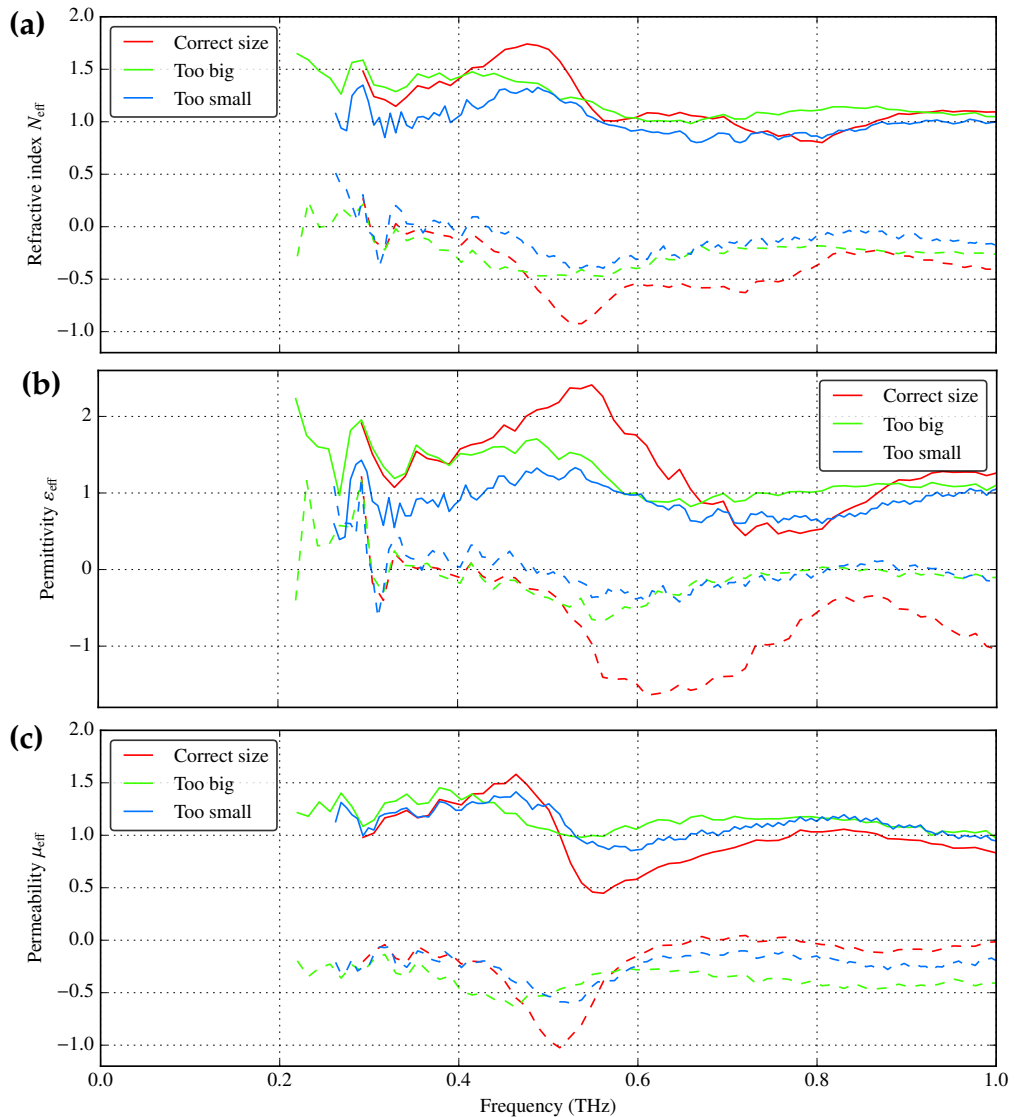
With the aim to resolve this issue which affected all microsphere samples, we developed the novel sieving technique described in the experimental section of this thesis. Fig. 5.27 compares the independently measured spectra of $N_{\text{eff}}(f)$, $\varepsilon_{\text{eff}}(f)$ and $\mu_{\text{eff}}(f)$ for three different fractions of one sample. The green line corresponds to the oversized fraction that remained above the first sieve, the red line to the correctly sized fraction that passed the first sieve but remained above the second one, and the blue line to the remaining fraction that passed both sieves.

Moderate narrowing of the resonance spectral shape can be observed for the correctly sized fraction, with the remaining fractions being shifted in the frequency as predicted. The intermediate fraction consistently exhibits more pronounced resonance in the permeability. Simultaneously all spectra measured are burdened with one or more severe errors of the characterisation method. Namely in Fig. 5.27, the simulations cannot explain the pronounced resonance in retrieved effective permittivity, which appears to be an artifact from the asymmetry of the sample between

two sapphire plates. This may be also the cause of the spectra of $\varepsilon_{\text{eff}}(f)$ and μ_{eff} usually deviating from the expected values at higher frequencies.

However, the truly fundamental limitation are the dissipative losses in TiO_2 , already shown in Fig. 5.24. They impose a tight upper bound for the figure of merit of any terahertz metamaterial based on TiO_2 resonators.

Figure 5.27: Comparison of retrieved effective parameters for three fractions of the microspheres sample: (a) effective index of refraction, (b) permittivity and (c) permeability.



Spheres in a metallic mesh We attempted to fabricate one layer of a negative-index metamaterial by embedding resonant particles into the holes of a metallic sieve. This kind of structures is predicted to have a negative index of refraction above the first Mie resonance of the spheres (see the green curve in Fig. 5.24), which should result from combining of negative permittivity and permeability. Thanks to high localization of the electric field inside the sphere, negative refraction is predicted even when the spheres are embedded in homogeneous $\varepsilon_r < 0$ medium. Note

this is in contrast with the split-ring resonators, where $\varepsilon_r < 0$ medium disrupts their magnetic resonance [205]

The issues in our case were mostly of geometrical and mechanical origin. Although it was possible to manufacture a sieve with proper size of holes which would hold microspheres during sieving, the spheres randomly fell out of it upon manipulation. We decided not to use any glue, since even a relatively thin layer thereof would substantially alter the spectra, increasing losses in the terahertz range.

An experiment involving a similar sample was published previously [208], with TiO_2 spheres sprinkled over a commercial mesh woven of steel wire, as sketched and accurately measured in Fig. 5.25b,d. The original publication reported very low transmittance, with inconclusive results as regards to the negative phase advance through the structure. The published structure was asymmetric, with the sphere displaced by $\Delta z \sim 15 \mu\text{m}$ along the wave propagation direction, and accordingly, the simulations processed with the scattering-parameter method yielded unphysical values of effective parameters.

5.7 Dielectric rods parallel to the magnetic field

Resonances in a low-permittivity array Dielectric rods aligned parallel to the magnetic field exhibit spectra similar to the sphere arrays (see Fig. 5.29), with clearly identifiable Mie resonances with magnetic and electric dipoles. Unlike sphere arrays, the computation of the rod array behaviour under near-perpendicular incidence is a two-dimensional problem.

Photonic crystals composed of dielectric rods in a square lattice have been examined thoroughly since the early 1990s [209, 210]. For structures intended to operate at optical or near-infrared frequencies, the permittivity of the constituent materials was usually relatively low, typically up to the permittivity of silicon $\varepsilon_r \leq 12$.

In the left panel of Fig. 5.28, the low permittivity in the structure causes its low-frequency behaviour to be similar to the one-dimensional photonic crystal. At the lower edge of the Bragg band gap (X1 subplot of 5.28a), the electromagnetic wave concentrates the electric field in the layer of dielectric rods, as indicated by tiny arrows. The magnetic field energy is roughly complementary, located predominantly in the air between them. As already described on the example of 1-D PhC, at the upper edge of the band the situation is opposite, with most of the magnetic-field energy localized around the dielectric. The number of nodal planes of the electric or magnetic field does not change between the lower and upper edges of a Bragg band gap.

Resonances in the high-permittivity array In the microwave and terahertz ranges, the permittivity of many materials turns out to be much higher than 12. This fact gives rise to the main difference between the panels in Fig. 5.28. In the right panel, the dielectric permittivity $\varepsilon_r = 100$ moves the first Mie resonance [40] in the first band gap.

This band gap starts in the X_1 point, where each unit cell is divided by one nodal plane of the magnetic field. In contrast, the next photonic band starts in the Γ_2 point where no such nodal plane exists. This corresponds to a drop in the real part of effective index of refraction, a behaviour that is typical for all individual resonances.

Figure 5.28: Dispersion curves for an array of dielectric rods parallel to the magnetic field. The side plots show the shapes of the fields in the (x, z) plane, at the frequencies of the band edges. The magnetic field is plotted as orange-violet color map and the electric field is represented by vectors. The rod radius was chosen to 12 % of the period. (a) On the left, a relatively low permittivity $\varepsilon_r = 12$ places the magnetic resonance above the first Bragg band gap. (b) For high permittivity dielectric $\varepsilon_r = 100$, the magnetic resonance forms the first band gap.

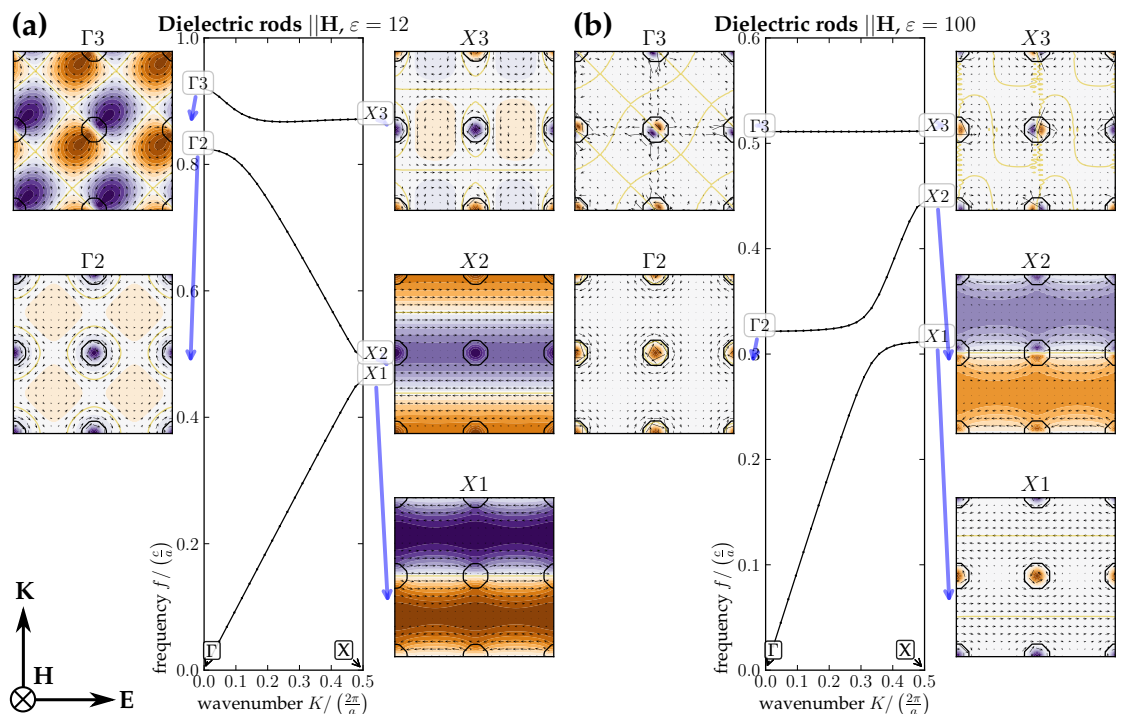
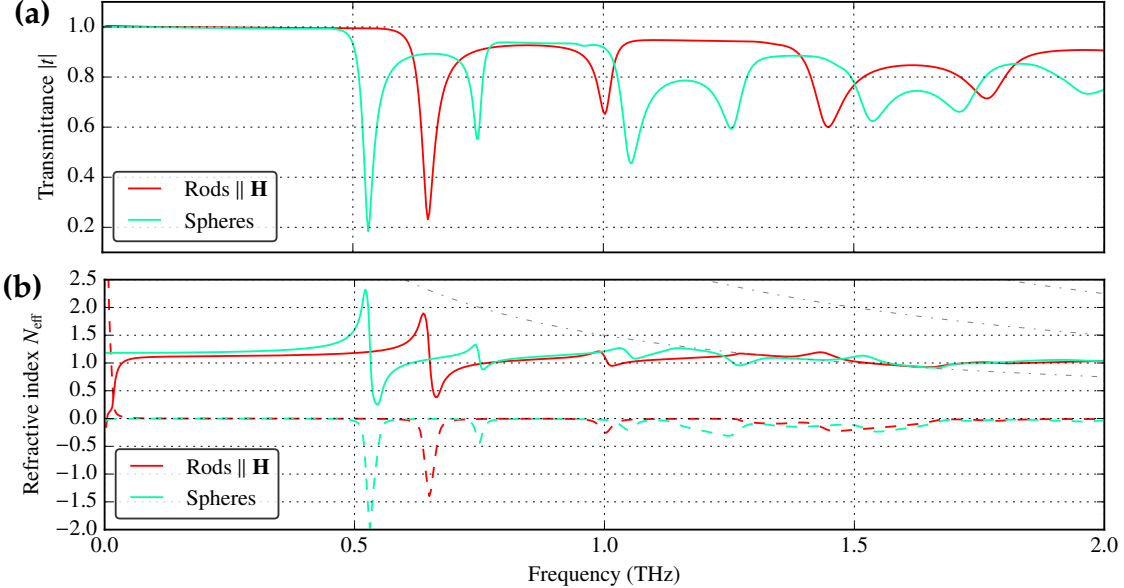


Figure 5.29: Comparison of (a) transmittance and (b) effective index of refraction N_{eff} for arrays of dielectric spheres (with radius $\rho_s = 30 \mu\text{m}$) and of dielectric rods (with radius $\rho_r = 19 \mu\text{m}$) in a $100\mu\text{m}$ unit cell, both made of TiO_2 . The choice of radii used ensures the same volume filling fraction.



5.8 Dielectric rods parallel to the electric field

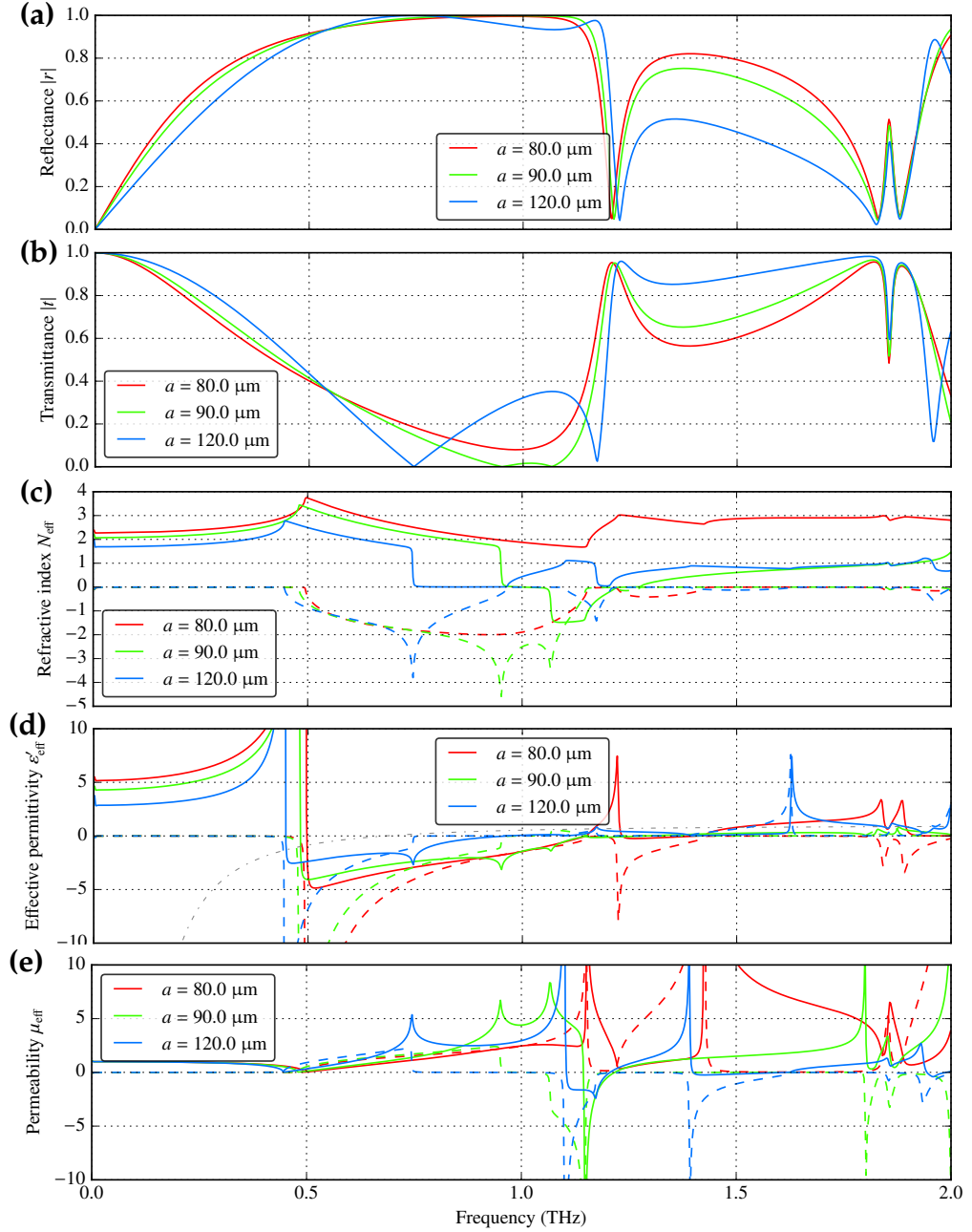
Sparse rod array The discussion of the previous structure has proven that the choice of permittivity and geometry obviously leads to a qualitative change in the structure behaviour. Similar changes are also observed for dielectric rods parallel to the electric field.

Fig. 5.30 compares the spectra of effective parameters for three rod arrays of equal radius $\rho = 10 \mu\text{m}$ and dielectric permittivity $\epsilon_r(f = 1 \text{ THz}) = 89.5 + 0.23i$. The latter was chosen to be close to that of porous polycrystalline rutile, but the losses were artificially reduced for better readability of the spectral features. The three structures differ only by the unit cell size $a \in \{80, 90, 120\} \mu\text{m}$.

Starting with the blue curves in Fig. 5.30 representing a sparse array with $a = 12\rho = 120 \mu\text{m}$, one can identify two points of near-zero transmittance around 745 and 1170 GHz with two individual resonances. Each of them introduces a familiar shape in the spectrum of $N_{\text{eff}}(f)$. From the effective permittivity $\epsilon_{\text{eff}}(f)$ and permeability $\mu_{\text{eff}}(f)$, the first resonance can be identified as an electric one, and the second as a magnetic one. The electric resonance has a strong dipole moment and introduces a broader band gap than any of the resonances shown in Fig. 5.29. At frequencies close to the upper edge of the band gap, the dielectric structure behaves in a similar way to the wire array and plasma; this effect has been proposed to introduce negative permittivity in one all-dielectric metamaterial design [205].

In spite of the strength of the first resonance, the corresponding region of $\epsilon'_{\text{eff}}(f) < 0$ does not overlap with that of $\mu'_{\text{eff}}(f) < 0$ and no negative index of refraction is obtained for the sparse rod array with $a = 120 \mu\text{m}$. The resulting spectra of all parameters are qualitatively similar to that of the electro-magnetic resonator with the capacitor radius $\rho_c \gtrsim 18 \mu\text{m}$ (cf. Figs. 5.18 and 5.21b).

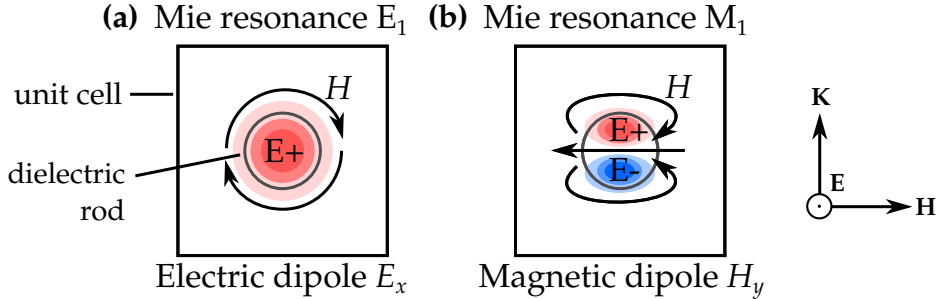
Figure 5.30: Amplitude of (a) reflectance, (b) transmittance (c) effective index of refraction N_{eff} , (d) effective permittivity $\epsilon'_{\text{eff}} = \epsilon'_{\text{eff}} + i\epsilon''_{\text{eff}}$ and (e) effective permeability $\mu_{\text{eff}} = \mu'_{\text{eff}} + i\mu''_{\text{eff}}$ for a rod array of realistic TiO_2 dielectric model with constant radius $\rho = 10 \mu\text{m}$ and grid resolution of $1 \mu\text{m}$. Similar to other plots, the real part is plotted solid, the imaginary one dashed.



Effect of inter-cell coupling By increasing the filling fraction of the dielectric rod, the electric and magnetic resonances can be efficiently tuned upwards and downwards in the frequency, respectively. The reason can be deduced from the symmetry of the magnetic field shapes for $\mathbf{K} \sim 0$.

The electric resonance (Fig. 5.31a), with the electric field pointing parallel to the rod, and the magnetic field circulating around it, introduce opposite orientation of the magnetic field at the cell boundaries. A reduction of the cell size a also re-

Figure 5.31: Cross-sections of first two resonant modes in the dielectric rod. The red and blue colours show positive and negative values of the electric field, while the magnetic field is represented by the arrows. (a) The electric Mie resonance, (b) the magnetic Mie resonance.



duces the effective inductance of the rod per unit length, thus shifting the electric resonance to a higher frequency.

On the contrary, the magnetic field surrounding the rod near at the magnetic Mie resonance (Fig. 5.31b) is oriented parallel with the field of the neighbouring cell. Thus the reduction of a decreases the frequency of the magnetic resonance.

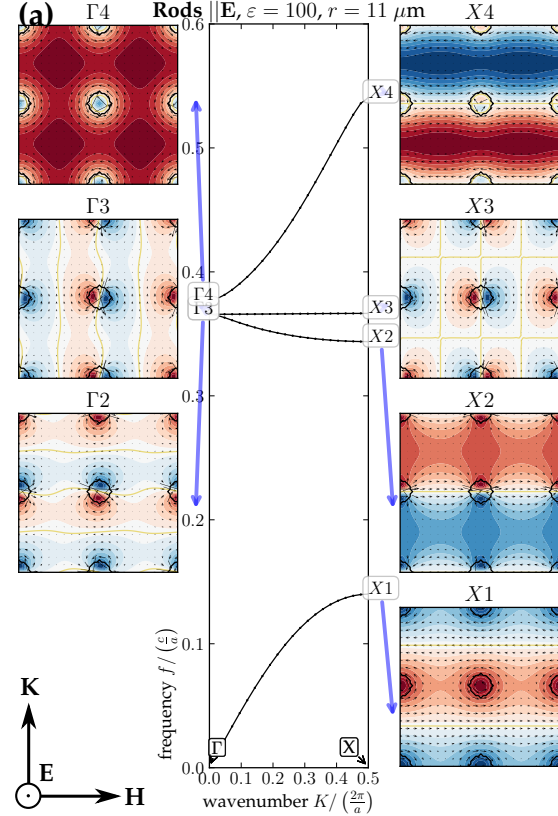
Note that this strong coupling is specific for this particular rod orientation. In the previous chapter we discussed similar high-permittivity rods oriented parallel to the magnetic field. In the first resonance, the electric field also circulated around the rod axis, but the majority of its energy was confined to the dielectric volume (cf. Fig. 5.28b-X1). The inter-cell coupling of the magnetic resonance was thus much weaker, and similar argument applied also to higher resonances. As a result, the resonant frequencies of dielectric rods parallel to the *magnetic* field cannot be efficiently tuned against each other.

Medium-density rod array Through moderate reduction of the unit cell size a to 90 μm , as represented by the green line in Fig. 5.30, the electric and magnetic resonant frequencies approach each other, shifting to $f_E \approx 950$ and $f_M \approx 1070$ GHz, respectively. This eventually leads to an overlap of the $\epsilon'_{\text{eff}}(f) < 0$ and $\mu'_{\text{eff}}(f) < 0$ regions, and a negative-index band is formed between 1130 and 1200 GHz.

At the upper-frequency edge of the band with $N'_{\text{eff}} < 0$, either the effective permeability or permittivity becomes positive, for $a \lesssim 92 \mu\text{m}$ or $a \gtrsim 92 \mu\text{m}$, respectively. This is another subtle, but qualitative change in the structure behaviour.

At the exact parameter a for the cross-over, the effective permittivity and permeability change their sign at the same frequency, and a *zero-width band gap* is obtained. Unlike the Fabry-Pérot resonances in 1-D PhC, this band gap is located at $N'_{\text{eff}} = 0$, which results in a peculiar regime of operation – in the idealized loss-less model, the wave would not exponentially decay nor would acquire any phase advance in the metamaterial volume; all unit cells would oscillate in phase. Still, its group velocity would be nonzero, and any spatial modulation of the wave envelope would propagate through the cells. This can be viewed as a complementary phenomenon to the extremely narrow photonic bands where, due to the vanishing inter-cell coupling, the phase velocity is orders of magnitude higher than the group velocity (cf. the second band in Fig. 5.21b).

Figure 5.32: Behaviour of the rods $\parallel \mathbf{E}$, with permittivity $\varepsilon = 100$ and radius $r = 11 \mu\text{m}$.



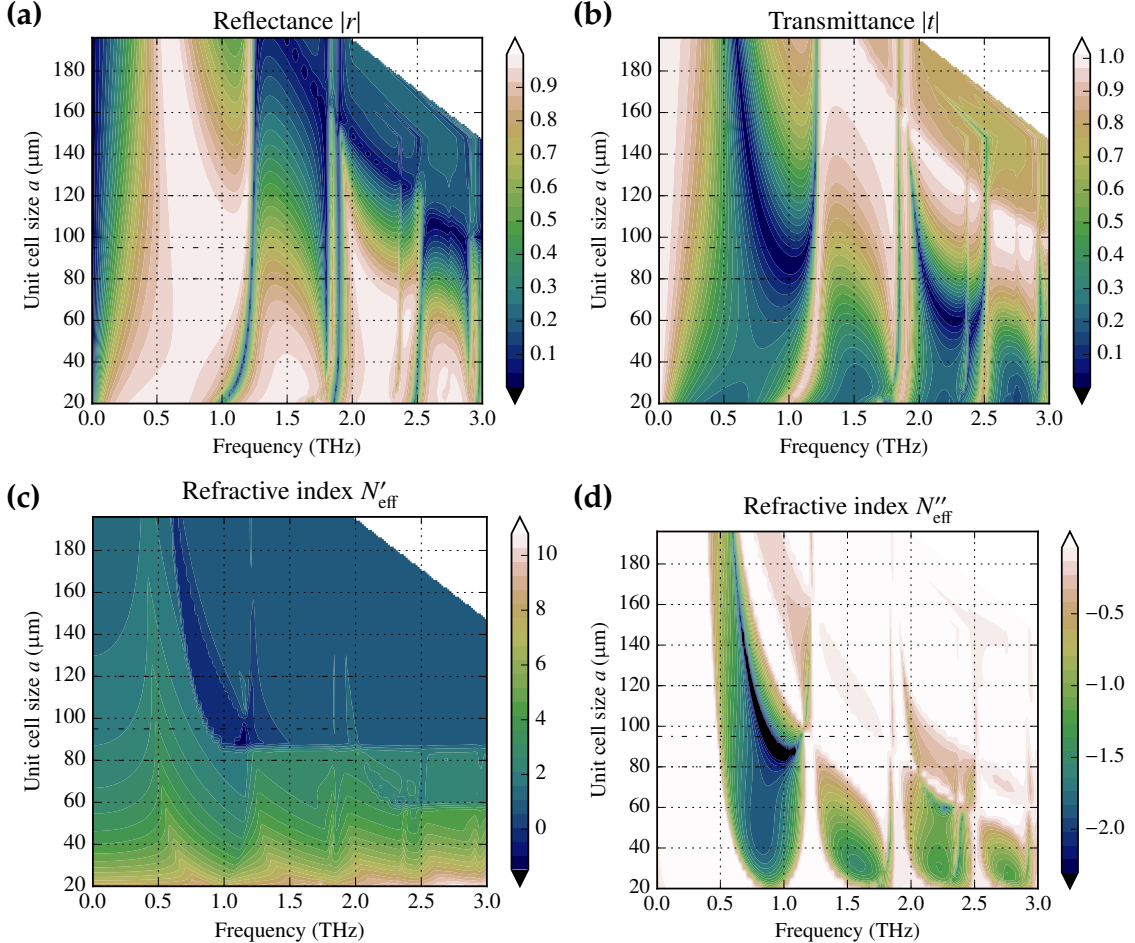
Both points of near-zero transmittance at f_E and f_M , indicating individual resonances, come closer to each other with further reduction of a . The maximum amplitude of transmittance $|t|$ between both resonances decreases approximately with the second power of the frequency difference:

$$\max_{f \in (f_E, f_M)} |t| \propto \frac{1}{(f_E - f_M)^2}, \quad (5.18)$$

hence the transmitted spectral intensity drops with the fourth power of the difference of the resonant frequencies, $(f_E - f_M)^4$, and can maintain very low values over this spectral region. Simultaneously, the transmittance rapidly grows above f_M and reaches almost 100 % relatively close to this low-transmittance region. We proposed [99] that with the aforementioned geometry, a single layer of unit cells could find its application as a *dielectric-rod array filter*. It would possess a better extinction ratio, and a better-defined stop-band than a dielectric slab of similar material can achieve through Fabry-Pérot resonances.

Dense rod array Further reduction of the unit cell size a to $80 \mu\text{m}$ does not lead to a cross-over of the resonant frequencies, as might be expected. Instead, the individual resonances disappear and an ordinary Bragg band gap remains, spanning from 480 to 1150 GHz. The corresponding transmittance curve (plotted in red in Fig. 5.30b) does not touch zero anywhere in the spectrum.

Figure 5.33: (a) Reflectance, (b) transmittance, (c) the real and (d) the imaginary part of the retrieved refractive index of an array of dielectric rods made of TiO_2 , with a constant radius $\rho = 10 \mu m$ and a variable unit cell size $20 \mu m < a < 200 \mu m$. Three selected values of radius, discussed in the text, are marked by horizontal black dash-dotted lines.



Consequently, there is no individual resonance, nor any fast drop in the spectrum of $N'_{\text{eff}}(f)$ (see Fig. 5.30c). The effective index of refraction N'_{eff} maintains high values over the whole spectrum, which precludes to describe the structure by means of local effective parameters of permittivity and permeability anywhere above the middle of the first photonic band. This kind of behaviour was already encountered in the spectra of one-dimensional photonic crystal (Figs. 5.2, 5.2).

However, the effective index of refraction $N_{\text{eff}}(f)$ is still valid, and its spectrum for $a = 80 \mu m$ approximately maintains the shape that N'_{eff} had for $a = 90 \mu m$ and even $a = 120 \mu m$. Most notably, the negative-index band around 1200 GHz (spanning between the -1th and the 0th Brillouin-zone boundaries) on the green curve has its analogy in a similarly narrow band on the red curve (between the 1th to the 2nd Brillouin-zone boundaries). Also the higher frequency features tend to be similar. This suggests that the only change between $a = 90 \mu m$ and $a = 80 \mu m$ that can be observed without an inspection of the internal fields is in the *phase* that the wave acquires per one unit cell.

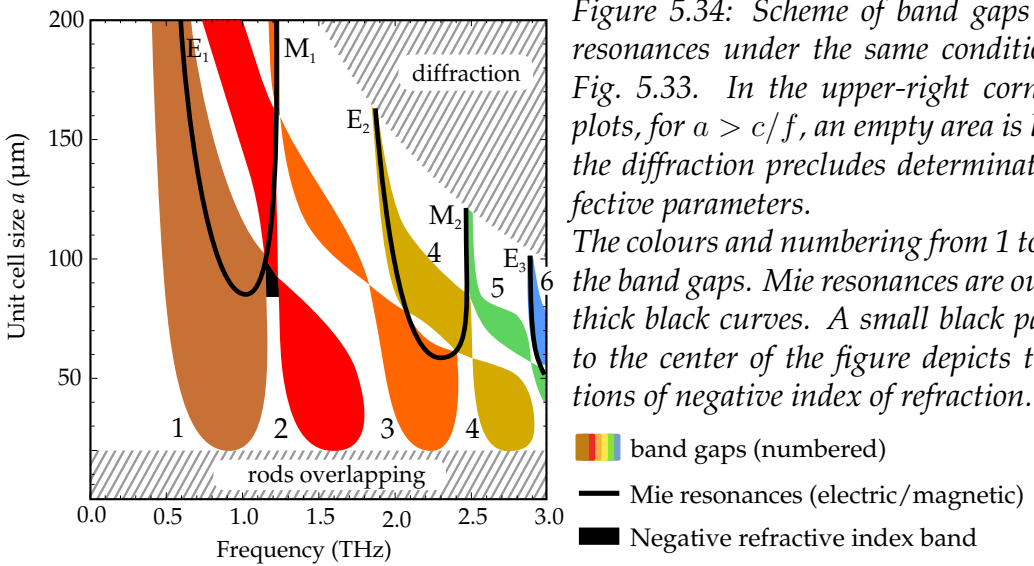


Figure 5.34: Scheme of band gaps and Mie resonances under the same conditions as in Fig. 5.33. In the upper-right corner of the plots, for $a > c/f$, an empty area is left where the diffraction precludes determination of effective parameters.

The colours and numbering from 1 to 6 denote the band gaps. Mie resonances are outlined by thick black curves. A small black patch close to the center of the figure depicts the conditions of negative index of refraction.

- band gaps (numbered)
- Mie resonances (electric/magnetic)
- Negative refractive index band

Continuous scan through the unit cell sizes For illustration, we add a high-resolution continuous scan through the unit cell size a in Fig. 5.33, with other parameters shared with the previous plots in Fig. 5.30. The individual Mie resonances can be identified as the sets of points where transmittance $|t|$ comes close to zero, real part of effective index of refraction N'_{eff} drops and its imaginary part N''_{eff} has a sharp peak. The photonic band gaps are all areas where $N''_{\text{eff}} \neq 0$ in Fig. 5.33d.

For easier interpretation, the interplay of the individual resonances and the band gaps is redrawn in Fig. 5.34, where each photonic band gap is represented as a coloured area and the individual resonances as thick black lines. The small black patch between the first and second band gaps covers all (a, f) combinations necessary for reaching $N'_{\text{eff}} < 0$, provided that the dielectric is titanium dioxide with permittivity $\varepsilon_r \approx 92$.

In accordance with the previous discussion, the electric and magnetic Mie resonances approach each other when the unit cell size a decreases from 120 to 90 μm , and eventually they meet and vanish for $a \lesssim 85 \mu\text{m}$, forming an "U"-shaped curve. Using a as the scanning parameter enables to illustrate clearly the shift of individual resonances. With this choice, the frequencies of the band gaps roughly follow the $1/a$ curves, but they are strongly influenced by the individual resonances. Each individual resonance is always contained inside a band gap.

In photonic bands, the real part of refractive index grows as a function of frequency; from the beginning to the end of each photonic band, it gains a difference of one Brillouin zone. The only way how N'_{eff} can descend by one Brillouin-zone boundary is by means of an individual resonance. A simple arithmetic condition for reaching negative index of refraction $N'_{\text{eff}}(f_1) < 0$, at a given frequency f_1 , is therefore that the number of photonic band gaps counted from $f = 0$ to f_1 must be strictly less than the number of individual resonances.

This simple rule eliminates the possibility of obtaining $N'_{\text{eff}} < 0$ from any higher-order Mie resonances, although from Figs. 5.33 and 5.34 it can be seen that these persist even for smaller unit cell sizes than $a = 85 \mu\text{m}$. The author further conjectures that the presence of two Mie resonances in the first band gap in the spectrum is a

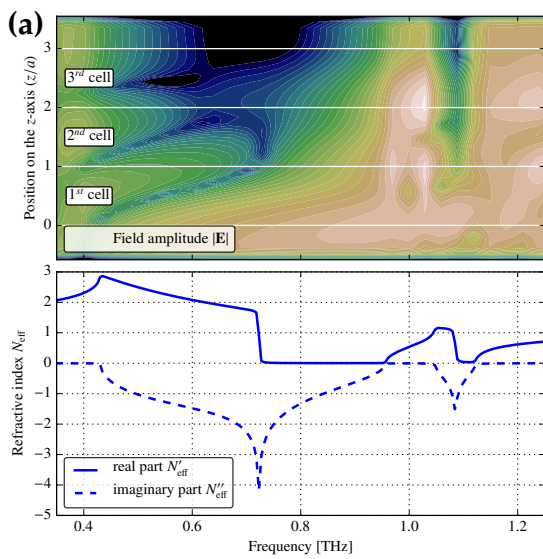
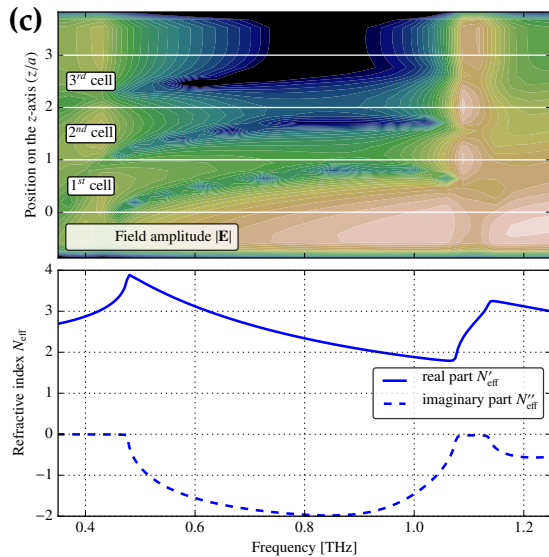
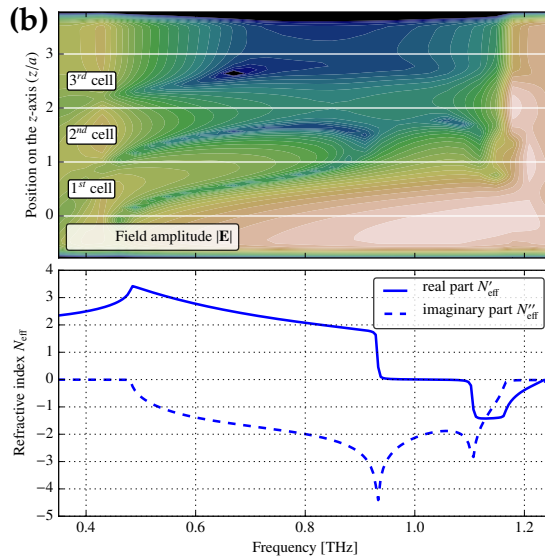
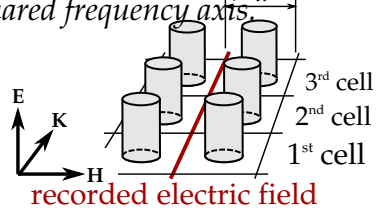


Figure 5.35: Spatially resolved spectra of the electric field $|E_x(z, f)|$ for the unit cell sizes (a) $a = 120 \mu\text{m}$, (b) $a = 90 \mu\text{m}$ and (c) $a = 80 \mu\text{m}$. Dark blue represents the lowest field magnitude and white the highest one, logarithmic color map of the field amplitude is used.

For easier comparison, the effective index of refraction was added below each plot of the fields, with a shared frequency axis.



necessary and sufficient condition for $N'_{\text{eff}} < 0$ to occur in any known metamaterial that can be described by local parameters.

Inspection of the frequency-dependent shape of the field While the PWEM plot gives all information about the field shapes at the band edges (Fig. 5.32), it does not tell anything for frequencies lying in the band gap. Inspection the fields within a band gap is needed to explain the physical reason behind the peculiar disappearance of Mie resonances. It requires a new kind of plots based on time-domain simulations which show how the electric field amplitude depends simultaneously on the position on the z -axis, along which the wave propagates, and on the frequency.

A structure of dielectric rods arranged in three layers was used as a sample sufficiently thick to illustrate the behaviour of the field in the metamaterial cells. Since the above discussion is based on the phase advance of the wave across a cell,

it is sufficient to observe the fields at the central line between the rods only, as drawn in the inset drawing in Fig. 5.35. During the simulation, the electric field amplitude was stored in each FDTD step and for each point along the line.

At the end of the simulation, the Fourier transform of the recorded field was computed in each point and the magnitude of the temporal spectra $|E_x(z, f)|$ was plotted in Figs. 5.35a,b,c. To the author's knowledge, such kind of plots has not been published in any paper yet.

In Fig. 5.35a, the case of sparse rods clearly illustrates that beginning from the lower edge of the first band gap, at 0.42 THz, up to the electric resonance at 0.745 THz, one nodal plane per unit cell crosses the line where field is recorded. The nodal plane can be identified as sets of points where the field intensity drops to very low values, and it introduces a $+ \pi$ shift of the field phase between adjacent cells. Unfortunately, the field pattern close to the resonant frequency is hard to interpret due to boundary effects on the finite structure, but above the resonance one can clearly see that no nodal planes are present. This is in accordance with the predicted exponential decay of evanescent waves when $N'_{\text{eff}} = 0$ and $N''_{\text{eff}} < 0$. The electric dipole of the rods is opposite to the surrounding field in this region, but the nodal planes form closed surfaces around each rod, and the phase difference recorded along the line between the unit cells is zero. From 970 GHz onwards, the second photonic band starts which allows the electromagnetic energy propagate through the structure.

In the second case of the medium-density rod array (Fig. 5.35b), both resonances are located in the first band gap. At the frequency of the first resonance, one nodal plane per each unit cell is removed and the phase advance across the unit cell is reduced from $+ \pi$ to 0. The second resonance further reduces this phase difference, from 0 to $- \pi$, which introduces one nodal plane per unit cell again. Accordingly, faint nodal planes can be observed again in the first band gap between 1100 and 1150 GHz.

Finally, upon reduction of the unit cell size to 80 μm (Fig. 5.35c), the number of nodal planes becomes a constant over the whole band gap, with one nodal plane dividing each unit cell.

The cause of the Mie resonances vanishing Fig. 5.35 shows that the disappearance of Mie resonances for $a \lesssim 85 \mu\text{m}$ is caused by a change in the nodal surface topology. When the rods are far from each other ($a \gtrsim 85 \mu\text{m}$), the individual Mie resonances create closed regions dominated by the near field of the resonance, which are delimited by roughly elliptical nodal surface. Thus in Fig. 5.35b, between 930 and 1100 GHz, no nodal plane is intersected by the line where the electric field is recorded.

Upon reducing the unit-cell size ($a \lesssim 85 \mu\text{m}$) at the same frequency, the regions of opposite fields start to overlap with those from the neighbouring cells and the nodal surfaces interconnect with each other. The wave propagating through an unit cell then changes its sign twice. This manifests itself as a 2π phase change compared to the $a = 90 \mu\text{m}$ case, and by a qualitative change of the N'_{eff} spectrum towards a shape typical for one-dimensional photonic crystals.

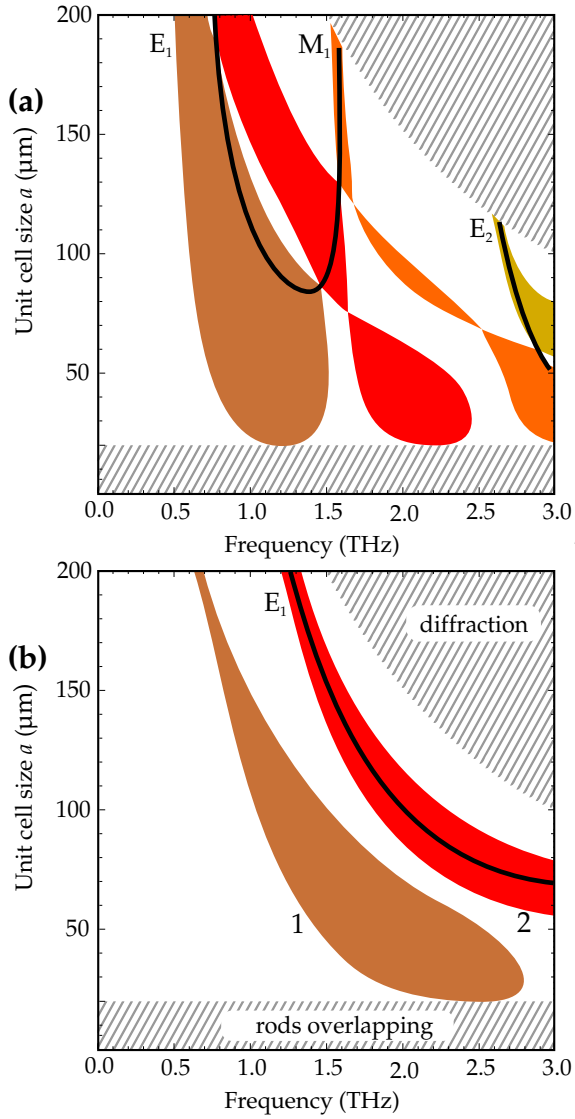


Figure 5.36: Scheme of band gaps and Mie resonances similar to Fig. 5.34, but for (a) halved dielectric permittivity $\epsilon_r = 50$ and (b) further reduced permittivity to that of silicon $\epsilon_r = 12$.

The Mie resonances shift to higher frequencies relative to the band gaps and no $N'_{\text{eff}} < 0$ region is formed for any unit cell size.

Lower dielectric permittivity Both individual Mie resonances and Bragg-type band gaps depend on the dielectric permittivity ε_r . However, the frequency of Mie resonances are more sensitive, and consequently the critical point where the first and second Mie resonances merge shifts to the upper edge of the first gap (see Fig. 5.36a) when ε_r is reduced from that of porous titanium dioxide in the terahertz range ($\varepsilon_r = 92$) to a lower value $\varepsilon_r = 50$. As a result, the negative-index band then cannot be found for any unit cell size. Thus, the dielectric permittivity contrast of at least 50 appears to be essential for obtaining a negative refractive index from any dielectric metamaterial.

Construction of an optical or near-infrared metamaterial restricts the choice of dielectric permittivity compared to the terahertz range. The permittivity of silicon, $\varepsilon_r \approx 12$, is one of the highest available in the near infrared range. The band structure corresponding to $\varepsilon_r = 12$ in Fig. 5.36b shows that for any unit cell size, the first Mie resonance in silicon rod array would always be preceded by at least one band gap of the Bragg type.

The above discussion also shows that the dielectric rods do not have to be geometrically touching to start behaving like a dielectric slab in a 1-D PhC. This is in line with the observation that the scattering cross-section of sub-wavelength objects tends to be greater than their geometrical extent. Strong enough near-field interaction is sufficient for a topological change of nodal planes. The exact critical ratio of the radius to the unit cell size ρ/a depends on the dielectric permittivity. In the array of rods parallel to the electric field, this qualitative change occurs for a particularly low filling fraction, but it should occur in other kinds of structures as well, provided their unit cells are small enough to promote strong near-field interactions between neighbouring resonant elements.

Rod-array metamaterials in the literature A very similar structure was studied in Ref. [18] purely as a metamaterial; each rod was viewed as a separate dielectric resonator, with an analytical formula used to establish the frequencies of Mie resonances as if it were isolated in space. Since the inter-cell coupling is neglected in the paper, its authors predicted that the electric and magnetic resonances would be found even for a relatively low permittivity $\varepsilon_r = 12$. Based on this, its authors concluded that a metamaterial with $N'_{\text{eff}} < 0$ can be built of silicon rods – which is in direct contradiction with our results presented above, and in Ref. [99].

Ref. [109] presents a wedge-refraction experiment with a similar metamaterial, made of bars with a square cross-section parallel to the electric field. The bars have very high permittivity of $\varepsilon_r = 600$, but still the geometry of the bars is equivalent to a *dense array* of cylindrical rods with $a/\rho \sim 4.5$. Thus, it should exhibit no individual resonances and no negative index of refraction. In this paper it is demonstrated [109, Fig. 3bc] that negative refraction occurs at the wedge, and moreover it is more or less maintained upon randomization of the rod positions. The discrepancy can be explained by a relatively high angle of the wedge around 20° , which actually prevents the use of the effective index of refraction.

The impact of Mie resonances on the band-gap structure was studied earlier in Ref. [45], but the related discussion neglected the near-field effect on the resonant frequency. The somewhat coarse simulations in the paper unfortunately did not

include sufficiently detailed scans of the a/ρ ratio and, thus, they could not resolve the qualitative change in the structure behaviour in sufficient detail.

Finally, a similar structure was studied recently in Ref. [17]. Again, the Mie resonance frequencies were deduced from the analytical formula, without taking into account the near-field coupling. This paper correctly points out that different choices of the rod parameters, ε_r and a/ρ , can exchange the position of the Bragg and Mie resonances in the spectrum.

The relevant papers (Refs. [45, 109, 18, 17, 99]) come from the last ten years, although they are based on experimental and numerical methods that could be used already several decades ago. This confirms the author's view that the publications are incited by relatively recent merging of the *metamaterial* and *photonic crystal* paradigms as sketched in Fig. 2.18.

Implications for all-dielectric negative-index metamaterials In Refs. [17] and [99], the structure is regarded as a *metamaterial* when the lowest band gap contains one or both Mie resonances. Otherwise, when the first band gap is of Bragg type, the structure should be classified among *photonic crystals*. The terminology difference has been discussed in the theoretical section, with the conclusion that one structure can be a representative of metamaterials and photonic crystals simultaneously, depending on the paradigm one prefers to use for its description.

This notation is rather formal, since it is based on the *phase criterion* introduced on page 67 and it does not affect the flow of energy. The disappearance of resonances in the spectra is, however, an objective reality; moreover, the fast resonant changes in N'_{eff} are required for the spectra to conform to the Kramers-Kronig relations.

The sufficiently high permittivity required for the *metamaterial* regime can be found in the microwave and terahertz ranges in a variety of materials, such as titanium dioxide with $\varepsilon_r \approx 92$ [125] or in various ferroelectrics like strontium titanate [211]. However, practical applications of the high-permittivity dielectrics in the THz range can be restricted by their high dielectric losses due to low-frequency phonon absorption tails. To our knowledge, there is no material providing such high permittivity in the near-infrared or optical ranges [205]. Our attempts to optimize the rod profile, e.g., by leaving its core hollow, did not provide any improvement in reduction of the minimum permittivity contrast. These facts suggest it is likely not possible to use exclusively dielectrics to build an optical metamaterial with $N'_{\text{eff}} < 0$.

5.9 Metallic sheet with slits

Low-frequency behaviour of a thin sheet When discussing the electromagnetic behaviour of metallic wires parallel to the electric field, we mentioned that wires with the opposite orientation – parallel to the magnetic field – would not appreciably interact with the wave. The situation changes if the wires are widened into stripes, with their transverse dimension (i.e., parallel to the electric field) not much smaller than their periodicity a_x . They may be then equivalently described as a

Figure 5.37: Amplitude of (a) reflectance and (b) transmittance of a single sheet of gold $d_z = 20 \mu\text{m}$ thick with different width of slits d_x . Unit cell size $a = 100 \mu\text{m}$. The grid resolution was $1 \mu\text{m}$.

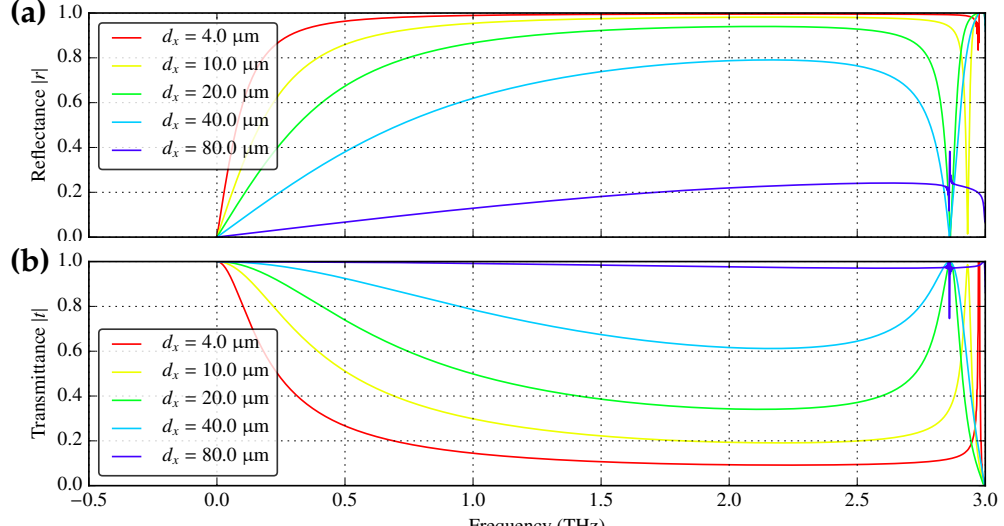
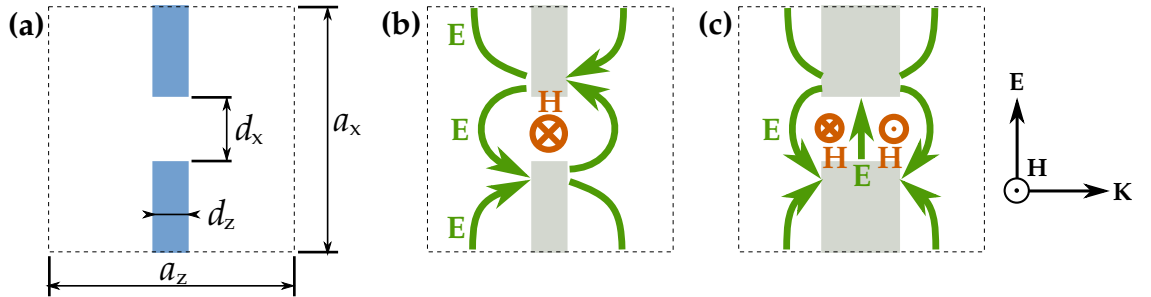


Figure 5.38: Side view of one unit cell of the slit array. (a) The geometry of the x - z cross-section of a single unit cell, which was chosen to be centered to the slit between two metal stripes. The metal stripes extend infinitely along the y -axis. (b) Sketch of the electric and magnetic fields of the first resonance, (c) second resonance for a thicker structure (cf. upper right corner of Fig. 5.40a)

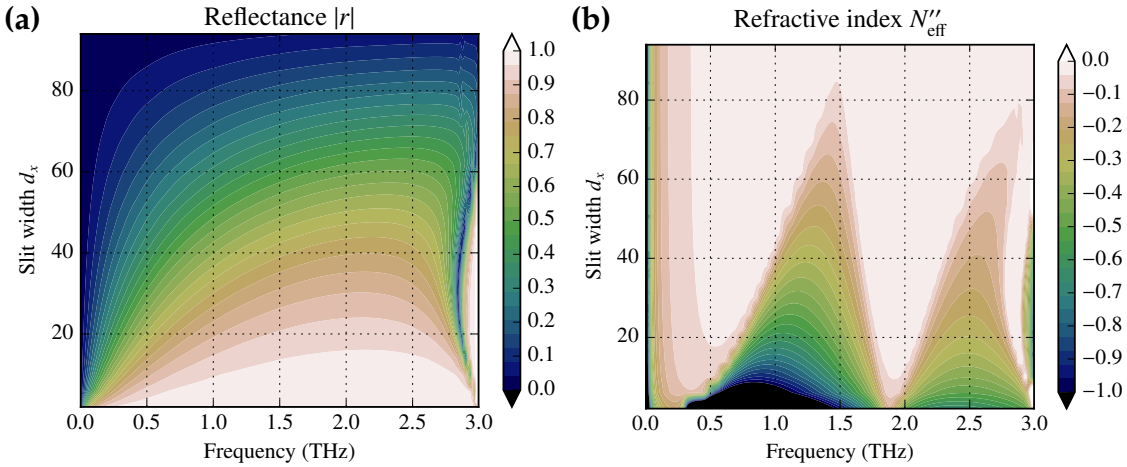


thin metallic sheet divided by slits that have a uniform width d_x and are oriented parallel to the magnetic field, as sketched in Fig. 5.38a.

When the wavelength is significantly longer than the slit width d_x , a single sheet partially reflects the incident radiation (Fig. 5.37). The reflectance amplitude $|r|$ decreases monotonously with the slit width d_x . It also vanishes in the low-frequency limit for any $d_x > 0$, since the macroscopic structure is not conductive in the direction of the electric field. The low-pass filtering capability of this structure is illustrated in more detail by the continuous scan through d_x shown in Fig. 5.39a. The unit-cell size in the x -direction for both presented figures was $a_x = 100 \mu\text{m}$. The upper frequency limit in the plots was determined by the onset of the first diffraction order, at $c/a_x = 3.0 \text{ THz}$.

At a frequency slightly below the onset of diffraction, a relatively narrow notch in the reflectance spectrum is observed, which corresponds to an individual resonance. The frequency where $|r|$ drops near zero depends on the slit width d_x , and on the slab thickness d_z as discussed later. In the above figures where d_z was fixed to

Figure 5.39: (a) Reflectance of a $20\ \mu\text{m}$ thick metallic sheet, with slits of periodicity $a_x = 100\ \mu\text{m}$ and of variable width d_x . (b) The imaginary part of the retrieved refractive index for a metamaterial built by stacking the same slits with periodicity $a_z = 100\ \mu\text{m}$. The values retrieved by the scattering parameter method become invalid near 3 THz, see accompanying text.



$20\ \mu\text{m}$, the lowest frequency of the notch around 2.8 THz is reached for $d_x/a_x \sim 0.3$ (see Fig. 5.39a).

For a narrower or wider slit, the frequency of the notch increases and it eventually approaches the diffraction limit of 3.0 THz. The notch also becomes narrower, but in simulations with a high spectral resolution and low losses, it does not appreciably reduce its depth – some frequency can always be found at which nearly 100 % of the energy is transmitted through the structure.

Standing surface plasmon resonance The effect, known as *extraordinary transmission*, is mediated by excitation of resonant fields on the metallic surface. The field distribution is similar to surface plasmons-polaritons (SPP) propagating parallel to the x -axis as sketched in Fig. 5.38b. It should be more precisely referred to as *spoof surface plasmons*, since the wave is bound to the metallic sheet predominantly because of its corrugation rather than inductive response of the metal. If there were no corrugation, the surface plasmons at terahertz frequencies would propagate in the *Zenneck regime* [212] and their decay length above a flat metallic surface would be much larger than their wavelength. The notch in reflectance is always observed at the exact frequency where the plasmon wavelength is equal to the unit cell size a_x .

A closely related phenomenon on corrugated surfaces of metallic diffraction gratings, the *Wood's anomaly*, is also caused by surface plasmons. It was discovered in 1902 as a sharp drop in the reflectance of metallic gratings [213] under incidence angles that enable the incident wave to couple to surface plasmons. It has incited many theoretical studies starting with that of Lord Rayleigh [214] from 1907.

Since the structure and the incident fields are both symmetric along the x -axis, equal amplitudes of the surface plasmons propagating in the $+x$ and $-x$ directions

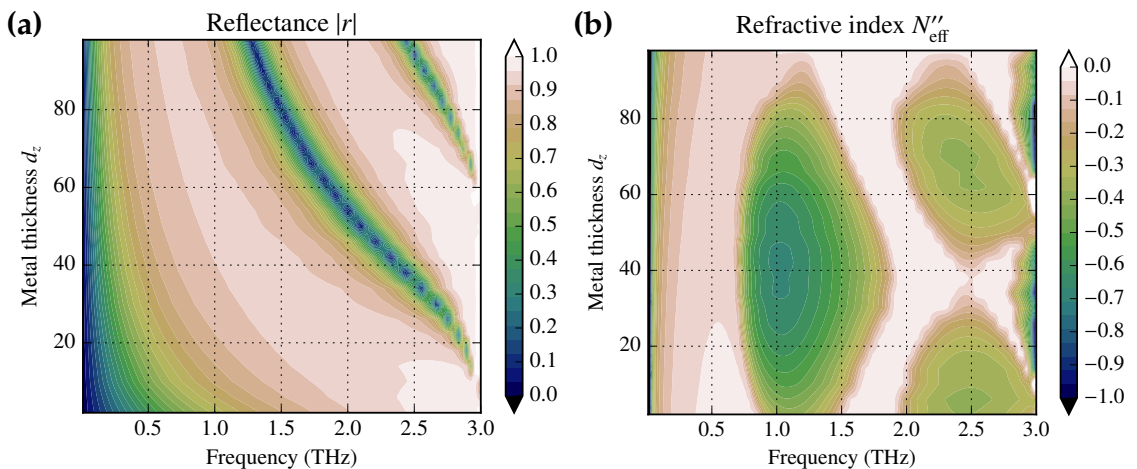
are excited. They form a standing plasmonic resonance, with the points of maximum oscillating current (antinodes) located in the centres of metallic bars. The extraordinary transmission relies on the incoming plane wave coupling to the spoof surface plasmons, transfer of energy of SPPs to the spoof surface plasmons on the rear side of the structure, and re-radiation of the plane wave.

In a numerical study of SPP-assisted transmission through a single slit, Lalanne *et al.* have determined [215] the optimum slit width for wave-plasmon coupling as $d_x \approx 0.23\lambda$, which matches noticeably well the slit width d_x corresponding to the lowest frequency of the zero-reflectance condition (see Fig. 5.39a). A stronger coupling thus appears to down-tune the frequency, but it is not the main determining factor for the peak transmittance efficiency; since the extraordinary transmission is a resonant process, it can achieve a high amplitude of transmittance even through arbitrarily narrow slits.

The extraordinary transmission in slit arrays requires strict periodicity of the slits along the x -axis, and also symmetric front and rear sides of the structure along the z -axis. Our numerical experiment (not shown here) has proven that the energy transfer is suppressed when a dielectric substrate is added on one side of the structure. When the dielectric substrate was added symmetrically from both sides, the extraordinary transmission was restored and its resonant frequency was lower than without the dielectric.

We also observed that the dielectric does not have to touch the metal directly; a distance similar to the unit cell size was sufficient for the reflectance notch to be suppressed. We thus conjecture the approximate decay length of the surface plasmons along the z -axis, both in front of the structure and behind it, is not much smaller than a_x .

Figure 5.40: (a) Reflectance of a metallic sheet with slits of periodicity $a_x = 100 \mu\text{m}$ and of $d_x = 20 \mu\text{m}$, with variable thickness d_z . (b) The imaginary part of the refractive index for a metamaterial built by stacking the same slits with periodicity $a_z = 100 \mu\text{m}$. The values were retrieved by the scattering parameter method, so the upper part of the panel (b) is not reliable, as commented in the text.



Effect of the metallic slab thickness In the approximation of a thin slit with $d_z \ll a_x$, the highest transmittance was observed when the surface plasmon wavelength λ_{SPP} matched the unit cell size a_x . In the limit of thin sheets, this frequency approaches the diffraction limit of c/a_x , since surface plasmons in the terahertz range are only weakly bound to the metal surface and their phase velocity is similar to the speed of light in vacuum, c . Upon scaling the simulation into the optical range, the limiting frequency for thin metallic sheets was reduced below c/a_x and, moreover, the exact behaviour of the structure has proven to depend on the choice of metal.

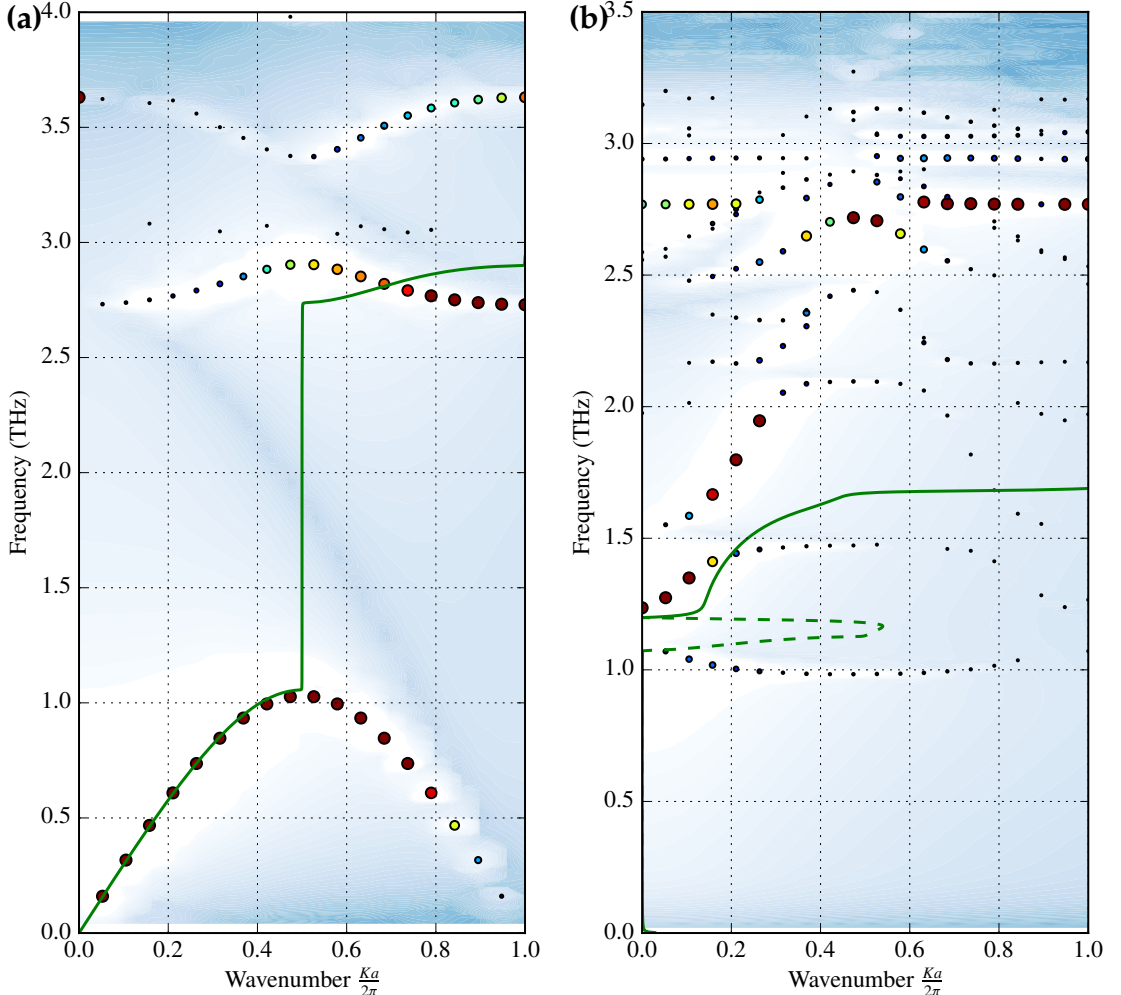
For thicker sheets of metal, the effective optical path of surface plasmons travelling across one unit cell is increased by its portion in the inner slit surface, as it was shown experimentally in Ref. [216]. The frequency of the zero-reflectance notch thus decreases when the sheet thickness is enhanced, since a longer SPP wavelength is needed to compensate for the increased circumference of the cross-section of the metallic bar. For thick enough slabs with $d_z \gtrsim a/2$, the frequency of the zero-reflectance notch approximately follows the inverse of the thickness (see Fig. 5.40a). In the upper-right corner of Fig. 5.40a, the second zero-reflectance region can be found, which corresponds to the second longitudinal waveguide mode drawn in Fig. 5.38c.

Effective parameters of the sheet-slit array The previous paragraphs described the reflectance and transmittance of a single layer. Multiple layers can be arranged into an infinite stack with a given unit cell size a_z along the wave propagation, and their effective parameters can be computed in the same way as with other metamaterials.

However, one has to verify whether the scattering parameter method gives correct results, since the structures exhibit a strong coupling between the neighbouring cells. A great portion of the resonant energy is transferred by the surface plasmons that were shown not to be well localized in a single unit cell. On the contrary, they couple strongly with those on nearby metallic surfaces, forming transversally propagating slot-waveguide modes [216]. The current-driven homogenisation (CDH) setup is more suitable for simulations of such structures with strong coupling between the neighbouring cells, since it simulates one unit cell in its periodic environment exactly. The results of the two methods are compared in Fig. 5.41a, with the accurate CDH dispersion curves indicated by points, and the s-parameter results overlaid as green curves.

The first photonic band is obviously accurately matched by both simulation setups. In the second band, located close to the diffraction edge where the dispersion is determined by excitation of surface plasmons, the scattering parameter method completely fails to predict not only its exact shape, but even the sign of the group velocity.

Figure 5.41: Current-driven homogenisation results for (a) an infinite array of metallic slabs $20\ \mu\text{m}$ thick of periodicity $a_z = 60\ \mu\text{m}$, divided by slits of $d_x = 20\ \mu\text{m}$ with the periodicity $a_x = 100\ \mu\text{m}$. (b) The same for a fishnet with the hole periodicity $a_x = a_y = 250\ \mu\text{m}$, the slab periodicity $a_z = 52\ \mu\text{m}$ and the circular holes had radius of $55\ \mu\text{m}$ (the same proportions as in Ref. [217]). The CDH approach predicts a negative index of refraction (points), whereas the s-parameter approach gives unrealistic values (green line).

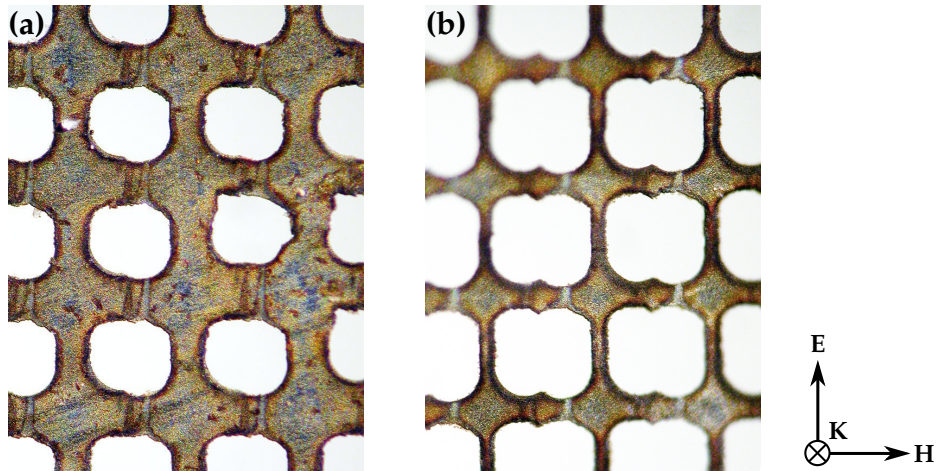


5.10 Fishnet

Extraordinary transmission in fishnets By adding conductive connections across the slits in the above described structure, a perforated metallic sheet is formed which is also denoted as a *mesh*, *sub-wavelength hole array*, or within the context of metamaterials, as a *fishnet*. Already in the 1950s, an array of perforated metallic sheets was proposed to form an artificial dielectric with an index of refraction $0 < N'_{\text{eff}} < 1$, but the electromagnetic wave propagated parallel to the slabs [87, p. 58]. The spectral selectivity of a single metallic mesh perpendicular to the wave vector was employed in the 1960s to set up a microwave and far-infrared filter [218, 219, 220].

The interest in sub-wavelength hole arrays was revived when periodic patterning of a metallic surface near a sub-wavelength hole was shown [221] to enable the

Figure 5.42: Micrographs of fishnets cut from a $5\text{ }\mu\text{m}$ thick stainless steel foil, (a) holes of ca. $180 \times 200\text{ }\mu\text{m}$, (b) holes of ca. $230 \times 255\text{ }\mu\text{m}$, cut by a "z"-shaped movement of the laser beam. The periodicity of both fishnets is $300 \times 300\text{ }\mu\text{m}$, real size of both images is $1.2 \times 0.9\text{ mm}$.



extraordinary optical transmission which can be orders of magnitude larger than the transmission estimated from the geometrical hole dimensions. In a similar way as in the slit array, the incident light couples to surface plasmons, the energy is efficiently transferred through the hole, and finally re-radiated again at the rear side.

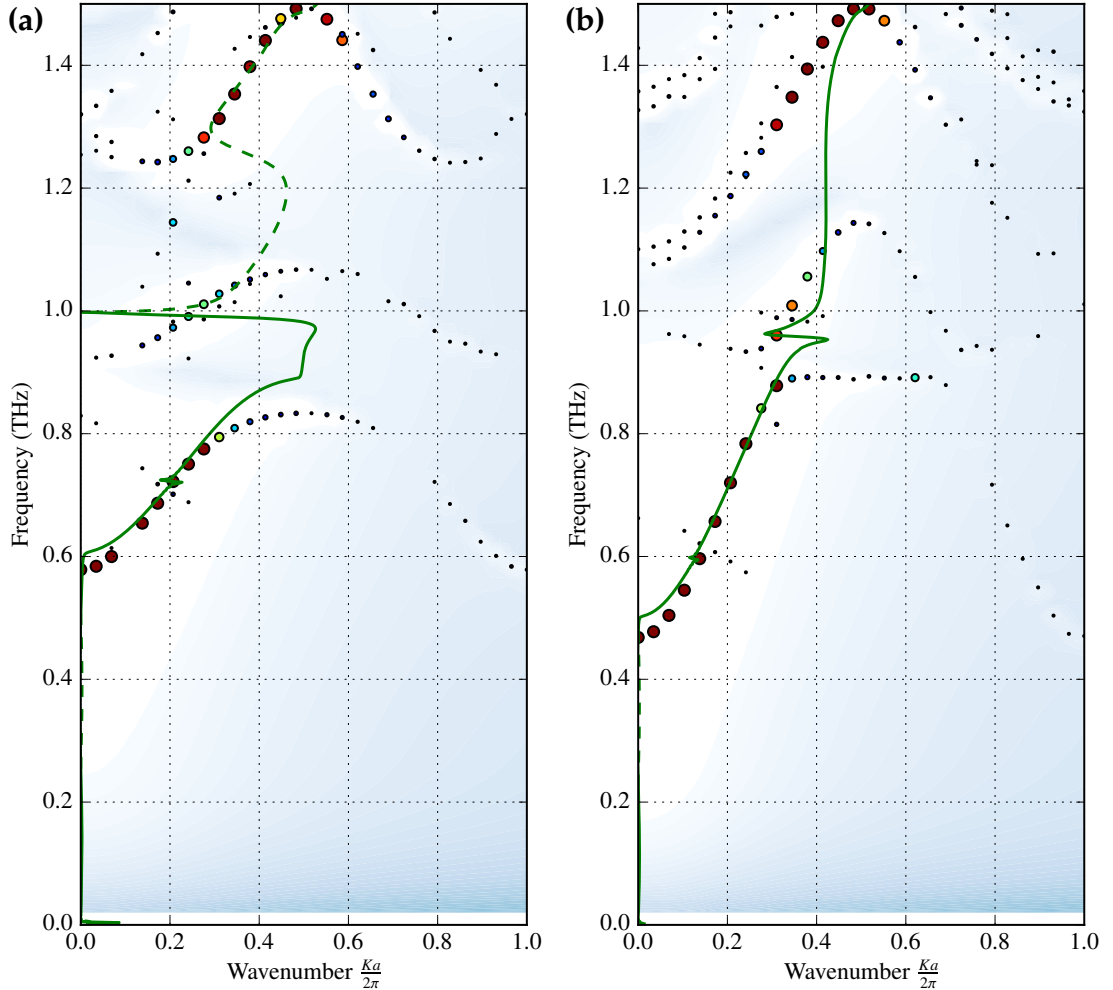
Negative index of refraction With a convenient choice of geometrical parameters, the waves radiated from the opposite side of the sheet have negative phase advance compared to the incident ones, leading to a negative phase advance along the unit cell and to the formation of a $N'_{\text{eff}} < 0$ band. An important improvement over the previous designs of negative-index metamaterials is that fishnets achieve relatively low losses even in the near-infrared and optical ranges, since their simple geometry is optimised for short conduction paths.

Simultaneously, the occurrence of $N'_{\text{eff}} < 0$ is relatively sensitive to the choice of parameters of the structure, most importantly, to the spacing of the holes in the x - y plane, to their dimensions and to the spacing of the metallic sheets along the z -axis, in the following way:

1. The transverse periodicity of the holes determines the frequency of operation, by a mechanism similar to that described in the previous chapter.
2. The dimensions of the holes influence the coupling strength, but the resonant frequency is affected only weakly. Small holes lead to a weak coupling of the surface plasmons and to a narrow photonic band with $N'_{\text{eff}} < 0$. In contrast, too large holes lead to broad photonic bands which, however, never reach $N'_{\text{eff}} < 0$.

If the holes are anisotropic, the described effect is more sensitive to the hole dimensions parallel to the magnetic field. The anisotropic shape of the holes was shown to influence the impedance, allowing one to suppress reflections [222].

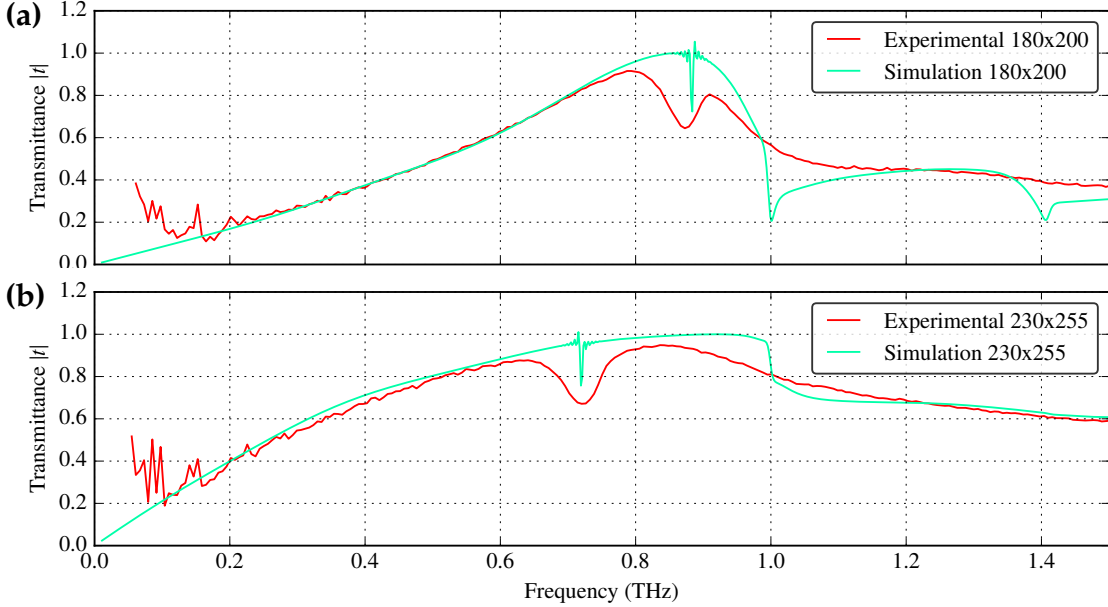
Figure 5.43: Current-driven homogenisation results for two samples of fishnets shown in Fig. 5.42; (a) holes of $180 \times 200 \mu\text{m}$, (b) holes of $230 \times 255 \mu\text{m}$



3. Finally, the spacing of the metallic sheets along the z -axis determines the strength of the interaction with the waves. When the layers are overly sparse, the positive phase acquired between them overpowers the effect of plasmonic resonances and prevents the formation of a $N'_{\text{eff}} < 0$ band. When they are very dense, the near-field coupling apparently becomes the dominant mechanism of energy transport, which is the case of numerous experimental samples. For instance, in Ref. [223], the sheet distance ($a_z = 83 \text{ nm}$) was less than 10 % of the transverse hole periodicity ($a_x = a_y = 860 \text{ nm}$). The scattering parameter method is obviously not applicable for this kind of structures.

Comparison of homogenisation methods for fishnets The conventional explanation is that the negative refractive index of fishnets arises from the combination of negative effective permittivity and permeability. The former, $\varepsilon'_{\text{eff}} < 0$ is attributed to the inductive effect of the metallic connections which should develop an electric dipole opposite to the incident electric field in a way similar to the wires oriented

Figure 5.44: Experimental and simulated amplitude of transmittance for fishnets (a) with $180 \times 200 \mu\text{m}$ holes, and (b) with $230 \times 255 \mu\text{m}$ holes.



along the x -axis. The magnetic response is formed by individual resonances localised close to the fishnet holes, which exhibit a magnetic dipole moment.

Some papers note that the s-parameter method may not be applicable to fishnets [222][199, p. 102], which is indicated by differences in retrieved parameters depending on the number of layers. At the same time, this does not imply that the infinite structure cannot be assigned a negative index of refraction; a wedge formed of a fishnet metamaterial was demonstrated to refract terahertz rays under negative angles [224] as predicted.

For illustration, we computed the dispersion curves of the fishnet from Ref. [217] in Fig. 5.41b. To approximately match the frequency band of operation with other structures described, we up-scaled the dimensions of their structure; the exact numbers are given in the figure description. The dispersion curves indicated by bubbles were retrieved using current-driven homogenisation. We believe this homogenisation approach is free of artifacts also for this kind of structure.

This structure shows a narrow band between 980 and 1080 with a negative index of refraction. As indicated by the dashed green curve in Fig. 5.41b, even the scattering parameter method detects this $N'_{\text{eff}} < 0$ band, but the found frequency is erroneously shifted up by about 100 GHz. The error in higher bands is even more pronounced. The scattering-parameter method eventually fails to predict anything above the onset of diffraction at 1200 GHz.

Experimental results Two samples of fishnets, fabricated by femtosecond laser machining of a steel foil, are photographed in Fig. 5.42. Their hole periodicity was $300 \times 300 \mu\text{m}$. They differed by their hole dimensions; the first one had approximately elliptical holes with axes $d_x \times d_y = 180 \times 200 \mu\text{m}$, the second one featured much narrower metallic bridges between the holes with $d_x \times d_y = 230 \times 250 \mu\text{m}$. The

holes were cut to the shape of rounded rectangles, which however did not change the electromagnetic behaviour.

The dispersion of such a metamaterial had again to be characterised using the current-driven homogenisation. We chose the layer periodicity $a_z = 200 \mu\text{m}$ and presented the corresponding dispersion curves in Fig. 5.43a,b. For both samples, the first photonic band was relatively well retrieved also by the scattering parameter method (green curves). In the portion of spectrum approaching the diffraction onset at 1 THz, only the CDH results seem to be valid.

For the fishnet with smaller holes in Fig. 5.43a, the second photonic band starts with a positive group velocity at 920 GHz. The corresponding photonic band in the right panel, however, starts with a negative group velocity, changing to the positive one in the middle of the first Brillouin zone for $Ka/2\pi \approx 0.25$. This effect can be explained as anticrossing of two photonic bands.

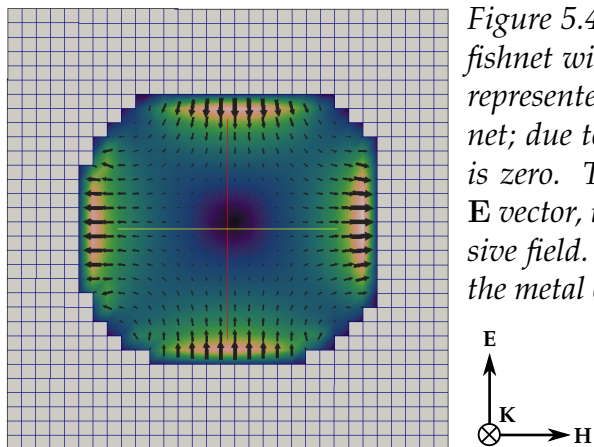


Figure 5.45: Electric field of the quadrupole mode in a fishnet with $180 \times 200 \mu\text{m}$ hole sizes. Field vectors are represented by black arrows in the x-y plane of the fishnet; due to symmetry, the E_z component in this plane is zero. The colour map shows the magnitude of the \mathbf{E} vector, the brighter values correspond to more intensive field. The surrounding light-gray area represents the metal of the fishnet.

Quadrupole resonance in experimental spectra The corresponding experimental transmittance spectra of single layers of both fishnet samples are presented in Fig. 5.44 (red curves). They were compared with the computed transmittance (green curves).

Typically the voxel sizes of 2 or 4 μm were used throughout the thesis as a good tradeoff providing reasonable simulation time and accuracy of results, including the CDH computation of fishnets in Figs. 5.43a,b. In contrast, for the computation of Figs. 5.43 and 5.44, the FDTD simulation was deliberately set to a very coarse resolution, with a voxel dimension of 10 μm . Still, the lower-frequency part experimental and computed reflectance spectra yielded a notably good match.

In the experimental spectra of fishnets, between 0.5 and 1.0 THz, a distinct notch in transmittance was observed. The discretisation error has helped to explain its origin. With a coarse simulation grid, the twofold mirror symmetry of the fishnet unit cell was broken, since the simulation defined a different number of voxels in the rounded hole edges.

Simultaneously, it also eliminated the symmetry of the fields in the first quadrupole mode, introducing a slight electric dipole into its field pattern (see Fig.

5.45). As a result, the quadrupole started to couple with the incident plane wave, and narrow resonances emerged also in the simulated spectra at 880 and 710 GHz, respectively (green lines in Figs. 5.44a,b). The resonance notches observed in the experiment are thus conclusively explained by the simulations.

These resonances can be also observed in Fig. 5.43a,b as weak photonic branches crossing the first photonic band in its middle, although the periodic boundary conditions change their frequencies. The different symmetries of resonances stipulate that the waves coupled to the quadrupole mode of the fishnet propagate with group velocity direction opposite to that one coupled to the dipole mode.

Chapter 6

Conclusion

“If you want to build a ship, don’t drum up people to collect wood and don’t assign them tasks and work, but rather teach them to long for the endless immensity of the sea.” — Antoine de Saint-Exupéry

Theoretical contributions The theoretical section of this thesis aimed to present an accessible introduction to the electrodynamics of periodic structures. It started from the fundamental Maxwell equations, developed the concept of waves propagating in vacuum and in resonant media, and shown how the local medium responds to oscillating electric field as a damped oscillator and how it influences the dispersion curves. In the following chapter, the nonlocal response was introduced, and it was described how it causes the material properties to depend not only on the frequency, but also on the magnitude of the wave vector, which is known as spatial dispersion.

This phenomenon is common in optics, but in homogeneous materials it is usually negligible. When the electrodynamics of periodic structures is concerned, the spatial dispersion is often particularly pronounced and should not be neglected. More general shapes of the dispersion curves in spatially-dispersive media were illustrated in several figures.

The dispersion curves were also shown to become periodic with regard to the wavevector, which is a result of the Bloch’s theorem; the chapter further introduced the concepts of isofrequency contours, Brillouin zones and high-symmetry points in the reciprocal space, and discussed the conditions under which the notions of group, phase and information velocity are applicable.

Nowadays, perhaps more than ever earlier, it is important to maintain an outlook over the history of the rapid scientific development. A historical review follows which traces back the origin of numerous concepts much earlier than the majority of metamaterial-related papers advertise. The historical part promoted the author’s view on the notions of *artificial dielectrics* and *negative-index media*, which appear to have developed independently, to be unified around the middle of twentieth century. In a similar manner, it was argued that the resulting paradigm of *negative-index metamaterials* unified with the concept of *photonic crystals* around the millennium. The process of unification always sheds new light on the physical interpretation and is beneficial for conceptual development of the field. The historical

review became a basis for outlining the boundary between metamaterials and photonic crystals, which concluded the theoretical section.

Methodological contributions The preparation of this thesis, which encompasses over 90 plots that show the results from over 4000 separate computations, necessitated the development of an efficient and convenient platform for numerical simulations of electromagnetic waves in periodic structures. The computations are defined in the form of scripts in the Python programming language. At the expense of a possibly slower learning curve than the programs with a graphical user interface may offer, a great advantage of scripting is a seamless integration with further processing of the simulation results that would otherwise be prohibitively tedious. The scripts can also be modified for automated parametric scans, optimisation of the structure performance and to match experimental data.

All scripts, containing roughly 5000 lines of Python code in total, were published online as open-source software [117] with the hope that they would be reused by others for future numerical research.

In the Numerical chapter, the internal operation of the finite-difference time-domain computation method is described in detail. Particular attention was paid to a realistic definition of Lorentz-Drude models for dielectrics and metals, including author's empirical rules for the numerical stability of the FDTD simulation.

The second part of the section describes how the same numerical algorithm can be used in different geometries to retrieve physical properties of the structure: the customary *scattering-parameter method* is elaborated including its limitations and pitfalls, and finally it is compared to the *current-driven homogenisation* method, which is less computationally efficient, but more robust against artifacts. Both methods were extensively employed and compared in the results.

The inherent ambiguity of the scattering parameters method is often cited in the literature. We resolved the ambiguity in our own original way, based on the purely mathematical consideration of the arccosine discontinuities in the complex plane. The correction algorithm was incorporated in the simulation post-processing scripts and its application to all presented results proved that it works reliably.

Summary of the results The Results chapter presented an overview of the electromagnetic behaviour of ten most common classes of metamaterials, in a didactic approach that the author felt to be missing in the available literature.

1. It started with a one-dimensional photonic crystal, which can be viewed as the simplest periodic structure. Its dispersion curves consist of alternating photonic bands and band gaps, but no individual resonances can occur. The conditions for the formation of a zero-width photonic band gap are shown in parametric scans. The low-frequency and high-frequency limits for the effective index of refraction are demonstrated.
2. Replacing the dielectric layer with an array of metallic wires parallel to the electric field does not change the high-frequency behaviour qualitatively, but below the plasma frequency, it introduces a plasma-like response with negative effective permittivity. The resulting plasma frequency is determined by

the geometry; Fig. 5.7 compared the numeric results with analytic models, showing a good match.

3. Periodic gaps in the wires introduce the individual resonances with an electric dipole. Their spectra of effective parameters were described in detail, since they are typical also for resonances in other structures. Parametric scans through wire radius and cut distance were shown to have nontrivial effects on the resonant frequency. Our experimental data from cut-wire array on silicon substrate were compared to numerical model, and the difference was explained as an effect of asymmetry and losses in the real sample.
4. The individual resonances with an electric dipole were compared to their counterparts with a magnetic dipole forming the fundamental resonance of split-ring resonators. The resonator with a single splitting in the ring is asymmetric, and it was demonstrated that erroneous results for this structure are retrieved by any homogenisation method that does not account for the asymmetry. The version with a symmetric splitting, however, can be homogenised to obtain negative permeability. Further, a combination of the double-split ring resonator with the wire array was shown to yield the negative index of refraction with compatible results between the s-parameters method a current-driven homogenisation.
5. On the contrary, the discrepancy between these two approaches to homogenisation cannot be neglected when a central shunt conductor is added to a symmetric split-ring resonator. Then the electric type resonance becomes the fundamental one, and by continuous changes in the geometry one can tune the electric and magnetic resonance frequencies. While it might be intuitively expected that both resonances would form a region of negative refractive index, the simulations shown that the spatial dispersion causes the dispersion curves to bend into a concave shape instead, enabling the structure to support multiple modes at the same frequency. Consequently, the scattering-parameter method cannot determine the effective index of refraction.
6. Dielectric spherical resonators were shown to exhibit individual resonances of Mie type, the first of which is analogous to the resonance in split-ring resonator. With the exactly defined dielectric model of the constituent dielectric, we could deduce minimum dissipative losses that can be achieved in an experiment and shown what impact they have on the resonance spectra. Further we accompanied the computed spectra with our experimental results, arguing that the substantial deviation between these arose from the inhomogeneity of the resonators in the sample. Taking the inhomogeneity into account yielded a reasonable match with the experiment. Extended sieving of the spheres improved the resonance deeper, but no negative permeability was reached.
7. The spectra of dielectric rods parallel to the magnetic field were compared to that of dielectric spheres, pointing out their similarity. The resonant modes for low- and high-permittivity dielectrics were compared, too, to illustrate that

- continuous changes in the dielectric permittivity lead to a qualitative change – a crossover of the Mie and Bragg resonances in the spectra.
8. A similar, and even more pronounced, change was observed in the dielectric rods parallel to the electric field. Depending on the filling fraction and permittivity contrast, the structure can behave differently in different portions of spectra: either as a one-dimensional photonic crystal, similar to a wire array, or exhibit negative index of refraction. By extensive parametric scans we demonstrated that the desirable latter mode of operation cannot be achieved, for any known geometry, when the dielectric contrast is less than roughly 50, which precludes building negative-index metamaterial solely from any low-loss dielectric commonly used in photonics.
 9. On the example of a metallic sheet with slits parallel to the magnetic field we showed the effect of extraordinary transmission. We argue that it is mediated by standing surface plasmons, frequency of which depends on the slit periodicity and is almost independent of their width. Further we demonstrated that with increasing the metal thickness, the extraordinary transmission down-tunes with accordance to the dispersion of slot-waveguide modes.
 10. Finally, we showed that the extraordinary transmission mediates the propagation of waves also in fishnet metamaterials made of stacked perforated metallic sheets. Current-driven homogenisation plots for three different fishnets were compared to the scattering-parameter method, revealing that the latter is hardly applicable to this kind of structures, due to strong near-field coupling between neighbouring cells. Fishnets also support additional waves carried by quadrupole resonances, which was also observed in terahertz spectra of samples manufactured in our laboratory. Nevertheless, the simulations predicted that under a careful choice of geometry and illumination, fishnets exhibit a band of negative refractive index.

There remain many topics that are related to the subject of the present thesis, which were not discussed here, such as other crystal families than the square/cubic one, possibly including also quasicrystals or disorder. Except for the fishnet samples, the discussion was restricted to structures sharing symmetries with the incoming fields; more general classes of structures would involve bianisotropy/chirality. Also the nonlinear response of all structures can be studied, but one has to be aware that the Bloch's theorem and most of the presented theory assume a strictly linear response. However, direct numerical simulations of these phenomena can be presumably achieved with a relatively easy adaptation of the simulation scripts.

Another particularly useful direction of research would consist in adding the support of gyrotropy into the MEEP library, i.e. non-hermitian form of the permittivity or permeability tensors which breaks the time-reversal symmetry. This would open wide research possibilities of linear metamaterial devices with pronounced non-reciprocal effects.

Conclusions for metamaterial homogenisation Throughout the thesis, we encountered many structures that can be described by effective parameters corre-

sponding to a virtual homogeneous medium with the same macroscopic behaviour, and we argued that our decision to view the structure as homogeneous may form a good criterion to define the notion of *metamaterials*. However, different kinds of technical or conceptual difficulties arise during the homogenisation.

The observation of a *negative refraction* at the interface of air and a given structure does not imply that it has a *negative effective index of refraction*, $N'_{\text{eff}} < 0$, since this homogenised parameter may not be defined at all. Some form of anisotropy is more or less present in all periodic structures; very often it is strong enough to preclude the use of N'_{eff} . On page 27 we have argued that one exception is when the light propagates nearly parallel to an optical axis of the anisotropic medium – this warrants assigning effective parameters to most metamaterials. The zero-width band gaps with a cusp in isofrequency contours present an exception from this exception, as suggested on page 124.

Some metamaterials have such a strong spatial dispersion that their dispersion curves allow *additional waves* sharing the same frequency and direction of propagation (Fig. 5.21a, 2.12), and this is another complication that precludes the description of the metamaterial by a single spectrum of N_{eff} .

When a scientific method is used beyond its scope, sometimes it leads to a mathematical error or returns results which are obviously invalid. We showed on several examples that the widely used *scattering parameter method*, unfortunately, does not indicate its limits of applicability. By its means, a finite slab of a metamaterial can always be assigned some effective parameters (see page 94). However, even when the spatial dispersion is not strong enough to enable the existence of *additional waves* as is the case of Fig. 5.41a, the near-field coupling between neighbouring cells may be relatively strong. Then the scattering-parameter method fails to predict the behaviour of an infinite periodic lattice and N_{eff} has to be determined by a more robust approach, such as the current-driven homogenisation. We suggest that the scattering-parameter method results should always be checked using the basic criteria of validity, such as the absence of non-resonant skips in the spectra, their compliance to Kramers-Kronig relations and their negligible sensitivity to the number of simulated unit cells.

Finally, even when the scattering parameter method yields a physically sound index of refraction, it does not guarantee that the retrieved effective impedance Z_{eff} is valid nor that the medium may be described by means of the effective local permittivity ε_{eff} and permeability μ_{eff} . These effective parameters require the unit cell to be much smaller than the Bloch's wavelength. In most metamaterials, this condition is fulfilled in one or few narrow portions of the spectrum only, namely where $|N'_{\text{eff}}| \ll c/(2af)$. Otherwise the spectra of ε_{eff} or μ_{eff} acquire typical antiresonance artifacts, which have incited disputes stretching over several papers (starting with Ref. [106]). We argued that the Landau-Lifshitz form of permittivity $\varepsilon_r^{\text{LL}}(\omega, \mathbf{K})$ is required to fully account for the spatial dispersion.

The described non-implications are summed up by the following scheme:

$$\begin{array}{ccc} \text{negative} & & \text{s-parameter} \\ \text{refraction} & \not\Rightarrow & \text{method} \\ & & \text{applicable} \end{array} \quad \not\Rightarrow \quad \begin{array}{c} \exists N'_{\text{eff}} < 0 \\ \exists \varepsilon'_{\text{eff}} < 0 \\ \exists \mu'_{\text{eff}} < 0 \end{array} \quad (6.1)$$

Let us note that implications opposite to these shown may not hold, either. For instance, in Figs. 5.20 and 5.21, the array of the combined split-ring resonators may have clearly defined electric and magnetic individual resonances, yet the index of refraction N_{eff} is not applicable when they overlap.

Closing words While metamaterials were successfully tested in the radio-frequency and microwave ranges, e.g., for compact antennas or magnetic resonance imaging [225], probably the majority of related papers are dedicated to achieving negative index of refraction or a cloaking effect, with as high frequency and as low losses as possible. On the way to this tantalizing aim and to fast publication, too often they use an overly simplistic theoretical description or inadequate characterisation approach, or both.

The rapid growth of the number of papers related to metamaterials observed in the last two decades is certainly beneficial for the overall growth of knowledge. However, one should not forget about the price to be paid for it. Some of the concepts which were developed decades ago seem to be re-invented and published as novel. Aside of it, a significant portion of papers deals with the same class of structures, presenting only a minute quantitative improvement over the previous results, and they fail to bring any conceptual progress. This way, they dilute the information density of even high-impacted journals. This is exacerbated by the fact that, in the author's experience, even the metamaterial monographs are mostly assembled of separate papers that are unrelated to each other and by far not covering all relevant theory.

In contrast, the genuinely tough issues seem to be rather underexposed. In the infrared and optical range, these are most importantly the ubiquitous dissipative losses. They are common for high-permittivity dielectrics and metals, while the permittivity of any known low-loss material appears insufficient for metamaterial behaviour [99]. Also, all contemporary superconductors lose their superconducting properties above terahertz frequencies. To the knowledge of the author, all experimental demonstrations of such metamaterials are restricted to tiny samples which remain relatively transparent. Active amplification in unit cells, using either lumped components [202] or stimulated emission, may partially compensate the losses, but it appears very hard to achieve necessary linearity and homogeneity.

The sub-diffraction imaging has yet another fundamental issue aside of the dissipative losses. It requires to suppress the spatial dispersion, which arises from nonzero dimensions of the unit cells. If the future progress in nanotechnology succeeds in overcoming this obstacle, the question remains whether it would not become also more than sufficient for the fabrication of superior measurement techniques, completely eliminating the need of any metamaterial super- or hyper-lens.

The challenges which the metamaterial research faces nowadays may be overcome once. However, it appears much more likely to the author that the related research will be beneficial indirectly, by inciting development in an unexpected direction, be it in nanofabrication, material science, solid-state physics, nonlinear optics, theoretical electrodynamics, or any other field of physics and technology.

It would be beneficial to avoid regarding metamaterials as mere means for putting into practice the notorious – but so far, mostly elusive – list of practical

tasks they seem to promise. Instead, in line with the quotation from the start of this section, it can be much more inspiring and useful to *long for the endless immensity* of different phenomena that emerge from the wave interaction with periodic structures.

Index

- additional boundary conditions, 40
additional wave, 141
amplitude vector, 14
anticrossing, 22
antiresonance, 62, 132, 145
apodization, 81
artificial dielectrics, 59
artificial plasma, 59, 122
avoided crossing, *see* anticrossing

band gap, 50
 Bragg band gap, 52, 53
 complete, 54
 direct and indirect, 52
 in a planar waveguide, 54
 photonic, 52
 photonic, of zero order, 62
biisotropy, 134
Blackmann-Nutall window, 92
Bloch's
 lattice, 89
 theorem, proof, 44
 wave, 43
 wave in vacuum, 47
 wave vector, 45
Bragg condition, 117
branch cuts of arccosine, 87
Brillouin zone, 48
 irreducible, 48

carpet cloak, 57
conductivity, 73
constitutive relations, 13
Courant factor, 68
 maximum value of, 70
crystallographic systems, 42
current-driven homogenisation, 89

Debye relaxator, 19
defect mode, 54

dielectric mirrors, 53
dielectric-rod array filter, 157
diluted metal, 122
Dirac point for photons-polaritons, 118
dispersion
 anomalous, 22, 41
 curves, folding of, 47, 116
 in dielectrics, 16
 in vacuum, 15
 numerical, 67
 spatial, 29
distributed impedance, *see* s-parameter method

effective, 78
electric polarisation, 16
electromagnetic cloak, 57
emergence in metamaterials, 64
equifrequency contours, *see* isofrequency contours
evanescent wave, 79
extraordinary transmission, 167

Fano resonance, 83
figure of merit, 145
filter diagonalisation method, 92
fishnet, 170
Fourier-Plancherel theorem, 80
frequency, 14
 angular, 14
 effective plasma f., 122
 of oscillator resonance, 18
 plasma f., 72
 scattering f. in metals, 72
Fresnel coefficients, 39
Fresnel inversion, 77

gauge freedom in electrodynamics, 32
granulometry, 112
Hann window, 81

Hilbert transform, 21
 homogenization, 59, 65
 hyperlens, 60

imaginary, 85
 impedance of medium, 39
 index of refraction, 25
 effective, 26
 negative, 29, 55
 negative, history of, 55
 inner, 139
 isofrequency contours, 24
 curvature of, 26
 isotropic, 146

leapfrog algorithm, 67
 limit
 long-wavelength , 58
 static, 58

magnons
 bulk, 55

Maxwell equations, 13

media
 left-handed, 55

medium
 anisotropic, 23
 hyperbolic, 28
 isotropic, 25
 linear, 23
 local, 16
 nonlocal, 29
 right-handed, 15
 spatially dispersive, 29

mesh, 170

metallic delay dielectrics, 122

metamaterial, 164
 cut-wire pair, 134
 double split-ring, 133
 fishnet, 60
 fabrication, 115
 history, 59
 omega structure, 134
 strip pair, 134
 swiss-roll, 134

metasurfaces, 61

Mie resonances, 144

mode functions, 43
 Moivre theorem, 87
 multipole, 52

Nicolson-Ross-Weir method, *see*
 s-parameter method

nodal plane, 64, 117
 nodal surface, *see* nodal plane
 nonlocality, *see* spatial dispersion

ordinary, 70

oscillator
 damped harmonic, 17
 damping rate, 18
 strength, 18

padding, 79

perfectly matched layers, 78

periodicity, 42

permeability
 local, 19
 near zero, 56
 negative, 55
 of vacuum, 13

permittivity
 as a function of frequency, 30
 effective, 59
 Landau-Lifshitz form, 31
 near zero, 56
 negative, 55
 of vacuum, 13
 relative of a dielectric, 17

phase of a wave, 14

photonic crystal, 164
 fiber, 55
 history, 54

plane-wave expansion method, 76

polariton branches, 22

Poynting vector, 40

Purcell effect, 51

quadrupole, 52

reciprocal space, 48

reflectance
 of interface, 39

refraction
 index of, 25

index of, effective, 26
Snell law, 25

resonance
 Fabry-Pérot, 118
 Fano resonance, 135
 individual magnetic, 131
 plasmonic, 126
 strength of, 128

resonances
 individual, 51
 individual in cut wires, 126

response function, *see* dispersion 16
 magnetic, 19

reststrahlen bands, 55

right-handed triplet, 15

ringing artifacts, 81

s-parameter method, 77

scattering parameter method, 118

self inductance of wire, 122

simulation
 critical frequency of, 68
 temporal resolution of, 68

single-interface, 95

Snell law, 25

spatial walk-off, 27

split-ring resonator
 history, 60
 spectra, 131
 symmetric, 131

spoof surface plasmons, 167

spray-drying technique, 107

stabilized biconjugate gradient, 76

staggered grid, 67

staircasing errors, 67

stop bands, *see* band gap

sub-wavelength hole array, 170

superlens, 60

surface magnons, 23

surface phonon-polaritons, 23

surface plasmons, 23
 Zenneck regime, 167

tensor
 of permittivity, 23
 of wavefront projection, 15

time-domain terahertz spectroscopy, 103

transform
 Fourier, 17

transformation optics, 57

transmittance
 of interface, 39

unfolding, 94

unit cell, 42

vacuum impedance, 81

velocity
 dispersion of group v., 27
 group v., 26
 negative phase velocity, 40
 of information propagation, 41
 of light in vacuum, 15

voxel, 66

wave
 additional, 38
 evanescent, 51, 55
 harmonic, 14
 longitudinal, 14
 plane wave, 14
 transverse, 14

wave equation
 in vacuum, 14

Wave propagation retrieval method, 95

wave vector, 14, 24
 of Bloch's wave, 45

Wigner-Seitz cell, 42

Wood's anomaly, 167

woodpile structure, 54

yablonovite, 54

zero-index metamaterials, 57

zero-width band gap, 118, 157

Table 6.1: Table of abbreviations

| Abbreviation | Meaning |
|---------------|---|
| 1-D, 2-D, 3-D | One-, two- and three-dimensional |
| CDH | Current-Driven Homogenisation |
| EDB | (Formulation of Maxwell equations using the E, D and B vectors) |
| EOT | Extraordinary optical transmission |
| FDFD | Finite-difference frequency-domain (algorithm) |
| FDM | Filter diagonalisation method (algorithm) |
| FDTD | Finite-difference time-domain (algorithm) |
| FEM | Finite-element method (algorithm) |
| FFT | Fast Fourier transform (algorithm) |
| FOM | Figure of Merit |
| FRoI | Frequency range of interest |
| GVD | Group velocity dispersion |
| IFC | Isofrequency contours |
| LHM | Left-Handed (Meta)Material |
| MM | Metamaterial |
| NGV | Negative group velocity |
| NRI | Negative refractive index |
| NRW | Nicolson-Ross-Weir (algorithm) |
| PBG | Photonic band-gap |
| PhC | Photonic crystal |
| PWEM | Plane-wave expansion method (algorithm) |
| RHM | Right-Handed (Meta)Material |
| SPP | Surface Plasmon-Polariton |
| SRR | Split-ring resonator |
| sSRR | Symmetric split-ring resonator |
| STO | Strontium titanate, SrTiO_3 (ferroelectric material) |
| TDTS | Time-domain terahertz spectroscopy |

Table 6.2: Symbols used, approximately in the order they are introduced in text

| Symbol | Meaning |
|---|---|
| \mathbf{E} | Electric field |
| E_0 | Amplitude of the electric field |
| \mathbf{D} | Electric displacement |
| \mathbf{H} | Magnetic field |
| \mathbf{B} | Magnetic displacement |
| ε_0 | Vacuum permittivity, $8.85 \cdot 10^{-12} \text{ F/m}$ |
| μ_0 | Vacuum permeability, $1.25 \cdot 10^{-6} \text{ H/m}$ |
| r, t | reflectance, transmittance |
| i | Imaginary unit, $i^2 = -1$ |
| e | Euler constant, $e = 2.718\dots$ |
| π | $\pi = 3.141\dots$ |
| f | Frequency |
| ω | Angular frequency, $\omega = 2\pi f$ |
| \mathbf{k} | Wave vector in homogeneous media |
| \mathbf{K} | Wave vector of the Bloch wave in periodic media |
| t, τ | Time |
| c | Speed of light in vacuum, $c = 2.998 \cdot 10^8 \text{ m/s}$ |
| $f(t), F(\omega)$ | Function in the time domain, and in the frequency domain |
| χ_e, χ_m | Electric and magnetic susceptibility in the local approximantion |
| $\varepsilon_r(\omega), \mu_r(\omega)$ | Relative permittivity and permeability in the local approximation |
| $\varepsilon_r(\omega, \mathbf{k})$ | Relative permittivity for nonlocal media |
| $\mu_r(\omega, \mathbf{k})$ | Relative permeability for nonlocal media |
| $\varepsilon_r^{\text{LL}}(\omega, \mathbf{k})$ | Relative permittivity in the Landau-Lifshitz (EDB) formulation |
| N_{eff} | Effective index of refraction (of periodic media) |
| Z_{eff} | Effective impedance |
| $\varepsilon_{\text{eff}}, \mu_{\text{eff}}$ | Effective permittivity and permeability (of periodic media) |
| \mathbf{r}, ρ | Position in space (radius vector) |
| $\mathbf{a}_{1,2,3}, a$ | Lattice vectors, unit cell size in the cubic lattice |
| \mathbb{R} | Real numbers |
| \mathbb{Z} | Integers |
| \mathbb{C} | Complex numbers |
| h | Planck constant, $h = 6.626 \cdot 10^{-34} \text{ J s}$ |

Bibliography

- [1] J. D. Hunter. Matplotlib: A 2D graphics environment. *Computing In Science & Engineering* **9**, 90–95 (2007).
- [2] A. F. Oskooi et al. MEEP: A flexible free-software package for electromagnetic simulations by the FDTD method. *Comput. Phys. Commun.* **181**, 687–702 (Jan. 2010).
- [3] S. Johnson and J. D. Joannopoulos. Block-iterative frequency-domain methods for Maxwell’s equations in a planewave basis. *Opt. Express* **8**, 173–190 (2001).
- [4] L. Ozyuzer et al. Emission of coherent THz radiation from superconductors. *Science* **318**, 1291–1293 (2007).
- [5] N. Engheta and R. W. Ziolkowski. *Metamaterials: physics and engineering explorations*. John Wiley & Sons, 2006.
- [6] C. M. Krowne and Y. Zhang. *Physics of negative refraction and negative index materials: optical and electronic aspects and diversified approaches*. Springer, 2007.
- [7] G. V. Eleftheriades and K. G. Balmain. *Negative-refraction metamaterials: fundamental principles and applications*. John Wiley & Sons, 2005.
- [8] C. F. Klingshirn. *Semiconductor optics*. Springer, 2007.
- [9] J. D. Jackson. *Classical electrodynamics*. Wiley New York etc., 1962.
- [10] V. G. Veselago. The Electrodynamics of Substances with Simultaneously Negative Values of ϵ and μ . *Phys. Usp.* **10**, 509–514 (1968).
- [11] M. Born and E. Wolf. *Principles of optics: electromagnetic theory of propagation, interference and diffraction of light*. CUP Archive, 1999.
- [12] M. A. Noginov and V. A. Podolskiy. *Tutorials in metamaterials*. CRC Press, 2011.
- [13] L. D. Landau et al. *Electrodynamics of continuous media*. Elsevier, 1984, page 359.
- [14] V. M. Agranovich and Y. N. Gartstein. Spatial dispersion and negative refraction of light. *Phys. Usp.* **49**, 1029 (2006).
- [15] V. M. Agranovich and Y. N. Gartstein. Physics of negative refraction and negative index materials: optical and electronic aspects and diversified approaches. In: edited by C. M. Krowne and Y. Zhang. Springer, 2007. Chapter Spatial Dispersion, Polaritons, and Negative Refraction.

- [16] J. D. Joannopoulos et al. *Photonic crystals: molding the flow of light*. Princeton university press, 2011.
- [17] M. Rybin et al. Photonic properties of two-dimensional high-contrast periodic structures: Numerical calculations. *Phys. Solid State* **56**, 588–593 (2014).
- [18] K. Vynck et al. All-dielectric rod-type metamaterials at optical frequencies. *Phys. Rev. Lett.* **102**, 133901 (2009).
- [19] M. Wubs et al. Nonlocal modification and quantum optical generalization of effective-medium theory for metamaterials. In: *SPIE NanoScience+ Engineering*. International Society for Optics and Photonics. 2013, 88061F–88061F.
- [20] M. Dresselhaus. Optical properties of solids. *Proc. of Int. School of Phys. Enrico Fermi*, 243 (1966).
- [21] I. V. Lindell et al. BW media—Media with negative parameters, capable of supporting backward waves. *Microwave Opt. Technol. Lett.* **31**, 129–133 (2001).
- [22] V. Shalaev and W. Cai. *Optical metamaterials: fundamentals and applications*. Springer, 2010.
- [23] A. D. Boardman, N. King, and L. Velasco. Negative refraction in perspective. *Electromagnetics* **25**, 365–389 (2005).
- [24] S. M. Mikki and A. A. Kishk. Electromagnetic wave propagation in nonlocal media: Negative group velocity and beyond. *Progress In Electromagnetics Research B* **14**, 149–174 (2009).
- [25] V. Makarov and A. Rukhadze. The permittivity of a monatomic gas with spatial dispersion. *J. Exp. Theor. Phys.* **98**, 305–315 (2004).
- [26] C. R. Fietz. Homogenization of metamaterials with spatial dispersion. PhD thesis. 2011.
- [27] J. Skaar and C. A. Dirdal. Diamagnetism and the dispersion of the magnetic permeability. *arXiv preprint arXiv:1410.5999* (2014).
- [28] A. P. Vinogradov. On the form of constitutive equations in electrodynamics. *Phys. Usp.* **45**, 331 (2002).
- [29] V. Agranovich et al. Linear and nonlinear wave propagation in negative refraction metamaterials. *Phys. Rev. B* **69**, 165112 (2004).
- [30] V. M. Agranovich and V. L. Ginzburg. Crystal optics with allowance for spatial dispersion; exciton theory. *Soviet Physics Uspekhi* **5**, 323 (1962).
- [31] S. Pekar and M. Strashnikova. Spatial dispersion and additional light waves in the region of exciton absorption in CdS. *Zhurnal Eksperimentalnoi i Teoreticheskoi Fiziki* **68**, 2047–2054 (1975).
- [32] A. Bungay, Y. P. Svirko, and N. Zheludev. Equivalency of the Casimir and the Landau-Lifshitz approaches to continuous-media electrodynamics and optical activity on reflection. *Phys. Rev. B* **47**, 11730 (1993).
- [33] A. A. Golubkov and V. A. Makarov. Boundary conditions for electromagnetic field on the surface of media with weak spatial dispersion. *Phys. Usp.* **38**, 325–332 (1995).

- [34] M. Lapine, L. Jelinek, and R. Marqués. Surface mesoscopic effects in finite metamaterials. *Optics express* **20**, 18297–18302 (2012).
- [35] G. Dolling et al. Simultaneous negative phase and group velocity of light in a metamaterial. *Science* **312**, 892–894 (2006).
- [36] M. Hill. The uncertainty principle for Fourier transforms on the real line (2013).
- [37] S. G. Johnson and J. D. Joannopoulos. Introduction to photonic crystals: Bloch's theorem, band diagrams, and gaps (but no defects). *Photonic Crystal Tutorial*, 1–16 (2003).
- [38] L. Brillouin. *Wave propagation in periodic structures: electric filters and crystal lattices*. Courier Corporation, 2003.
- [39] M. Vanwolleghem et al. Unidirectional band gaps in uniformly magnetized two-dimensional magnetophotonic crystals. *Phys. Rev. B* **80**, 121102 (2009).
- [40] S. O'Brien and J. B. Pendry. Photonic band-gap effects and magnetic activity in dielectric composites. *J. Phys.: Condens. Matter* **14**, 4035 (2002).
- [41] V. Yannopapas and A. Moroz. Negative refractive index metamaterials from inherently non-magnetic materials for deep infrared to terahertz frequency ranges. *J. Phys.: Condens. Matter* **17**, 3717 (2005).
- [42] S. Chakrabarti and S. A. Ramakrishna. Magnetic response of split ring resonator metamaterials: From effective medium dispersion to photonic band gaps. *Pramana* **78**, 483–492 (2012).
- [43] N. A. Mortensen et al. On the unambiguous determination of effective optical properties of periodic metamaterials: a one-dimensional case study. *Journal of the European Optical Society-Rapid publications* **5** (2010).
- [44] P. Yeh, A. Yariv, and C.-S. Hong. Electromagnetic propagation in periodic stratified media. I. General theory. *JOSA* **67**, 423–438 (1977).
- [45] L. Shi, X. Jiang, and C. Li. Effects induced by Mie resonance in two-dimensional photonic crystals. *J. Phys.: Condens. Matter* **19**, 176214 (2007).
- [46] D. Felbacq and G. Bouchitté. Theory of mesoscopic magnetism in photonic crystals. *Phys. Rev. Lett.* **94**, 183902 (2005).
- [47] R. Merlin. Metamaterials and the Landau–Lifshitz permeability argument: large permittivity begets high-frequency magnetism. *Proceedings of the National Academy of Sciences* **106**, 1693–1698 (2009).
- [48] A. Laktionov, A. Merzlikin, and A. Vinogradov. Mechanism of formation of band gaps in one-dimensional photonic quasi-crystals. *J. Commun. Technol. Electron.* **53**, 890–894 (2008).
- [49] D. R. Smith and J. B. Pendry. Homogenization of metamaterials by field averaging. *JOSA B* **23**, 391–403 (2006).
- [50] A. Sihvola. *Electromagnetic emergence in metamaterials*. Springer, 2002.

- [51] E. Shamonina and L. Solymar. Metamaterials: How the subject started. *Metamaterials* **1**, 12–18 (2007).
- [52] G. V. Eleftheriades and M. Selvanayagam. Transforming electromagnetics using metamaterials. *Microwave Magazine, IEEE* **13**, 26–38 (2012).
- [53] H. Paudyal, M. Johrib, and A. Tiwari. From Left Handed Materials to Invisible Cloak: Recent Advances. *Himalayan Physics* **4**, 18–26 (2013).
- [54] A. Moroz. *Some negative refractive index material headlines long before Veselago work and going back as far as to 1905.* 2009. URL: <http://www.wave-scattering.com/negative.html> (visited on 07/30/2015).
- [55] W. Friedrich, P. Knipping, and M. Laue. Interferenzerscheinungen bei roentgenstrahlen. *Ann. Phys.* **346**, 971–988 (1913).
- [56] W. Bragg and W. Bragg. The reflection of X-rays by crystals. *Proc. Roy. Soc. London. Series A, Containing Papers of a Mathematical and Physical Character*, 428–438 (1913).
- [57] H. Nemec et al. Highly tunable photonic crystal filter for the terahertz range. *Opt. Lett.* **30**, 549–551 (2005).
- [58] K. Ho, C. Chan, and C. Soukoulis. *Periodic dielectric structure for production of photonic band gap and devices incorporating the same.* US Patent 5,335,240. 1994. URL: <https://www.google.com.ar/patents/US5335240>.
- [59] W. Sweatt and T. Christenson. *Method for the fabrication of three-dimensional microstructures by deep X-ray lithography.* US Patent 6,875,544. 2005. URL: <https://www.google.com.ar/patents/US6875544>.
- [60] E. Yablonovitch. Inhibited Spontaneous Emission in Solid-State Physics and Electronics. *Phys. Rev. Lett.* **58**, 2059–2062 20(1987). URL: <http://link.aps.org/doi/10.1103/PhysRevLett.58.2059>.
- [61] R. Zengerle. Light propagation in singly and doubly periodic planar waveguides. *J. Mod. Opt.* **34**, 1589–1617 (1987).
- [62] P. Russell. Photonic crystal fibers: a historical account. *IEEE Leos Newsletter* **21**, 11–15 (2007).
- [63] H. Pažoutová. Analysis and simulations of selected negative refractive index structures. Czech Technical University, Prague, 2011.
- [64] A. Schuster. *An introduction to the theory of optics.* E. Arnold, 1904.
- [65] L. Mandelstam. Lectures on optics, relativity theory and quantum mechanics. Nauka Eds., Moscow, 1972. 440 pp. Under the revision by corresponding member of the Academy of Sciences of USSRSM Rytov.(Russian Title: *Lektsii po optike, teorii otnositel'nosti i kvantovoi mehanike*) **1**, 440 (1971).
- [66] D. Sivukhin. The energy of electromagnetic waves in dispersive media. *Opt. Spektrosk* **3**, 2 (1957).
- [67] V. Pafomov. Cerenkov radiation in anisotropic ferrites. *SOVIET PHYSICS JETP-USSR* **3**, 597–600 (1956).

- [68] R. Silin. Possibility of creating plane-parallel lenses. *Opt. Spectrosc.* **44**, 109–110 (1978).
- [69] A. A. Basharin et al. Epsilon near zero based phenomena in metamaterials. *Phys. Rev. B* **87**, 155130 (2013).
- [70] B. T. Schwartz and R. Piestun. Total external reflection from metamaterials with ultralow refractive index. *JOSA B* **20**, 2448–2453 (2003).
- [71] L. Dollin. On the possibility of comparison of three-dimensional electromagnetic systems with nonuniform anisotropic filling. *Izv. VUZov Radiofizika* **4**, 964–967 (1961).
- [72] M. Kerker. Invisible bodies. *JOSA* **65**, 376–379 (1975).
- [73] D. Schurig et al. Metamaterial electromagnetic cloak at microwave frequencies. *Science* **314**, 977–980 (2006).
- [74] J. Valentine et al. An optical cloak made of dielectrics. *Nat. Mater.* **8**, 568–571 (2009).
- [75] N. Wang et al. Homogeneous anisotropic dielectric invisibility carpet cloak made of Al₂O₃ plates. *EPL (Europhys. Lett.)* **104**, 14003 (2013).
- [76] W. Weber. On the relationship of the science of the diamagnetism with the sciences of magnetism and electricity. *Ann. Phys* **87**, 145–189 (1852).
- [77] W. J. A. F. *Artificial dielectric polarizer*. US Patent 2,921,312. 1960. URL: <http://www.google.com/patents/US2921312>.
- [78] D. L. Anderson. *Artificial dielectric lens structure*. US Patent 3,329,958. 1967. URL: <http://www.google.ru/patents/US3329958>.
- [79] H. P. W. *Artificial dielectric using interspersed rods*. US Patent 3,254,345. 1966. URL: <http://www.google.com.py/patents/US3254345>.
- [80] L. Rayleigh. On the influence of obstacles arranged in rectangular order upon the properties of a medium. *The London, Edinburgh, and Dublin Philos. Mag. and Journal of Science* **34**, 481–502 (1892).
- [81] J. C. Bose. On the rotation of plane of polarisation of electric waves by a twisted structure. *Proc. Roy. Soc. London* **63**, 146–152 (1898).
- [82] D. Emerson. *Jagadis Chandra Bose: Millimetre wave research in the nineteenth century*. 1998. URL: <https://www.cv.nrao.edu/~demerson/bose/bose.html> (visited on 07/30/2015).
- [83] J. Brown and W. Jackson. The properties of artificial dielectrics at centimetre wavelengths. *Proceedings of the IEE-Part B: Radio Electron. Eng.ing* **102**, 11–16 (1955).
- [84] W. E. Kock. Metallic delay lenses. *Bell System Technical Journal* **27**, 58–82 (1948).
- [85] W. Rotman. Plasma simulation by artificial dielectrics and parallel-plate media. *Antennas and Propagation, IRE Transactions on* **10**, 82–95 (1962).
- [86] G. Merkel. *Simulation of a simple Lorentz plasma with a random distribution of inductively loaded dipoles*. Technical report. DTIC Document, 1973.

- [87] J. Brown. Artificial dielectrics having refractive indices less than unity. *Proceedings of the IEE-Part IV: Institution Monographs* **100**, 51–62 (1953).
- [88] L. Lewin. The electrical constants of a material loaded with spherical particles. *J. Inst. Electr. Eng.-Part III: Radio and Communication Engineering* **94**, 65–68 (1947).
- [89] S. A. Schelkunoff and H. T. Friis. *Antennas: theory and practice*. Volume 639. Wiley New York, 1952.
- [90] J. B. Pendry et al. Magnetism from conductors and enhanced nonlinear phenomena. *Microwave Theory and Techniques, IEEE Transactions on* **47**, 2075–2084 (1999).
- [91] D. R. Smith et al. Composite medium with simultaneously negative permeability and permittivity. *Phys. Rev. Lett.* **84**, 4184 (2000).
- [92] J. B. Pendry. Negative refraction makes a perfect lens. *Phys. Rev. Lett.* **85**, 3966 (2000).
- [93] J. Zhou, T. Koschny, and C. M. Soukoulis. An efficient way to reduce losses of left-handed metamaterials. *Opt. Express* **16**, 11147–11152 (2008).
- [94] G. V. Naik, J. Kim, and A. Boltasseva. Oxides and nitrides as alternative plasmonic materials in the optical range. *Opt. Mater. Express* **1**, 1090–1099 (2011).
- [95] N. I. Zheludev. The road ahead for metamaterials. *Science* **328**, 582–583 (2010).
- [96] R. Zhao et al. Repulsive Casimir force in chiral metamaterials. *Phys. Rev. Lett.* **103**, 103602 (2009).
- [97] M. G. Silveirinha and S. I. Maslovski. Comment on “Repulsive Casimir Force in Chiral Metamaterials”. *Phys. Rev. Lett.* **105**, 189301 (2010).
- [98] T. Paul et al. Reflection and transmission of light at periodic layered metamaterial films. *Phys. Rev. B* **84**, 115142 (2011).
- [99] F. Dominec et al. Transition between metamaterial and photonic-crystal behavior in arrays of dielectric rods. *Opt. Express* **22**, 30492–30503 (2014).
- [100] M. V. Rybin et al. Phase diagram for the transition from photonic crystals to dielectric metamaterials. *arXiv preprint arXiv:1507.08901* (2015).
- [101] J. Li et al. Photonic band gap from a stack of positive and negative index materials. *Phys. Rev. Lett.* **90**, 083901 (2003).
- [102] Y. Chen et al. Derivation and characterization of dispersion of defect modes in photonic band gap from stacks of positive and negative index materials. *Phys. Lett. A* **351**, 446–451 (2006).
- [103] N. C. Panoiu et al. Zero-n bandgap in photonic crystal superlattices. *JOSA B* **23**, 506–513 (2006).
- [104] S. Kocaman et al. Zero phase delay in negative-refractive-index photonic crystal superlattices. *Nat. Photonics* **5**, 499–505 (2011).

- [105] L.-G. Wang, H. Chen, and S.-Y. Zhu. Omnidirectional gap and defect mode of one-dimensional photonic crystals with single-negative materials. *Phys. Rev. B* **70**, 245102 (2004).
- [106] T. Koschny et al. Resonant and antiresonant frequency dependence of the effective parameters of metamaterials. *Phys. Rev. E* **68**, 065602 (2003).
- [107] H. Wallen et al. Anti-resonant response of resonant inclusions? In: *General Assembly and Scientific Symposium, 2011 XXXth URSI*. IEEE. 2011, pages 1–4.
- [108] I. Tsukerman. Nonlocal homogenization of metamaterials by dual interpolation of fields. *JOSA B* **28**, 2956–2965 (2011).
- [109] L. Peng et al. Experimental observation of left-handed behavior in an array of standard dielectric resonators. *Phys. Rev. Lett.* **98**, 157403 (2007).
- [110] The Metamorphose collaboration. *Metamaterials - Definition*. Online. Last visited December 2015. URL: <http://www.metamorphose-vi.org/index.php/metamaterials>.
- [111] A. Taflove and S. Hagness. *Computational Electrodynamics: The Finite-Difference Time-Domain Method* (Artech House, 2005).
- [112] K. S. Yee et al. Numerical solution of initial boundary value problems involving Maxwell's equations in isotropic media. *IEEE Trans. Antennas Propag* **14**, 302–307 (1966).
- [113] A. Farjadpour et al. Improving accuracy by subpixel smoothing in the finite-difference time domain. *Opt. Lett.* **31**, 2972–2974 (2006).
- [114] A. Deinega and I. Valuev. Subpixel smoothing for conductive and dispersive media in the finite-difference time-domain method. *Opt. Lett.* **32**, 3429–3431 (2007).
- [115] A. F. Oskooi, C. Kottke, and S. G. Johnson. Accurate finite-difference time-domain simulation of anisotropic media by subpixel smoothing. *Opt. Lett.* **34**, 2778–2780 (Sept. 2009).
- [116] J. Hamm, F. Renn, and O. Hess. Dispersive Media Subcell Averaging in the FDTD Method using Corrective Surface Currents (2013).
- [117] F. Dominec. *MEEP metamaterial simulation scripts*. Online. Last visited May 2014. URL: https://github.com/FilipDominec/meep%5C_metamaterials.
- [118] A. D. Rakic et al. Optical properties of metallic films for vertical-cavity optoelectronic devices. *Appl. Opt.* **37**, 5271–5283 (1998).
- [119] J. D. Joannopoulos, S. G. Johnson, et al. *The Joannopoulos Research Group at MIT*. Online. Last visited October 2015. URL: <http://ab-initio.mit.edu/photons/index.html>.
- [120] F. Dominec. *MPB plotting script*. Online. Last visited October 2015. URL: <https://github.com/FilipDominec/mpb-plotting>.
- [121] A. Nicolson and G. Ross. Measurement of the intrinsic properties of materials by time-domain techniques. *Instrumentation and Measurement, IEEE Transactions on* **19**, 377–382 (1970).

- [122] W. B. Weir. Automatic measurement of complex dielectric constant and permeability at microwave frequencies. *Proceedings of the IEEE* **62**, 33–36 (1974).
- [123] T. Terao. Finite-difference frequency-domain method to study photonic crystals with dispersive metamaterials. *Japanese J. Appl. Phys.* **50**, 2204 (2011).
- [124] A. Oskooi and S. G. Johnson. Distinguishing correct from incorrect PML proposals and a corrected unsplit PML for anisotropic, dispersive media. *J. Comput. Phys.* **230**, 2369–2377 (2011).
- [125] H. Němec et al. Tunable terahertz metamaterials with negative permeability. *Phys. Rev. B* **79**, 241108 (2009).
- [126] D. R. Smith et al. Determination of effective permittivity and permeability of metamaterials from reflection and transmission coefficients. *Phys. Rev. B* **65**, 195104 (2002).
- [127] D. R. Smith et al. Electromagnetic parameter retrieval from inhomogeneous metamaterials. *Phys. Rev. E* **71**, 036617 (2005).
- [128] C. R. Simovski. Material parameters of metamaterials (a review). *Opt. Spectrosc.* **107**, 726–753 (2009).
- [129] V. A. Markel and I. Tsukerman. Current-driven homogenization and effective medium parameters for finite samples. *Phys. Rev. B* **88**, 125131 (2013).
- [130] C. R. Simovski. Bloch material parameters of magneto-dielectric metamaterials and the concept of Bloch lattices. *Metamaterials* **1**, 62–80 (2007).
- [131] A. Andryieuski et al. Bloch-mode analysis for retrieving effective parameters of metamaterials. *Phys. Rev. B* **86**, 035127 (2012).
- [132] C. Rockstuhl et al. Transition from thin-film to bulk properties of metamaterials. *Phys. Rev. B* **77**, 035126 (2008).
- [133] A. Andryieuski, R. Malureanu, and A. V. Lavrinenko. Homogenization of metamaterials: Parameters retrieval methods and intrinsic problems. In: *Transparent Optical Networks (ICTON), 2010 12th International Conference on*. IEEE. 2010, pages 1–5.
- [134] M. G. Silveirinha. Metamaterial homogenization approach with application to the characterization of microstructured composites with negative parameters. *Phys. Rev. B* **75**, 115104 (2007).
- [135] C. Fietz and G. Shvets. Current-driven metamaterial homogenization. *Physica B* **405**, 2930–2934 (2010).
- [136] V. A. Mandelshtam and H. S. Taylor. Harmonic inversion of time signals and its applications. *The J. Chem. Phys.* **107**, 6756–6769 (1997).
- [137] K. Cao. A comparative study of the filter diagonalization method and decimated signal diagonalization method for one-dimensional NMR data processing. *UCI Undergraduate Res. J* **5**, 1–8 (2002).
- [138] K. Chalapat et al. Wideband reference-plane invariant method for measuring electromagnetic parameters of materials. *Microwave Theory and Techniques, IEEE Transactions on* **57**, 2257–2267 (2009).

- [139] H. Němec et al. Resonant magnetic response of TiO₂ microspheres at terahertz frequencies. *Appl. Phys. Lett.* **100**, 061117–061117 (2012).
- [140] X. Chen et al. Robust method to retrieve the constitutive effective parameters of metamaterials. *Phys. Rev. E* **70**, 016608 (2004).
- [141] Z. Szabo et al. A unique extraction of metamaterial parameters based on Kramers–Kronig relationship. *Microwave Theory and Techniques, IEEE Transactions on* **58**, 2646–2653 (2010).
- [142] C. Menzel et al. Retrieving effective parameters for metamaterials at oblique incidence. *Phys. Rev. B* **77**, 195328 (2008).
- [143] Z. Li, K. Aydin, and E. Ozbay. Determination of the effective constitutive parameters of bianisotropic metamaterials from reflection and transmission coefficients. *Phys. Rev. E* **79**, 026610 (2009).
- [144] J. Yang et al. Retrieving the effective parameters of metamaterials from the single interface scattering problem. *Appl. Phys. Lett.* **97**, 061102 (2010).
- [145] S. Zhang et al. Optical negative-index bulk metamaterials consisting of 2D perforated metal-dielectric stacks. *Opt. Express* **14**, 6778–6787 (2006).
- [146] C. Rockstuhl et al. Light propagation in a fishnet metamaterial. *Phys. Rev. B* **78**, 155102 (2008).
- [147] J. Petschulat et al. Multipole approach to metamaterials. *Phys. Rev. A* **78**, 043811 (2008).
- [148] S. Sun, S. Chui, and L. Zhou. Effective-medium properties of metamaterials: a quasimode theory. *Phys. Rev. E* **79**, 066604 (2009).
- [149] C. R. Simovski. On electromagnetic characterization and homogenization of nanostructured metamaterials. *J. Opt.* **13**, 013001 (2011).
- [150] R. A. Lewis. A review of terahertz sources. *J. Phys. D: Appl. Phys.* **47**, 374001 (2014).
- [151] Y.-S. Lee. *Principles of terahertz science and technology*. 2008.
- [152] C. M. O’Sullivan and J. A. Murphy. Field Guide to Terahertz Sources, Detectors, and Optics. In: SPIE. 2012. URL: <http://spie.org/samples/FG28.pdf>.
- [153] P. Alexej. Terahertz spectroscopy of ferroelectrics and related materials. PhD thesis. Charles University, Prague, 2004.
- [154] H. Němec. Time-resolved terahertz spectroscopy applied to the investigation of magnetic materials and photonic structures. PhD thesis. Charles University, Prague, 2006.
- [155] L. Fekete. Ultrafast carrier dynamics in semiconductors studied by Time-resolved terahertz spectroscopy. PhD thesis. Charles University, Prague, 2008.
- [156] J. Šibík. Application of metamaterial structures in terahertz spectral range. Charles University, Prague, 2010.

- [157] R. Yahiaoui. Caractérisation de métamatériaux pour applications millimétriques et submillimétriques. PhD thesis. Bordeaux 1, 2011.
- [158] Z. Mics. Dynamics of delocalized states in molecular systems studied by time-resolved THz spectroscopy. PhD thesis. Charles University, Prague, 2012.
- [159] V. Skoromets. Tunable materials and structures for terahertz spectral range. PhD thesis. Charles University, Prague, 2013.
- [160] M. Asada, S. Suzuki, and N. Kishimoto. Resonant tunneling diodes for sub-terahertz and terahertz oscillators. *Japanese J. Appl. Phys.* **47**, 4375 (2008).
- [161] E. Brown et al. Oscillations up to 712 GHz in InAs/AlSb resonant-tunneling diodes. *Appl. Phys. Lett.* **58**, 2291–2293 (1991).
- [162] B. Thomas et al. First results of a 1.2 THz MMIC sub-harmonic mixer based GaAs Schottky diodes for planetary atmospheric remote sensing. *ISST Proc*, 100–102 (2012).
- [163] A. Leitenstorfer et al. Detectors and sources for ultrabroadband electro-optic sampling: Experiment and theory. *Appl. Phys. Lett.* **74**, 1516–1518 (1999).
- [164] P. Han et al. Use of the organic crystal DAST for terahertz beam applications. *Opt. Lett.* **25**, 675–677 (2000).
- [165] D. Auston et al. Cherenkov radiation from femtosecond optical pulses in electro-optic media. *Phys. Rev. Lett.* **53**, 1555 (1984).
- [166] T. Löffler, F. Jacob, and H. Roskos. Generation of terahertz pulses by photoionization of electrically biased air. *Appl. Phys. Lett.* **77**, 453–455 (2000).
- [167] Y. Chen et al. Terahertz pulse generation from noble gases. *Appl. Phys. Lett.* **91**, 251116 (2007).
- [168] L. Yu-Tong et al. High power terahertz pulses generated in intense laser-plasma interactions. *Chin. Phys. B* **21**, 095203 (2012).
- [169] P. Gu et al. Generation of coherent cw-terahertz radiation using a tunable dual-wavelength external cavity laser diode. *Japanese J. Appl. Phys.* **38**, L1246 (1999).
- [170] D. Auston, K. Cheung, and P. Smith. Picosecond photoconducting Hertzian dipoles. *Appl. Phys. Lett.* **45**, 284–286 (1984).
- [171] J. Darrow et al. Subpicosecond electromagnetic pulses from large-aperture photoconducting antennas. *Opt. Lett.* **15**, 323–325 (1990).
- [172] B. Hu et al. Optically steerable photoconducting antennas. *Appl. Phys. Lett.* **56**, 886–888 (1990).
- [173] A. Corchia et al. Effects of magnetic field and optical fluence on terahertz emission in gallium arsenide. *Phys. Rev. B* **64**, 205204 (2001).
- [174] J. Heyman et al. Terahertz emission from GaAs and InAs in a magnetic field. *Phys. Rev. B* **64**, 085202 (2001).

- [175] T. Chang, T. Bridges, and E. Burkhardt. CW submillimeter laser action in optically pumped methyl fluoride, methyl alcohol, and vinyl chloride gases. *Appl. Phys. Lett.* **17**, 249–251 (1970).
- [176] X. Yin, B. W.-H. Ng, and D. Abbott. *Terahertz imaging for biomedical applications: Pattern Recognit. and tomographic reconstruction*. Springer Science & Business Media, 2012.
- [177] F. Kadlec, P. Kužel, and J.-L. Coutaz. Optical rectification at metal surfaces. *Opt. Lett.* **29**, 2674–2676 (2004).
- [178] F. Kadlec, P. Kuzel, and J.-L. Coutaz. Study of terahertz radiation generated by optical rectification on thin gold films. *Opt. Lett.* **30**, 1402–1404 (2005).
- [179] G. Ramakrishnan et al. Surface plasmon-enhanced terahertz emission from a hemicyanine self-assembled monolayer. *Opt. Express* **20**, 4067–4073 (2012).
- [180] G. Doucas et al. First observation of Smith-Purcell radiation from relativistic electrons. *Phys. Rev. Lett.* **69**, 1761 (1992).
- [181] K. Tantiwanichapan, X. Wang, and R. Swan Anna K and Paiella. Graphene on nanoscale gratings for the generation of terahertz Smith-Purcell radiation. *Appl. Phys. Lett.* **105**, 241102 (2014).
- [182] D. Face et al. High quality tantalum superconducting tunnel junctions for microwave mixing in the quantum limit. *Appl. Phys. Lett.* **48**, 1098–1100 (1986).
- [183] Q. Wu and X.-C. Zhang. Ultrafast electro-optic field sensors. *Appl. Phys. Lett.* **68**, 1604–1606 (1996).
- [184] J. Riordan et al. Free-space transient magneto-optic sampling. *Appl. Phys. Lett.* **71**, 1452–1454 (1997).
- [185] M. Van Exter, C. Fattinger, and D. Grischkowsky. Terahertz time-domain spectroscopy of water vapor. *Opt. Lett.* **14**, 1128–1130 (1989).
- [186] P. Kužel et al. Gouy shift correction for highly accurate refractive index retrieval in time-domain terahertz spectroscopy. *Opt. Express* **18**, 15338–15348 (2010).
- [187] M. D. Abràmoff, P. J. Magalhães, and S. J. Ram. Image processing with ImageJ. *Biophotonics international* **11**, 36–43 (2004).
- [188] F. Dominec. *Calculating size distribution of powder particles using ImageJ*, <http://f.dominec.eu/granulo/index.html>, Last visited April 2015. Online.
- [189] R. Yahiaoui et al. Tunable THz metamaterials based on an array of paraelectric SrTiO₃ rods. *Appl. Phys. A* **103**, 689–692 (2011).
- [190] F. Dominec. *TrioStepper, controller for three stepper motors*, Last visited May 2014. <https://github.com/FilipDominec/triostepper>, Online.
- [191] M. Silveirinha et al. Nonlocal homogenization of an array of cubic particles made of resonant rings. *Metamaterials* **3**, 115–128 (2009).
- [192] R. Marques et al. Bulk metamaterials made of resonant rings. *Proceedings of the IEEE* **99**, 1660–1668 (2011).

- [193] J. Pendry et al. Extremely low frequency plasmons in metallic mesostructures. *Phys. Rev. Lett.* **76**, 4773 (1996).
- [194] S. Maslovski, S. Tretyakov, and P. Belov. Wire media with negative effective permittivity: A quasi-static model. *Microw. Opt. Techn. Lett.* **35**, 47–51 (2002).
- [195] G. Mie. Beiträge zur Optik trüber Medien, speziell kolloidaler Metallösungen. *Ann. Phys.* **330**, 377–445 (1908).
- [196] L. Solymar and E. Shamonina. *Waves in metamaterials*. Oxford University Press, 2009.
- [197] R. Marques, L. Jelinek, and F. Mesa. Negative refraction from balanced quasi-planar chiral inclusions. *Microwave and Optical Technology Letters* **49**, 2606–2609 (2007).
- [198] L. Jelinek et al. Periodic arrangements of chiral scatterers providing negative refractive index bi-isotropic media. *Physical Review B* **77**, 205110 (2008).
- [199] C. Croënne. Contrôle de la propagation et du rayonnement électromagnétiques par les métamatériaux. PhD thesis. Université des Sciences et Technologie de Lille, Lille I, 2009.
- [200] N. Gibbons et al. Scalable cylindrical metallo-dielectric metamaterials. In: *Quantum Electron. and Laser Science Conference*. Optical Society of America. 2010, JWA3.
- [201] A. Wang et al. Fiber metamaterials with negative magnetic permeability in the terahertz. *Opt. Mater. Express* **1**, 115–120 (2011).
- [202] L. Jelinek and J. Machac. An FET-based unit cell for an active magnetic metamaterial. *arXiv preprint arXiv:1106.4144* (2011).
- [203] T. Koschny et al. Effective medium theory of left-handed materials. *Phys. Rev. Lett.* **93**, 107402 (2004).
- [204] J. Baena, L. Jelinek, and R. Marqués. Towards a systematic design of isotropic bulk magnetic metamaterials using the cubic point groups of symmetry. *Physical Review B* **76**, 245115 (2007).
- [205] L. Jelinek and R. Marqués. Artificial magnetism and left-handed media from dielectric rings and rods. *Journal of Physics: Condensed Matter* **22**, 025902 (2009).
- [206] R. Richtmyer. Dielectric resonators. *J. Appl. Phys.* **10**, 391–398 (1939).
- [207] J.-F. Baumard and F. Gervais. Plasmon and polar optical phonons in reduced rutile TiO_(2-x). *Phys. Review B* **15**, 2316 (1977).
- [208] Y. Yakiyama et al. Terahertz response of metamaterials constructed of TiO₂ spheres and a metal-mesh. In: *2012 37th International Conference on Infrared, Millimeter, and Terahertz Waves*. 2012.
- [209] M. Plihal et al. Two-dimensional photonic band structures. *Opt. Commun.* **80**, 199–204 (1991).
- [210] J. Pendry and A. MacKinnon. Calculation of photon dispersion relations. *Phys. Rev. Lett.* **69**, 2772–2775 (1992).

- [211] V. Skoromets et al. Tuning of dielectric properties of SrTiO₃ in the terahertz range. *Phys. Rev. B* **84**, 174121 (2011).
- [212] M. Navarro-Cía et al. Terahertz imaging of sub-wavelength particles with Zenneck surface waves. *Appl. Phys. Lett.* **103** (2013).
- [213] R. W. Wood. On a remarkable case of uneven distribution of light in a diffraction grating spectrum. *Proc. Phys. Soc. London* **18**, 269 (1902).
- [214] L. Rayleigh. On the dynamical theory of gratings. *Proc. Roy. Soc. London. Series A, Containing Papers of a Mathematical and Physical Character* **79**, 399–416 (1907).
- [215] P. Lalanne, J. Hugonin, and J. Rodier. Theory of surface plasmon generation at nanoslit apertures. *Phys. Rev. Lett.* **95**, 263902 (2005).
- [216] J. Weiner. The electromagnetics of light transmission through subwavelength slits in metallic films. *Opt. Express* **19**, 16139–16153 (2011).
- [217] M. Navarro-Cía et al. Dual-band double-negative-index fishnet metamaterial at millimeter-waves. *Opt. Lett.* **36**, 4245–4247 (2011).
- [218] R. Ulrich. Effective low-pass filters for far infrared frequencies. *Infrared Phys.* **7**, 65–74 (1967).
- [219] R. Ulrich. Far-infrared properties of metallic mesh and its complementary structure. *Infrared Phys.* **7**, 37–55 (1967).
- [220] P. Vogel and L. Genzel. Transmission and reflection of metallic mesh in the far infrared. *Infrared Phys.* **4**, 257–262 (1964).
- [221] T. W. Ebbesen et al. Extraordinary optical transmission through sub-wavelength hole arrays. *Nature* **391**, 667–669 (1998).
- [222] C. Croënne et al. Left handed dispersion of a stack of subwavelength hole metal arrays at terahertz frequencies. *Appl. Phys. Lett.* **94**, 133112 (2009).
- [223] J. Valentine et al. Development of bulk optical negative index fishnet metamaterials: Achieving a low-loss and broadband response through coupling. *Proceedings of the IEEE* **99**, 1682–1690 (2011).
- [224] S. Wang et al. Composite left/right-handed stacked hole arrays at submillimeter wavelengths. *J. Appl. Phys.* **107**, 074510 (2010).
- [225] M. J. Freire, R. Marques, and L. Jelinek. Experimental demonstration of a $\mu=-1$ metamaterial lens for magnetic resonance imaging. *Applied Physics Letters* **93**, 231108 (2008).